ADVANCED ELECTRON DIFFRACTION TECHNIQUES FOR STRUCTURAL ELUCIDATION OF MICROPOROUS MATERIALS

PhD DEGREE ON SUSTAINABLE CHEMISTRY

Juan Ignacio Tirado Castaño

Directors:

Dr. Jose Luis Jordá Moret

Dr. Partha Pratim Das

València, December 2024

INSTITUTO DE TECNOLOGÍA QUÍMICA

EXCELENCIA SEVERO OCHOA 07/2013-06/2017 07/2017-06/2021 2023-2026

CSIC Consejo Superior de Investigaciones Científicas

UNIVERSITAT POLITÈCNICA DE VALÈNCIA

"Why water boils at 100ºC and methane at -161ºC; why blood is red and grass is green; why diamond is hard and wax is soft; why graphite writes on paper and silk is strong; why glaciers flow and iron get hard when you hammer it; how muscles contract; how sunlight makes plants grow and how living organisms have been able to evolve into ever more complex forms…? The answers to all these problems have come from structural analysis."

Max Perutz, July 1996 (Churchill College, Cambridge)

Acknowledgments

Me gustaría en especial dedicar esta tesis a mis padres y a mi familia incluido mis hermanos, abuelos, primos y tíos. Me habéis dado todo y apoyado a lo largo de mi vida desde bebe, adolescente y etapa adulta. Por esos días ayudándome con la tarea en el cole, borrando libros de texto, llevándome al cole, a baloncesto, a violín, apuntándome a excursiones. Por esas tantas mudanzas, comidas, matriculas de universidad y, sobre todo, y simplemente, gracias por estar ahí presente. Gracias a todos. Y gracias a Dios por darme la familia que tengo. Os quiero. Y gracias al ángel que me regalaste. Eres mi mayor descubrimiento Clara.

Me gustaría agradecer a mis directores de tesis Jose Luis Jordá Moret y Partha Pratim Das. Muchas gracias. ধন্যবাদ. Thank you so much for this amazing and heartwarming support during these five years. Por darme la oportunidad de realizar una tesis doctoral en el ITQ. These years have been plenty of emotions, long videocalls and many visits to València and many 3DED experiments. Gracias por las correcciones de tesis y de artículos y por responder a todas mis dudas. También me gustaría agradecer a los autores y colaboraciones de los distintos trabajos: Fernando Rey, Susana Valencia, Andrés Sala, German Sastre, Lukas Palatinus, Stavros, Sergi Plana. Además del servicio de microscopia e instrumentación de la UPV: Manolo, Ximo, Jose Luis, Merche y Alicia.

Aunque sea el único de mi grupo, me siento en la necesidad máxima de agradecer con especial atención a mis mastodontales y tremendos compañeros y compañeras de todas las plantas del ITQ que me han acompañado en mis visitas por los pasillos y laboratorios, en las comidas en el Nexus y coffee, first dates, cenas, carreras y aventuras viajando. Sergio y Carmen, Andrés, Fran, Hilario, Alex, los Jordis, Raul, Amravati, Álvaro, las Cristinas y Miguel, Paloma y Bea, Juanan y Silvia, Susi, Silvia y Jose, Rosella, Sebas, Elena, Luis itq pelo corto, Luis itq pelo largo, los Adrianes, los Albertos, Carles, Jose, Wilson, Nilu, Carmen y Ferran, Christian, Dani, Camilo y Gonzalo, Francesco, Miquel, Yongkun, Lluís, los Carlos (Mori, Company y Montero), Oscar y Bea, Luciana, Quique, Miriam, Matea, Ander y Maria, Pilar, Mario, Pablos, Ömer, Pau, Reisel, Alechania, Álvaro, Sara, Mercedes, German, Javi Ceuta, Marcos, y muchas otras personas que no haya mencionado. Solamente esas miradas y sonrisas cruzadas por los pasillos son suficientes. Todos ellos han hecho sentirme en abrigado, haciéndome pertenecer a un equipo muy grande de investigación y de amistad. Solo os puedo decir: Como andamios. Qué perrouuws. Andaa andaaa.

Este trabajo ha sido posible gracias al Instituto de Tecnología Química (ITQ), que me ofreció la posibilidad de realizar esta tesis doctoral, y al Ministerio de Ciencia y Educación que me otorgó un contrato predoctoral (PRE2018-083623), permitiéndome llevar a cabo esta tesis doctoral dentro del programa Severo Ochoa (SEV-2016-0683-18-3). Asimismo, expreso mi gratitud a los Servicios de Microscopia de la Universitat Politécnica de València por facilitarme los recursos de microscopia necesarios. Agradezco también a la Unión Europea y al Gobierno de España por la financiación de este trabajo a través de los proyectos CEX2021–001230-S, PID2022-136934OB-100 y TED2021–130191B-C41. Y a la Generalitat Valenciana (Prometeo 2021/077). Además, parte de este estudio forma parte del programa Advanced Materials y apoyado por el MCIN con financiación parcial de los fondos Next Generation EU (PRTR-C17. I1) y por la Generalitat Valenciana (MFA/2022/012 and MFA/2022/047).

Abstract

Microporous materials such as zeolites have been highlighted due to their broad impact on catalytic processes and industry. The knowledge of their crystalline structure and the study of their properties and applications are intrinsically related. Therefore, conventional diffraction techniques such as single-crystal and powder X-ray diffraction (SCXRD and PXRD) have been the usual methods to retrieve structural information. However, the limitation in growing crystals large enough for SCXRD and the strong peak overlapping in PXRD patterns frequently hamper the structure determination of these materials, with complex structures and large unit cell parameters. Therefore, studying state-of-the-art diffraction techniques for structural characterization in new microporous materials, such as zeolites, is paramount. The incentive of this work is to investigate Electron Diffraction Tomography (EDT), also known as Three-Dimensional Electron Diffraction (3DED). These methods can be an exceptional technique for structural analysis of microporous materials using conventional and already available Transmission Electron Microscopes (TEM). These techniques generate single-nanocrystal diffraction patterns with enhanced scattering intensities using electron beams. These patterns are acquired as the nanocrystal rotates within the TEM's goniometer, resulting in electron diffraction (ED) patterns from single small crystals of nanometer-scale dimensions. These methods require developing and optimizing all experimental parameters, often demanding TEM expertise operators. Additionally, strong multiple diffractions ("dynamical effects") can hinder the collection of accurate intensities. Moreover, many materials suffer structural damage by the interaction with the electron beam. To address this issue, the combination of the precession electron diffraction tomography (PEDT) technique, which applies a precession of the beam, together with a fast 3DED procedure will minimize these effects, leading to a successful data collection, processing, and structure determination.

This methodology has been applied to solve the structure new microporous materials, named ITQ-70 and ITQ-35, in *as-made* form containing organic guest molecules, and one already known as-made zeolites structure with two different guest organic molecules, ITQ-52. This approach will lead to the complete atomic localization of the hybrid inorganic and organic zeolitic materials through the approachability of 3DED techniques combined with X-ray diffraction refinements. This will offer a promising general protocol for developing a novel characterization tool for an accurate structure determination from small crystal materials.

Keywords: 3D electron diffraction, zeolites, electron crystallography, precession electron diffraction, continuous rotation electron diffraction.

Resumen

Los materiales microporosos como las zeolitas han sido destacados por su amplio impacto en procesos catalíticos, medio ambiente e industria. El conocimiento de la estructura cristalina de la materia y el estudio de sus propiedades y aplicaciones están intrínsecamente relacionadas. Por lo tanto, las técnicas convencionales de difracción como la difracción de rayos X en monocristal y la difracción de rayos X en polvo (SCXRD y PXRD, respectivamente) han sido los métodos habituales para obtener información sobre la disposición estructural de los átomos. Sin embargo, la limitación para obtener cristales lo suficientemente grandes para ser medidos por SCXRD y la fuerte superposición de picos en los patrones de PXRD dificultan con frecuencia la determinación estructural de estos materiales con estructuras complejas y unidades de parámetros de celda grandes. Es por ello por lo que el desarrollo de nuevas técnicas de difracción que permitan la determinación estructural es de suma importancia. Por lo tanto, es fundamental estudiar técnicas de difracción de última generación para la caracterización estructural en nuevos materiales microporosos, como las zeolitas. El objetivo de este trabajo es investigar la Tomografía de Difracción de Electrones (EDT), también conocida como Difracción de Electrones Tridimensional (3DED). Estos métodos pueden ser una técnica excepcional para el análisis estructural de materiales microporosos utilizando Microscopios Electrónicos de Transmisión (TEM) convencionales y ya disponibles. Estas técnicas generan patrones de difracción de monocristales de tamaño nanométrico con intensidades de dispersión mejoradas utilizando haces de electrones. Estos patrones se adquieren mientras el nanocristal gira dentro del goniómetro del TEM, resultando en patrones de difracción de electrones (ED) de pequeños cristales individuales de dimensiones nanométricas. Además, estos métodos requieren el desarrollo y la optimización de todos los parámetros experimentales que a menudo exigen experiencia en TEM. Además, muchos materiales sufren daños estructurales por la interacción con el haz de electrones. Para abordar este problema, la combinación de la técnica de tomografía por difracción de electrones con precesión (PEDT), que aplica una precesión del haz, junto con un manual de 3DED fácil de usar, minimizará estos efectos, permitiendo una adquisición de datos, procesamiento y determinación de estructuras exitosos.

Esta metodología se ha aplicado para resolver la estructura de nuevos materiales microporosos denominados ITQ-70 e ITQ-35, en forma sin calcinar, así como una zeolita ya conocida en forma sin calcinar con dos moléculas orgánicas diferentes en su interior como la ITQ-52. Todas estas estructuras se presentan en forma sin calcinar conteniendo agentes directores de estructura en su interior. Este enfoque conducirá a la localización atómica completa de materiales de zeolita híbridos inorgánicos y orgánicos mediante la accesibilidad de técnicas de difracción de rayos X y 3DED. Este avance ofrecerá un protocolo general prometedor para desarrollar una nueva herramienta de caracterización para una determinación precisa de la estructura de materiales cristalinos pequeños.

Resum

Els materials microporosos com les zeolites han sigut destacats pel seu ampli impacte en processos catalítics, medi ambient i indústria. El coneixement de l'estructura cristal·lina de la matèria i l'estudi de les seues propietats i aplicacions estan intrínsecament relacionats. Per tant, les tècniques convencionals de difracció com la difracció de raigs X en monocristall i la difracció de raigs X en pols (SCXRD i PXRD, respectivament) han sigut els mètodes habituals per a obtindre informació sobre la disposició estructural dels àtoms. No obstant això, la limitació per a obtindre cristalls prou grans per a ser mesurats per SCXRD i la forta superposició de pics en els patrons de PXRD dificulten freqüentment la determinació estructural d'aquests materials amb estructures complexes i unitats de paràmetres de cel·la grans. És per això pel que el desenvolupament de noves tècniques de difracció que permeten la determinació estructural és de summa importància. Per tant, és fonamental estudiar tècniques de difracció d'última generació per a la caracterització estructural en nous materials microporosos, com les zeolites. L'objectiu d'aquest treball és investigar la Tomografia de Difracció d'Electrons (EDT), també coneguda com a Difracció d'Electrons Tridimensional (3DED). Aquests mètodes poden ser una tècnica excepcional per a l'anàlisi estructural de materials microporosos utilitzant Microscopis Electrònics de Transmissió (TEM) convencionals i ja disponibles. Aquestes tècniques generen patrons de difracció de monocristalls de grandària nanomètrica amb intensitats de dispersió millorades utilitzant feixos d'electrons. Aquests patrons s'adquireixen mentre el nanocristall gira dins del goniòmetre del TEM, resultant en patrons de difracció d'electrons (ED) de xicotets cristalls individuals de dimensions nanomètriques. A més, aquests mètodes requereixen el desenvolupament i l'optimització de tots els paràmetres experimentals que sovint exigeixen experiència en TEM. A més, els forts efectes de difracció múltiple o efectes dinàmics poden dificultar l'obtenció precisa d'intensitats cinemàtiques a més que molts materials pateixen danys estructurals causats per la interacció amb el feix d'electrons. Per a abordar aquest problema, la combinació amb la tècnica de tomografia de difracció d'electrons amb precessió (PEDT), que aplica una precessió del feix juntament amb un manual de 3DED fàcil d'utilitzar, minimitzarà aquests efectes; portant a una recol·lecció de dades, processament i determinació d'estructures exitosos.

Aquesta metodologia s'ha aplicat per a resoldre l'estructura de nous materials microporosos denominats ITQ-70 i ITQ-35, en forma sense calcinar, així com una zeolita ja coneguda en forma sense calcinar amb dues molècules orgàniques diferents en el seu interior com la ITQ-52. Totes aquestes estructures es presenten en forma sense calcinar contenint agents directors d'estructura en el seu interior. Aquest enfocament conduirà a la localització atòmica completa de materials de zeolita híbrids inorgànics i orgànics mitjançant l'accessibilitat de tècniques de difracció de raigs X i 3DED. Aquest avanç oferirà un protocol general prometedor per a desenvolupar una nova ferramenta de caracterització per a una determinació precisa de l'estructura de materials cristal·lins xicotets.

CONTENTS

List of abbreviations and symbols

2D	**two-dimensional**
3D	**three-dimensional**
3DED	**Three-dimensional Electron Diffraction**
ADP	**Atomic Displacement Parameter**
ADT	**Automated Diffraction Tomography**
CBD	**Convergent Beam Electron Diffraction**
CBU	**Composite Building Unit**
COF	**Covalent Organic Framework**
cRED	**Continuous Rotation Electron Diffraction**
D4R	**Double-four-ring**
EA	**Elemental Analysis**
ED	**Electron Diffraction**
EDS	**Energy-Dispersive X-ray Spectroscopy**
EDT	**Electron Diffraction Tomography**
FESEM	**Field Emission Scanning Electron Microscopy**
HRTEM	**High-Resolution Transmission Electron Microscope**
ITQ	**Instituto de Tecnología Química**
MAS-NMR	**Magical Angle Spinning Nuclear Magnetic Resonance**
MicroED	**Microcrystal Electron Diffraction**
MOF	**Metal-Organic Framework**
NBD	**Nano-beam Electron Diffraction. Also, NED or NBED**
NMR	**Nuclear Magnetic Resonance**
OSDA	**Organic Structure Directing Agent**
PEDT	**Precession Electron Diffraction Tomography**
PETS	**Process Electron Tilt Series**
PXRD	**Powder X-Ray Diffraction**
RED	**Rotation Electron Diffraction**
SAED	**Selected-Area Aperture**
SDA	**Structure Directing Agent**
SEM	**Scanning Electron Microscopy**
SXRD	**Synchrotron X-Ray Diffraction**
TEM	**Transmission Electron Microscope**
TGA	**Thermogravimetric analysis**
TMS	**Tetramethylsilane**
UPV	**Universitat Politècnica de València**
XRD	**X-Ray Diffraction**

CHAPTER 1.
INTRODUCTION

1.1. INTRODUCING CRYSTALLOGRAPHY

Solid materials can have an orderly arrangement of atoms and molecules that repeats in three dimensions. This is known as the crystalline state. The study of this atomic structure and its chemical and physical properties is called crystallography, a field that has profoundly impacted the world since it began.

The most employed family of techniques that provide an exploration of the crystalline structural properties of the materials are currently divided into three well-developed categories using photons (X-rays), neutrons, and electrons. All these techniques can be applied either to a single crystal of the sample or to a polycrystalline powder sample.

These techniques use various radiation sources and instruments, and although the best method depends on the specific problem, they are mutually complementary for a comprehensive structural understanding. See **Fig. 1** for a graphical representation.

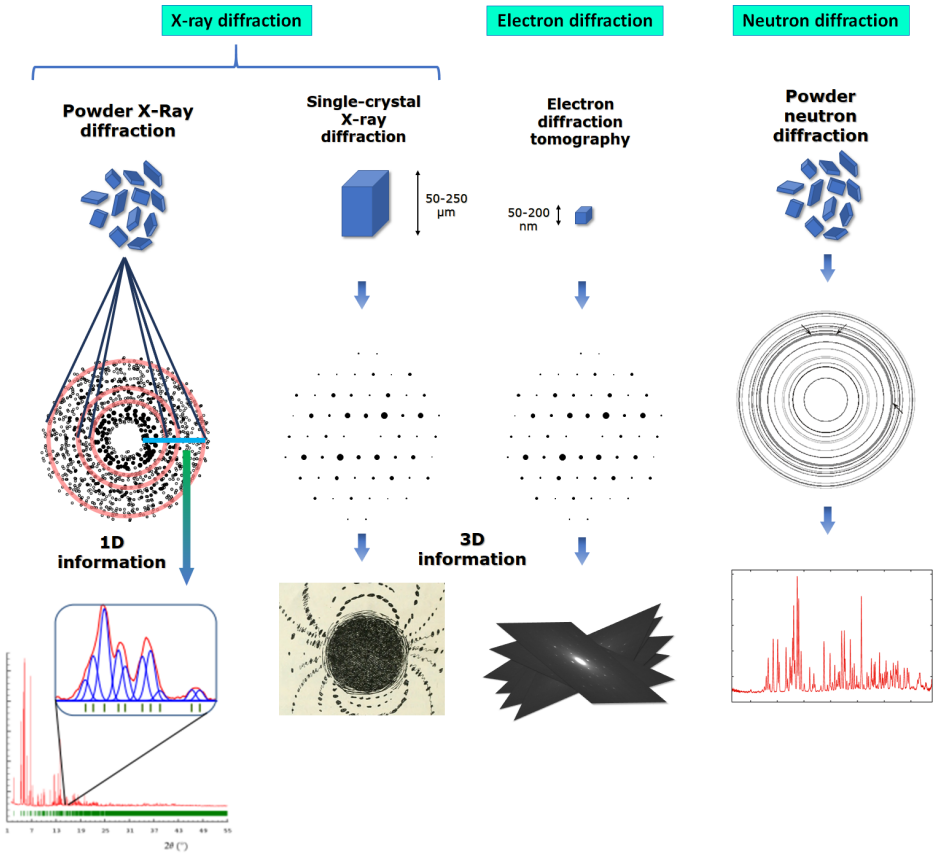

Figure 1. Examples of fundamental data collection principles for Powder X-ray Diffraction, Single Crystal X-ray Diffraction, Single-Crystal Electron Diffraction, and Neutron Diffraction techniques.

1.1.1. SINGLE-CRYSTAL X-RAY DIFFRACTION (SCXRD)

One of history's most common crystalline characterization techniques is single-crystal X-ray diffraction (SCXRD). In these experiments, a crystal is placed in the center of the diffractometer. The key points about SCXRD include:

1. **Crystal size**: The sample requires one single crystal, typically ranging from 100 to 250 μm, although growing large enough crystals of one single phase suitable for these experiments is frequently challenging, (**Fig. 1**). Nowadays the use of synchrotron radiation sources has allowed reducing the required crystal size up to around 10 microns.
2. **Crystal quality**: Crystal candidates should have a regular shape, be preferably twinning-free, and have the least number of defects possible.
3. **Reflection conditions**: in the case of SCXRD, the individual intensities, distributed in 3 dimensions, can be easily identified, and measured with high precision, thus providing sufficient information and making usually the determination of the crystalline structure a simple and straight procedure.

1.1.2. POLYCRYSTAL X-RAY DIFFRACTION (PXRD)

Polycrystal or powder X-ray diffraction is the primary characterization technique that extracts the crystal structure from a mixture of crystals of polycrystalline solid powder samples. It has been the most widely used because it is available in many laboratories, is a non-destructive technique, and samples can be easily prepared.

However, the reduction of the information available from a 3D dataset to a single-dimensional pattern produces a severe overlapping of the detected diffraction peaks, reducing the data quality and introducing uncertainties when assigning the measured intensities.

1.1.3. NEUTRON DIFFRACTION

The interaction of neutrons with matter is weaker than that of X-rays or electrons. This interaction occurs with the atomic nuclei and is more sensitive to light atoms, including hydrogen or deuterium. Moreover, it is sensible to the spin magnetic moment, allowing the study of magnetic structures.

While this technique is notably effective for determining the structural positions of light nuclei, such as the atoms that form the organic structure-directing agents of zeolites, its practical application to the materials examined in this study is not feasible. This limitation arises from the extremely strong interaction of neutrons with the hydrogen atoms of the organic molecules, which would require replacing completely their hydrogen atoms with deuterium before the measurement.

1.2. ELECTRON CRYSTALLOGRAPHY

1.2.1. ELECTRON DIFFRACTION

In the early 2000s, advancements in electron diffraction techniques significantly allowed the construction of reciprocal spheres using zone-axis patterns (also called in-zone axis patterns). The Cambridge Crystallographic Data Centre (CCDC), a non-profit organization that hosts one of the largest databases of small-molecule organic and metal-organic crystal structures, recognizes the widespread growth and importance of ED techniques on the number of structures deposited.[1] This method is commonly combined with HRTEM, using a transmission electron microscope, and with XRD techniques using XRD diffractometers. It involves the alignment of a crystal specimen to a specific crystallographic axis parallel to the incident electron beam. The resulting diffraction patterns, collected from localized crystal regions, become highly symmetrical. Thus, many material structures are determined by collecting a small number of ED patterns using SAED from specific crystal orientations. In contrast, these diffraction strategies have limitations, such as the limited number of orientations at which electrons are diffracted, determined by the Bragg condition, and the exposure time of the crystal to the electron beam, which restricts reflections to zone axes. Additionally, the accuracy of collected data and data processing were limited by the dynamical effects and the requirement for precise crystal alignment.

Electron diffraction is closely linked to the Ewald sphere concept. A vector extends from the origin to the point where the Ewald sphere intersects a reciprocal lattice point, fulfilling Bragg's condition, as shown in **Fig. 2**.

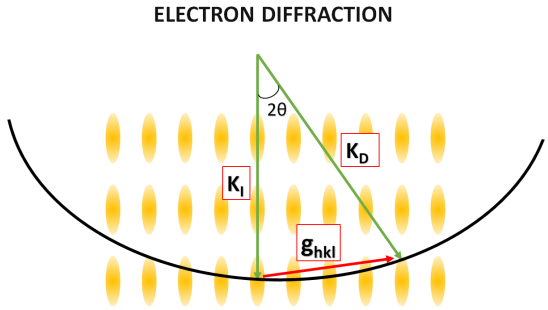

Figure 2. Ewald sphere construction. When the Ewald sphere intersects reciprocal spots, the elastic scattering waves fulfill Bragg diffraction of electrons by crystals via this equation $g_{hkl} = |K| = 2 \cdot \sin\theta / \lambda$*. The change in the wave vector due to scattering,* g_{hkl}*, is given by ghkl = KD - KI.* K_I *and* K_D *stand for incident and scattered reciprocal-lattice vectors, respectively.*

Different types of signals are generated during the interaction of an electron beam with matter, each providing different information on material properties, as shown in **Fig. 3**. The most significant signals in the case of electron diffraction methods are focused on those coming from primary electron interactions, such as elastic

scattering, when the goal is to understand the crystallographic properties of a material. Scattering occurs as either elastic (no kinetic energy loss) or inelastic (with kinetic energy loss). Elastic scattering conserves electron wavelength and follows Bragg's law when interacting with a crystal. Inelastic scattering results in a variety of longer wavelengths, contributing to the background around sharp diffraction spots in a diffraction pattern.[2]

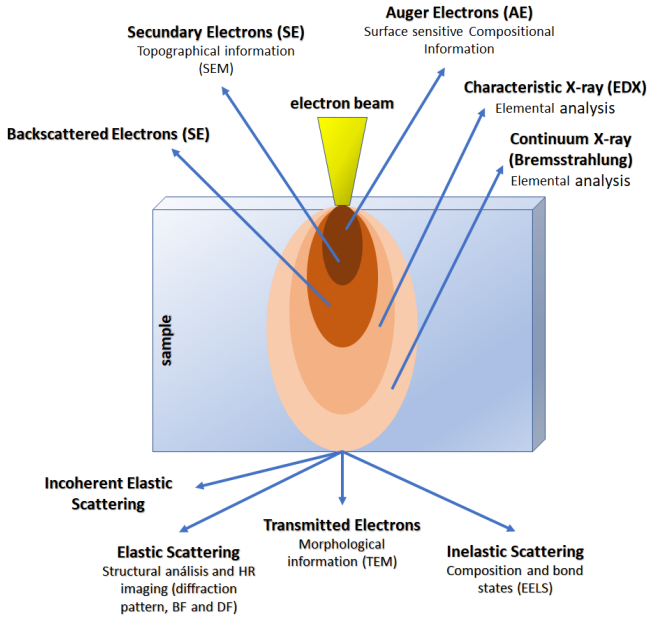

Figure 3. Electron-matter interaction volume: different types of signals generated.

Electron diffraction data presents unique advantages compared to X-ray diffraction:

- **Wavelength:** With a significantly shorter wavelength than X-rays (by ten orders of magnitude), electrons result in a flatter Ewald sphere, almost approaching flatness, as illustrated in **Fig. 4**. Consequently, this leads to a smaller scattering angle that covers more reflections.
- **Electrostatic potentials:** The strength of the interaction between electrons and matter is notably higher compared to that of X-rays. Due to the stronger Coulombic interaction of electrons with both atomic nuclei and electrons ($>10^3$-10^4) than X-rays, the electron density map is physically described as electrostatic potential, whereas X-rays exclusively interact with the electrons (electron density) of the crystal's atoms.
- **Fine structural details:** The reduced dependence of the electron diffraction structure amplitudes on the atomic number or nuclear charge number (Z) can lead to improved detection sensitivity for lighter atoms, including hydrogen atom detection.[3]

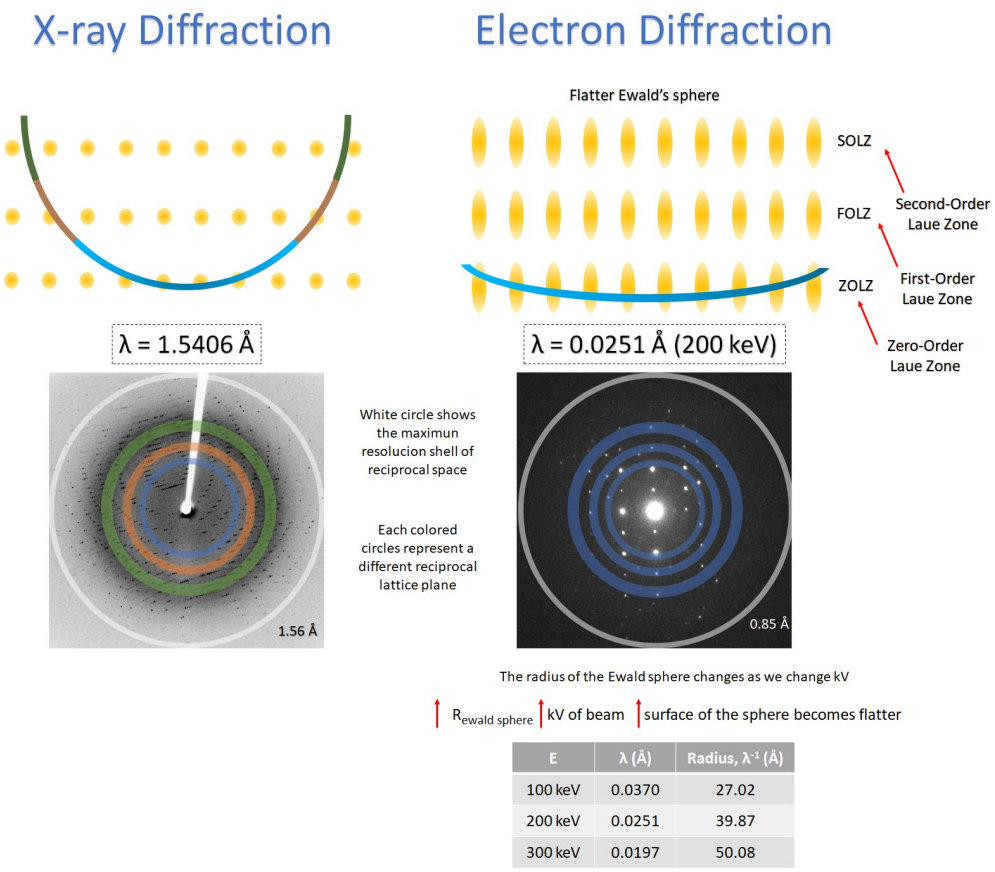

E	λ (Å)	Radius, λ^{-1} (Å)
100 keV	0.0370	27.02
200 keV	0.0251	39.87
300 keV	0.0197	50.08

Figure 4. Comparison between X-ray and electron diffraction techniques.

- **Sample size:** In ED, the strong interaction of electrons and the ability to focus on small-sized crystals enables the measurement of small nano-sized individual crystals, eliminating the need to grow sufficiently large crystals for the single-crystal XRD method. Consequently, ED can provide not only an alternative for analyzing complex zeolites with low symmetry and large unit cell parameters, but also a way for single-phase identification from a sample of mixed phases by measuring its individual crystals, thus addressing the demands of PXRD technique.

Although electron diffraction is a valuable technique, it possesses certain limitations when compared to XRD, as evaluated below:

- **Unit cell parameters:** XRD unit cell parameters can be more accurate than those obtained by 3DED under certain conditions due to hysteresis in electromagnetic lens compared to physical stages that modern XRD diffractometers offer.[4,5]

- **Multiple diffraction effects,** also called **dynamical diffraction effects**: Electrons interact strongly with matter, causing multiple scattering phenomena within the crystal structure, also affecting the kinematical intensities extraction, which is critical for intensities analysis and, hence, structure determination.
- **Beam damage:** Longer exposure times of the electron beam deteriorate the crystal integrity, losing the crystallinity and hence reducing the quality of the data measured.
- **Expertise:** Proficiency in electron diffraction (ED) experiments is essential, particularly in the calibration, setup, and data collection with the transmission electron microscope (TEM).
- **Time-consuming:** Sample preparation, data collection, and precise instrument calibration ensuring optimal specimen thickness and orientation is time-consuming.

While electrons have these advantages, it's important to note that both electron and X-ray diffraction techniques have their own strengths and limitations. The choice between them depends on the specific characteristics of the material being studied and the information required.

As previously noted, the in-zone axis electron diffraction (ED) method, while widely used, has certain limitations. These include a restricted number of zones acquiring a limited number of reflections, the necessity for data acquisition from different crystals, the requirement for expertise in aligning and collecting data at specific crystal orientations, prolonged exposure to the beam leading to beam damage during orientation, and the influence of dynamical effects. However, it is important to note that the methods employed in this thesis do not rely on in-zone axis electron diffraction. Instead, alternative approaches were used to overcome these challenges, as discussed in the subsequent sections.

1.2.2. TRANSMISSION ELECTRON MICROSCOPE

The experiments of electron diffraction characterization techniques are employed using electrons that are produced by Transmission Electron Microscopes (TEM). The electron gun generates these electrons, passing through a high vacuum system in the TEM column. A set of electromagnetic lenses, including the condenser, objective, intermediate, and projector lenses, directs the path of electrons to the sample specimen and, ultimately, to the viewing screen or camera system where imaging or diffraction is formed. Electromagnetic lenses operate based on the principles of electromagnetic induction. By applying magnetic fields, they can bend and focus the path of electrons, creating highly magnified images and diffraction patterns. These components comprise general TEMs, which can be seen in **Fig.5**.

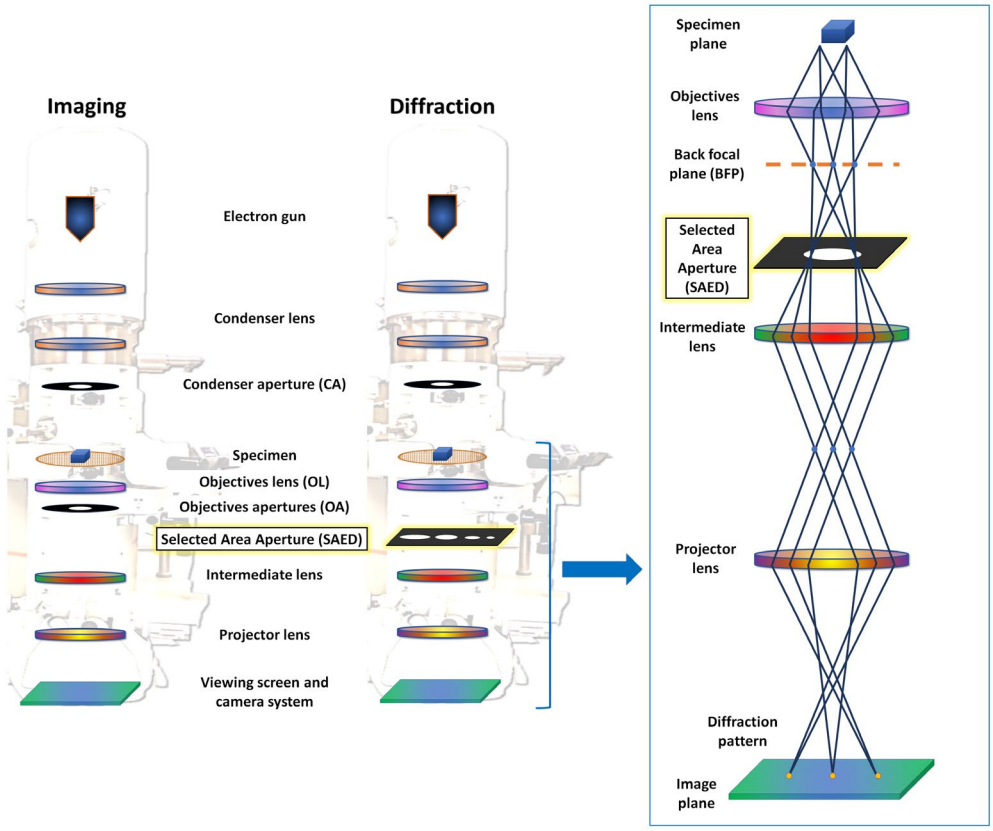

Figure 5. Electromagnetic lens components of a TEM in imaging and diffraction mode (left and middle) and a schematic view of diffraction mode (right).

- **Electron gun:** The role of an electron gun involves electron generation and subsequent acceleration. It comprises a filament that emits electrons when heated. Various types of filaments are employed for this purpose, including LaB_6 single crystals, field emission guns (FEG), and tungsten (W) filaments.
- **Condenser lens (CL) system:** Ensures precise direction electron beam direction onto the specimen by controlling its convergence and position. CLs are located above the specimen. See **Fig. 6** for a cross-section of a condenser lens. The condenser lens system is usually composed of two or more lenses, which are also provided with condenser apertures (CA). CAs are physical holey plates with predetermined sizes and are physical perforated plates that control the size and convergence angle of the electron beam. They obstruct unwanted electrons, thereby diminishing the electron count reaching the

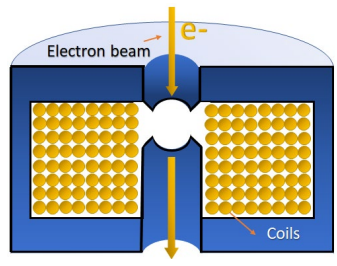

Figure 6. Schematic diagram of an electromagnetic lens

sample. This aspect is critical for electron diffraction experiments when analyzing beam-sensitive samples. In order to minimize the electron dose in the specimen, the smallest condenser aperture (C2) with a diameter size of 10 μm, in the case of JEOLs microscopes, will be selected. Additionally, by increasing the beam-convergence angle (α), the probe current will also increase; hence, more radiation damage will be suffered to the specimen. **Fig. 7** illustrates the different convergence angles accessible through a TEM.

- **Objective lens (OL) system:** placed below the specimen, magnify and focus the transmitted electron beam, thus optimizing the resolution and correcting various aberrations for high-resolution images.
- **Selected-area aperture (SAED):** A physical holey plate with predetermined sizes located in the first intermediate image plane formed by the objective lens. The distinction in diffraction, compared to the other two TEM approaches, imaging, and spectroscopy, arises from the diffraction equipment, namely, the Selected Area Aperture electron diffraction (SAED), microdiffraction, or convergent-beam electron diffraction, which all are the different types of forming ED patterns in a TEM. The selected-area aperture is performed as a small aperture inserted into the TEM imaging system, after the sample. This configuration enables the capture of those electron beams that have crossed the sample and have been chosen by the selective area aperture. In this mode, the incident beams are parallel. On the other hand, microdiffraction is performed by focusing the electron beam, typically with a small probe size, by setting the illumination system to the Nanobeam Diffraction (NBD), also called small convergence angle micro-area illumination mode in the TEM. In Convergent Beam Electron Diffraction (CBED), the beam is focused onto a small area of the specimen (conical electron beam), and the resulting diffraction patterns are analyzed. Therefore, in NBD and CBED, the electron beam is precisely focused to converge on the specimen across a range of angles, with smaller angles, while in SAED mode beams are parallel. The distinction lies in the relative final area of the beam. SAED encompasses larger areas, up to 500 nm, while NBD and CBED employ smaller beams, approximately 1 nm.

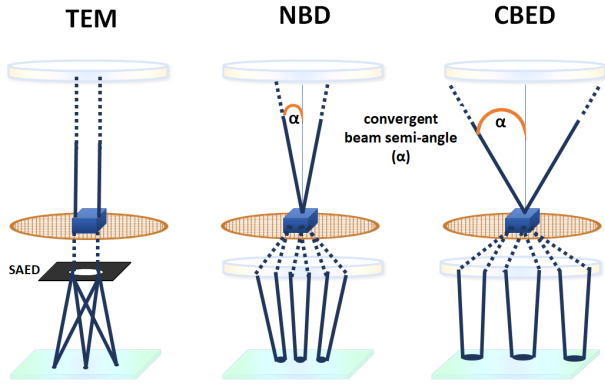

Figure 7. Convergent semi-angle beam (α) scheme and different diffraction techniques.

- **Intermediate lens:** further magnify and control the beam working with the objective lens. It is positioned below the objective lens and reveals finer details in the specimen, contributing to higher-quality images before it reaches the projector lens.
- **Projector lens:** positioned after the intermediate lens, magnifying and projecting the electron image onto the imaging system. In diffraction mode, adjusting its intensity changes the camera length to cover diffraction spots at higher or lower-order Laue zones.
- **Image recording systems:** These are devices that are installed below the projector lens and record images and diffraction patterns, including photographic films, image plates, CCD cameras, metal−oxide−semiconductor (CMOS), or single electron detectors.

It is important to remark that electron microscopy, particularly high-resolution transmission electron microscopy (HRTEM) imaging, has also been fundamental in examining many zeolite structure types, contributing significantly to the field of structural analysis. Zeolite structures have been solved by HRTEM, obtaining the crystal symmetry and phase information from well-defined high-resolution images in combination with XRD and electron diffraction (ED) methods. [6,7,8,9] However, this technique is significant but is beyond the thesis scope and will not be further discussed.

1.2.3. BEAM DAMAGE, DYNAMICAL DIFFRACTION AND EXCITATION ERROR

Wave-particle duality, introduced by Louis de Broglie in 1924, suggests that all particles have both wave-like and particle-like characteristics. This duality is especially manifested in electrons, where it becomes evident in diffraction experiments.[10] Electron beam damage refers to phenomena, including structural and chemical changes, knock-on damage, heating, or sample charging that can occur in a sample when exposed to a high-energy electron beam in the TEM. This phenomenon can impact the quality of imaging and structural analysis and must be considered when working with sensitive samples such as metal-organic frameworks (MOFs), covalent-organic frameworks (COFs), organic compounds, or zeolites. The most representative limitation is the amorphization effects, resulting in the loss of crystallinity. This also results in a noticeable reduction in the number of discernible peaks in the patterns. The electron dose ranges that zeolite can handle frequently depend on the sample volume and chemical composition.[11]

The second limitation intrinsic to ED is the physical phenomenon called multiple scattering, multiple diffraction, or dynamical effects. The interaction between high-energy already scattered electrons and the crystal lattice can produce a second scattering of those electrons. Thus, the diffracted beams act as new incident beams preventing the direct proportionality of intensities to the square of structure factor amplitudes. This phenomenon leads to a violation of kinematically forbidden reflections and produces a non-homogeneous distribution of intensities-indicating a violation of the Friedel pair rule too. The Friedel pair rule, based on the Fourier

transform of a real function, is relevant for electron diffraction patterns of crystals with inversion symmetry or non-resonant scattering. This rule implies that the reflections with inverse indices (-h, -k, -l) should have the same intensities as their counterparts (h, k, l), indicating the preservation of centrosymmetry in the squared amplitude of the Fourier transform, where the phase changes signs.

The violation of the Friedel law, caused by dynamical effects directly impact the weaker reflections, which are more statistically abundant at higher resolutions. The dynamical effects, arising from multiple scattering, lead to an uneven intensity distribution, particularly for weak reflections, which distort the intensity data. For this reason, this phenomenon hampers the correct determination of structural details, especially in high-resolution regions, where the weak reflections are crucial for accurate model building. Therefore, the violation of Friedel's law significantly reduces the accuracy and resolution of 3DED results. As electron beams interact with crystal atoms in the specimen, the challenges associated with multiple diffraction or dynamical effects increase with the thickness of the crystal sample, as presented in **Fig. 8**. In such cases where electron diffraction data have been collected with enhanced dynamical effects, the structure solution and structural refinement become significantly challenging. One of the strategies to tackle this problem arises from the refinement technique called dynamical refinement which is employed to address and mitigate these challenges, as will be further discussed.

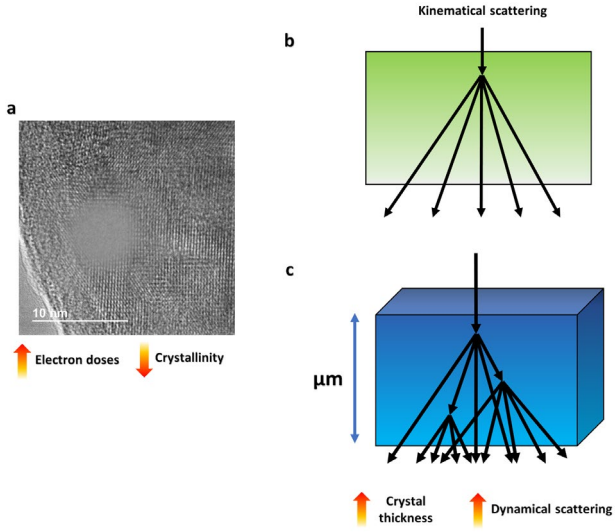

Figure 8. (a) Example of damage induced by a high-energy electron beam in an organic compound sample (b) Schematic of kinematical scattering from weak interaction (c) Schematic of dynamical scattering and thickness dependence. The thicker the crystal sample, the higher the likelihood of dynamical or multiple diffraction effects.

The third limitation would come from the physical phenomenon called excitation error, which occurs when the Ewald sphere, affected by the scattering of the electron beam, cuts (integrates) each diffraction intensities in a different manner. **Fig. 9**

illustrates the intersection of the Ewald sphere with the volume of spike-like diffraction spots. It is important to note that these spots are significantly distanced from the center of the Laue zone, indicating a divergence from the expected condition. Applying a precession of the beam and continuous-rotation method that will be further described will aid in integrating the intensities over the excitation error.

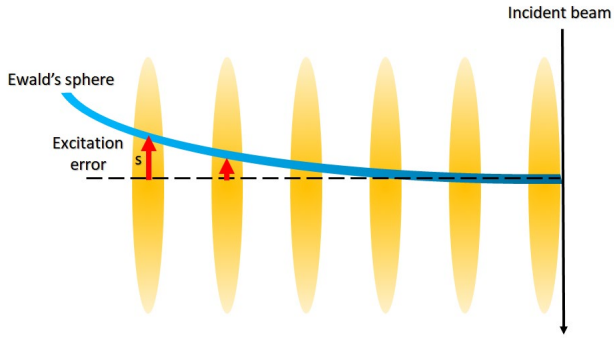

*Figure 9. Excitation error. The vector **s** refers to how far deviates from the exact center of integration or Bragg condition.*

All these limitations must be considered to understand the complete crystal structure that cannot be conceived without considering the defects in the crystal lattice. The defects can indicate various issues or disorders in the structure refinement by observing the difference Fourier map, which will be used to visualize the discrepancies between the observed and calculated electron density. The types of defects or issues include high Residual Electron Density arising from model inaccuracies such as missing atoms, incorrect atom positions, multiple occupancy, or thermal vibrations, some atoms in the crystal vibrate more vigorously due to thermal energy. The disorder effects can manifest in the direct space indicated by elongated ellipsoid as anisotropic displacement parameters or positional disorder (one atom can occupy two or more crystallographic sites). Disorder effects can also manifest in the reciprocal space lattice as diffuse scattering in addition to the well-defined Bragg reflections characteristic of ordered lattices.

One of the effects of the disorder is produced by the presence of organic guest molecules within zeolite materials. The study of the disorder of these organic molecules, located within the pores or cavities of the zeolites and also known as structure-directing agents (SDA), can, in some cases, alter the molecules themselves (or, in extreme instances, the entire molecule). These alterations can result in the molecules exhibiting multiple crystallographically independent orientations according to their space group symmetry (except for the space group P1). The definition of structure-directing agents (SDA) will be included in the subsequent sections. This consequence can be understood if different atom types are at the same site in more unit cells. The partially disordered structures can hamper the successive refinements

of their parameters, including atom coordinates or anisotropic displacement parameters. Although several strategies can be employed for successful refinement of the SDA structure, such as working at low temperatures within the TEM to decrease thermal vibrations and enhance beam stability, not all disorders can be completely reduced.

1.2.4. ZONE AXIS ED PATTERNS

Microscopists and electron crystallographers have initially used oriented zone axis patterns (ZAPs) techniques to obtain the crystallographic orientation and the structure solution.[12,13] When the electron beam is parallel to a zone axis of the crystal, the diffraction pattern is collected by the camera detector, showing a symmetrical arrangement of spots that correspond to the reciprocal lattice planes perpendicular to the zone axis (**Fig. 10**). After collecting and indexing data from various zone axis patterns, the next step is to merge the information to identify the crystal structure. This process involves merging data from different patterns to create a detailed representation of the crystal lattice. However, the primary limitation is the relatively low number of available reflections. Additionally, several secondary factors can affect the analysis, including significant sensitivity to sample thickness, the need for precise alignment of the microscope, the requirement for a stable specimen position, careful selection of the zone axis to avoid ambiguity or confusion, and the complexities introduced by strong dynamical interactions. These factors can add complexity to the structural solution of detailed compound materials.[14]

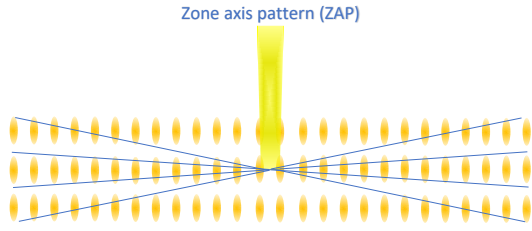

Figure 10. Zone axis pattern electron diffraction (ZAP) scheme.

1.2.5. BEAM PRECESSION

The precession of the electron beam has emerged as a tool for enhancing data quality to address the challenge of strong dynamical interaction. The initial insights into the application of the precession electron diffraction technique for 3D reciprocal space reconstruction are based on collected zonal axis 2D electron diffraction patterns (DPs) derived from the work of Dorset, D. L., et al. The quality of intensities obtained by precession electron diffraction was evaluated for several representative materials, such as ITQ-1, ITQ-7, ITQ-29, ZSM-5, ZSM-10, mordenite, or MCM-68.[15,16] That work described precession electron diffraction as a powerful method for obtaining structural information from crystalline materials at the nanoscale, particularly important for complex structures such as zeolites. It involves tilting the primary electron beam in the electron microscope in a controlled manner, which results in a series of diffraction patterns being recorded at different precession angles.

The precession technique involves a scanning and de-scanning process that activates the illumination deflector coil systems to produce a precession movement (describing a conical path) of the electron beam as it interacts with the crystal, as seen in **Fig. 11**. This precession movement wobbles the Ewald sphere in the diffraction space so that the intensities at the detector are integrated. Thus, the intensities approach those predicted by kinematical diffraction theory. This motion provides more precise and interpretable diffraction patterns, higher-resolution reflections, and an extended integration of intensities. Additionally, this method provides information that is less sensitive to crystal orientation, thickness variations, and defects, improves the signal-to-noise ratio, and enhances the elucidation of complex crystal structures where conventional diffraction methods might struggle. The application of this precession is carried out using an external hardware device known as NANOMEGAS DIGISTAR P1000, which is connected to and situated outside the TEM system. This device is provided by NanoMEGAS SPRL, Belgium, and is technically viable for use with any electron microscope.

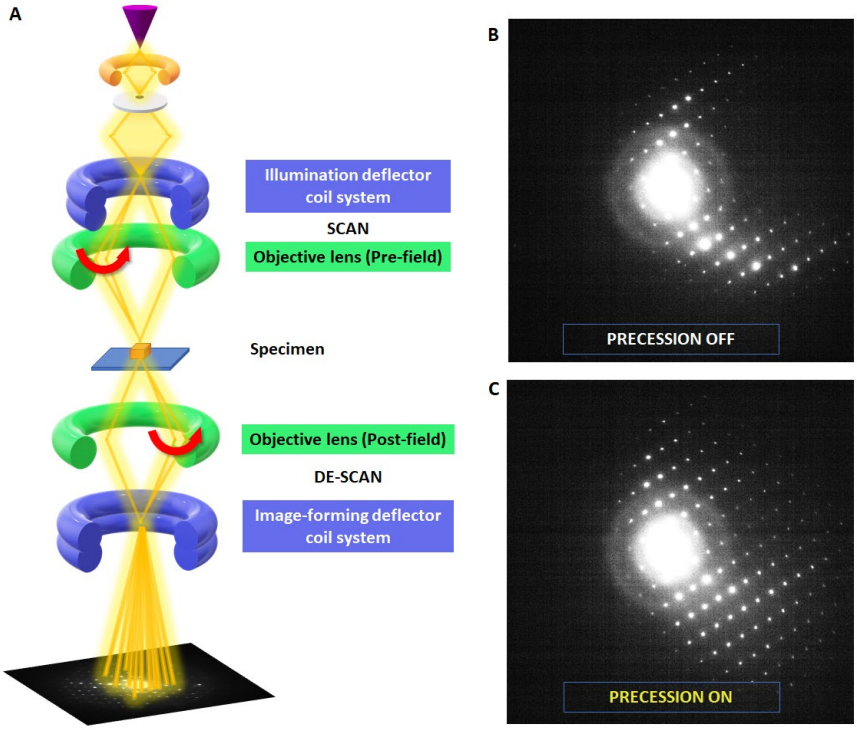

Figure 11. A) Diagram of the electron beam path when a beam precession (yellow beam) is applied. B) Electron diffraction pattern when precession is not applied C) when precession (1°) is applied.

1.3. THREE-DIMENSIONAL ELECTRON DIFFRACTION METHODS (3DED)

In recent decades, fast developments in electron diffraction (ED) have led to the widespread acceptance and application of innovative techniques, particularly three-dimensional electron diffraction (3DED) methods. The core concept of 3DED unifies various data collection protocols, that will be further described, such as Automated electron Diffraction Tomography (ADT), Precession Electron Diffraction Tomography (PEDT), Rotation Electron Diffraction (RED), Microcrystal Electron Diffraction (MicroED) and Continuous Rotation Electron Diffraction (cRED), optimizing them under a single term.[17] A general diagram of the 3DED general methods is shown in **Fig. 12**. **Fig. 13** shows a timeline of all the main developments that contributed to the current state of the technique. All protocols share the unifying element of extracting integrated intensities from off-zones, involving the cutting of sections of reciprocal space, electron diffraction (ED) patterns, or frames recorded by a transmission electron microscope (TEM) camera. This process includes reconstructing 3D reciprocal space, symmetry, and unit cell parameter determination while tilting a nanometric-sized crystal using the TEM goniometer stage.

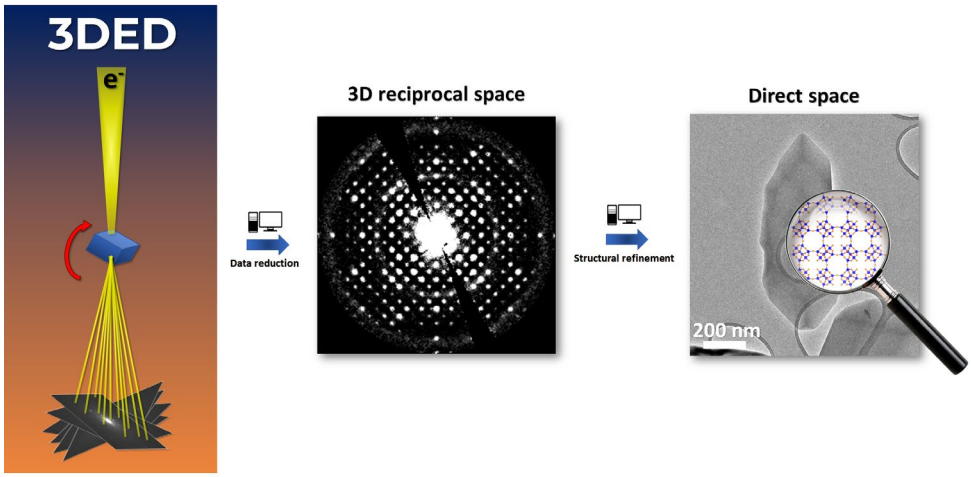

Figure 12. General chart of three-dimensional electron diffraction technique.

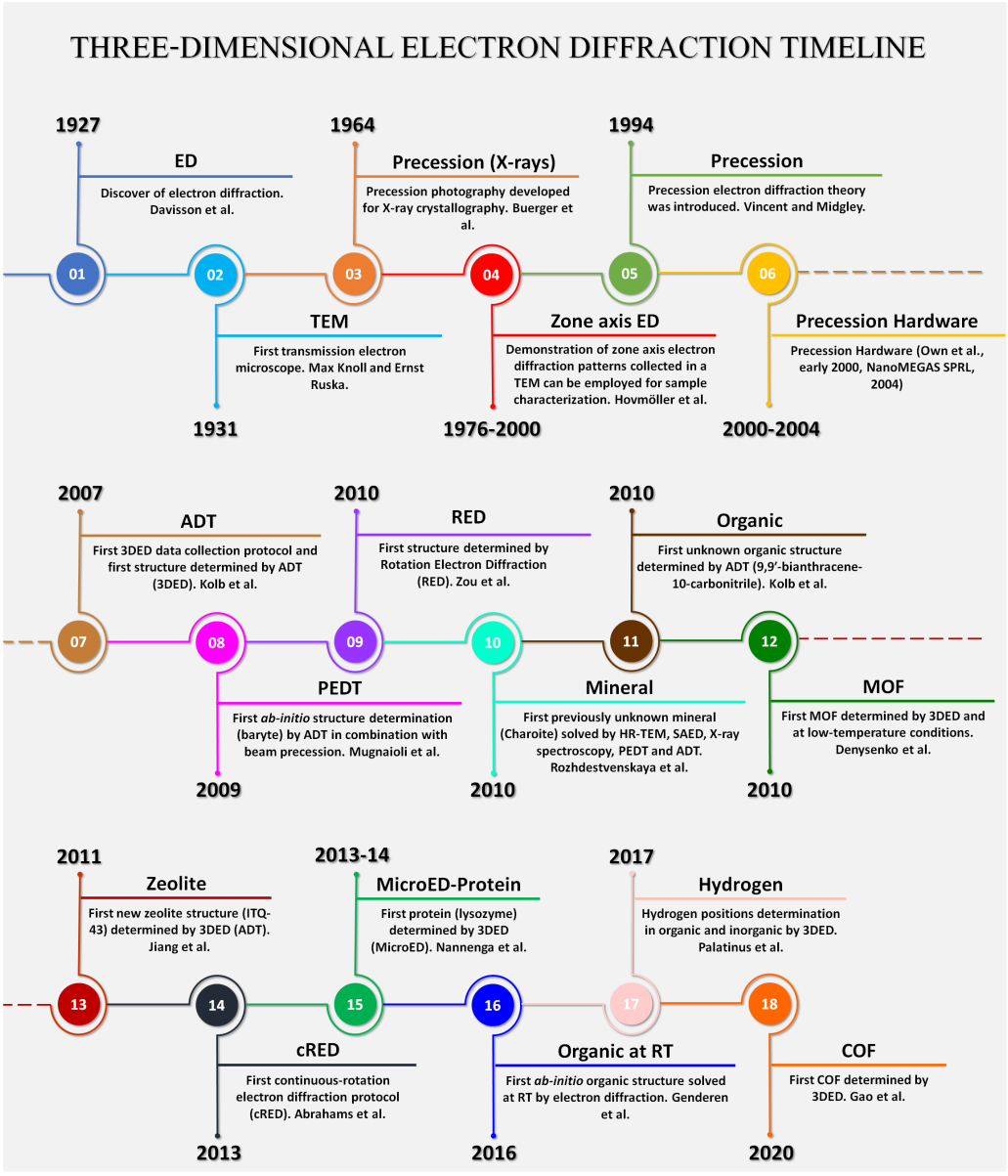

Figure 13. Three-dimensional electron diffraction timeline. The list of the following references is given in order of appearance in the timeline.[18,19,20,21,22,23,24,25,26,27,28,29,30,31,32,33,34,35]

1.3.1. AUTOMATED ELECTRON DIFFRACTION (ADT)

The beginning of 3DED can be considered in 2007 by the term Automated Diffraction Tomography (ADT).[24] The main objective of this technique/protocol was the mechanical tilting of a crystal along a predefined path and collecting randomly oriented off-zone 2D diffraction patterns at each tilt angle. This process generates a tomographic dataset of 2D patterns that can be reconstructed into a 3D reciprocal space, as shown in **Fig. 14a**. Although the data collection was initially carried out within the TEM by reducing the beam size and applying a semi-parallel beam [in Nanobeam electron diffraction mode (NBD) nanoelectron diffraction (NED), or also called nanobeam electron diffraction (NBED) method], it is possible to use the available selected area aperture electron diffraction (SAED) illumination mode. The number of observed reflections increases due to the larger integration of reciprocal lattice points in the Ewald sphere. The number of these points crossing the Ewald sphere increases, and then high-order diffraction spots appear. The only software package created for data processing then was the *ADT3D*[36] program. Nowadays, other programs like PETS2[37] have been developed for this purpose. This program consists of a data analysis workflow that includes reconstructing the diffraction space volume, determining the unit-cell parameters, identifying the possible space groups, and indexing and extracting reflection intensities.

Although this technique is limited by step-wise rotation mode, resulting in longer total data collection times, it has enabled the collection of numerous material structures with considering high data quality and low radiation damage.[38,39,40,41,42] After that, the combination of this technique with Precession Electron Diffraction Tomography (PEDT), which is introduced in the following section, allowed to improve the accuracy of the diffraction patterns collected in ADT, as seen in **Fig. 14b**.

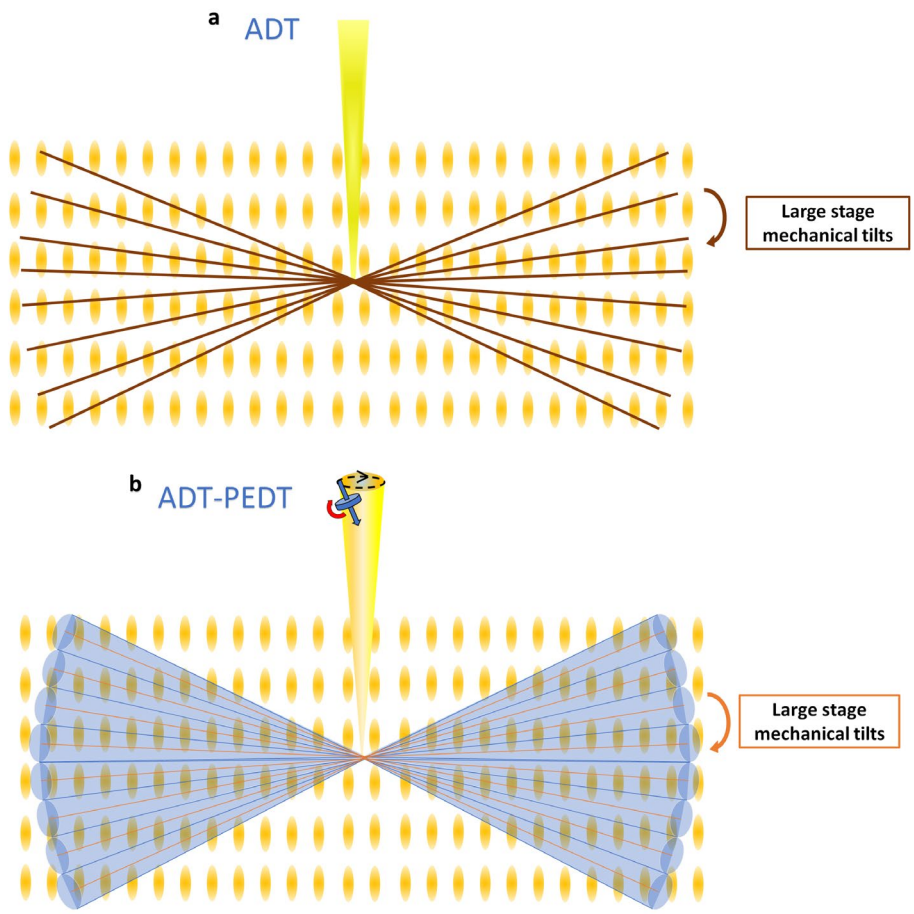

Figure 14. (a) Stepwise acquisition of Automated Diffraction Tomography (ADT). (b) Beam precession combined with automated diffraction tomography (ADT-PEDT)

1.3.2. PRECESSION ELECTRON DIFFRACTION TOMOGRAPHY (PEDT)

With the advent of new technologies, such as the electron beam precession developed by Vincent & Midgley in 1994,[22] additional strategies for collecting ED patterns were incorporated. Therefore, an advanced technique/protocol called precession electron diffraction tomography (PEDT) was introduced in 2009 (**Fig. 11**).[25] As mentioned before, PEDT involves a scanning and de-scanning process that activates the illumination deflector coil systems to produce a precession movement (describing a conical path) of the electron beam as it interacts with the crystal, as seen in **Fig. 11 and 14b**.

The precession device requires careful alignment. Typically, the precession angles range between 0.6 and 1.5 degrees, depending on the selected tilt step for

data collection. In many cases, the precession angle is equal to the step size. For instance, when acquiring data for a zeolite, in which a tilt step of 1 degree was applied, the precession angle might be set at 1 degree.

However, limitations such as careful sample alignment, increased radiation damage, and longer total data collection times can be mitigated by combining it with faster approaches during the experimental setup.

Several software packages exist for processing precession data, such as ADT3D[36] as previously mentioned or PETS2.0.[37] PETS2.0 is a software designed for tilt series analysis of diffraction patterns, offering a range of features including peak hunting, lattice parameter determination, rocking curve analysis, refinement of optical distortions and frame orientations, integration of intensity data, 2D sections and 3D reconstruction of reciprocal space. It can be used in combination with Jana2020 for structure refinement.[43,44]

It is worth emphasizing the Fast-Automated Diffraction Tomography (Fast-ADT) protocol, which represents an optimized and automated evolution of ADT, following the same general idea of 3D electron diffraction protocols. While Fast-ADT was originally developed as a step-wise protocol, it can also incorporate beam precession during data collection, improving data quality and mitigating dynamical effects. It involves systematic and precise tracking of single nanocrystals through two sequential tilt scans of the goniometric stage: one for crystal tracking and another for diffraction pattern acquisition. This innovative approach significantly reduces acquisition time (to approximately 10 minutes) while expanding the tilt range and the covered reciprocal space to ±120°. Fast-ADT is compatible with a wide range of TEM and STEM microscopes, with STEMs offering advantages in visualization and low-dose imaging over TEMs. The technique is implemented using available Gatan cameras and Digital Micrograph versions, utilizing NBD or SAED mode in step-wise or continuous rotation mode (snapshot mode), although precession may be less suitable for continuous-rotation setups. Additionally, it can be integrated with beam precession during data collection. Fast-ADT has been successfully applied to various materials, including $BaSO_4$ crystals and layered silicates such as RUB-5.[45]

1.3.3. ROTATION ELECTRON DIFFRACTION (RED)

Rotation Electron Diffraction (RED) was the second diffraction tomography technique that emerged after ADT.[46] The primary distinction with ADT lies in the absence of PED as the reciprocal space is fined integrated due to the employment of large goniometer tilt steps together with the small beam tilting, using beam tilt steps smaller than 0.1° [goniometer tilt steps (mechanical tilts) + small beam tilt steps (electrical tils)], as seen in **Fig. 15**. A crystal sample is tilted and rotated by the TEM goniometer during data collection, typically around a single axis. This rotation allows for extensive sampling of the reciprocal space, providing a large number of diffraction patterns. However, this method results in long total data collection times and its implementation in all types of TEM is challenging compared to other methods since the absence of precession. However, despite its efficiency, certain areas of the

reciprocal space might be under-sampled, which would result in a low data redundancy due to the missing wedges promoted from the gap between two sequential collected ED frames. The available software for the data processing of RED data is the software RED.[46]

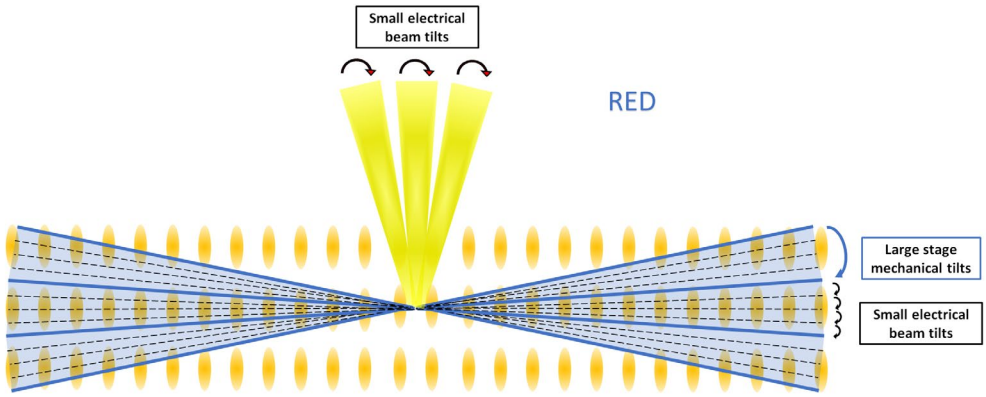

Figure 15. Stepwise acquisition of Rotation Electron Diffraction (RED).

1.3.4. CONTINUOUS ROTATION ELECTRON DIFFRACTION (cRED) AND MICROELECTRON DIFFRACTION (MicroED)

Introducing fast hybrid detectors into electron crystallography has revolutionized the acquisition methods for sampling reciprocal space. One such innovative acquisition method is the continuous rotation electron diffraction method (cRED), which involves the smooth and continuous sample rotation during electron diffraction data collection. This continuous motion ensures a more uniform and complete coverage of the reciprocal space, as illustrated in **Fig. 16**.[31]

The advent of new detectors has improved the 3DED data acquisition and introduced new characteristics, such as improved frame rate, dynamic range, and signal-to-noise ratio, in order to implement this continuous rotation acquisition method. A script routine, which is not available commercially, i.e., specific to a particular laboratory, within the Digital Micrograph™ software, integrates the direct detection cameras with the goniometer stage. This synchronization not only minimizes acquisition times, thereby reducing sample beam damage but also broadens the coverage of the reciprocal space, resulting in datasets with higher completeness. These properties are particularly valuable for complex structures where detailed information is critical for accurate analysis and interpretation.

MicroED, also known as Microcrystal Electron Diffraction, uses an ultra-low dose rate to minimize radiation damage and allows for rapidly collecting a large amount of data. It has been successfully used to determine the structures of various proteins, including lysozyme, and has the potential to be applied to a wide range of materials.[47,48] Nevertheless, there are some limitations. For example, the goniometer must be stable to ensure that the crystals remain consistently under the beam, and

this protocol may not be suitable in certain scenarios. For instance, if beam charging occurs, the crystal might not remain under the beam during continuous rotation data collection. Additionally, if the crystal is very small or has twin domains, tracking the crystals can be challenging. In such cases, stepwise data collection with PED can be convenient.

As illustrated in **Fig. 16**, the total duration between two electron diffraction patterns includes the exposure time, readout, and saving time. As a result, the detector captures the intensities integrated within the exposure time. This is where the distinctions among TEM detectors become evident. A faster detector would minimize the time gap between integrated frames. This approach represents a significant advancement in electron crystallography, enabling more efficient and comprehensive data collection while minimizing potential sample damage.

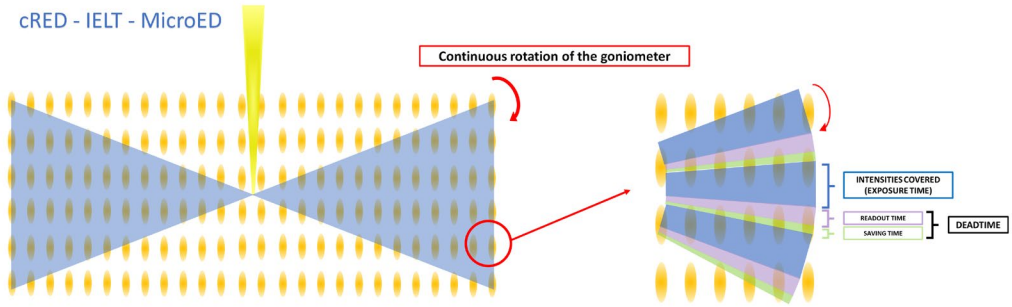

Figure 16. Continuous acquisition of Continuous Rotation Electron Diffraction (cRED), Integrated Electron Diffraction Tomography (IELT) or Microcrystal Electron Diffraction (MicroED).

Serial electron diffraction, on the other hand, involves scanning a beam of electrons across a sample and recording a diffraction pattern at each point, resulting in a series of diffraction patterns or a "serial" collection of data. This technique has the advantage of gathering a substantial amount of data relatively quickly and can be applied to a wide variety of materials, including biological samples. However, it is still under development, and future improvements are aimed at expanding its application to a broader range of materials.[49]

1.4. QUALITY DATA PARAMETERS

In the context of crystallography, the most common terms used to assess the quality and reliability of 3D electron diffraction data collected, similar to the X-ray diffraction data, are the following described:

1. **Signal-to-noise ratio (I/σ):** compares diffraction peak intensity (signal) to background noise. High I/σ leads to accurate crystal structure determination; low I/σ may yield errors, potentially leading to inaccuracies in the crystal structure determination. Therefore, achieving data with high I/σ is crucial for obtaining reliable and precise crystallographic results. An example is shown as peak intensities, in **Fig. 17**, with different signal-to-noise ratios.
2. **Redundancy:** Redundancy is the ratio of the total number of measured reflections to the number of independent reflections. The value describes the number of unique reflections measured during data collection. For instance, if the redundancy is 30, 15 crystals of the same crystal phase have been measured (or one crystal 15 times), yielding a set of 4000 reflections and 2000 unique reflections (15 x 4000 / 2000).

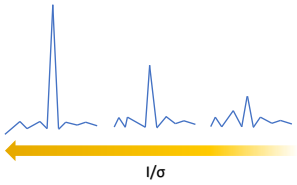

Figure 17. Signal-to-noise ratio (I/σ).

3. **Completeness (%):** Completeness, which is dependent on the crystal's symmetry and always correlated with resolution data, refers to how well the diffraction data, including diffraction spots from all possible crystallographic planes within the crystal lattice, represents the crystal's atom arrangement, i.e. the percentage of the dataset that includes the independent reflections to describe the symmetry and structure determination. Electron crystallographers highlight the importance of obtaining as good completeness as possible to ensure the robustness of their 3DED data (**Fig. 18**).
4. ***Rint*:** Statistical quality factor of the collected 3DED datasets referring to agreement of symmetry-related reflections, i.e. those intensities between more than two different ED patterns that should be identical due to crystal symmetry, equation 1.1. The lower the *Rint* factor, the better the agreement between different symmetry-equivalent reflections, which means the symmetry that is assumed is appropriate. There could be numerous factors contributing to these elevated R*int* values. These could include poor experimental data quality originating from higher dynamical scattering. Its analogue for SCXRD is *Rmerge*. *Rint* < 0.4 usually indicates

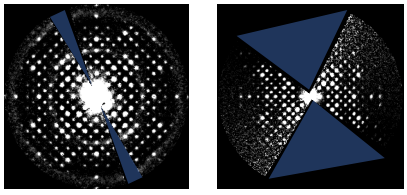

Figure 18. Missing wedge or missing cone.

poor-quality data; zero is considered the best fit. *Rint* is calculated in the following equation where F_o stands for observed structure factor amplitudes:

$$R_{int} = \frac{\sum|F_o^2 - < F_o >^2|}{\sum|F_o^2|} \quad (1.1)$$

1.5. KEY PARAMETERS FOR STRUCTURE MODEL REFINEMENT

The quality indicators for structural model refinement, often referred to as residual R-factors or discrepancy indices, indicate how well the refined structure predicts the observed data during crystal structure model refinement. The followings describe the quality indicators that allow crystallographers to properly evaluate the resulting structure models:

1. ***R_1*, *wR_2* and Goodness of Fit (*GooF*):** quality descriptors of final refined structure model. *R_1* is the main quality factor that expresses the agreement between the structure factor obtained from an experimental diffraction pattern (*Fobs*) and the structure factor calculated from the structural model (*Fc*). The closer match between the experimentally-obtained structure factor and the structure factor calculated from the refined structure, the lower the *R_1 factor*. In electron crystallography, an ideal R-value typically falls within the range of R1 < 30%. This parameter may increase due to errors in the data, such as dynamical scattering. *R_1* is described with the following equation 1.2:

$$R_1 = \frac{\sum|F_{obs}| - |F_{calc}|}{\sum|F_{obs}|} \quad (1.2)$$

The *wR2* factor represents the weighted residual used to identify inaccuracies in the modifications made to the structure model. Unlike the *R1* factor, it emphasizes larger deviations by considering the squaring of the F-values. Lower *wR2* values signify better agreement between the refined model and experimental data. It's calculated using the equation 1.3 that incorporates a weighting factor (*w*) based on the standard uncertainties of measured reflections:

$$wR_2 = \sqrt{\frac{\sum[w(F_o^2 - F_c^2)^2]}{\sum[w(F_o^2)^2]}} \quad (1.3)$$

GooF or goodness-of-fit is another mathematical descriptor that asses the agreement of the model with the data. The closer to unity, the better. It can

be expressed with this equation where *N* and *P* stand for several experimental intensities and several refined parameters, respectively, equation 1.4:

$$GooF = \sqrt{\frac{\sum[w(F_o^2 - F_c^2)^2]}{N - P}} \quad (1.4)$$

2. **Data-to-parameter ratio:** To achieve accurate refinement of the structural model against the experimental data, several parameters are typically refined for each independent atom within the asymmetric unit. These parameters commonly include atomic coordinates (x, y, and z), anisotropic displacement parameters (ADPs), occupancy factors, and a scale factor used to adjust all observed and calculated intensities to a uniform scale. The data-to-parameter ratio indicates the number of independent parameters versus the number of atoms in the asymmetric unit. This ratio should be greater than 10 for centrosymmetric structures and 8 for non-centrosymmetric structures because centrosymmetric structures have more symmetry and therefore require fewer parameters to describe them compared to non-centrosymmetric structures.
3. **Num. of restraints:** Restrains are additional conditions or limitations that can be employed to strengthen the data-to-parameter ratio during the refinement. In some cases, certain previously known and well-established restraints can be fixed during the refinement. For instance, according to the IZA database, [50] pure silica zeolites exhibit fixed geometric restraints such as specific Si-O, Si-Si, and O-O bond lengths of 1.61 Å, 3.07 Å, and 2.63 Å, respectively; and O-Si-O angles of 109.54° based on the tetrahedral geometry, as seen in **Fig. 19**. Pure germanate zeolitic frameworks, however, exhibit typical Ge-O bond lengths of 1.72 Å and O-Ge-O bond angles of 109.47º, due to the larger size of Ge compared to Si.

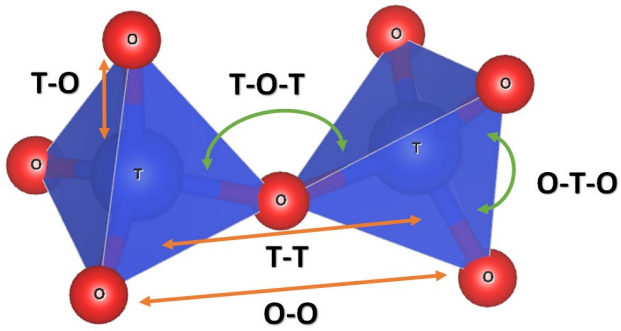

Figure 19. Distance and angles commonly used for zeolite determination. The Si-O distance (1.61 Å) and O-Si-O angle (109.54º) used during the as-made zeolite ITQ-70 structure refinement are shown.

1.6. DETECTORS AND DATA COLLECTION SCRIPTS

The best way to collect and visualize diffraction patterns in the TEM is through detectors. They are generally used for either high resolution imaging, EELS, or diffraction; and can be classified depending on their components and applications. TEM detectors are positioned such that the scattered beams hit the detector at a specific distance from the sample either side-mounted or bottom-mounted at the bottom part of a TEM along the beam path. or side-mounted. The distance that separates the sample height from the detector is normally larger than the distance in X-ray detectors due to the different 2θ ranges, as seen in **Fig. 20**. For 120 keV (0.03349 Å), 200 keV (0.03349 Å) and 300 keV (0.01969 Å) TEMs, the normal 2θ ranges are 2.4°-0.08°, 1.8°-0.06°, and 1.4°-0.05°, respectively meanwhile x-ray photons of 12 keV (λ=1.0332 Å) have a scattering angle 2θ of 62.20º for 1.0 Å reflections requiring a short detector distance and benefiting from a large detector. [51]This distance is virtually changed by the lens system in the TEM. Electrons reaching and hitting the detector generate a signal in the pixels. These signals are later converted into a digital signal and stored in the detector's readout electronics.

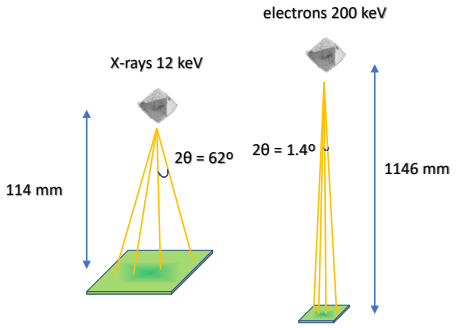

Figure 20. X-rays vs electron distance detectors. The shorter wavelength for electrons implies a lower scattering angle 2θ and hence larger distances.

TEM detectors that are being used for such 3D electron diffraction nowadays can be cataloged in three detector types:

- **CCD cameras:** Charge-coupled devices (CCD) are the most widely used detectors for ED pattern recording. They frequently require a beam stop that remove direct incident beam because they are composed of scintillators made of Yttrium Aluminum Garnet (YAG). These scintillators receive electrons that are converted to photons that are transferred to sensor chips through a fiber optic plate as a consequence they also have limited dynamical range (**Fig. 21**). Furthermore, CCD cameras have slow read-out time, i.e. each pixel is read out one at a time in a sequential manner, and limited read-out noise, within last-generation CCDs.
- **CMOS cameras:** Metal–oxide–semiconductor (CMOS) are direct detection. They do not require an electron-to-photon conversion. They can also be appropriated for electron diffraction tomography since they have low noise level, easy-to-use and

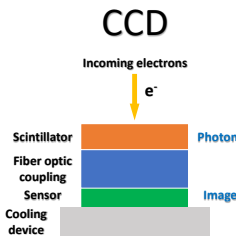

Figure 21. Structure of charge-coupled device (CCD)

offer high resolution ensuring that the camera chosen has the necessary specifications to meet the requirements of the experiment.

- **Direct electron detectors:** Hybrid pixel detectors (HPDs) or Medipix, Timepix, or Pixelated detectors. These detectors consist of a pixel array, where each pixel comprises a semiconductor sensor, typically made of N-doped silicon chips, that are directly exposed to electrons and have no scintillator; all the pixels of these single-electron sensitive cameras can be read out simultaneously, converting the single incident electron to hundreds of electron-hole pairs, as described in **Fig. 22**. This results in much faster readout times, zero background noise, low noise, high spatial resolution, and high sensitivity. All these advantages together enable this kind of detector to operate under low-dose illumination conditions, making them ideal for analyzing highly beam-sensitive materials such as zeolites, MOFs, COFs, or organic molecules while offering functionality for data collection protocols designed for beam-sensitive materials. This type of detector has experienced an increase in application in electron diffraction tomography due to its recent developments.[52]

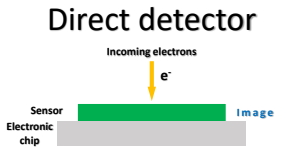

Figure 22. Direct electron detector or Hybrid pixel detectors (HPDs).

There are a few properties of TEM detectors, such as pixel binning that should be considered when collecting 3DED data. Pixel binning in TEM cameras involves combining charges from adjacent pixels to achieve faster readout speeds and improved signal-to-noise ratios. [53] If the detector is set to single-pixel readout, each pixel is read out individually. In contrast, in 2x2 binning, charges from adjacent pixels are combined, and the readout register is shifted down to sum the charges from the four pixels before being read out, resulting in a faster (twice) readout speed, as illustrated in **Fig. 23**. This binning process reduces spatial resolution but improves the signal-to-noise ratio and readout speed. Another aspect to consider during 3DED data collection is the pixel and the detector sizes. The pixel size is the measure of a pixel and is dependent on the camera length given in 1/nm or $1/Å^{-1}$ reciprocal space dimension. The detector size is measured in a number of pixels squared dimensions, for example, 1024x1024 pixels.

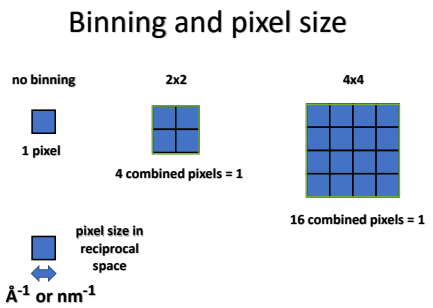

Figure 23. Binning and pixel size scheme.

In conclusion, while the selection of a detector is subject to the specific objectives of the experiment, several detector specifications are commonly considered: 1) Fast Readout, 2) Wide Dynamic Range, 3) Low Noise, 4) Large Detector Area, 5) High Frame Rate, 6) High Sensitivity.

1.7. TEM HOLDERS.

Any 3DED experiment type requires a significantly high tilt range during data collection, particularly considering low completeness in low-symmetry crystal samples. While the majority of TEM specimen holders are single-tilt, operating at room temperature, and capable of tilting ±15º around the 0º axis stage (α tilt), there are TEM holders that can rotate up to ±60º or ±70º in two directions along the α tilt. **Figures 24A and B** show a tomographic holder used for 3DED data acquisition. Some holders, known as cryo-holder tomography, have seen a rapid increase, which can reduce the temperature to 77 K under low-dose conditions. These holders are connected to a Dewar containing liquid nitrogen, and the holder's C is maintained at the liquid nitrogen temperature (**Fig. 24C**). The goal is to keep the crystal at this temperature within liquid nitrogen outside the TEM vacuum and then insert the cryo-holder into the TEM column chamber to keep crystal integrity intact.

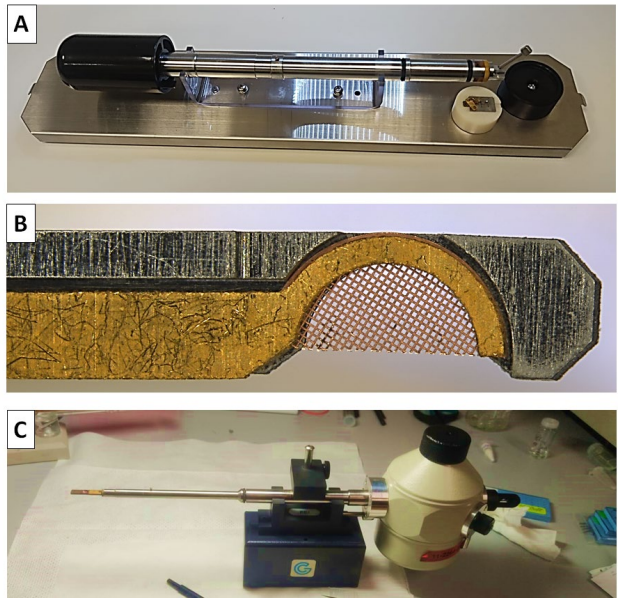

Figure 24. A) Complete view of the JEOL EM-21340HTR tomography holder, used in JEOL 2100F and JEOL 2100 TEM models. B) Close-up of the high-tilt Gatan specimen holder. The copper grid is halved to prevent collisions with the pole pieces of the microscope's objective lens system. C) Single Tilt Liquid Nitrogen Cryo Transfer Holder, Gatan Model 636 (for tomography). This holder features an enlarged Dewar to lower the temperature, ensuring the sample remains frozen during transfer and observation within the microscope.

1.8. WHAT ARE ZEOLITES?

1.8.1. ZEOLITES AND ORDERED POROUS SOLIDS.

Zeolites are solid microporous aluminosilicate materials composed of a framework of basic units that follow the formula unit $TO_{4/2}$, where T is typically Si^{+4} or Al^{+3} atoms (T = Al, Si) tetrahedrally coordinated to four oxygens. They represent a 3D crystalline framework of tetrahedra with adjacent T linked through shared oxygens (**Fig. 25**). Their principal characteristics are structures consisting of channels and cavities and well-defined pores that can play a role as molecular sieves with molecular dimensions that make them favorable catalysts and participate in separation and adsorption processes. Furthermore, their ability to hydrate and dehydrate reversibly makes them suitable to work as desiccants.[54] The formula composition for zeolites is often written as the following general formula:

$$M_{x/n} \cdot [(AlO_2)_x(SiO_2)_y] \cdot zH_2O$$

Where *M* stands for cations (positive ions such as Na^+, K^+, Ca^{2+}); *n* stands for valence of the cations; *x* and *y* stand for stoichiometric coefficients; *z* stands for the number of water molecules in the structure.

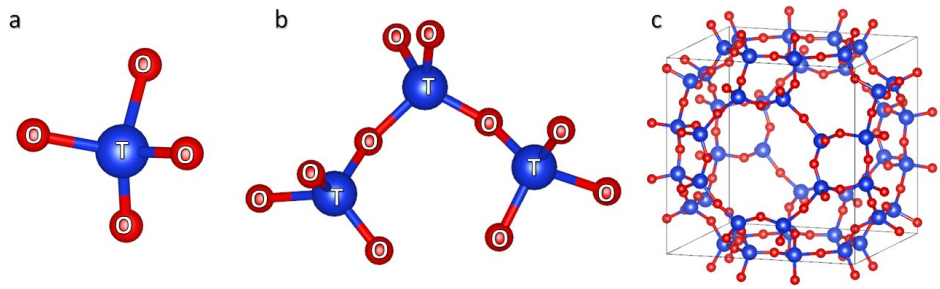

Figure 25. (a and b) Basic tetrahedra structure of zeolite. T stands for heteroatoms such as T: Si, Al, B… (c) Zeolite structure unit cell.

1.8.2. STRUCTURE OF ZEOLITES

The classification of zeolite structures relies on the connectivity and space distribution of aluminum and silicon tetrahedra within their crystalline framework. According to the International Zeolite Association (IZA) database, 255 zeolitic structures are currently collected;[50] however, when accounting for unresolved or unrecognized structures by the IZA, this number significantly increases.[55]

Zeolites are categorized based on their framework types, identified by three-letter codes, or Framework Type Code. Furthermore, the categorization of zeolites can also be based on the dimensionalities of their channel systems. The spatial arrangement of the porous system is crucial for molecule diffusion within the zeolite channels.

Zeolites exhibit channels in none, one, two, or all three spatial directions. Consequently, zeolites can be classified as dimensionless (e.g., AST, NON), monodirectional 1D (e.g., MTW, MRE), bidirectional 2D (e.g., MOR, MWW), or tridirectional 3D (e.g., IRY, LTA).

The pore size of microporous channels is a critical factor in the classification of zeolites. Zeolites can be categorized into small, medium, large, or extra-large pore types based on the size of the ring structures formed by the tetrahedra. These rings, known as 'R rings,' determine the size of the openings that provide access to the channels or cavities within the zeolite framework (see **Table 1**).

Table 1. Classification of zeolites based on pore size.

Pore size	Number of linked tetrahedra	Pore diameter (Å)	Zeolite example
Extra-large	>14	>7.5	IRR, VFI, CLO
Large	12	5.5-7.5	MOR, FAU, IWW
Medium	10	4.0-6.0	RHO, MEL, MFI
Small	8	3.5-5.0	CHA, LTA, IFY

Zeolites are characterized by a limited number of relatively small tetrahedral units. These formations are called Secondary Building Units (SBUs) (**Fig. 26**). The Composite Building Units (CBUs) generally represent complex building blocks that also describe zeolite structures (**Fig. 26**). The final structure of the zeolite is closely influenced by the quantity and nature of CBUs comprising its framework.

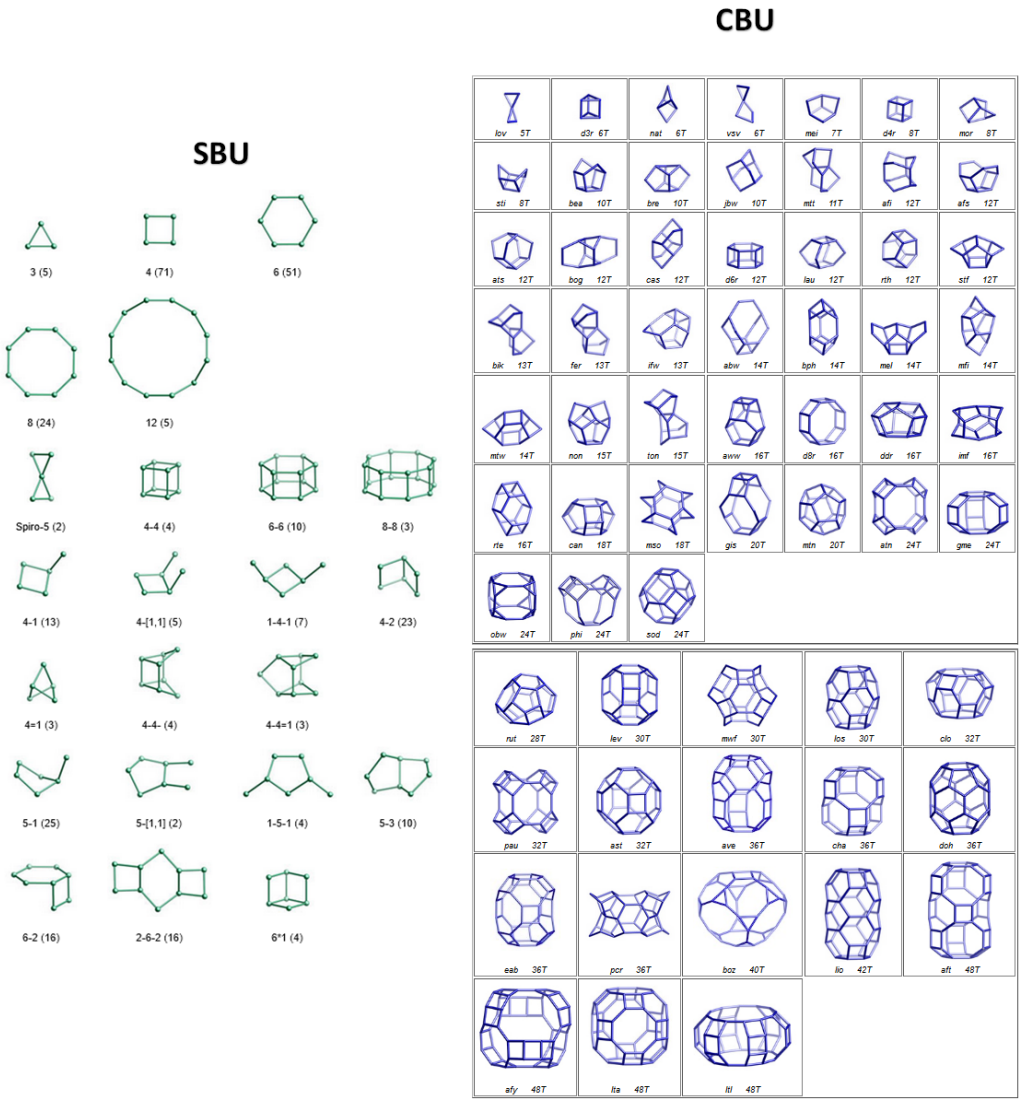

Figure 26. (Left) Secondary Building Units (SBU). The frequency of occurrence is given in parentheses. The (Right) Composite Building Units (CBU). Ordered by the number of T-atoms in the unit.[50]

1.8.3. SYNTHESIS, HETEROATOMS INCORPORATION AND STRUCTURE DIRECTING AGENTS

Hydrothermal synthesis is a common method for creating microporous aluminosilicate minerals. It involves reacting alumina and silica precursors in water under high temperature and pressure, usually in an autoclave. This process promotes the dissolution of precursors, nucleation of zeolite seeds, and their growth into larger crystals. The properties of the resulting zeolites can be controlled by adjusting synthesis parameters. Despite its complexity, this method is widely used in zeolite

research and production due to its ability to produce a variety of zeolites with diverse structures and properties. Numerous variables influence the synthetic procedure, including the mineralization agent, solvent, temperature, crystallization time, structure-directing agent (SDA), pH, gel composition, and concentration. **Fig. 27** illustrates the hydrothermal synthesis of the zeolites process.

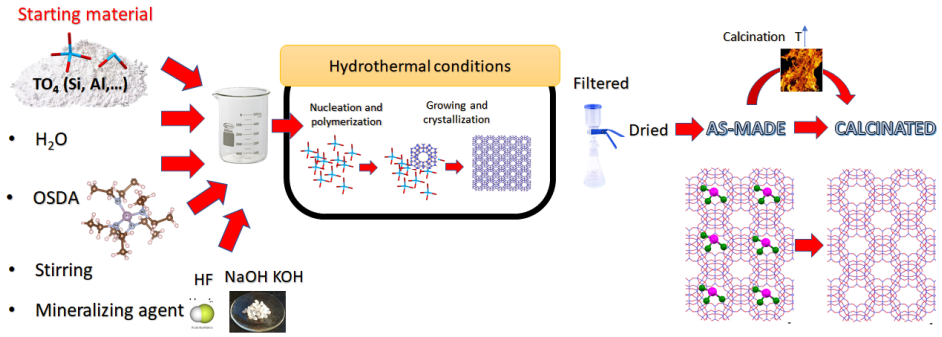

Figure 27. Hydrothermal synthesis of zeolites scheme.

Replacing part of the silicon atoms with other elements such as Al, Ti, B, P, Zn or Ge is possible in many cases. Introducing heteroatoms into the crystal network, generally located within the vacant coordination sites and channels, can influence the relative stability of secondary building units, forming new structures. These heteroatoms establish connections with neighboring Si atoms via O bridges (T-O-Si), which differ in length and angle from those formed exclusively by Si (Si-O-Si). For pure silica zeolites, the combination of TO_4 units (T = Si) leads to (SiO_2), with a complete charge balance in the structure. In contrast, the substitution of Si^{4+} by Al^{3+}, as well as the presence of connectivity defects of Si-O-Si (Q_3) in the form of $Si[(OSi)_3OH]$ or $Si[(OSi)_3O^-]$, creates a charge deficiency in the structure, requiring the incorporation of a cation into the system to compensate for the generated negative charge.

The integration of a variety of different heteroatoms has been documented, including trivalent (Ge, Ti, Sn, Zr), trivalent cations (Al, B, Ga, Fe, Cr), and divalent cations (Zn, Be). When Ge in incorporated to the structure replacing Si isomorphically, it has been widely described that the germanosilicate frameworks obtained tend to present low densities and extra-large pores.[30] Incorporating other elements from the periodic system (such as B, P, Zn, Ge) capable of formally forming tetrahedral oxide networks can give rise to materials known as zeotypes. These cover a wide variety of materials with properties similar to zeolites but with different chemical compositions, including aluminophosphates (AlPOs), silicoaluminophosphates (SAPOs), and germanates.

Among many variables that can influence the synthesis of zeolites, the SDA precursors based on both inorganic and organic cations have been widely used; in particular, the use of organic structure directing agents (OSDA) during the zeolite synthesis has yielded many novel zeolites with intrinsic structures and properties over the last decades. OSDAs are cationic compounds that promote the organization of different oxides within the synthesis gel. These cations located within the zeolite channel can control the degree of incorporation of trivalent elements such as (Al^{+3}, B^{+3}, and Fe^{+3}) and the amount of defect formation. Among the structure-directing agents, the scope of this thesis focuses on new organophosphorus-based SDAs that will be described in the following chapters.

1.8.4. APPLICATION OF 3DED METHODS FOR ZEOLITES STRUCTURE DETERMINATION

As mentioned before, the structure of zeolites has proven difficult to determine using conventional X-ray techniques due to their complex structures, long unit cell parameters, pseudo-symmetries, polyphasic samples, and broadening of peaks. As a result, the use of electron diffraction tomography for *ab initio* structure determination has gained popularity in recent years. [56] Moreover, in combination with PXRD, has played a key role in the discovery of nearly 80% of the new zeolite phases discovered in the last seven years. [57]

This section described some of the updated advances in 3DED methods that give insights for some questions based on structural characterization of zeolite framework and organic guest molecule elucidation:

1) The updated version of the Sir2008 program to include electron diffraction as a new tool for structure determination.[58] Furthermore, the use of the simulated annealing method implemented in SIR2014 can give rise to the non-*ab initio* structure determination algorithm for organic molecules such as OSDA within the zeolite framework. [59]
2) Advancements in dynamical refinement have led to progress in reducing the noise in reconstructed electrostatic potential maps. This has improved the visibility of guest molecules in zeolites, such as the chiral and pure silica zeolite STW_HPM-1 (STW topology). It has also enhanced the absolute structure determination of chiral zeolites.[60]
3) This study introduces electron crystallography methods, using HRTEM and PED, to determine the handedness of chiral zeolite nanocrystals, enabling advancements in enantioselective catalysis and separation.[61]
4) In 2011, the automatic electron diffraction tomography (ADT) method successfully employed the 3D electron diffraction (3DED) technique to determine the structure of the zeolite silicogermanate material ITQ-43,[30] marking the first instance of such an achievement.
5) Direct location of SDA in zeolite framework applying ultralow electron dose illumination settings with 3DED data provided from a continuous rotation electron diffraction protocol.[62]

6) Identify the positions of hydrogen atoms in organic and inorganic materials through PEDT and dynamical refinement. Hydrogens tend to be easier sensitive atoms with electrons than with X-rays as electrons have higher or relatively higher scattering factors at low atomic numbers.[7]
7) A recent review article suggests an explanation for the typical processes leading to common zeolite deterioration when exposed to electrons. The most common physical-chemical phenomena occurring in zeolite during TEM exposure include generally the amorphization process referring to the transformation of a crystalline phase into an amorphous phase, i.e. loss of crystallinity, the collapse of the framework, and morphology changes.[11]
8) Structure determination of biogenic guanine crystals (from spider integument, fish scales, and scallop eyes) by 3DED method and confirmed by analysis of powder XRD data.[63]
9) First two-dimensional zeolite is solved by 3DED methods with an intrinsic property of transitioning to a conventional 3D zeolite framework upon exposure to a transmission electron microscope vacuum.[64]
10) This is a review article that provides an overview of the significant impact of advanced electron crystallography techniques on the discovery of new zeolites. It underscores how the ITQ zeolite materials developed by Corma's group catalyzed the evolution of these techniques, with the advent of 3D ED methods accelerating the identification of novel structures. Remarkably, nearly 80% of newly discovered zeolite frameworks in recent years have been solved using a wide range of electron diffraction methods, including HRTEM and the latest 3DED techniques.[65]
11) The study highlights the importance of fluoride ions and germanium in stabilizing novel zeolite structures, contributing to the discovery of materials with potential catalytic applications. It describes the synthesis of a novel germanium-containing zeolite, IM-10, prepared using fluoride media and hexamethonium cations. IM-10 reveals tetragonal symmetry characterized by powder X-ray diffraction and Rietveld refinement, featuring a unique topology with a framework of double four-membered rings (D4R) and supercages that host hexamethonium ions.[66]
12) The following studies present the complete determination of OSDA containing zeolites through 3DED methods. The first one presents the use of 3DED and provides key insights into the crystallographic structure of the pure silica as-made zeolite ITQ-55 with ordered silanols.[67] The second one presents the determination of the accurate framework structure of SCM-25 using 3D electron diffraction data and Rietveld refinement against synchrotron powder X-ray diffraction data. It also shows the localization of possible ordered distribution of the cationic OSDAs in the cavities. [68]In the third work, the authors were able to determine the unique structure of PST-24 using advanced electron diffraction and synchrotron X-ray diffraction techniques and extract the difference Fourier map (F_o - F_c) of the average structure, refined against the cRED data, of the as-made Si-PST-24. These findings showed relatively

residual electron densities of the organic template within the d5r units. [69]This work shows different Fourier maps of SU-8 sample obtained by 3DED data which were further used, in combination with SCXRD, for the localization of the guest molecule within the pores, and hence for the complete structural analysis of the Van der Waals interactions between framework and organic molecule.[62]

CHAPTER 2. OBJECTIVES

The primary objectives of this doctoral thesis are the study of 3D Electron Diffraction methods and their application for the structural elucidation of novel zeolitic materials. The materials under study are in their as-made form, meaning they contain Organic Structure Directing Agent (OSDA) molecules within the pores and cavities. The complete structure determination includes not only the inorganic heteroatoms constituting the framework structure but also the structural localization of highly disordered organic guest molecules.

Therefore, the main objectives of this doctoral thesis are twofold:

The first objective is to study and optimize state-of-the-art 3D Electron Diffraction methods, including PEDT and cRED, for the structure determination of novel zeolites and related beam-sensitive materials using data from nanosized single-crystals.

The second objective is to apply these optimized techniques in combination with standard PXRD, and current structure determination methods, such as Simulated Annealing and Rietveld refinement, along with various chemical analysis methods. This approach will provide a more detailed structural characterization of three different *as-made* materials. Simultaneously, this methodology will validate the advances and reliability of the techniques, contributing to a more accurate understanding of the materials under study.

CHAPTER 3. CHARACTERIZATION METHODS

3.1. THREE-DIMENSIONAL ELECTRON DIFFRACTION (3DED)

3.1.1. GRID PREPARATION AND TEM HOLDERS

A clear summary experimental table showing the data acquisition, reduction, and refinement processes used in all samples examined in this thesis can be found in APPENDIX I.

All samples were prepared as white powders and carefully deposited onto TEM grids before being loaded into the TEM holders. The grids used included 200-mesh carbon-coated copper TEM grids and 200-mesh copper grids coated with an extra-thick 20–30 nm carbon layer (CFT200-CU-ET, supplied by Ted Pella). To preserve the integrity of the samples, which contain organic molecules within their cavities, no solvents (such as ethanol, water, or dichloroethane) were used during the preparation process, ensuring optimal conditions for 3DED analysis. Thus, the solid samples from all chapters of results were carefully ground and deposited directly, in a dry state, onto the TEM grids.

Due to the pole piece's design of some microscopes like JEOL 2100F, the grid may need to be cut in half and mounted in a specific holder as shown in **Fig. 24** and **Fig. 28** to maximize the tilt. Alternatively, the sample can be grinded and sprinkled directly onto the grid without using any liquids. This is followed by gently blowing on the grid to remove excess dust particles.

The two as-made zeolite ITQ-52 samples, which will be discussed in the following chapters, were measured using two different electron microscopes: the JEOL 2100F, located at the Electron Microscopy Service of the Universitat Politècnica de València (UPV) in València, Spain, and the JEOL JEM 2100-LaB_6, situated at the 'CCiTUB Centros Científicos y Tecnológicos' microscopy services in Barcelona, Spain. The samples were prepared in grids mounted on the High Tilt Specimen Holder (Gatan model EM-21340HTR), shown in **Figures 24a, 24b, and 28**. This type of holder allows tilting the sample up to 80° in small pole piece gaps, providing a large, unobstructed field of view for tomographic data collection. However, in this case, the holder was used to tilt a maximum of ±60º in both directions ensuring that the center of gravity is maintained during a stage tilt, reducing shifts during tomography.

The zeolites samples ITQ-52, ITQ-70, and ITQ-35 were analyzed using the FEI Tecnai G2 20 TEM at 200 keV. These samples were mounted on a Single Tilt Liquid Nitrogen Cryo Transfer Holder (Gatan Model 636), specifically designed for low-temperature tomography applications, as illustrated in **Fig. 24c**. This holder employs liquid nitrogen to maintain the low temperature required for applications related to ED measurements for beam-sensitive materials. It is also equipped with an external temperature controller, which is connected to the holder once it is inserted into the

TEM column, ensuring precise temperature control during the analysis. On the other hand, the as-made ITQ-52 sample, which was measured at room temperature, was mounted on a high-tilt tomography holder capable of tilting up to ± 80º.

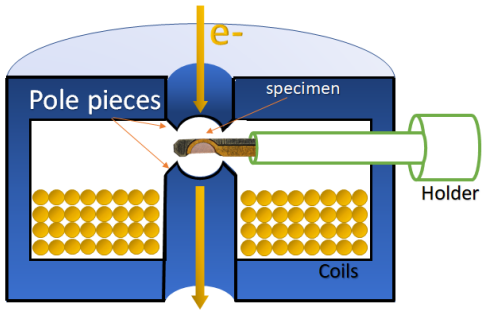

Figure 28. Section view of a TEM objective lens. The TEM pole piece gap is too small to tilt a complete specimen grid at higher angles. For this reason, the TEM grids are cut in half.

3.1.2. TRANSMISSION ELECTRON MICROSCOPES AND DETECTOR SYSTEM

In this study, all 3DED experiments on the zeolite samples were conducted using three transmission electron microscopes:

- **JEOL 2100F (200 keV)**

A TEM JEOL 2100F was used to carry out 3DED experiments on the standard samples and the two as-synthetized ITQ-52 samples. It works under 200 keV and is installed at the Electron Microscopy Service of the Universitat Politècnica de València (UPV) in València (Spain) (**Figures 29 and 30**). This microscope is a Field Emission Electron Microscope 200 keV model JEOL 2100F that can acquire high-resolution images with resolution up to 0.19 nm. Besides the high vacuum system and chamber, its main components are shown in **Fig. 30** and **Table 2**. This TEM also incorporates a high-resolution Energy dispersive X-ray (EDS) detector for nanometric and atomic scale elemental experiments. The TEM is equipped with a GATAN Orius SC600A CCD camera with an active area (unbinned) of 2688 x 2672 pixels for capturing images and diffraction patterns, with a dynamic range of 14 bits. For diffraction data acquisition, the camera was set to a 1048 x 1048 pixel area detector in 2x2 binning mode. Furthermore, it is complemented with a NanoMEGAS-Digistar P1000 beam precession device to acquire diffraction data with beam precession.

Figure 29. JEOL 2100F Transmission Electron Microscope (TEM) room situated at the Universitat Politècnica de València (UPV) microscope services. The operating voltage is set at 200 keV. The left section of the image showcases the high tension (HT) tank. The central portion displays the TEM, control panels, monitors, and the high vacuum system. The right section features the table used for grid preparation along with the Nanomegas precession device.

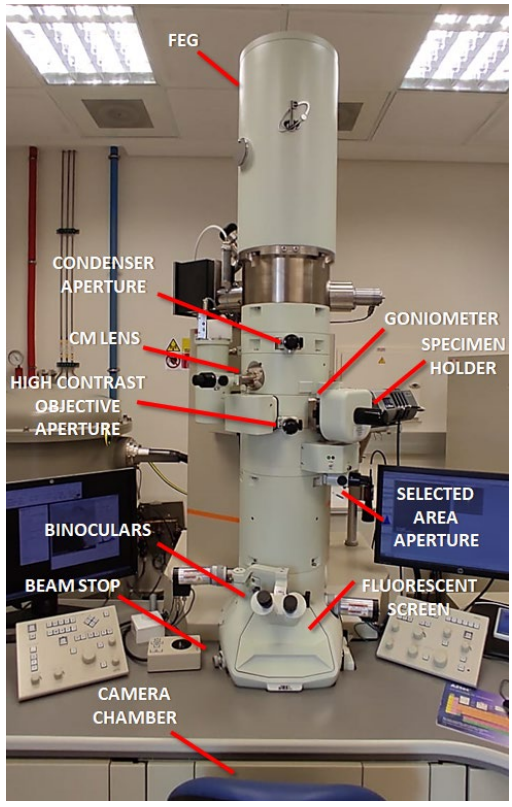

Figure 30. Components of a TEM outer column. This TEM is a JEOL 2100F (200 keV).

Table 2. JEOL 2100F TEM components

Illumination system	Imaging forming lenses	Specimen stage
• Zr/W Electron gun • 1ºCondenser lens (C1) • 2ºCondenser lens (C2) • 3ºCondenser Minilens (CM) • Four condenser apertures (CA): 10, 40, 100, 250 µm de diámetro • Stigmator, alignment and four system modes [TEM, EDS, NBD and Convergent Beam Electron Diffraction (CBD)]	• Six set systems of electromagnetic lens: Objective lens, OM lens, 1°, 2° y 3° intermediate lens y projector lens • Objective apertures • Stigmators	• Specimen exchanger (airlock system) • Specimen shift • Holder EM 21340 HTR: High Tilt Specimen +/- 60°

- **JEOL JEM 2100-LaB_6 (200 keV)**

A TEM JEOL JEM 2100-LaB_6 was used to carry out 3DED experiments on the two as-synthetized ITQ-52 samples. This TEM is equipped with a LaB_6 emission gun and works under 200 keV. It is situated at 'CCiTUB Centros científicos y tecnológicos' microscopy services, in Barcelona (Spain). The diffraction patterns were acquired at room temperature using a Gatan Orius SC1000A CCD camera with a dynamic range of 14 bits. This TEM is also equipped with accessories for EDS analysis, annular dark-field STEM detectors and NanoMEGAS Precession Device.

- **FEI Tecnai G2 20 TEM (200 keV)**

This TEM was used to carry out 3DED experiments on the as-made ITQ-70, ITQ-52, and ITQ-35 samples. This TEM is a FEI Tecnai G2 20 equipped with a thermionic cathode (LaB_6) at an acceleration voltage of 200 keV, as shown in **Fig. 31**. It is situated at 'The Institute of Physics of the Czech Academy of Sciences (FZU)', Prague, Czech Republic. This TEM is equipped with a Timepix Quad's hybrid pixel detector (Amsterdam Scientific Instruments), model QTPX-262k. The original chip design of this detector consists of a 256×256 pixel array with a 1.4cm × 1.4cm active area. Each pixel is 55 µm in size. For the acquisition of the DPs, this TEM is provided with self-written scripts[70] in Olympus Soft Imaging Solutions iTEM software for controlling the beam, goniometer, and detector.

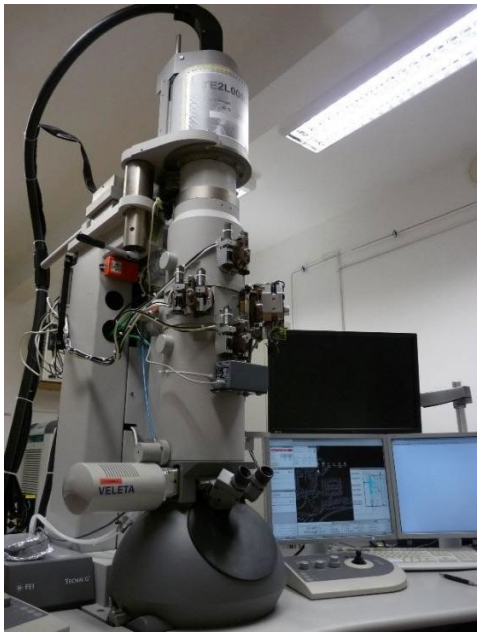

Figure 31. TEM model FEI Tecnai G2 20 image. The TEM is equipped with thermionic cathode (LaB_6) at an acceleration voltage of 200 keV installed at the Institute of Physics of the Czech Academy of Sciences (FZU) in Prague, Czech Republic.

3.1.3. PRECESSION EQUIPMENT

The three microscopes used in this thesis are equipped with the precession device Nanomegas Digistar P1000 for PEDT.[71] The following **Fig. 32** illustrates the PED device and the control board for precession alignment. The precession angle was carefully aligned before acquiring the diffraction patterns, which included the necessary adjustments to the electron microscope, such as beam tilt, image shift, and eucentric height. The acquisition of all diffraction patterns collected by PED was achieved with a beam precession semi-angle of 1.0º.

Figure 32. A) Precession NanoMEGAS Digistar P1000 device. B) Device control

3.1.4. cRED AND PEDT DATA COLLECTION

A 3DED experiment can be carried out in two illumination modes: SAED and NBD. Within these categories, one can acquire the DPs in continuous rotation or a stepwise mode combined with beam precession, as shown in the basic scheme in **Fig. 33**. SAED uses an area aperture whose position is mechanically modified so that the crystal is illuminated and the NBD uses the deflector coils to reduce the size of the beam to nanometers. The choice of both modes depends on the size and type of the crystal. For instance, the use of the smallest SAED aperture (10 µm in diameter), leaves a diffraction area of 200 nm, while, in NBD mode, the smallest C2 aperture (10 µm in diameter) can leave a diffraction area of 6 nm. This fine beam size is particularly advantageous for crystals containing closely spaced nanosized domains, ensuring that diffraction data is always acquired from the same region. Though in NBD mode the area of interest may move away from the illuminated beam during the tilt because of goniometer instability. Furthermore, with such small beam sizes, beam convergence effects must be considered. In NBD mode, a slightly convergent beam may result in diffraction spots being enlarged into disks, similar to those observed in CBED (Convergent Beam Electron Diffraction). The degree of convergence depends on the instrument's alignment and the choice of aperture. To mitigate this, the diffraction focus is typically adjusted during data acquisition (see APPENDIX II. Adjust the "Defocus" with the DIFF FOCUS dial) to minimize spot distortion and ensure sharp diffraction patterns. Additionally, such as overlapping reflections and inaccuracies in peak positioning, especially when diffraction spots appear elliptical or misaligned.

Throughout the course of this doctoral research, data were collected on isolated crystals with the assistance of three different developed script programs.

The initial script, known as the ultrafast Electron Diffraction Tomography (Ultrafast-EDT),[72] was implemented in the JEOL 2100F microscope using DigitalMicrograph (DM) scripting. This script can be used for continuous or stepwise rotation with beam precession with options for both SAED and NBD illumination modes. When the Diffraction Pattern (DP) sequence is acquired with continuous rotation of the crystal, the total collection time is significantly reduced from 30–60 minutes to just 3–6 minutes. Furthermore, this script features an automated stepwise rotation function, which enables the acquisition of diffraction frames while the crystal is rotated with 1-degree tilt steps.

The second script was the Fast-ADT acquisition routine developed by Ute Kolb's group,[45] which are installed in the JEOL 2100F and JEOL JEM 2100-LaB_6 microscopes. This script can be used in both NBD and SAED modes. In this thesis, Fast-ADT has been used in continuous and stepwise working in NBD mode.

The third script was a self-written Olympus Soft Imaging Solutions iTEM software developed by Lukas Palatinus' group and implemented in the FEI Tecnai G2 20 (200

keV). This script can be used in NBD mode and SAED illumination modes in continuous and stepwise data acquisition.

For the Ultrafast-EDT and Fast-ADT software, parameters controlling the goniometer stage (e.g., initial and final angles, tilt step), the beam and detector, and exposure time have been optimized. These parameters are detailed in a user-friendly manual included in Appendix II. This manual has been used for 3DED data collection with the JEOL 2100F.

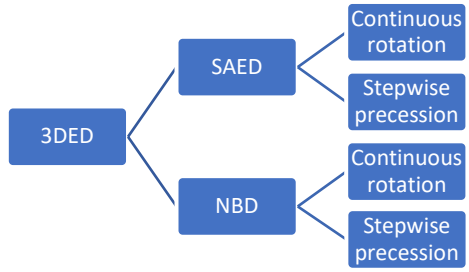

Figure 33. 3DED acquisition methods and illumination modes.

Frames generated using the Ultrafast-EDT and Fast-ADT data collection protocols are initially in *.dm3* format. These frames are then converted to *.tiff* format using Gatan Digital Micrograph software (version 3.42) or ImageJ software, and subsequently prepared for data processing with PETS2[73] or ADT3D[36] software. Whereas, for Olympus Soft Imaging Solutions iTEM software generated DPs as *.tif* file format. A separate file is generated (*.pts* file format) using the data acquisition program which contains experimental information such as precession angle, tilt step, exposure time, etc. These *.pts* files can directly be imported to PETS2 data processing program.

3.1.5. cRED AND PEDT DATA PROCESSING

All 3DED datasets (cRED and PEDT) obtained during this thesis were analyzed using PETS2.0 software. A graphical user interface (GUI) of this software can be seen in **Fig. 34**. PETS2.0 is capable of reading diffraction data files in raw frame format (***.tif***), provided with proper experimental information files in ***.pts*** format. The software performs several key tasks:

- **Determination of Unit Cell Parameters**: These are determined during data analysis.
- **Indexing and Integration:** Intensities are indexed and integrated to assign them to reciprocal lattice points.
- **Frame Integration and Processed File Generation**: Processed files for dynamical refinement.
- **Scaling and Merging:** Multiple datasets are scaled and merged directly.

After the final data processing, two files are generated:

a) A file with reflection indices with intensity values (***.hkl* file**).
b) A file with unit cell parameters and additional data processing information, such as mosaicity and integration methods (***.cif_pets* file**).

Furthermore, the integrated intensities can be saved as ***SAMPLENAME_dyn.cif_pets***, as long as the intensity has been processed to perform dynamical refinement.

The electron dose received by the crystals measured in the **FEI Tecnai** during the 3DED data was calculated using the procedure detailed in **APPENDIX II**.

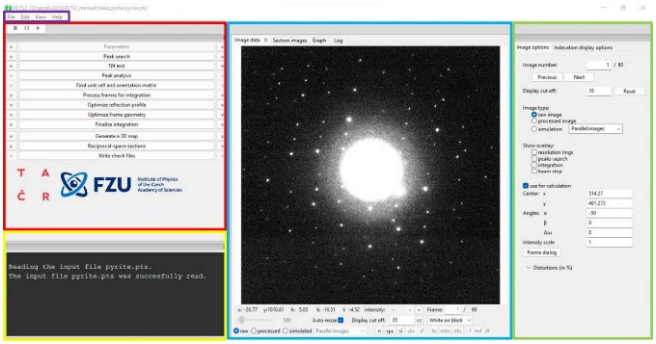

Figure 34. User Graphical Interface of PETS2.0.

3.1.6. STRUCTURE SOLUTION AND REFINEMENT

During the thesis, the structures of all collected datasets were solved using the two Direct Methods software packages: JANA2020 and SIR2019.[74,75] The structures were first solved by JANA2020/ SIR2019 under the assumption that the reflections are kinematic ($I \sim |Fhkl|^2$). To use the charge flipping algorithm, as implemented in

the program Superflip,[76] Jana 2020 software was used. To use the JANA2020 program, the required input files are intensity files in *.hkl* format and files with experimental or data processing information in *.cif_pets* format (or *_dyn.cif_pets* for dynamical refinement).

At the same time, the structures were further analyzed using SIR2019 to perform Simulated Annealing (SA). This approach was used to determine the distribution of OSDA of as-made zeolite samples studied in this thesis. A list of parameters was previously optimized specifically for refining the structural models starting with the Internal and External Degrees of Freedom (INTDIF and EXDOF, respectively). These INTDIF and EXDIF include translational positions (x, y, z), rotation (θ), and torsional angles. The cost function was defined as the R factor, and the total number of runs was established at 10 for all employed datasets. An anti-bump restraint, with a weight of 1.0 and a distance scale factor of 0.7, was implemented in all datasets to avoid proximity issues between the inorganic framework and the OSDA molecules. The function primarily ensured that the refined structures adhered to reasonable chemical geometry, reducing computational artifacts during SA optimization. However, simulations without the anti-bump function were also performed as a trial which revealed minor differences in OSDA positions but confirmed the overall consistency of the structural model, with no significant artifacts attributable to the anti-bump restraint. Dynamical occupancy corrections (DOC) were applied to the OSDA molecules to accommodate their specific positions. The input files were loaded in *.hkl*, *.cif,* and *.mol* formats.

3.2. POWDER X-RAY DIFFRACTION (PXRD)

PXRD measurements were performed in Bragg-Brentano geometry using a PANalytical EMPYREAN diffractometer, equipped with a goniometric head to align the capillaries prior to the measurements and a PIXcel1D-Medipix3 detector. Cu Kα1 (λ = 1.5406 Å) X-ray radiation was used for the measurements, employing a hybrid monochromator, and a tube voltage and intensity of 45 kV and 40 mA, respectively. The goniometer arm length was 240 mm, and a fixed divergence slit with an aperture of 1/4° was used. The measurements were performed at 298 K, with a continuous rotation of the capillaries. The collected data were then refined (Rietveld refinement) using the FULLProf[77] and JANA2020 software.

3.3. ADDITIONAL CHARACTERIZATION TECHNIQUES

Aside from the 3DED and PXRD techniques studied during the thesis, all the cationic OSDAs and inorganic solids have been characterized by Nuclear Magnetic Resonance (NMR), Chemical analysis (ICP-MS), Elemental Analysis (EA) and Scanning Electron Microscopy (SEM). Below is a brief description of all additional characterization techniques used during this doctoral thesis.

3.3.1 FIELD-EMISSION SCANNING ELECTRON MICROSCOPY (FESEM)

Scanning Electron Microscopy (SEM) is a technique that allows analyzing the morphology and size distribution of crystals in obtained samples by using a focused beam of electrons through a system of magnetic lenses, which, upon interacting with the sample, produces a series of phenomena such as the emission of Secondary Electrons (SE), Auger Electrons (AE), Backscattered Electrons (SE) or characteristic X-ray [Energy Dispersive X-ray Spectroscopy (EDS)] (see **Fig. 9** in Introduction section). Field Emission Scanning Electron Microscopy (FESEM) differs from SEM in the electron generation system. FESEM uses a field emission gun as the electron source, providing highly focused beams of high and low-energy electrons, significantly improving spatial resolution and allowing operation at low potentials (0.02-5 kV). This helps minimize charging effects in non-conductive materials.

The Secondary Electron Detector (SE2) has been used to obtain high-resolution FESEM images and study the shape and size of crystals and the presence of impurities or amorphous material in the zeolites of interest. Samples are prepared on SEM conductive double-sided carbon tape attached to a sample holder. The microscope used to capture the micrographs is a ULTRA55-ZEISS model. The accelerating voltages used range from 0.8 to 2 kV, depending on the conductivity of the analyzed sample.

Furthermore, this equipment also features an Energy Dispersive X-ray Spectroscopy (EDS) detector from Oxford Instruments. With this system, the X-ray photons emitted by the sample, whose wavelength is characteristic of each element, are detected. In this way, analytical, qualitative, and quantitative chemical information is obtained from areas of varying size on the surface of the materials.

3.3.2. COMPUTATIONAL METHODS

Therefore, it was decided to employ an alternative software to calculate the possible spatial configuration of OSDAs within the unit cell. For such purpose, the software zeoTsda was used to determine the optimal configuration of OSDA within the cavities of the germanate framework. [78] This advanced algorithm uses Monte Carlo simulations to fit the template within the zeolite unit cell and identifies the optimized minimum geometry by detecting the lowest van der Waals interaction energy between the zeolite and the template. Rather than screening multiple SDA candidates as the primary objective of this approach, we used two cif files as input files, i.e. unit cell matrix coordinates corresponding to both the SDA and the germanate framework with the fluorine anions, which were previously solved by 3DED data. The final coordinates are evaluated in terms of geometry stabilization rather than energy considering the time calculation dependence with the number of freedoms which is also dependent on

the number of template atoms. By previously assigning certain parameters such as, atom types, sp3, sp2, or sp hybridization, and atomic charges, the template molecule is introduced as a rigid body with translational and rotational parameters free to move whereas the zeolite atoms are kept fixed. The number of OSDA occluded per unit cell is considered a parameter to be optimized as well.

3.3.3. ELEMENTAL ANALYSIS (EA)

Elemental analysis (EA), also known as micro elemental analysis, is a characterization technique that has been applied to analyze carbon, hydrogen, and nitrogen (C, H, N) from both organic and inorganic species during the study of this thesis. This technique involves the thermal oxidation of samples at high temperatures (1100ºC), resulting in the production of CO_2, H_2O, and N_2. These compounds were then separated and quantified using gas chromatography with a 2.5 m long CHNS E3015 (Elemental Analysis) column and a thermal conductivity detector (TCD). The EURO EA 3000 Element Analyzer (EuroVector) was used as the model of the EA equipment, with sulfanilamide used as the reference compound. The required sample amount was approx. ±1 mg.

3.3.4. CHEMICAL ANALYSIS

Inductively Coupled Plasma (ICP) is a spectroscopic technique used to accurately determine the qualitative and quantitative chemical composition of solid materials viewed in this thesis. This technique relies on the emission of photons by atoms heated to high temperatures through an argon plasma. After exciting their electrons at high temperatures, these excited electrons return to their fundamental states emitting photons at specific energies characteristic of each element. Also, the intensity of the emitted photons is directly proportional to the concentration of the corresponding element. The elements analyzed by this technique were Si, P, N, and C. The ICP-MS used was the model Varian 715-ES. The calibrations were carried out with commercial standard solutions. The required sample amount was approx. ±30 mg.

3.3.5. THERMOGRAVIMETRIC ANALYSIS (TGA)

Thermogravimetric analysis (TGA) is an analytical technique that measures the weight changes of a material during a constant programmed rate of heating under a controlled atmosphere. Additionally, the Differential Thermal Analysis (DTA) curve is a temperature function that allows for the estimation of the temperature difference between endothermic and exothermic events occurring in the material during heating or cooling (by thermoelectric voltage) compared to an inert reference material. The DTA temperature will be considered for further calcination steps in the case of zeolites. The TGA experiments were carried out in a Mettler-Toledo TGA/SDTA581e. The required sample amount was approx. ±8 mg.

3.3.6. LIQUID AND SOLID NUCLEAR MAGNETIC RESONANCE (NMR)

Nuclear Magnetic Resonance (NMR) is a technique that studies the behavior of certain atomic nuclei with a non-zero spin in the presence of an applied magnetic field. It is based on the interaction of the magnetic moments of atomic nuclei (μ_n) with an external magnetic field (B) which alters the spin orientation and the energy of the atomic nucleus, resulting in a splitting of energy levels as shown in **Fig. 35**.

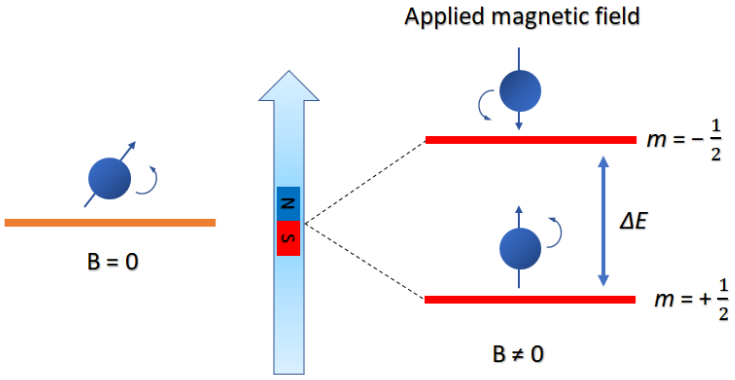

Figure 35. Energy levels of a nuclei with ½ spin in a magnetic field (B).

The nuclei of molecules are surrounded by electrons that generate a small local magnetic field induced, opposite to the external magnetic field. This shielding, called chemical shift (δ), is characteristic of each atom in a chemical environment and is expressed in parts per million (ppm). The determination of chemical shifts is independent of the applied field and provides information about the local environment of the analyzed nuclei.

The spectra recorded in liquid solution are composed of very narrow and well-defined signals. The thermal motion of the molecules averages the different interactions of the nuclear spin moment.

NMR measurements of liquids were carried out to characterize the synthesized organic cations and their corresponding synthetic intermediates. The analyzed atomic nuclei were ^{1}H, ^{13}C, and ^{31}P. The NMR spectra were recorded on a Bruker AV-300-SB spectrometer. For the measurements, at least 30 mg of the compound dissolved in 0.7 mL of deuterated solvent (D_2O, $CDCl_3$, etc.) were required.

In the solid state, the mobility of atoms is highly restricted, and the signals obtained are much broader than in the liquid state. This is a result of the accumulation of small variations in chemical environments and, consequently, nuclear spin

interactions. The interactions responsible for broadening the signals include chemical shift anisotropy (interactions between nearby nucleus-electrons), dipolar couplings (dipole-dipole interactions between neighboring nuclei), and quadrupolar coupling (asymmetric charge distribution interacting with gradient fields).

The use of high-resolution techniques in Solid-State NMR (ssNMR), such as High-Resolution Magic Angle Spinning (HR-MAS), significantly improves the resolution of solid-state spectra and enhances the information provided by spectroscopy in solids. This technique involves rapidly spinning (kHz) the samples around an inclined axis at an angle of 54.74° relative to the magnetic field (B) as seen in **Fig. 36**. This procedure eliminates dipolar interactions and partially reduces quadrupolar interactions. It also averages the chemical shift anisotropy, greatly reducing the signal broadening in the solid state.

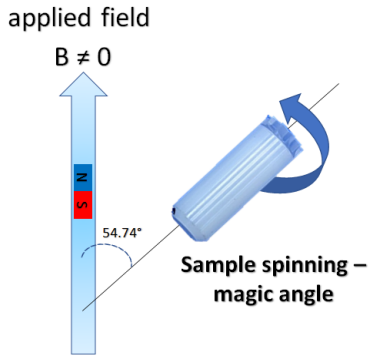

Figure 36. Magic angle spinning in solid state NMR.

The most interesting materials obtained in this study were analyzed using MAS-NMR applied to the nuclei of ^{29}Si and ^{19}F. The spectra were recorded using a Bruker AV-400-WB spectrometer at room temperature.

3.3.6.1. ^{19}F-NMR

Fluorine-19 nuclear magnetic resonance (^{19}F NMR) applied to non-calcined materials provides information about the environment of fluoride anions (F^-) in the zeolite framework. This anion is typically occluded within small cavities of the structure, resulting in resonances between -35 and -80 ppm. The presence of resonances at very high fields in the samples (between -100 and -160 ppm) corresponds to the presence of hexafluorosilicate $(SiF_6)^{2-}$ impurities in the materials. These salts are often partially soluble in hot water and can frequently be removed from the synthesized materials by thorough washing with boiling distilled water. Furthermore, in silicogermanate zeolites with well-known structure-building units (SBUs) such as the D4R, the analysis of ^{19}F MAS-NMR can provide information about the number of Si and Ge atoms forming those units (**Fig. 37**).[79]

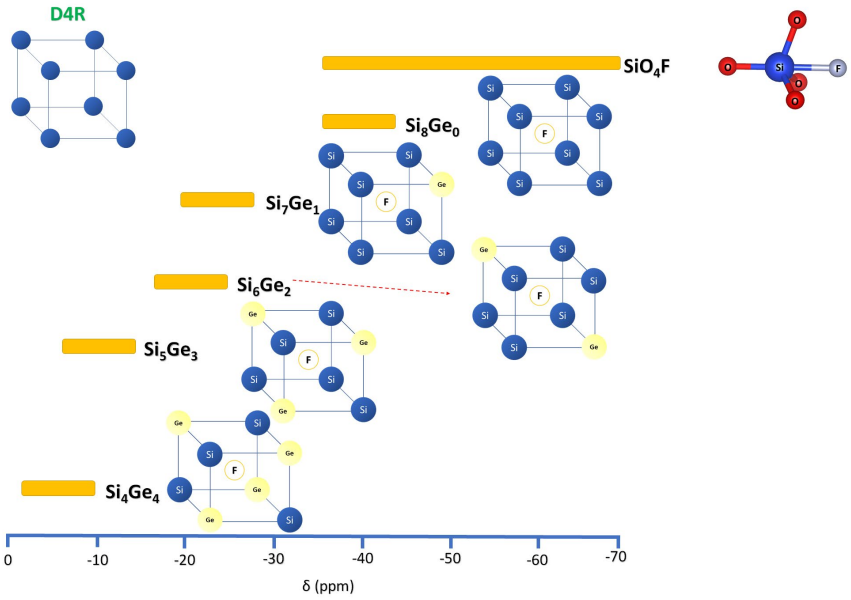

Figure 37. Chemical shifts of ^{19}F-MAS-NMR described for zeolites synthesized in a fluoride medium. Observed shifts for the D4R building unit with different Si/Ge ratios.

3.3.6.2. ^{29}Si-NMR

Nuclear Magnetic Resonance of silicon applied to solids (^{29}Si MAS-NMR) allows studying the coordination of Si species present in the solid framework. The method provides information concerning the presence of connectivity defects, either Si[(OSi)$_3$OH] or Si[(OSi)$_3$O$^-$] (Q_3), in various crystallographic sites occupied by silicon. Furthermore, it offers insights into the Si-O-Si angles within the crystal lattice of pure silica zeolites samples, leading to spectra with high resolution, as reported in the research conducted by Thomas et al. The Thomas-Klinowski equation can be used to describe the relationship between the framework Si-O-Si bond angle (θ) and the chemical shift (δ) observed in silicon-29 nuclear magnetic resonance (^{29}Si NMR) spectroscopy. The Thomas-Klinowski equation is shown below in equation 3.1, where δ is the chemical shift observed in the ^{29}Si NMR spectrum expressed in ppm from tetramethylsilane (an organosilicon compound with the formula Si(CH$_3$)$_4$ and abbreviated as TMS), and θ, expressed in degrees, is the Si-O-Si bond angle.[80] In the **Fig. 38** below illustrates the main chemical shifts observed in zeolites by ^{29}Si MAS-NMR.

$$\delta\ (ppm\ from\ TMS) = -25.44 - 0.5793 \cdot \theta \qquad (3.1)$$

The resonances between -105 and -120 ppm are assigned to Si in completely silica environments (Q_4). The resonances between -90 and -100 ppm correspond to Q_3

connectivity defects in the form of $Si[(OSi)_3OH]$ or $Si[(OSi)_3O^-]$. In some zeolites, the presence of Si in Q_2 environments, i.e., $Si[(OSi)_2(OH)_2]$, has been exceptionally reported.[81] The incorporation of Al or trivalent elements into the framework shifts the signals of neighboring Si to values between -80 and -110 ppm, depending on the number of neighboring Al atoms, in form of $Si[(OSi)_3(OAl)_1]$ (Q_3), $Si[(OSi)_2(OAl)_2]$ (Q_2), $Si[(OSi)_1(OAl)_3]$ (Q_1) or $Si[(OAl)_4]$ (Q_0). On the other hand, the presence of F^- in the materials shifts the ^{29}Si NMR resonances above -140 ppm due to the formation of pentacoordinated species $[SiO_4F]^-$.

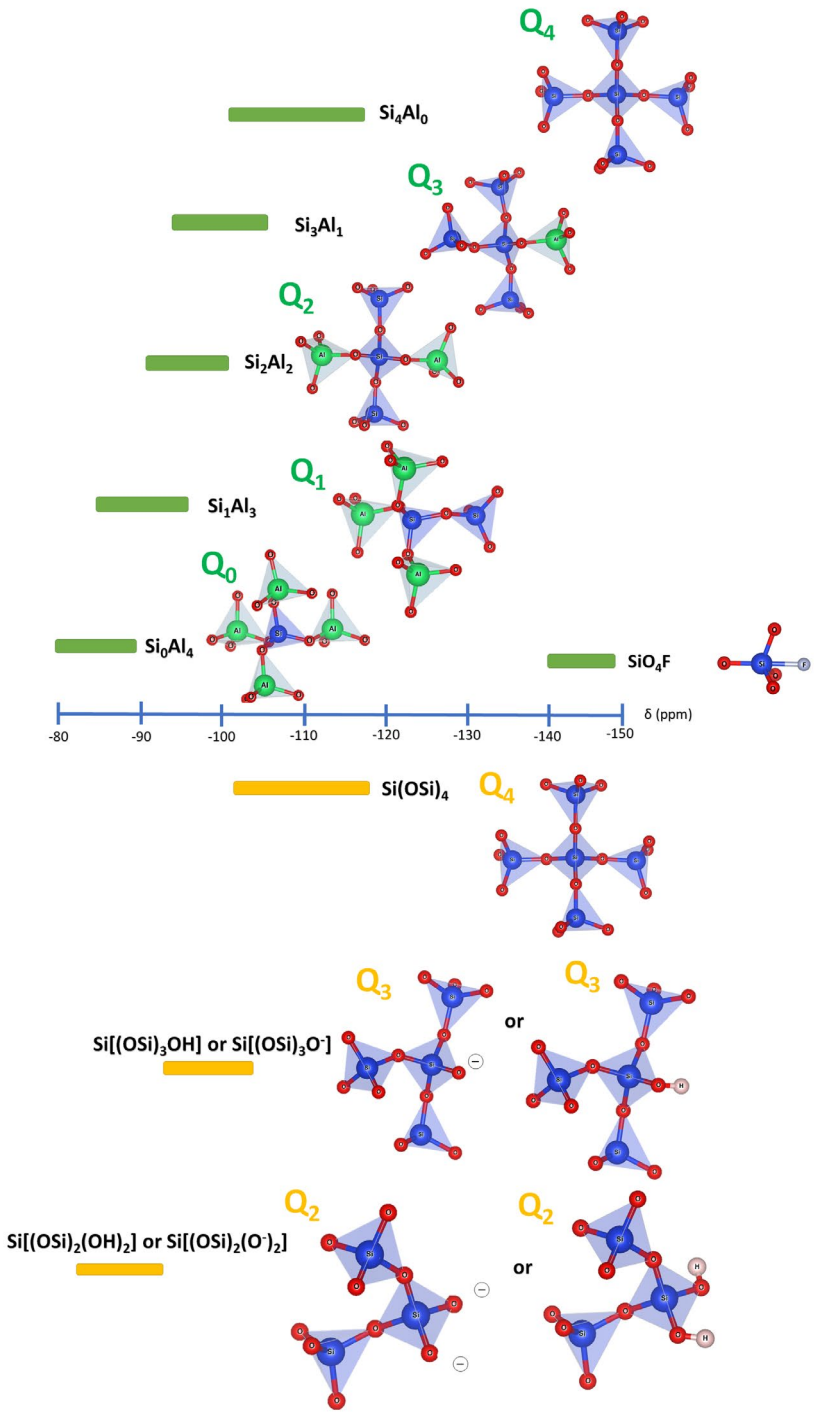

Figure 38. Typical chemical shifts in ^{29}Si-MAS-NMR of different silicon environments in zeolites.

CHAPTER 4. STRUCTURE DETERMINATION OF AS-MADE ZEOLITES ITQ-52

4.1. SYNTHESIS, CHEMICAL, THERMOGRAVIMETRIC, AND TEXTURAL ANALYSIS

This chapter delves into the structural analysis of two as-made zeolites using three-dimensional electron diffraction (especially two different 3DED data collection protocols, continuous rotation 3DED and stepwise PEDT). The reference for this study can be found in the following journal.[82] We have explored the complete atomic configuration of both the organic and inorganic frameworks in two synthetic zeolites exhibiting the ITQ-52 structure (IFW framework type).[83] These two zeolites were synthesized using their respective organic structure-directing agents: alkylphosphonium and aminophosphonium dications. These organophosphorus cations have been instrumental in synthesizing numerous zeolites such as ITQ-52 (IFW), ITQ-58,[72] ITQ-26 (IWS),[84] ITQ-27 (IWV),[85] ITQ-34 (ITR),[86] ITQ-49 (IRN),[87] ITQ-53,[88] AFX/CHA intergrowth,[89] ZEO-1,[90] ZEO-3[91] or RTH.[92]

The elucidation of as-made OSDA-containing zeolites using high-resolution powder X-ray diffraction (HR-PXRD) has been limited due to significant peak overlapping caused by large unit cell parameters and cell volumes. Additionally, these materials have many atoms per unit cell and reduced electron density contrast, further hampering the analysis. There are a few examples of organic molecules being located using powder X-ray diffraction data.[93,94,95,96,97.]

The samples studied were obtained as borosilicates using two OSDAs. The organic structure directing agents used during the synthesis were the 1,4-butanediylbis[tris(isopropyl)]phosphonium and the 1,4-butanediylbis[tris(dimethylamino)]phosphonium dications and were prepared as previously described in the bibliography.[72] The resulting zeolites are labeled as C-ITQ-52 and N-ITQ-52 respectively for simplicity. The molecular structure of the OSDAs can be seen in **Fig. 39**.

These OSDAs exhibit nearly identical compositions, differing only in the replacement of isopropyl groups with dimethylamino groups. Specifically, the tertiary carbon atoms in the isopropyl moieties are substituted with nitrogen atoms. However, there's a significant distinction between the positively charged tris(dimethylamino)phosphonium groups and the tri(isopropyl)phosphonium group. In the former, the charge is distributed among both the phosphorus and neighboring nitrogen atoms,[98] whereas in the latter, the charge is concentrated solely on the phosphorus atoms.

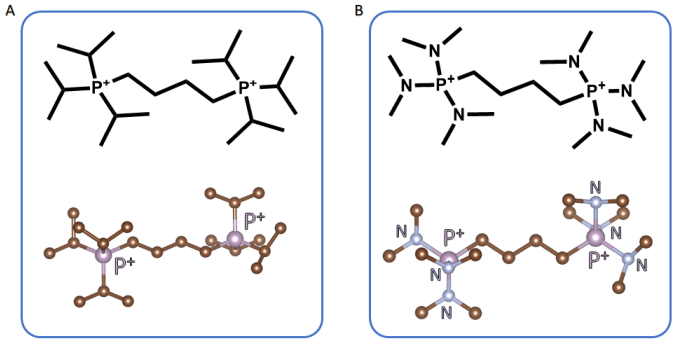

Figure 39. OSDA molecules used for the synthesis of (a) C-ITQ-52 and (b) N-ITQ-52. Pink: Phosphorus atoms, brown: carbon atoms, and blue: nitrogen atoms. Hydrogen atoms were omitted for clarity.

The use of these OSDAs during the synthesis of the zeolites can also be seen as well as chemical analyses alongside thermogravimetric and textural analysis. In the case of C-ITQ-52, a very minor quantity of ITQ-58 is observed as an impurity as shown in the powder pattern on the third page that follows (**Fig. 42**). This is evident from the presence of a weak diffraction peak in its powder X-ray diffraction pattern at an angle of 2θ = 8.12°.

Chemical and elemental analysis are summarized in **Table 3**.

Table 3. Chemical and elemental analysis of C-ITQ-52 and N-ITQ-52.

		Experimental values*	
Sample		**C-ITQ-52**	**N-ITQ-52**
Chemical analyses (wt%)	**Si**	35.48	37.38
	B	0.75	0.84
	P	2.76	2.62
	Si/B	18.3 (30)	17.2 (17)
	P/B	1.3	1.1
	P/(Si+B)	0.06	0.06
Elemental analyses (wt%)	**N**	-	3.7
	C	12.06	8.61
	H	2.27	1.95
	N/P	-	3.1 [3]
	C/P	11.3 [11]	8.3 [8]
	H/P	25.3 [25]	22.8 [23]

* In parenthesis, atomic ratio in the synthesis gel; in brackets, expected values for the OSDA molecule

The chemical analyses of the 1,4-butanediylbis[tris(isopropyl)]phosphonium containing ITQ-52 (C-ITQ-52) gave a Si/B ratio of 18.3, lower than that in the gel composition (Si/B = 30), and a P/(Si+B) of 0.06, values very similar to the N-ITQ-52 sample. As the zeolite ITQ-52 presents 64 T atoms per unit cell, it indicates the presence of 4 P atoms, i.e., 2 OSDA, per unit cell. Fluoride is not present in detectable amounts in the material.

The chemical analyses of the 1,4-butanediylbis[tris(dimethylamino)]phosphonium-containing ITQ-52 sample (N-ITQ-

52) indicate similar results, with a Si/B ratio of 17.2, very similar to the gel composition (Si/B=17), and a P/(Si+B) ratio of 0.06 that corresponds, taking also into account the structure already known of ITQ-52, to 2 OSDA cations per unit cell, as given in **Table 3**. Fluoride is not present in detectable amounts in the material.

The P/B ratio of C-ITQ-52 is 1.3 and P/B ratio of N-ITQ-52 is 1.1, suggesting that the positive charge of the OSDA is counterbalanced by the negative charge of the borosilicate framework (trivalent element). This possibility is reinforced by the absence of detectable F in the material.

The elemental analyses of C-ITQ-52 show a C/P ratio of 11.3, very close also to that of the pure OSDA (11). For N-ITQ-52, the elemental analyses show an N/P ratio of 3.1 and a C/P ratio of 8.3, very close to that of the pure OSDA (3 and 8, respectively). These results suggest that the OSDA does not decompose during zeolite crystallization and remains intact inside the channels filling the pores.

The surface morphology and structure of the two samples were examined by field emission scanning electron microscopy (**Fig. 40**). Both samples present small crystallites as rhombohedral crystallites with a non-homogeneous crystal size distribution, as seen in **Fig. 40**. Typically, crystals are obtained in a size range from 1.0 x 0.6 x 0.3 μm^3 for C-ITQ-52 to 0.1 x 0.1 x 0.1 μm^3 for N-ITQ-52.

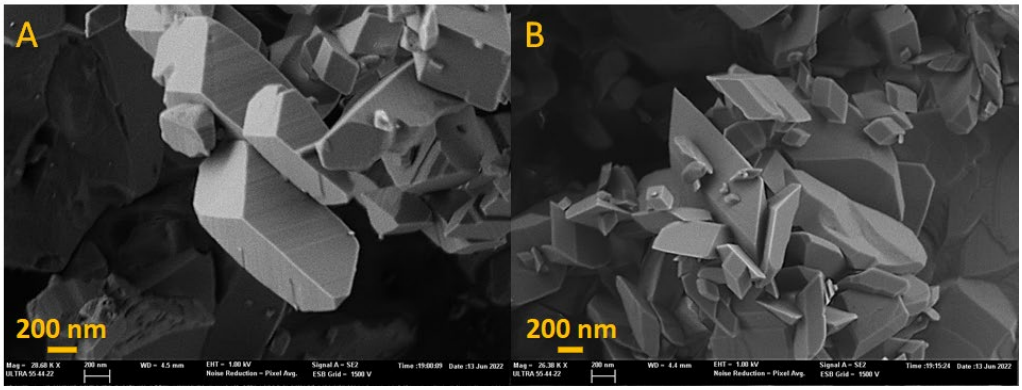

Figure 40. Field Emission Scanning Electron Microscope (FESEM) images of zeolites (a) C-ITQ-52 and (b) N-ITQ-52 crystals. Size range from 1.0 x 0.6 x 0.3 μm^3 for C-ITQ-52 to 0.1 x 0.1 x 0.1 μm^3 for N-ITQ-52.

In the Scanning Transmission Electron Microscope (STEM), an Energy Dispersive X-ray analysis (EDS) mapping technique revealed the presence of additional elements incorporated into the organic structure-directing agent (OSDA), beyond the silicon and oxygen framework, see **Fig. 41**. Specifically, quantitative EDS analysis yielded atomic P/Si ratios of 0.061 and 0.063 for the C-ITQ-52 and N-ITQ-52 samples, respectively. These ratios correspond to approximately 3.91 and 4.06 phosphorus (P) atoms per unit cell, considering the Si unit cell content. These findings align with the results obtained from chemical analysis.

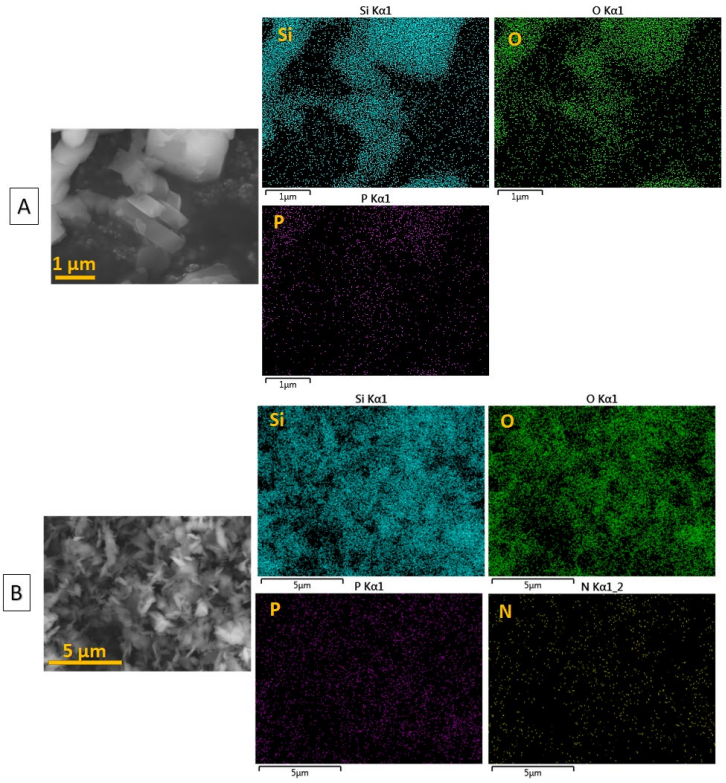

Figure 41. STEM images and EDS mapping of (A) C-ITQ-52 and (B) N-ITQ-52, showing elemental distribution: Si (Blue), O (Green), P (Pink), and N (Yellow).

4.2. PXRD CHARACTERIZATION

The phases of C-ITQ-52 and N-ITQ-52 samples were first measured in PXRD performed in Bragg-Brentano geometry using a PANalytical EMPYREAN diffractometer, equipped with a goniometric head to align the capillaries prior to the measurements and a PIXcel1D-Medipix3 detector. Cu Kα1 (λ = 1.5406 Å) X-ray radiation was used for the measurements, employing a hybrid monochromator, and a tube voltage and intensity of 45 kV and 40 mA, respectively. The goniometer arm length was 240 mm, and a fixed divergence slit with an aperture of 1/4° was used. The measurements were performed at 298 K, with a continuous rotation of the capillaries.

The Bragg intensities were analyzed throughout the indexation of the XRD pattern with the program JANA2020.[74] During the unit cell determination, the background was manually estimated, the peaks were searched automatically, and the pattern could be indexed in monoclinic symmetry. The following unit cell parameters were extracted from LeBail profile fitting of C-ITQ-52 corresponding pattern: a=17.4698 Å, b=17.9202 Å, c= 12.3290 Å, α=γ=90º, β = 90.642º; and N-ITQ-52 pattern:

a=17.4810 Å, b=17.9008 Å, c=12.3250 Å, α=γ=90º, β=90.525º. The powder patterns are shown below in **Fig. 42**. The peak positions of PXRD patterns of these two phases closely resemble.

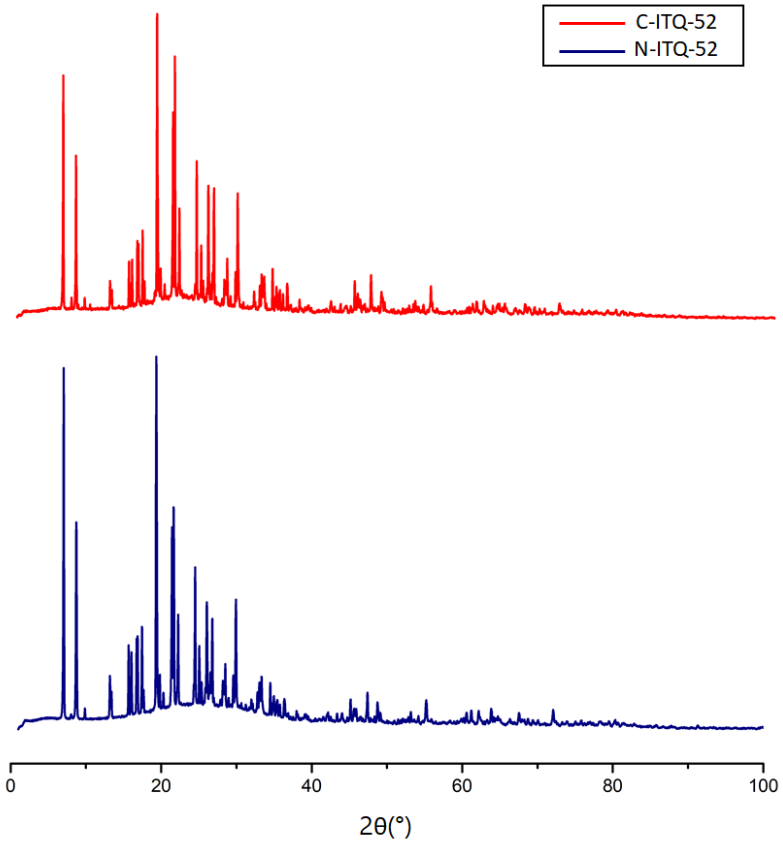

Figure 42. Powder X-Ray diffraction pattern of (red) C-ITQ-52 and (blue) N-ITQ-52.

4.3. 3DED CHARACTERIZATION

The C-ITQ-52 and N-ITQ-52 samples were measured in the following transmission electron microscopes:

1) Using a JEOL 2100F TEM (200 keV) located in the electron microscopy services of the *UPV,* València, Spain.[99]
2) Using a JEOL 2100-LaB_6 TEM (200 keV) located in the microscopy services of the *Scientific and Technological Centers of the University of Barcelona (CCiTUB),* Barcelona, Spain.[100]

3) Using an FEI Tecnai G2 20 (200 keV) equipped with a thermionic cathode (LaB_6) located in *CzechNanoLab Research Infrastructure-Institute of Physics of the Czech Academy of Sciences (FZU),* Prague, Czech Republic.[101]

4.3.1. DATA ACQUISITION: JEOL 2100F TEM

The two samples were first measured with a stepwise rotation precession assisted (PEDT) using the JEOL 2100F TEM (200 keV).

For the as-made C-ITQ-52, one selected crystal, 700 x 360 nm in size, was measured in selected area electron diffraction (SAED) mode using the largest SA aperture (250 µm) with the second smallest condenser lens aperture (40 µm) and five spot size. The crystal image and the selected aperture's size can be seen in **Fig. 43**. Diffraction patterns were acquired at room temperature with a stepwise rotation of the sample with 1.00° beam precession. The CCD detector setting (model GATAN Orius SC600A) was 2048x2048 pixels of area detector in a binning mode of 2x2. Exposure time per frame was set to 1 s, and the tilt step was 1.03° between each frame (**Table 4**). The selected crystal was recorded in precession stepwise using a tilt range of 71°, in which the initial tilt degree was set to -35.20° and the final tilt degree to +35.40°, resulting in 69 frames and approx. fifteen minutes of collection time.

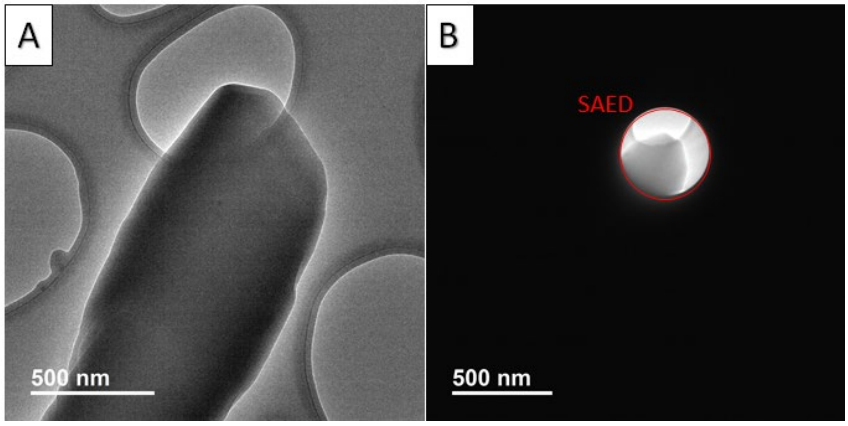

Figure 43. TEM image of (A) as-made C-ITQ-52 crystal used for structure determination and (B) SAED aperture size used for DPs acquisition. The crystal size measured 700 x 360 nm, with a SAED aperture (red circle) of 250 µm in diameter.

For the as-made N-ITQ-52 sample, a TEM grid was prepared by directly spreading the powder sample on the grid without solvent. Two crystals were measured (**Fig. 44**) due to low completeness (62%) processed in the first collected dataset for successful silicon framework structure determination considering the R_{int} factor (R_{int} = 22.52%, resolution = 1.00 Å). Therefore, a second crystal with R_{int} = 25.26%, resolution = 1.00 Å and completeness = 49 % was measured in order to merge these two datasets. Diffraction patterns were acquired at room temperature using a

precession degree calibrated to 1.00°. The CCD detector setting (model GATAN Orius SC600A) was 2048x2048 pixels of area detector in a binning mode of 2x2. A nanobeam (NBD) illumination mode was applied in both crystals using the second smallest condenser lens aperture (40 µm diameter), a semiparallel beam of 970 nm in diameter and 0.5 nm spot size in order to minimize the electron radiation rate (**Table 4**). To carry out a precession stepwise procedure, the exposure time per frame was set to 0.5 seconds, and a tilt step of 1° was set between each frame. The first selected crystal was recorded using a tilt range of 99°, in which the initial tilt degree was set to -58.0 ° and the final tilt degree to +40.0°, resulting in 113 frames and approximately 20 minutes of collection time. The second selected crystal was measured using a tilt range of 81°; the initial tilt degree was -40.00°, and the final tilt degree was +39.00°, resulting in 80 frames and approximately 15 minutes of collection time.

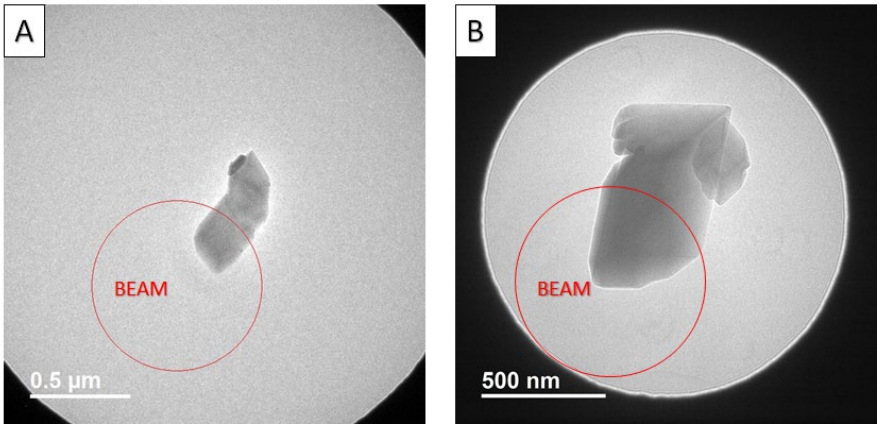

Figure 44. TEM images of the two crystals from as-made N-ITQ-52 sample (A) First crystal 700 x 250 nm in size (B) second crystal 550 x 300 nm in size. The red circle shows the nanobeam size of 970 nm in diameter. The datasets obtained from these two crystals were merged and used for structure determination.

The three 3DED datasets from N-ITQ-52 and C-ITQ-52 sample were processed by PETS2.0 software. All datasets were indexed as monoclinic unit cell: [C-ITQ-52] 1rd a=17.6360 Å, b=17.9920 Å, c= 12.3980 Å, β = 90.2860º; and [N-ITQ-52] 1st dataset a=17.8440 Å, b=18.1713 Å, c=13.2833 Å, β=90.8370º; 2nd dataset a=16.2042 Å, b=16.3852 Å, c=11.3469 Å, β=90.199º (**Table 4**). The 1rd dataset for C-ITQ-52 contained 1418 independent reflections (R_{int} = 20.26%, completeness = 66% and resolution = 1.0 Å). The two datasets for N-ITQ-52 contained 1481 and 1700 independent reflection, respectively (R_{int} = 22.52 and 25.26%, completeness = 62 and 49% and resolution = 1.0 Å). A single *.hkl* file was extracted from each dataset, and the two datasets from N-ITQ-52 were subsequently merged into one to achieve greater completeness, addressing the limited reciprocal space coverage of the individual measurements. This merging was performed using JANA2020 software, resulting in a unique dataset for each sample. The resulting *.hkl* files were imported

to Jana2020, and the *ab initio* structure solution model obtained from the charge-flipping algorithm was used as the initial model for the structure refinement. The structure solution of both samples gave a satisfactory SiO_2 framework model in the space group *I2/m* consisting of 10 Si and 19 O atoms in the asymmetric unit, corresponding to 64 Si and 128 O atoms per the unit cell, analogous to the original ITQ-52 literature, as shown in **Fig. 45**. Additionally, a diffuse electron density cloud occupying the 10R channel system was visually noticed (yellow cloud in **Fig. 45**). Subsequent attempts to refine kinematically the structure of the OSDA molecules within the channel systems were unsatisfactory, likely due to a low signal-to-noise ratio or an insufficient number of reflections, leading to a failure in convergence. Consequently, it was decided to perform 3DED measurements using a JEOL 2100-LaB_6 TEM microscope (see Section 4.3.2).

Table 4. 3DED data collection of C-ITQ-52 and N-ITQ-52 using the JEOL 2100F TEM with stepwise precession rotation in SAED and NBD modes, respectively. The experiments were conducted at room temperature with 200 keV electrons (λ = 0.02508 Å).

Sample	**C-ITQ-52**	**N-ITQ-52**	
Dataset	1	1	2
TEM	JEOL 2100F 200 keV	JEOL 2100F 200 keV	JEOL 2100F 200 keV
Protocol/Illumination mode	Stepwise PEDT in SAED	Stepwise PEDT in NBD	Stepwise PEDT in NBD
Sample preparation	Dry	Dry	Dry
Holder/Temperature	High Double Tilt (Gatan)/room temperature	High Double Tilt (Gatan)/room temperature	High Double Tilt (Gatan)/room temperature
Detector	GATAN Orius SC600A CCD	GATAN Orius SC600A CCD	GATAN Orius SC600A CCD
Data Acquisition Script	Ultrafast-EDT/DigitalMicrograph (DM) scripting	Ultrafast-EDT/DigitalMicrograph (DM) scripting	Ultrafast-EDT/DigitalMicrograph (DM) scripting
Crystal system	Monoclinic	Monoclinic	Monoclinic
Space group (Num.)	I12/m1	I12/m1	I12/m1
a (Å)	17.6360(18)	17.8646(15)	16.2042(21)
b (Å)	17.9920(19)	18.1839(22)	16.3852(31)
c (Å)	12.3980(32)	12.9483(32)	11.3469(14)
α (°)	90	90	90
β (°)	90.286(14)	92.274(15)	90.200(16)
γ (°)	90	90	90
Volume (Å³)	3934.03	4202.92	3012.7
Z	64	64	64
Crystal size (nm)	700 x 360	700 x 250	550 x 300
Precession degree (°)	1.0	1.0	1.0
NBD diameter beam (nm)	-	970	970
SAED aperture diameter (μm)	250	-	-
Initial angle (°)	-35.0	-58.0	-40.0
Final angle (°)	35	40	39
Tilt step (°)	1	1	1
Exposure time per frame (s)	1	0.5	0.5
Num. Frames	69	113	80
Total data collection time (min)	15	20	15
Total exposure time (s)	69	56	40
Data Reduction/Software	PETS2.0	PETS2.0	PETS2.0
Coverage (%)	66	62	49
Resolution (Å)	1	1	1
Num Reflections (unique/total)	942/1418	727/1481	841/1700
Redundancy	2.41	3.06	3.53
R_{int} (%) [max. Resolution (Å)]	20.26 [1]	22.52 [1]	25.26 [1]
Structure Solution Software	JANA2020	JANA2020	JANA2020

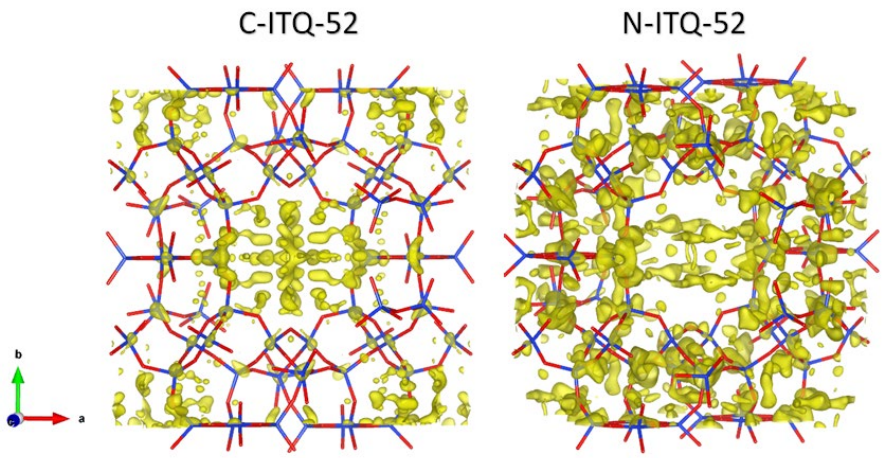

Figure 45. SiO_2 framework and positive peaks from the electron density map of C-ITQ-52 (left) and N-ITQ-52 (right) samples, extracted from 3DED datasets collected using a JEOL 2100F TEM. Silicon atoms are represented by blue sticks, and oxygen atoms by red sticks. The electron density map is displayed at a 2σ contour level by yellow clouds.

4.3.2. DATA ACQUISITION: JEOL 2100-LaB_6 TEM

The two samples were then measured by stepwise PEDT using a JEOL 2100-LaB_6 TEM (200 keV).

The two powdered as-made samples were mounted on a JEOL JEM-2100 electron transmission microscope 200 keV with a thermionic cathode (LaB_6) using a double-tilt tomography sample holder. The diffraction patterns were acquired with a CCD camera (model Gatan Orius SC1000A), by stepwise PEDT with 1.00º of precession angle at room temperature. In order to collect the data in precession stepwise procedure, a fast and automated developed routine called Fast-ADT consisting of two subsequent tilt scans of the goniometric stage; one to obtain a crystal tracking file and a second one to acquire an electron diffraction tomography was implemented and employed.[45]

In the case of the C-ITQ-52, a crystal of 1300 x 770 nm in size, as shown in **Fig. 46**, was measured by stepwise PEDT and applying nanobeam mode (NBD). The smallest condenser lens aperture (10 µm diameter), a semi-parallel beam of 300 nm in diameter and 15 nm spot size and alpha 5 for a larger convergence angle degree was used. In order to carry out a precession stepwise procedure, the exposure time per frame was set to 0.8 seconds, and a tilt step of 1° was set between each frame (**Table 5**). The selected crystal was recorded using a tilt range of 101°, in which the initial tilt degree was set to -50° and the final tilt degree to 50°, resulting in one single dataset of 101 frames and approx. thirty minutes of collection time.

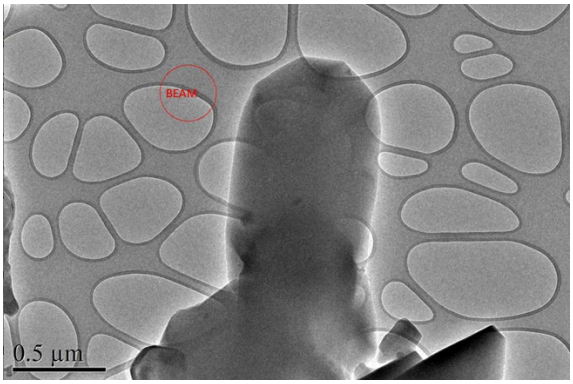

Figure 46. TEM image of C-ITQ-52 crystal used for structure determination. 300 nm semiparallel beam size is shown as red circle.

In the case of the N-ITQ-52, a selected crystal of 900 x 390 nm in size, as shown in **Fig. 47**, was measured applying nanobeam mode (NBD), the smallest condenser lens aperture (10 µm diameter), a semiparallel beam of 300 nm in diameter, 15 nm spot size and alpha 5 for a larger convergence angle degree. In order to carry out a precession stepwise procedure, the exposure time per frame was set to 0.5 seconds and a tilt step of 1° was set between each frame (**Table 5**). The selected crystal was recorded using a tilt range of 108°, in which the initial tilt degree was set to -50° and the final tilt degree to 57°, resulting in one single dataset of 108 frames and approximately forty-five minutes of collection time.

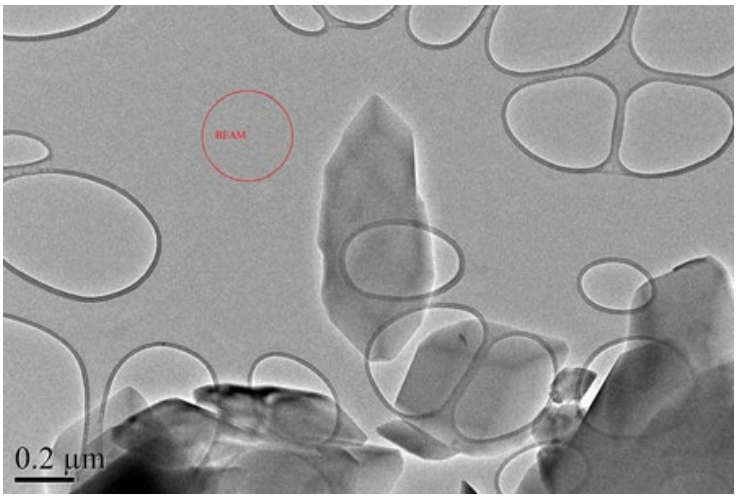

Figure 47. TEM image of as-made N-ITQ-52 crystal used for structure determination. The crystal size measured 900 x 390 nm. 300 nm semiparallel beam size is shown as red circle.

Table 5. 3DED collection data of C-ITQ-52 and N-ITQ-52 from JEOL 2100-LaB_6 TEM. 200 keV electrons (λ=0.02508 Å) at room temperature were used.

Sample	C-ITQ-52	N-ITQ-52
Dataset	1	1
TEM	JEOL 2100-LaB_6 200 keV	JEOL 2100-LaB_6 200 keV
Protocol/Illumination mode	Stepwise PEDT in NBD	Stepwise PEDT in NBD
Sample preparation	Dry	Dry
Holder/Temperature	High Double Tilt (Gatan)/room temperature	High Double Tilt (Gatan)/room temperature
Detector	Gatan Orius SC1000A CCD	Gatan Orius SC1000A CCD
Data Acquisition Script	Fast-ADT acquisition routine/DigitalMicrograph (DM) scripting	Fast-ADT acquisition routine/DigitalMicrograph (DM) scripting
β (°)	90.406(25)	90.327(18)
γ (°)	90	90
Volume (Å³)	3859.17	3843.21
Z	64	64
Crystal size (nm)	1300 x 770	900 x 390
Precession degree (°)	1.0	1.0
NBD diameter beam (nm)	300	300
Initial angle (°)	-50.0	-50.0
Final angle (°)	50	57
Tilt step (°)	1.00	1.00
Exposure time per frame (s)	0.8	0.5
Num. Frames	101	108
Total data collection time (min)	30	45
Total exposure time (s)	81	54
Data Reduction/Software	PETS2.0	PETS2.0
Coverage (%)	67	63
Resolution (Å)	1.00	1.00
Num. Reflections (unique/total)	631/1401	693/1309
Redundancy	3.21	3.04
R_{int} (%) [max. Resolution (Å)]	17.31 [1]	14.48 [1]
Structure Solution Software	JANA2020	JANA2020

The two 3DED datasets from C-ITQ-52 and N-ITQ-52 samples were processed by PETS2.0 software. All datasets were indexed as monoclinic unit cell: [C-ITQ-52] *a*=17.4752 Å, *b*=17.9264 Å, *c*= 12.3194 Å, *β* = 90.4063º; and [N-ITQ-52] *a*=17.5578 Å, *b*= 17.9148 Å, *c*=12.2185 Å, *β*=90.3277º (**Table 5**). The dataset for C-ITQ-52 contained 1401 independent reflection (R_{int} = 20.26%, completeness = 66% and resolution = 1.0 Å) while the dataset for N-ITQ-52 contained 1309 independent reflections (R_{int} = 14.48%, completeness = 63% and resolution = 1.0 Å). A single *.hkl* file was extracted for each dataset using JANA2020.

The resulting *.hkl* files were imported to Jana2020, and the *ab initio* structure solution model obtained from the charge-flipping algorithm was used as the initial model for the structure refinement. The structure solution of both samples gave a satisfactory SiO_2 framework model in the space group *I2/m* consisting of 10 Si and 19 O atoms in the asymmetric unit, and 64 Si and 128 O atoms per the unit cell, analogous to the original ITQ-52 literature, as shown in **Fig. 48**. Similarly, to data from JEOL 2100F, a diffuse electron density cloud occupying the 10R channel system was visually noticed (yellow cloud in **Fig. 48**). Subsequent attempts to refine kinematically the structure of the OSDA molecules within the channel systems were unsatisfactory, likely due to a low signal-to-noise ratio or an insufficient number of

reflections, leading to a failure in convergence. Therefore, it was decided to take the 3DED measurements with a FEI Tecnai G2 TEM microscope (see section 4.3.3).

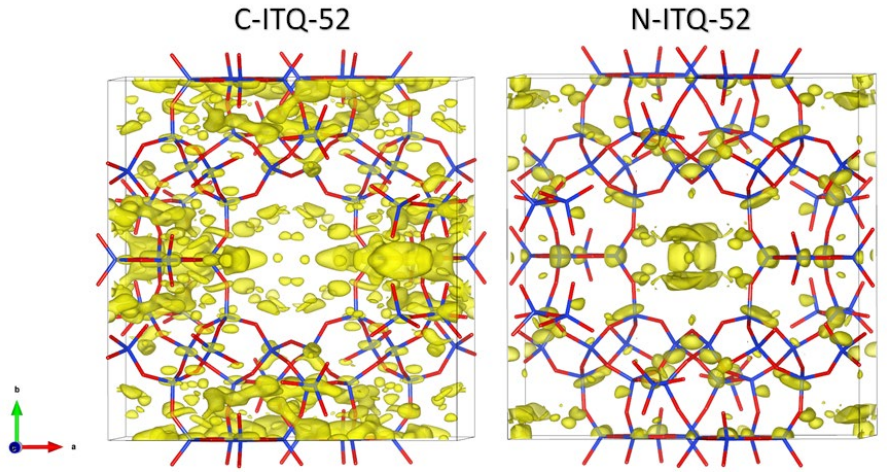

Figure 48. SiO_2 framework and positive peaks from the electron density map of C-ITQ-52 (left) and N-ITQ-52 (right) samples, extracted from 3DED datasets collected using a JEOL 2100-LaB_6 TEM. Silicon atoms are represented by blue sticks, and oxygen atoms by red sticks. The electron density map is displayed at a 2σ contour level by yellow clouds.

4.3.3. DATA ACQUISITION: FEI TECNAI G2 TEM

The two samples as white powder were directly deposited without solvent on a copper TEM grid covered by a carbon-continuous 200 mesh film. The two samples were mounted in a FEI tomography holder and measured using a FEI Tecnai G2 TEM, operated at 200 kV. The C-ITQ-52 sample was analyzed by cRED and N-ITQ-52 by stepwise PEDT. The decision to change the 3DED procedure was due to the small size of the crystals in the N-ITQ-52 sample, which made it difficult to maintain a stable position under the beam. The precession angle was set to 1° using a NanoMEGAS-Digistar system. To acquire the diffraction patterns automatically, self-written scripts in Olympus Soft Imaging Solutions iTEM software for controlling the beam, goniometer, and detector were employed following the Fast ADT protocol.

The 3DED data of the as-made C-ITQ-52 was obtained from a crystal size 1050 x 600 nm crystal using NBD illumination mode and employing a continuous goniometer tilting (tilt speed of 1.036°/s) (**Table 6**). The experimental setup included a small condenser lens aperture (20 µm diameter), a semi-parallel beam with a diameter of 1075 nm, and a spot size of 3. The image of the crystal diameter of the beam can be seen in **Fig. 49**. Each frame had an exposure time of 0.482 s, resulting in an integration step of 0.499° between frames, with a total of 224 frames collected. The crystal was recorded during continuous tilting from -52° to 60°, covering a tilt range of 113°. The entire data collection took approximately 2 minutes, with the crystal

receiving a total exposure time of 2 minutes. The estimated total electron dose received by the crystal was 1.836 electrons/Å² per frame, and the electron dose rate was 0.017 electrons/s·Å².

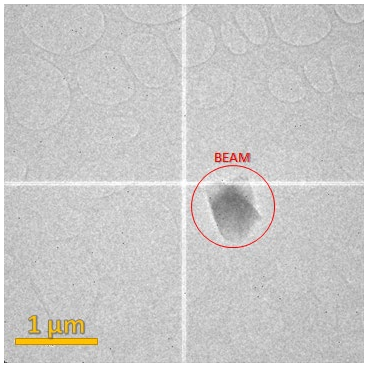

Figure 49. TEM image of C-ITQ-52 crystal used for structure determination. 1075 nm semiparallel beam size is shown as red circle.

Table 6. 3DED collection data of C-ITQ-52 using continuous rotation NBD from FEI Tecnai G2 20 TEM. 200 keV electrons (λ=0.02508 Å) and a 1075 nm beam (NBD) at room temperature were used.

Sample	**C-ITQ-52**
TEM	FEI Tecnai G2 20 200 keV
Protocol/Illumination mode	cRED in NBD
Sample preparation	Dry
Holder/Temperature	Cryo Transfer Tomography, Gatan/295 K
Detector	Timepix Quad's hybrid pixel
Data Acquisition Script	Fast-ADT acquisition routine/DigitalMicrograph (DM) scripting
Crystal system	Monoclinic
Space group (Num.)	I12/m1 (12)
a (Å)	17.5121(14)
b (Å)	17.9858(11)
c (Å)	12.3557(8)
α (°)	90
β (°)	90.222(2)
γ (°)	90
Volume (Å³)	3891.63
Z	64
Crystal size (nm)	1050 x 600
Initial angle (°)	-52.0
Final angle (°)	60
Exposure time per frame (s)	0.482
Num. Frames	224
Tilt speed (°/s)	1.036
Total data collection time (s)	108
Total exposure time (s)	108
Electron dose rate (e/s·Å²)	0.017
Total, accumulated electron dose (e/Å²)	1.836
Data Reduction/Software	PETS2.0
Completeness (%)	54
Resolution (Å)	0.55
Num. Reflections (unique/total)	5585/15558
Redundancy	2.47
R_{int} (%)	17.3
Structure Solution Software	JANA2020

The 3DED data collection from the as-made N-ITQ-52 sample resulted in limited reciprocal space coverage during data. Specifically, the first dataset, derived from a

crystal measuring 550 x 350 nm (**Fig. 50**), exhibited a low completeness of 76% (see **Table 7**). This limitation hindered the generation of a more accurate residual electron density map, which would have been essential for determining the OSDA model. Therefore, the data from a second crystal (780 x 550 nm in size), as shown in **Fig. 50**, was collected.

For the data collection, the illumination conditions were set in NBD mode. A small condenser lens aperture (20 µm diameter), a semi-parallel beam with a diameter of 1075 nm, and spot size 3 to operate under low dose conditions were used (**Table 7**). For data acquisition in precession stepwise mode, the exposure time per frame was set to 0.5 s, and a tilt step of 1° was set between each frame.

The first crystal was recorded from an initial tilt of -55° to a final tilt of 55°. This covered a tilt range of 111°, resulting in 111 frames. The entire data collection took approximately 480 seconds, with the crystal receiving a total exposure time of 55.5 s. The total exposure time is lower than the data collection time due to the beam blanking applied after the collection of each frame in order to automatically re-center the crystal.

The second crystal was measured over a tilt range of 121°, with an initial tilt of -60° and a final tilt of 60°. This resulted in 121 frames. The entire data collection took approximately 540 s, with the crystal receiving a total exposure time of 60.5 s.

The crystals of N-ITQ-52 received total accumulated electron doses of 2.775 electrons/Å² and 3.025 electrons/Å² for the first and second crystals, respectively. Both crystals were exposed to an electron dose rate of 0.05 electrons/s·Å², which is notably higher than the electron dose rate received by the C-ITQ-52 sample measured by continuous rotation NBD (0.017 electrons/s·Å²). Despite the difference in dose rates, the total accumulated electron dose was similar for both samples, with 1.836 electrons/Å² for C-ITQ-52 and 2.775 and 3.025 electrons/Å² for N-ITQ-52. This is due to the application of beam blanking during the stepwise 3DED experiment.

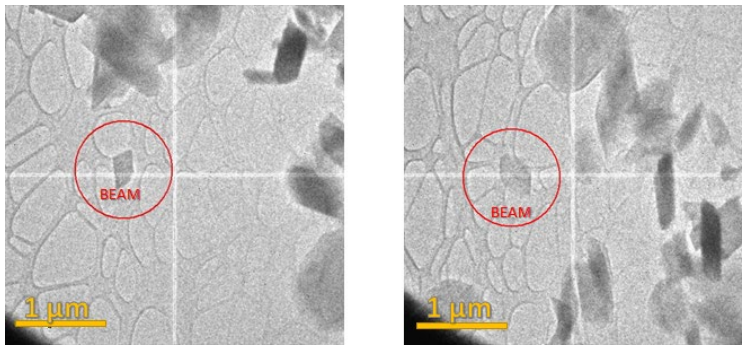

Figure 50. TEM images of as-made N-ITQ-52 crystals. These two crystals were merged and used for the structure determination. 1075 nm semiparallel beam size is shown as red circle.

Table 7. 3DED data collection of N-ITQ-52 at room temperature using 1° of precession with a stepwise rotation. 200 keV electrons (λ=0.02508 Å) and a 1075 nm beam (NBD).

Sample	**N-ITQ-52**		
Dataset	Individual dataset 1	Individual dataset 2	Merged Data
TEM	FEI Tecnai G2 20 200 keV	FEI Tecnai G2 20 200 keV	FEI Tecnai G2 20 200 keV
Protocol/Illumination mode	Stepwise PEDT in NBD	Stepwise PEDT in NBD	Stepwise PEDT in NBD
Sample preparation	Dry	Dry	Dry
Holder/Temperature	Cryo Transfer Tomography, Gatan/295 K	Cryo Transfer Tomography, Gatan/295 K	Cryo Transfer Tomography, Gatan/295 K
Detector	Timepix Quad's hybrid pixel	Timepix Quad's hybrid pixel	Timepix Quad's hybrid pixel
Data Acquisition Script	Self-written scripts in Olympus Soft Imaging Solutions iTEM software	Self-written scripts in Olympus Soft Imaging Solutions iTEM software	Self-written scripts in Olympus Soft Imaging Solutions iTEM software
Crystal system	Monoclinic	Monoclinic	Monoclinic
Space group (Num.)	I12/m1 (12)	I12/m1 (12)	I12/m1 (12)
a (Å)	17.301(2)	17.289(2)	17.284(3)
b (Å)	17.7251(15)	17.750(2)	17.754(3)
c (Å)	12.2431(18)	12.170(2)	12.223(3)
α (°)	90	90	90
β (°)	90.562(4)	90.020(13)*	90.405(17)
γ (°)	90	90	90
Volume (Å^3)	3754.32	3734.74	3750.64
Z	64	64	64
Crystal size (nm)	550 x 350	780 x 550	-
Initial angle (°)	-55.0	-60.0	-
Final angle (°)	55	60	-
Tilt step (°)	1	1	-
Exposure time per frame (s)	0.5	0.5	-
Num. Frames	111	121	232
Total data collection time (s)	480	540	-
Total exposure time (s) * **	55.5	60.5	-
Electron dose rate (e/s·Å^2)	0.05	0.05	-
Total accumulated electron dose (e/Å^2)	2.775	3.025	-
Data Reduction/Software	PETS2.0	PETS2.0	PETS2.0
Completeness (%)	76	85	90
Resolution (Å)	0.58	0.63	0.58**
Num. Reflections (unique/total)	1841/7501	1998/7031	3684/16674
Redundancy	2.96	2.92	3.3
R_{int} (%)	16.53	21.44	24.58
Structure Solution Software	JANA2020	JANA2020	JANA2020

* The strong observed difference in the beta angle observed is due to differences in mosaicity

** This value corresponds to the defined maximum resolution during the data integration

*** Total exposure time is lower than data collection time due to the beam blanking applied after the collection of each frame in order to automatically re-center the crystal.

4.4. DATA REDUCTION AND FRAMEWORK STRUCTURE SOLUTION

Data reduction and generation of *.hkl* files were conducted using the PETS 2.0 program. The resulting parameters are presented in **Tables 6** and **7** for C-ITQ-52 and N-ITQ-52 samples respectively. All the frames collected from the two crystals of the N-ITQ-52 sample were directly merged with the new feature developed in PETS2.0 throughout the transformation of the orientation angles of each frame to a single orientation matrix. The generated merged dataset with 232 frames containing 3684

independent reflections was collected from the precession-assisted 3DED experiments.

All individual datasets, including the merged dataset, were indexed as body-centered monoclinic lattices, potentially belonging to the space group *I12/m1*. The unit cell parameters were compared to those derived from the LeBail method applied to PXRD data, as shown in **Table 8** and **9**. The differences between the unit cell parameters obtained by 3DED and PXRD for the C-ITQ-52 sample are relatively small, indicating a close match between the two methods. On the other hand, the differences between the 3DED and PXRD measurements of N-ITQ-52 are more pronounced than those observed in C-ITQ-52, especially in the *a* and *b* parameters, which have differences of 0.20 Å and 0.15 Å, respectively. However, the difference in the *β* angle is less significant, at 0.12°. Overall, the differences in unit cell parameters between 3DED and PXRD are generally small but are more pronounced in the N-ITQ-52 sample compared to the C-ITQ-52 sample. This might indicate a small deviation in the precision of the 3DED measurements over PXRD. Nonetheless, the data suggest 3DED can offer a close approximation to the values obtained from PXRD.

Table 8. Comparison of unit cell of C-ITQ-52 sample obtained by 3DED and PXRD.

Sample C-ITQ-52	Unit Cell Parameters (3DED)	Unit Cell Parameters (PXRD LeBail)	Unit cell parameters Δ
a (Å)	17.51	17.46	0.05
b (Å)	17.98	17.92	0.06
c (Å)	12.35	12.32	0.03
β (°)	90.22	90.64	0.42

Table 9. Comparison of unit cell of N-ITQ-52 obtained by 3DED and PXRD (merged dataset).

Sample N-ITQ-52 (merged dataset)	Unit Cell Parameters (3DED)	Unit Cell Parameters (PXRD LeBail)	Unit cell parameters Δ
a (Å)	17.28	17.48	0.20
b (Å)	17.75	17.90	0.15
c (Å)	12.22	12.32	0.10
β (°)	90.40	90.52	0.12

The number of independent reflections increased to 5585 and 3684 in contrast to previous TEM measurements. Additionally, the resolution improved, and the reciprocal space coverage expanded to 54% and 90%. The R_{int} values significantly decreased to 17.3% and 24.58%, with resolutions of 0.55 Å and 0.58 Å, respectively. These resolution values, in real space, corresponded to the maximal d* where intensity peaks appeared in DP frames, reciprocal space. Less than 5-10 peaks appeared at these resolutions' shells. These peaks are pointed and highlighted within the green circle in the raw DPs displayed in PETS (**Fig. 51**). Nevertheless, high-resolution shells with $I/\sigma < 2$, beyond 0.42 Å for the C-ITQ-52 dataset and 0.58 Å for the N-ITQ-52 dataset, were excluded during the integration process. This is reflected in the final integration displayed in PETS in **Fig. 52 and 53**, respectively. Although the completeness for C-ITQ-52 appears relatively low at 54%, the resolution remains robust enough to proceed with further structure determination steps.

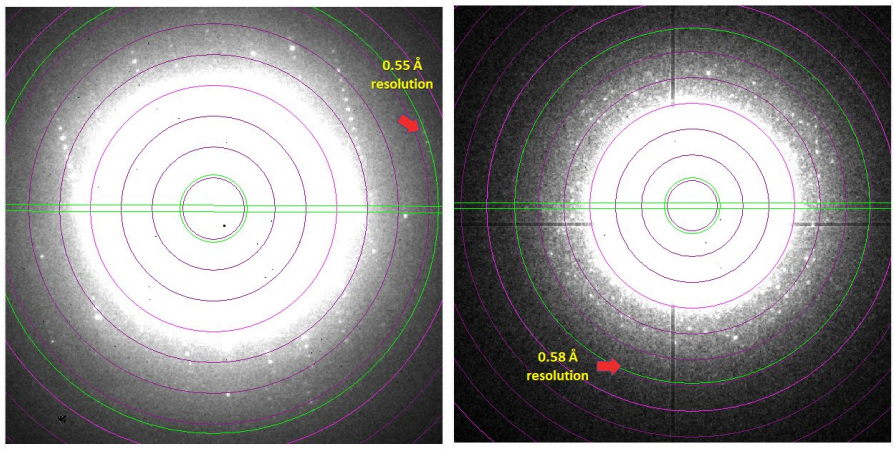

Figure 51. Raw diffraction patterns (DPs) displayed in PETS for the (left) C-ITQ-52 datasets and (right) N-ITQ-52 sample. The left image corresponds to frame 46 out of 224, acquired at 0.55 Å (1.82 Å in reciprocal space), and the right image represents frame 98 out of 232, acquired at 0.58 Å (1.7 Å in reciprocal space).

Statistics for Laue class 2/m

d*-range	d-range	Nobs	Nall	Nthr	compl.	rdnd.	I/s	Rint(obs)	Rint(all)
0.00-1.11	Inf-0.90	2269	2333	2925	0.80	3.01	86.15	14.93	14.94
1.11-1.40	0.90-0.71	1853	2322	2880	0.81	3.02	6.79	32.41	33.54
1.40-1.61	0.71-0.62	1015	2322	2865	0.81	3.01	2.45	36.78	46.06
1.61-1.77	0.62-0.57	316	2294	2850	0.80	2.51	0.98	44.36	78.23
1.77-1.90	0.57-0.53	64	2102	2875	0.73	2.17	0.53	47.50	132.02
1.90-2.02	0.53-0.49	42	1362	2836	0.48	2.06	0.47	36.73	134.26
2.02-2.13	0.49-0.47	18	1037	2846	0.36	1.85	0.32	65.27	202.22
2.13-2.23	0.47-0.45	4	814	2844	0.29	1.49	0.21	19.47	321.45
2.23-2.32	0.45-0.43	3	618	2871	0.22	1.15	0.21	0.00	288.81
2.32-2.40	0.43-0.42	1	354	2845	0.12	1.02	0.11	0.00	125.11
0.00-2.40	Inf.-0.42	5585	15558	28637	0.54	2.47	23.72	16.30	17.30

Figure 52. Final integration statistics for the C-ITQ-52 dataset.

Statistics for Laue class 2/m

d*-range	d-range	Nobs	Nall	Nthr	compl.	rdnd.	I/s	Rint(obs)	Rint(all)
0.00-0.97	Inf-1.03	1468	1700	1904	0.89	3.32	38.75	15.43	15.78
0.97-1.23	1.03-0.81	818	1655	1845	0.90	3.36	2.74	26.70	39.41
1.23-1.41	0.81-0.71	612	1695	1885	0.90	3.36	1.67	26.53	48.83
1.41-1.55	0.71-0.65	307	1673	1855	0.90	3.37	0.89	32.09	82.99
1.55-1.67	0.65-0.60	119	1636	1818	0.90	3.37	0.54	46.81	143.72
1.67-1.77	0.60-0.56	82	1704	1889	0.90	3.37	0.44	45.72	166.90
1.77-1.86	0.56-0.54	53	1649	1829	0.90	3.37	0.37	64.95	216.31
1.86-1.95	0.54-0.51	66	1653	1831	0.90	3.33	0.39	58.72	212.72
1.95-2.03	0.51-0.49	88	1645	1834	0.90	3.18	0.43	58.76	194.21
2.03-2.10	0.49-0.48	71	1664	1863	0.89	2.96	0.39	54.35	203.08
0.00-2.10	Inf.-0.48	3684	16674	18553	0.90	3.30	6.42	16.58	24.58

Figure 53. Final integration statistics for the merged N-ITQ-52 dataset.

The 0kl, h0l and hk0 plane sections of the 3D reconstructed reciprocal space of C-ITQ-52 and N-ITQ-52 samples can be respectively seen in **Figures 54 and 55**.

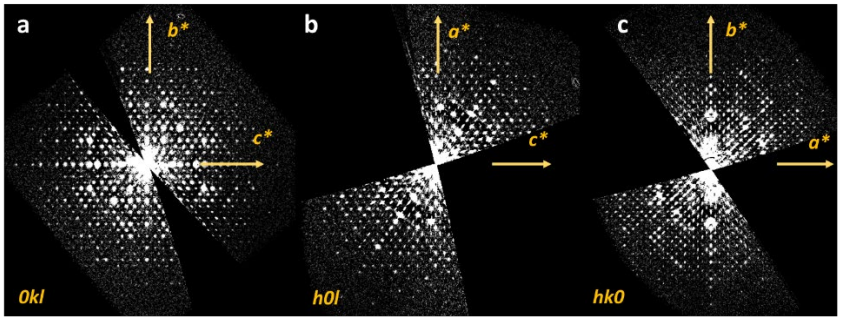

Figure 54. (a) 0kl, (b) h0l and (c) hk0 plane sections of the 3D reconstructed reciprocal space of C-ITQ-52.

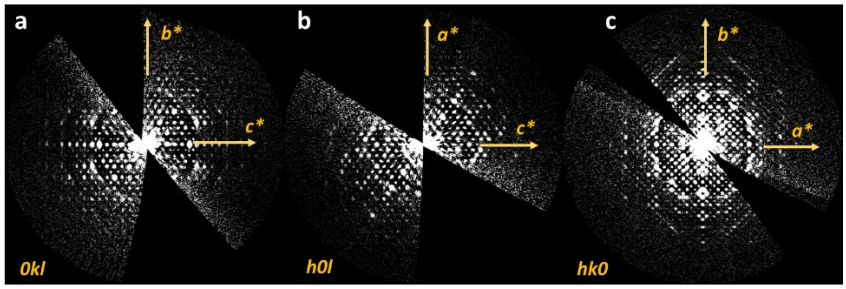

Figure 55. (a) 0kl, (b) h0l and (c) hk0 plane sections of the 3D reconstructed reciprocal space of N-ITQ-52.

After optimizing the orientation angles, reflection intensities were extracted using PETS2. For the C-ITQ-52 data, a single-peaked profile fitting was used, which is common in continuous rotation data, while for the N-ITQ-52 data, a double-peaked profile fitting was employed, as is typical for precession data. The resulting *.hkl* files were imported to Jana2020, and the *ab initio* structure solution model obtained from the charge-flipping algorithm was used as the initial model for the structure refinement. Both samples yielded similar silicon frameworks in the absence of OSDA, featuring 64 Si and 128 O atoms per the unit cell and 10 Si and 19 O atoms in the asymmetric unit for each as-made. The resulting parameters are presented in **Tables 6** and **7** for C-ITQ-52 and N-ITQ-52. For simplicity, during the data determination the framework was treated as pure silica.

Initially, the kinematical refinement performed for each as-made sample produced a difference electron density map within the voids of the inorganic framework, potentially revealing the presence of organic guest molecules for the first time. The resulting density maps for C-ITQ-52 and N-ITQ-52 are visible as yellow clouds in **Fig.**

56 and 57, respectively. At first glance, it appears that the methylene chain of the OSDAs is aligned parallel to the c-axis and perpendicular to the 10R pore, positioned at the center of the unit cell cages, as indicated by the black circles in the figures. The isosurface levels are 0.40 for both C-ITQ-52 and N-ITQ-52. In the initial stages, the C, N, and P atomic positions of the OSDA were directly assigned to the electron difference map. However, this strategy led to a less-than-ideal refinement, marked by a lack of convergence and substantial discrepancies in atomic coordinates. Nevertheless, it was opted to employ these calculated structures as starting models for the Simulated Annealing method implemented in SIR2019, attempting for a more accurate determination of the OSDAs. This decision was driven by the effectiveness that this method showed in initially locating OSDAs molecules within pores of as-made zeolites: SYSU-3,[102] ZEO-2,[95] SCM-25,[68] SU-74-MPMD,[103] and the new open-framework germanate GeO-JU90.[104]

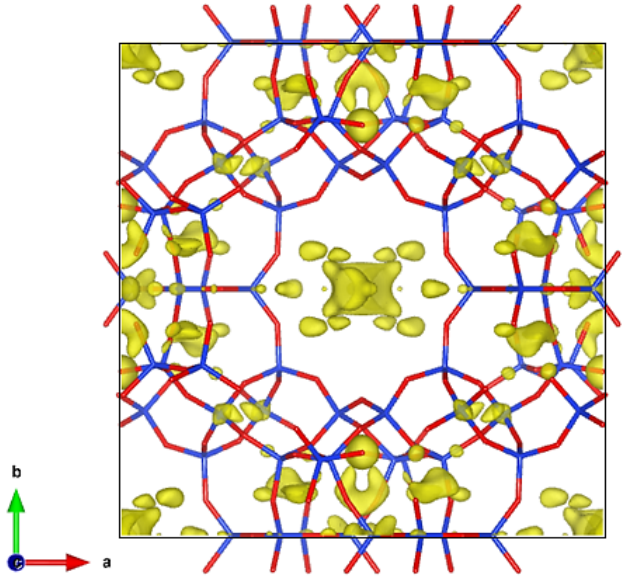

Figure 56. Initial difference electron density map calculated from kinematical refinement against 3DED data, showing only the framework structure of C-ITQ-52 along the channel direction. The framework structure highlights its 10-ring channel. The location of the OSDAs is shown without the framework structure, viewed from the front of the channel along c-axis. The positive isosurface level is 0.40σ. Si atoms are shown in blue, O atoms in red, and H atoms have been omitted for clarity.

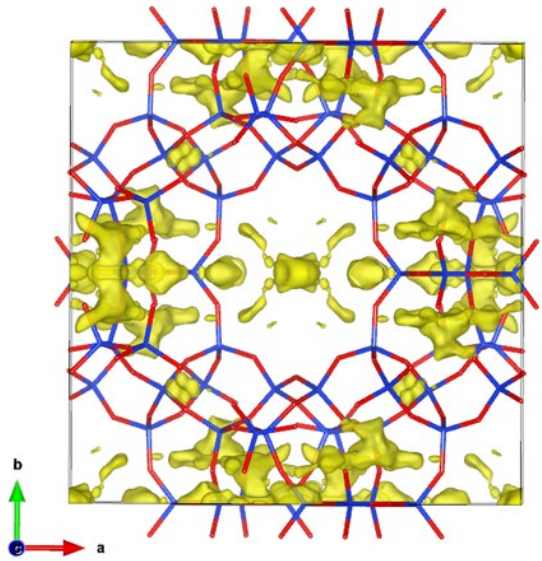

Figure 57. Initial difference electron density map calculated from kinematical refinement against 3DED data, showing only the framework structure of N-ITQ-52 along the channel direction. The framework structure highlights its 10-ring channel. The location of the OSDAs is shown without the framework structure, viewed from the front of the channel along c-axis. The positive isosurface level is 0.40σ. Si atoms are shown in blue, O atoms in red, and H atoms have been omitted for clarity.

4.5. LOCATION OF THE OSDA BY SIMULATED ANNEALING

The Simulated Annealing (SA) method was applied for each as-made pair of 3D structure models - one representing the SiO_2 framework and the other describing the organic guest molecule. These framework 3D models were derived from the silicon framework structure obtained through 3DED data, and the OSDA 3D models were manually drawn and generated as *.mol* files with the help of the software tool Chemdraw 19.0.[105] The determination of these molecular structures was crucial, as they were novel and had not been previously solved or cataloged in any existing database like the Cambridge Structural Database (CSD) and Protein Data Bank (PDB).

Chemical analysis revealed that the quantity of OSDA molecules in each unit cell for both samples is roughly 2. As a result, the initial content per unit cell that was applied in SA was Si 64 O 128 P 4 C 44 for C-ITQ-52 and Si 64 O 128 P 4 C 32 N 12 for N-ITQ-52. It is worth noting that only carbon atoms were assigned to the methylene groups of the organic template, excluding the hydrogen atoms due to the intensive computations required by the program. During SA, a resolution cutoff of 1.0 Å was used, using the R factor as a cost function, and the total number of runs was set at 10 for both data sets. Internal and External Degrees of Freedom (INTDIF and EXDOF, respectively) for the Si network were held constant. However, for the OSDA,

INTDIF and EXDIF were subsequently allowed to vary freely, although bond distances and angles were considered from Chemdraw 19.0. These INTDIF and EXDIF include translational positions (x, y, z), rotation (θ), and torsional angles. An anti-bump restraint with a weight of 1.0 and a scale factor on distances of 0.7 was activated to prevent close contact between the Si framework and OSDA molecule. Dynamical occupancy corrections (DOC) were employed for the OSDA molecule to account for its special positions. Following the SA process, all solutions exhibited visual similarity, sharing identical R factors for C-ITQ-52 (49.31, 49.33, 49.33, 49.36, 49.38, 49.46, 49.89, 49.90, 49.93, 51.08). Notably, none of the solutions did the Si framework collapse with the OSDA molecule. The solution with the lowest R factor (49.31) was selected for subsequent structural analysis (**Fig. 58b**). In the case of N-ITQ-52, the SA solutions displayed visual similarities and produced nearly identical R factors (61.23, 61.24, 61.26, 61.26, 61.28, 61.28, 61.30, 61.30, 61.43, 61.43). The solution with the lowest R factor (61.23) was selected for further structural analysis (**Fig. 58d**). Notably, both OSDAs were consistently positioned in the central cavity during the SA process, aligning with the locations observed in the difference Fourier map derived from the 3DED data prior to SA (**Fig. 58a** and **c**). Based on these observations, it was decided to refine these structural solution models against the 3DED data.

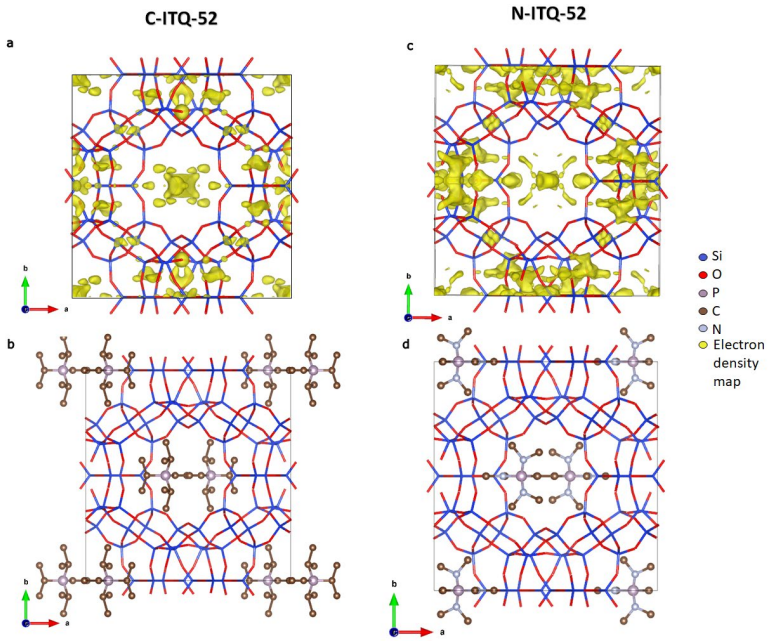

Figure 58. (a) and (c) Structural representation and electrostatic potential map (difference Fourier map) of C-ITQ-52 and N-ITQ-52, respectively, obtained from 3DED data along the c-axis. (b) and (d) Structural models of C-ITQ-52 and N-ITQ-52, respectively, derived using the simulated annealing method, viewed along the c-axis. Positive isosurfaces at 0.40σ are highlighted in yellow. Silicon atoms are shown in blue, oxygen in red, phosphorus in purple, nitrogen in light blue, and carbon in brown.

4.6. KINEMATICAL AND DYNAMICAL REFINEMENT FROM 3DED DATA

The two most optimal SA structure models were used for kinematical refinement against 3DED data using JANA2020 software. The Anisotropic Displacement Parameters (ADP) for each kind of atom type were constrained to be equal and refined isotropically. The occupancy factor for all atoms from the organic guest molecule were kept fixed to one. The distance and angle restraints applied during the kinematic refinement are detailed in **Tables 10** and **11**. For the silicon framework, distance restrains Si-O = 1.61(1) Å and angle restrains O-Si-O = 109.47(10)° were applied. The OSDA molecule was treated as a rigid body. For the organic guest molecule of C-ITQ-52, distance restrains: P-C = 1.80(10) Å, C-C = 1.52(10) Å and angle restrains $C(sp^3)$-P-$C(sp^3)$ = 109.47(10) Å and $C(sp^3)$-$C(sp^3)$-$C(sp^3)$ = 109.47(10) Å were applied. For the organic guest molecule of N-ITQ-52, distance restrains: P-N = 1.63(10) Å, C-C = 1.52(10) Å, N-C = 1.48(10) Å; and angle restrains N-P-N = 109.47(1)°, N-C-C = 114.2(1) ° and P-N-C = 119.29(1)° were used. After several cycles of the refinement process for each sample, the refinement converged, resulting in the organic guest molecules positioned along the main cavity of the silicon framework, as illustrated in **Fig. 59**. The final refinement converged to the structure model with the agreement factors R1 = 0.3761 for all 3703 reflections with Fo > 3σ(Fo). wR2 = 0.629 and GooF = 9.53 for C-ITQ-52 and R1 = 0.3416 for all 3985 reflections with Fo > 3σ(Fo). wR2 = 0.8332 and GooF = 8.91 for N-ITQ-52, as shown in **Tables 10** and **11**.

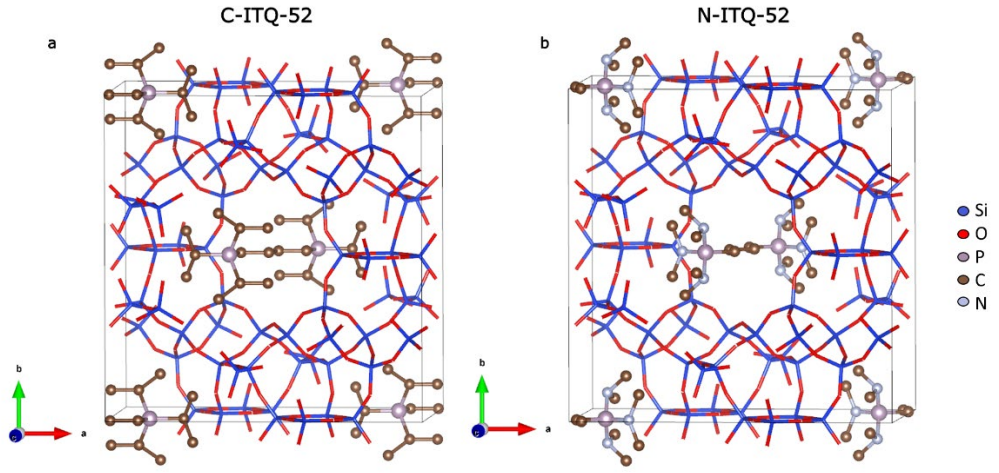

Figure 59. Structures of (a) C-ITQ-52 and (b) N-ITQ-52 as determined by kinematical refinement against 3DED data, viewed along the c-axis. Silicon atoms are shown in blue, oxygen in red, phosphorus in purple, nitrogen in sky blue, and carbon in brown.

Table 10. Kinematical refinement parameters for as-made C-ITQ-52 against 3DED data.

Sample	C-ITQ-52
Crystal system	Monoclinic
Refined composition	$Si\ O_2\ P_{0.062}\ C_{0.687}$
Space group (Num.)	I12/m1 (12)
a (Å)	17.5122
b (Å)	17.9857
c (Å)	12.3557
β (°)	90.222
Volume (Å^3)	3891.635
Z	64
Wavelength (Å)	0.02508
Num. Unique reflections (I > 3 sigma(I))	2116
Num. total reflections	3703
Num. Constraints	55
Num. Geometric Restrains	157
Distance Si-O (1.61 Å±0.01)	40
Angle O-Si-O (109.47°±0.1)	60
Distance P-C (1.80 Å±0.001)	8
Distance C-C (1.52 Å±0.001)	15
Angle C-C-C (109.47°±0.01)	8
Angle P-C-C (109.47°±0.01)	14
Angle C-P-C (109.47°±0.01)	12
Num. Structural refined parameters	78
GooF	9.53
wR2	0.6298
R_1	0.3761

Table 11. Kinematical refinement parameters for as-made N-ITQ-52 against 3DED data.

Sample	N-ITQ-52
Crystal system	Monoclinic
Refined composition	$Si\ O_2\ P_{0.062}\ N_{0.187}\ C_{0.5}$
Space group (Num.)	I12/m1 (12)
a (Å)	17.2837
b (Å)	17.7539
c (Å)	12.2233
β (°)	90.4047
Volume (Å^3)	3750.64
Z	64
Wavelength (Å)	0.02508
Num. Unique reflections (I > 3 sigma(I))	1855
Num. total reflections	3985
Num. Constraints	55
Num. Geometric Restrains	149
Distance Si-O (1.61 Å±0.01)	40
Angle O-Si-O (109.47°±0.1)	60
Distance P-N (1.66 Å±0.01)	6
Distance P-C (1.80 Å±0.001)	2
Distance C-C (1.52 Å±0.001)	3
Distance N-C (1.47 Å±0.001)	11
Angle N-P-N (109.47°±0.01)	6
Angle N-P-C (109.47°±0.01)	6
Angle P-N-C (109.47°±0.01)	9
Angle C-N-C (109.47°±0.01)	3
Angle C-C-C (109.47°±0.01)	2
Angle P-C-C (109.47°±0.01)	1
Num. Structural refined parameters	78
GooF	8.91
wR2	0.8332
R_1	0.3416

The dynamical refinement of the 3DED data collected from the N-ITQ-52 sample was performed using JANA2020. Due to the low completeness of the C-ITQ-52 data, dynamical refinement was not attempted for that sample. After a 9-day refinement

process, convergence was achieved, yielding the structure shown in **Fig. 60**, with the following R-factors: GooF = 4.05, R1 = 29.19%, and wR2 = 18.17%. However, the dynamical refinement of the thermal parameters and occupancies for all atoms associated with the OSDA revealed a significant deviation of 3.16(5) Å between the Csp^3 atoms of the methylene chain (**Fig. 60b**). This discrepancy indicated incorrect structural convergence, leading to the exclusion of this result. Consequently, the structure model obtained from the kinematical refinement was used for subsequent Rietveld refinement against the powder pattern.

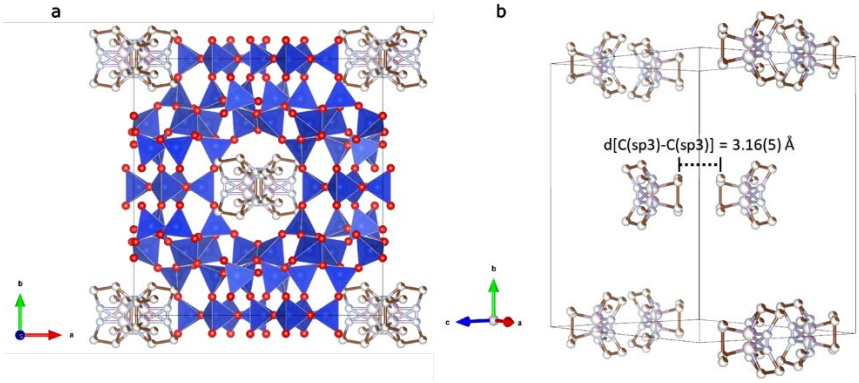

Figure 60. Refined structure model from dynamical refinement against 3DED data from N-ITQ-52 sample.

4.7. REFINEMENT AGAINST POWDER XRD DATA

The two complete as-made ITQ-52 models obtained during kinematical refinement against 3DED data were used as starting models for the Rietveld refinement, using the PXRD data, with JANA2020. The isotropic thermal parameters were constrained to be equal for each atom type. The fractional occupancy factor of all atoms, except Si, were fixed to the 1.

The distance and angle restraints applied during the refinements for both samples are detailed in **Table 12**, along with the corresponding refinement parameters, residuals, and agreement factors. For the silicon framework, a Si-O distance restraint of 1.61(1) Å and an O-Si-O angle restraint of 109.47(10)° were imposed. In the case of C-ITQ-52, the OSDA was refined using distance restraints of P-C (1.80 Å±0.001) and C-C (1.52 Å±0.001), along with angle restraints of C-C-C, P-C-C, and C-P-C at 109.47°±0.01. These restraints were based on typical sp^3 hybridization, tetrahedral geometry, and standard bond lengths as specified in Volume C of the International Tables for Crystallography. For N-ITQ-52, the OSDA refinement included similar P-C and C-C distance restraints, as well as additional restraints for P-N (1.66 Å±0.001) and N-C (1.47 Å±0.001). Angle restraints were applied for N-P-N, N-P-C, P-N-C, C-N-C, C-C-C, and P-C-C, all set at 109.47°±0.01.

Given that these as-made samples are based on a borosilicate framework, T-site occupancies were refined during this step to identify possible preferential locations for boron atoms within the structure. This refinement was important to determine the specific T-sites where boron atoms might be isomorphically replacing silicon within the framework. The electron density contributions from hydrogen atoms were included in the occupancy calculations of their respective bonded carbon atoms.

The final refinement converged with the agreement factors for C-ITQ-52, R_1 = 0.188 for 2546 reflections with Fo > 3σ(Fo), GooF = 3.28, Rwp = 0.141 and Rexp = 0.104; and for N-ITQ-52, R_1 = 0.124 for 2534 reflections with Fo > 3σ(Fo) and 0.1495, GooF = 3.63, R_{wp} = 0.087, R_{exp} = 0.061. A total of 11 profile parameters were refined for both samples: lattice parameters *a*, *b*, and *c*; *β* angle; unit cell volume; zero shift; divergence correction; and the pseudo-Voigt peak shape function parameters (GU, GV, GW, and LY). The final refined coordinates of C-ITQ-52 and N-ITQ-52 are shown in **Tables 13** and **14**. The final refined structures are shown in **Fig. 61**, while the refined PXRD patterns are shown in **Fig. 62** and **63**. The slightly higher residuals observed in the 3DED and PXRD data for C-ITQ-52 compared to N-ITQ-52 might result from differences in the quality of the samples.

Table 12. Crystallographic data for Rietveld refinement using PXRD data of C-ITQ-52 and N-ITQ-52.

Sample	C-ITQ-52	N-ITQ-52
Crystal system	Monoclinic	Monoclinic
Chemical Composition	$Si_{0.95}$ $B_{0.05}$ O_2 $P_{0.06}$ $C_{0.69}$ $H_{1.56}$	$Si_{0.95}$ $B_{0.05}$ O_2 $P_{0.06}$ $N_{0.19}$ $C_{0.50}$ $H_{1.4}$
Refined composition	$Si_{0.96}$ $B_{0.04}O_2$ $P_{0.06}$ $C_{0.95}$	$Si_{0.95}$ $B_{0.05}$ O_2 $P_{0.06}$ $N_{0.19}$ $C_{0.73}$
Space group	*I2/m*	*I2/m*
***a* (Å)**	17.5050(7)	17.4918(6)
***b* (Å)**	17.9620(6)	17.9016(5)
***c* (Å)**	12.3600(5)	12.3304(4)
***β* (°)**	90.6466(19)	90.5283(16)
Volume (Å^3)	3886.0(3)	3860.9(2)
Z	64	64
2θ range (°)	5.12 to 109.93	5.14 to 109.86
Wavelength (Å)	1.540598	1.540598
Num. unique reflections (I > 3 sigma(I))	2546	2534
Num. geometric restrains	118	118
Distance Si-O (1.61 Å±0.01)	40	40
Angle O-Si-O (109.47°±0.1)	60	60
Distance P-C (1.80 Å±0.001)	3	1
Distance C-C (1.52 Å±0.001)	5	2
Distance P-N (1.66 Å±0.001)	0	2
Distance N-C (1.47 Å±0.001)	0	3
Angle N-P-N (109.47°±0.01)	0	1
Angle N-P-C (109.47°±0.01)	0	2
Angle P-N-C (109.47°±0.01)	0	4
Angle C-N-C (109.47°±0.01)	0	2
Angle C-C-C (109.47°±0.01)	3	1
Angle P-C-C (109.47°±0.01)	4	1
Angle C-P-C (109.47°±0.01)	3	0
Num. structural parameters refined	99	99
Num. profile parameters refined	11	11
R_{wp}	14.14	8.78
R_p	10.41	6.10
GooF	3.28	3.63
wR_2	18.42	13.21
R_1	18.81	12.41

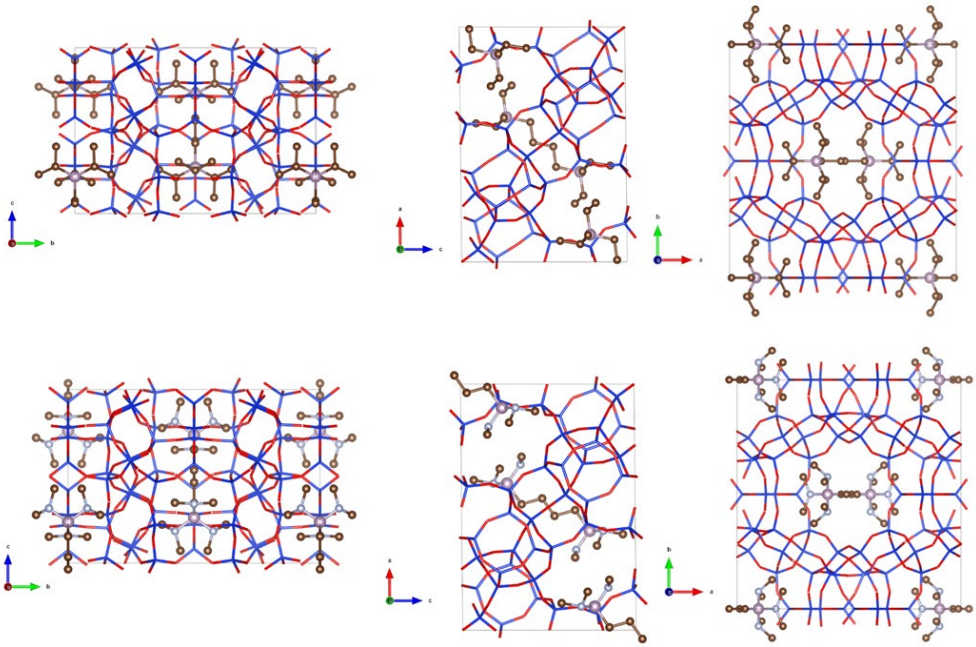

Figure 61. Location of the OSDA refined by PXRD in C-ITQ-52 (top) and N-ITQ-52 (bottom) viewed along a, b and c axis, respectively. Blue: Si; red: O, white: P; brown: C, cyan: N.

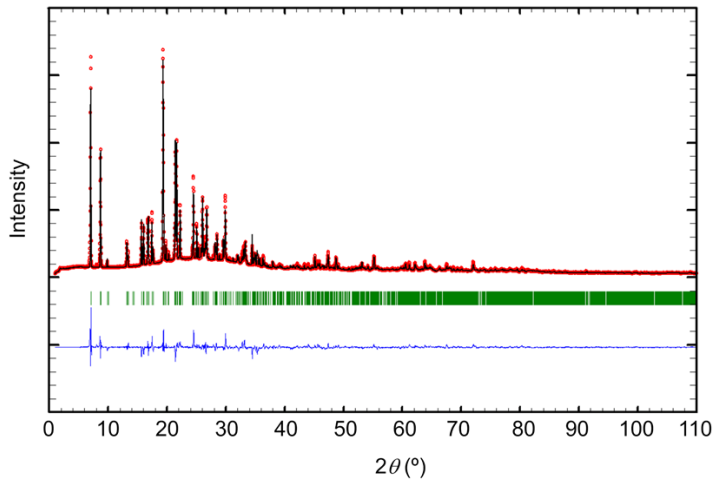

Figure 62. Rietveld refinement using PXRD of C-ITQ-52 sample. Observed (red points), calculated (black) and the difference between observed and calculated (blue line). The vertical tick marks below the pattern give the positions of the Bragg reflections. Cu Kα radiation (λ = 1.5406 Å).

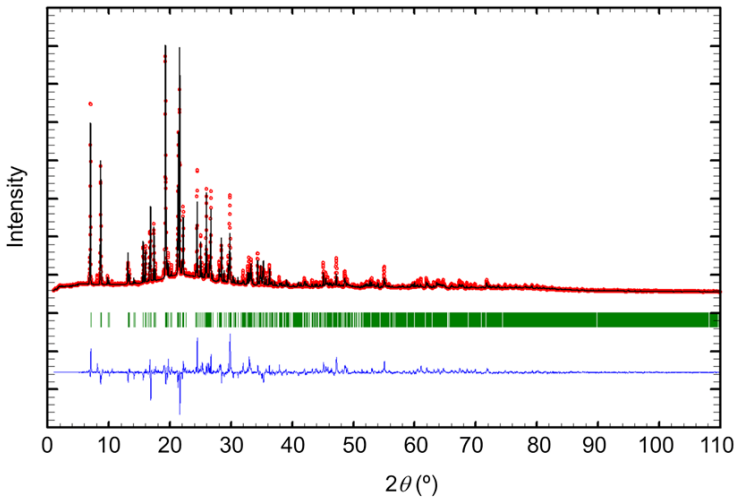

Figure 63. Rietveld refinement using PXRD of N-ITQ-52 sample. Observed (red points), calculated (black) and the difference between observed and calculated (blue line). The vertical tick marks below the pattern give the positions of the Bragg reflections. Cu Kα radiation (λ = 1.5406 Å).

Table 13. Atomic coordinates, thermal displacement parameters and multiplicity for C-ITQ-52 using PXRD data.[a]

Atom	Atom type	x	y	z	Occupancy [b]	Uiso [c]	Multiplicity & Wyckoff
Si1	Si	0.35592(17)	0	-0.9365(2)	1	0.0393(14)	4i
Si2	Si	0.20241(13)	0.25205(10)	-0.58964(17)	1	0.0393(14)	8j
Si3	Si	0.22585(13)	0	-0.7875(2)	0.68(3)	0.0393(14)	4i
B3	B	0.22585(13)	0	-0.7875(2)	0.32(3)	0.0393(14)	4i
Si4	Si	0.08915(11)	0.35388(14)	-0.46877(13)	1	0.0393(14)	8j
Si5	Si	0.17801(13)	0.5	0.0946(2)	1	0.0393(14)	4i
Si6	Si	0.03433(16)	0.5	0.2253(2)	1	0.0393(14)	4i
Si7	Si	0.17779(11)	0.15758(9)	-0.78439(18)	1	0.0393(14)	8j
Si8	Si	0.16673(11)	0.34596(15)	-0.01911(16)	1	0.0393(14)	8j
Si9	Si	0.06737(10)	0.34785(13)	-0.22203(14)	1	0.0393(14)	8j
Si10	Si	-0.04608(10)	0.25064(14)	-0.09927(13)	0.83(2)	0.0393(14)	8j
B10	B	-0.04608(10)	0.25064(14)	-0.09927(13)	0.17(2)	0.0393(14)	8j
O1	O	0.17968(17)	0.18450(12)	-0.6684(2)	1	0.037(2)	8j
O2	O	0.12434(14)	0.28817(17)	-0.5402(2)	1	0.037(2)	8j
O3	O	0.08234(17)	0.5	0.3374(3)	1	0.037(2)	4i
O4	O	0.24704(18)	0.31337(12)	-0.6551(2)	1	0.037(2)	8j
O5	O	0.22446(16)	0.5	0.1932(3)	1	0.037(2)	4i
O6	O	0	0.2130(3)	0	1	0.037(2)	4g
O7	O	0.13898(12)	0.3535(3)	-0.1404(2)	1	0.037(2)	8j
O8	O	0.09800(12)	0.33278(13)	-0.3426(2)	1	0.037(2)	8j
O9	O	0.25846(16)	0.22019(16)	-0.4888(3)	1	0.037(2)	8j
O10	O	-0.09569(13)	0.31902(15)	-0.0557(2)	1	0.037(2)	8j
O11	O	0.1323(2)	0.42766(10)	-0.4914(2)	1	0.037(2)	8j
O12	O	0.27433(18)	0	-0.8911(2)	1	0.037(2)	4i
O13	O	0.17627(12)	0.06905(10)	-0.7861(3)	1	0.037(2)	8j
O14	O	0.01267(19)	0.27957(14)	-0.18641(16)	1	0.037(2)	8j
O15	O	0.19756(13)	0.42516(9)	0.0230(3)	1	0.037(2)	8j
O16	O	0	0.3641(3)	-0.5	1	0.037(2)	4h
O17	O	0.09273(18)	0.5	0.1254(2)	1	0.037(2)	4i
O18	O	-0.10216(17)	0.18965(13)	-0.1544(3)	1	0.037(2)	8j
O19	O	-0.01894(17)	0.42627(9)	0.2194(2)	1	0.037(2)	8j
P1	P	0.6089(10)	0.5	0.2700(18)	1	0.61(2)	4i
C1	C	0.587(2)	0.5	0.412(2)	1.33	0.61(2)	4i
C2	C	0.502(2)	0.5	0.4386(2)	1.33	0.61(2)	4i
C3	C	0.7109(9)	0.5	0.253(3)	1.16	0.61(2)	4i
C4	C	0.5688(10)	0.58184(8)	0.207(2)	1.16	0.61(2)	8j
C5	C	0.607(2)	0.65083(15)	0.254(3)	1.5	0.61(2)	8j
C6	C	0.7448(12)	0.43091(8)	0.306(3)	1.5	0.61(2)	8j
C7	C	0.582(3)	0.5789(12)	0.086(2)	1.5	0.61(2)	8

[a] Numbers in parentheses are the esd's in the units of the least significant digit given. Parameters without an esd were not refined. Coordinates equal to 0 or 0.5 are fixed by symmetry.

[b] Total occupancy of each T-site is constrained to be equal to 1. Electrons corresponding to H atoms are included in the occupancy of their bonded C.

[c] All atoms with the same atom type have been refined with a common value of Uiso (in $Å^2$).

Table 14. Atomic coordinates, thermal displacement parameters and multiplicity for N-ITQ-52 using PXRD data.[a]

Atom	Atom type	x	y	z	Occupancy[b]	Uiso [c]	Multiplicity & Wyckoff
Si1	Si	-0.1286(3)	0.5	0.5745(4)	1	0.0434(9)	4i
Si2	Si	-0.2053(3)	0.7512(3)	0.5828(4)	0.80(2)	0.0434(9)	8j
B2	B	-0.2053(3)	0.7512(3)	0.5828(4)	0.20(2)	0.0434(9)	4i
Si3	Si	-0.2673(3)	0.5	0.7229(5)	1	0.0434(9)	4i
Si4	Si	-0.08761(17)	0.6509(2)	0.4708(3)	1	0.0434(9)	8j
Si5	Si	-0.1653(4)	0.5	0.9229(5)	1	0.0434(9)	4i
Si6	Si	-0.0227(3)	0.5	0.7762(5)	1	0.0434(9)	4i
Si7	Si	-0.3244(2)	0.65852(19)	0.7002(4)	1	0.0434(9)	8j
Si8	Si	-0.1674(3)	0.3434(2)	1.0184(4)	0.77(2)	0.0434(9)	8j
B8	B	-0.1674(3)	0.3434(2)	1.0184(4)	0.23(2)	0.0434(9)	8j
Si9	Si	-0.0674(3)	0.6544(2)	0.2238(3)	1	0.0434(9)	8j
Si10	Si	0.0495(2)	0.7474(3)	0.1029(3)	1	0.0434(9)	8j
O1	O	-0.3144(5)	0.6948(4)	0.8177(5)	1	0.065(2)	8j
O2	O	-0.1263(2)	0.7181(3)	0.5373(5)	1	0.065(2)	8j
O3	O	-0.0537(3)	0.5	0.6518(4)	1	0.065(2)	4i
O4	O	-0.2559(4)	0.6828(2)	0.6235(6)	1	0.065(2)	8j
O5	O	-0.2382(3)	0.5	0.8453(5)	1	0.065(2)	4i
O6	O	0	0.7718(6)	0	1	0.065(2)	4g
O7	O	-0.1351(4)	0.6675(4)	0.1388(5)	1	0.065(2)	8j
O8	O	-0.0990(3)	0.6695(3)	0.3439(3)	1	0.065(2)	8j
O9	O	-0.2521(4)	0.7990(5)	0.4936(6)	1	0.065(2)	8j
O10	O	-0.1083(4)	0.3155(4)	0.9315(6)	1	0.065(2)	8j
O11	O	-0.1264(3)	0.57099(17)	0.4937(4)	1	0.065(2)	8j
O12	O	-0.2146(3)	0.5	0.6177(4)	1	0.065(2)	4i
O13	O	-0.3217(2)	0.57101(15)	0.7120(6)	1	0.065(2)	8j
O14	O	-0.0032(4)	0.7142(3)	0.1961(3)	1	0.065(2)	8j
O15	O	-0.1780(4)	0.43055(16)	1.0032(4)	1	0.065(2)	8j
O16	O	0	0.6464(5)	0.5	1	0.065(2)	4h
O17	O	-0.0775(3)	0.5	0.8814(4)	1	0.065(2)	4i
O18	O	-0.4049(4)	0.6811(4)	0.6475(6)	1	0.065(2)	8j
O19	O	-0.0323(4)	0.57165(18)	0.2119(6)	1	0.065(2)	8j
P1	P	0.3972(8)	0.5	0.7309(8)	1	0.931(19)	4i
N1	N	0.3949(10)	0.57547(17)	0.8082(8)	1	0.931(19)	8j
N2	N	0.3221(5)	0.5	0.6476(12)	1	0.931(19)	4i
C1	C	0.4835(5)	0.5	0.6530(3)	1.33	0.931(19)	4i
C2	C	0.46349(14)	0.5	0.5329(3)	1.33	0.931(19)	4i
C3	C	0.334(2)	0.6253(11)	0.770(2)	1.5	0.931(19)	8j
C4	C	0.299(2)	0.4226(2)	0.624(4)	1.5	0.931(19)	8j
C5	C	0.381(2)	0.5536(3)	0.9210(9)	1.5	0.931(19)	8j

[a] Numbers in parentheses are the esd's in the units of the least significant digit given. Parameters without an esd were not refined. Coordinates equal to 0 or 0.5 are fixed by symmetry.

[b] Total occupancy of each T-site is constrained to be equal to 1. Electrons corresponding to H atoms are included in the occupancy of their bonded C.

[c] All atoms with the same atom type have been refined with a common value of Uiso (in Å^2).

The interatomic bond distances for the refined OSDA structures of C-ITQ-52 and N-ITQ-52 align closely with the theoretical bond lengths for P-N, P-C, N-C, and C-C bonds, as shown in **Table 15** and **16**. For the C-ITQ-52 sample, the bond distances such as P1-C1 (1.83 Å) and C1-C2 (1.52 Å) are consistent with the expected values. The refined bond angles and distances suggest that the structural models are reliable, with only minor deviations observed in some cases, which fall within acceptable ranges.

Table 15. Interatomic bond distances (in Å) for the refined OSDA of the C-ITQ-52. The numbers in parentheses represent the estimated standard deviations (esd's) for the least significant digit.

Atom 1	Atom 2	Length (Å)	Theorical length (Å)
P1	C1	1.80(4)	1.80
P1	C3	1.80(3)	
P1	C4	1.802(18)	
C1	C2	1.53(5)	1.52
C2	C2	1.520(7)	
C3	C6	1.52(3)	
C4	C5	1.53(2)	
C4	C7	1.52(4)	

Table 16. Interatomic bond distances (in Å) for the refined OSDA of the N-ITQ-52. The numbers in parentheses represent the estimated standard deviations (esd's) for the least significant digit.

Atom 1	Atom 2	Length (Å)	Theorical length (Å)
P1	N1	1.654(9)	1.66
P1	N2	1.660(17)	
P1	C1	1.797(16)	1.80
N1	C3	1.46(4)	1.47
N1	C5	1.467(16)	
N2	C4	1.472(15)	
C1	C2	1.519(6)	1.52
C2	C2	1.519(6)	

4.8. STRUCTURAL COMPARISON OF OSDA MOLECULES IN C-ITQ-52 AND N-ITQ-52

Although presenting almost identical frameworks, C-ITQ-52 and N-ITQ-52 show a different preferential location of the boron atoms. In C-ITQ-52 boron replaces Si preferentially in the T-sites T3 (32 % B) and T10 (17 % B), while in N-ITQ-52 the substitution occurs in two different sites, T2 (20 % B) and T8 (23 % B) as seen in atomic coordinates in **Tables 13** and **14**. The remaining sites appear as 100% Si. This gives Si/B ratios for the samples of 17.6 and 23.2 respectively, close to the values expected from the chemical analysis (17.2 and 18.3).

The complete structural models obtained from Rietveld refinement against PXRD data are displayed in **Fig. 64**. This figure illustrates the superposition of the two as-made structures, C-ITQ-52 (red) and N-ITQ-52 (blue), highlighting the nearly identical positioning of the OSDAs within the framework, which exhibits local 2/m symmetry. Additionally, this figure shows a detailed superposition of the two structures, confirming the coincidence of the framework atoms and the closely aligned positions of the OSDA molecules in both samples. The structural similarity between the OSDAs, where the only variation is the substitution of carbon atoms with nitrogen, accounts for these similarities. However, differences in boron distribution across the T sites of the inorganic framework (IFW) structure appear to be influenced by the differing positive charge densities of the organocations used during synthesis. Higher charge density seems to direct boron to occupy T3 and T10 sites (as seen in C-ITQ-52), while lower charge density favors boron positioning at T8 and T2 sites (as

observed in N-ITQ-52). Each ITQ-52 cage hosts two halves of OSDA molecules, centered at the 10R connection between neighboring cavities, resulting in an average of one OSDA per cavity. The minimum distance between the charged phosphorus atoms and the oxygen atoms of the zeolitic walls is at least 5.1 Å in C-ITQ-52 and 4.9 Å in N-ITQ-52, as shown in **Figures 65a and b**. In both structures, the distance between the phosphorus atoms and the T sites with the highest boron content, T3 in C-ITQ-52 and T8 in N-ITQ-52, measures 5.8 Å.

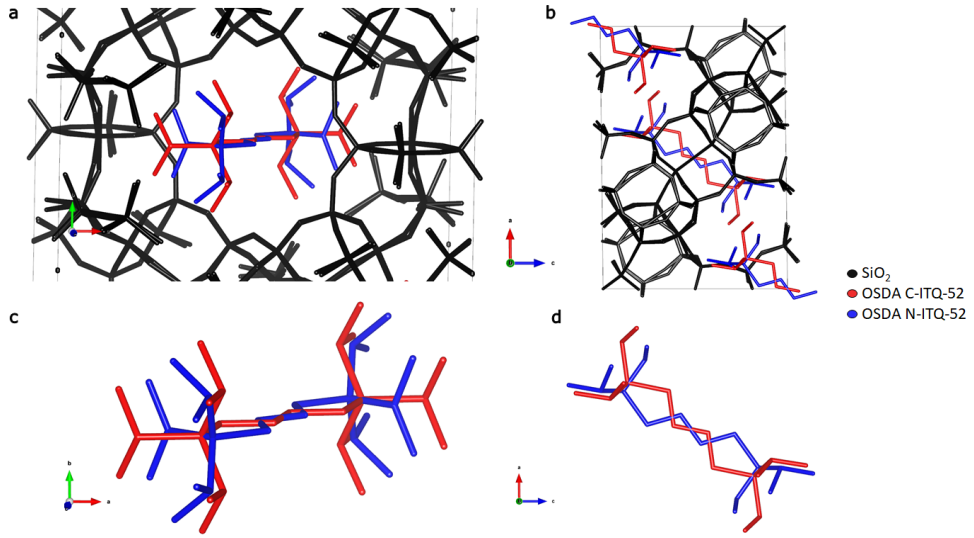

Figure 64. Comparison of the structures of C-ITQ-52 and N-ITQ-52 obtained by Rietveld refinement using the PXRD data. Overlapped structures a) viewed along c axis b) viewed along c axis, and organic OSDA molecules c) viewed along c axis and d) along b axis. Silicon and oxygen atoms colored in black, OSDA for C-ITQ-52 colored in red and OSDA for N-ITQ-52 colored in blue.

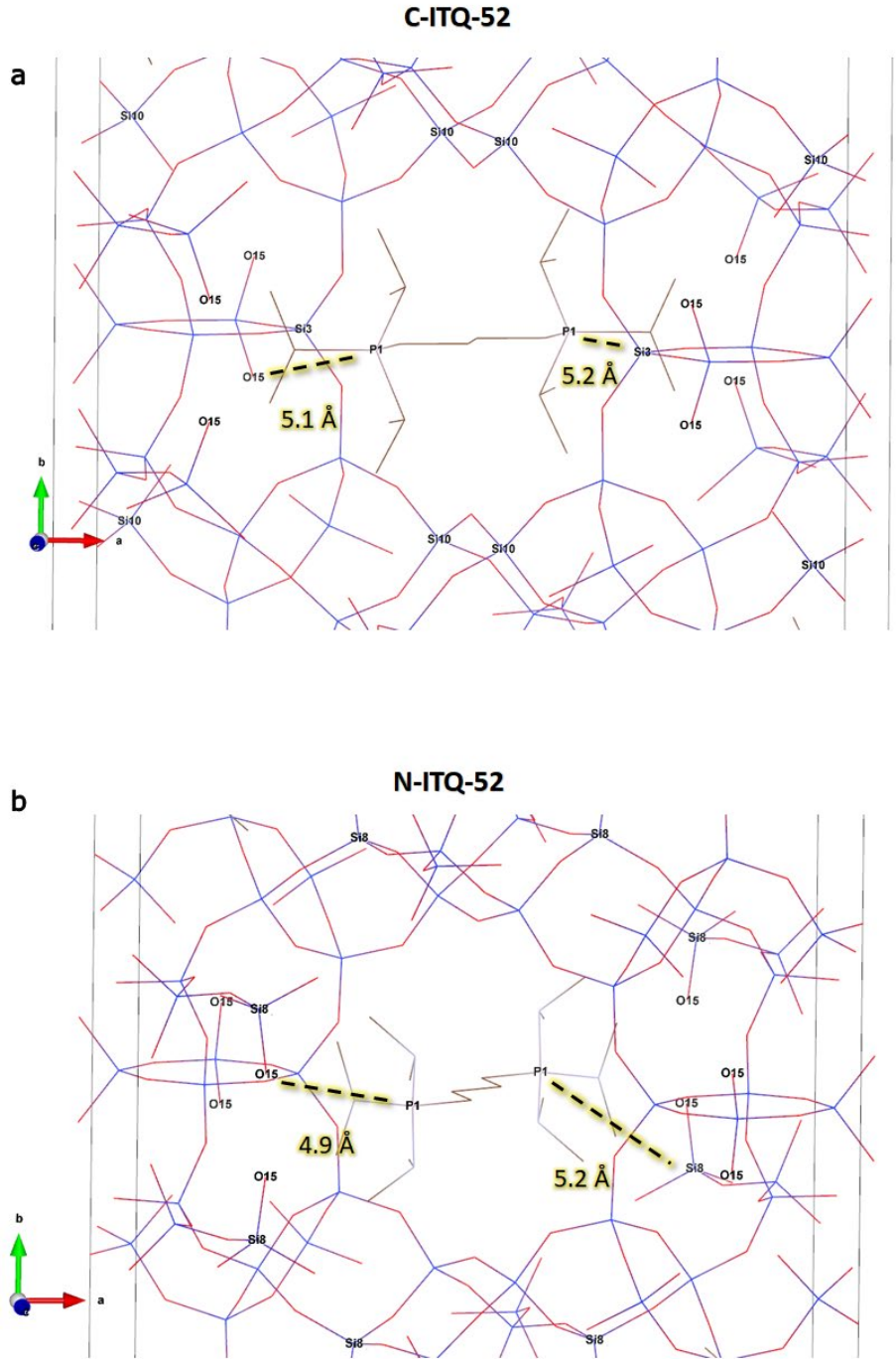

Figure 65. P–O and P–B bond distances in the refined structures of (a) C-ITQ-52 and (b) N-ITQ-52, analyzed against PXRD data and visualized along the a, b, and c axes. The atom color scheme is as follows: silicon (blue), oxygen (red), phosphorus (white), carbon (brown), and nitrogen (cyan).

Appendix I presents a summary of the data acquisition, reduction, and refinement processes described in Chapter 4.

CHAPTER 5. STRUCTURE DETERMINATION OF AS-MADE ZEOLITE ITQ-70

5.1. SYNTHESIS, CHEMICAL, THERMOGRAVIMETRIC, AND TEXTURAL ANALYSIS

This chapter presents the synthesis, characterization, and structure determination of a new pure silica zeolite material with an ordered interrupted framework, named ITQ-70, and the location of the occluded P-OSDA cations in its structural pores. The combination of 3DED, NMR, and PXRD techniques has led to the complete structure characterization of the as-made form. This zeolite was exclusively synthesized in a basic medium with a purely siliceous composition, using tetrakis(diethylamino)phosphonium as the organic structure-directing agent (OSDA), an organophosphorus cation. The structure of the OSDA employed during the synthesis of the new as-made ITQ-70 is described in **Fig. 66**, and the synthesis details can be seen in the literature and the doctoral thesis of Andrés Sala Gascón.[106,107]

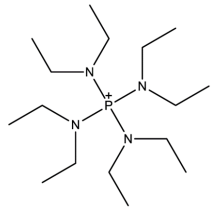

Figure 66. Structure of the tetrakis(diethylamino)phosphonium cation used as OSDA during the synthesis of the as-made ITQ-70.

As it was shown in the previous chapter, the use of phosphorus-containing organic structure-directing agents (P-OSDAs) has led to the crystallization of zeolites with multidirectional large pores and relatively low framework densities.[108,109,110,111,112] This is attributed to the high stability of organophosphorus cations, which allows for long zeolite crystallization periods under hydrothermal conditions at high pHs. Recently, Lin et al. reported the formation of a pure silica tridirectional extra-large pore zeolite using a tetraalkylphosphonium cation under alkaline conditions, resulting in an extra-large pore with low framework density zeolite.[113] This result supports the advantage of using P-OSDAs for synthesizing extra-large pore zeolites, which can produce stable materials with high adsorption capacities and minimal diffusional restrictions for reactants and products.

The tetrakis(diethylamino)phosphonium (TDAP) cation used in the synthesis of zeolite ITQ-70 was commercially obtained in its bromide form and converted to its hydroxide forms through ionic exchange with an anion exchange resin (Amberlite IRN-78). A scheme of the hydrothermal synthesis can be seen in **Fig. 67**. The product was collected and titrated with HCl (0.1N) using phenolphthalein as an indicator to determine the hydroxide concentration of the solution.

In a Teflon plate-shaped container with a volume of 4 mL, an aqueous solution of OSDA hydroxide (0.65 M, 1.85 ml, 1.2 mmol) and colloidal silica (Ludox AS-40, 0.45 g, 3 mmol) were mixed. The mixture was stirred magnetically for 12 hours. Finally, the amount of water was adjusted by evaporation and/or addition until the mixture reached the following final composition expressed in molar ratios:

$$SiO_2: 0.4\ OSDA(OH): 5\ H_2O.$$

The synthesis gel was transferred to a 15 mL Teflon container and placed in a steel autoclave. The autoclave was maintained at 150ºC with stirring for 15 days. The resulting material was recovered by filtration, washed with distilled water (1 L), and dried at 100 ºC for 6 h, resulting in zeolite ITQ-70 as a white solid (177 mg, 82% yield based on SiO_2). This process produced a white, solid crystalline phase with high synthesis yields exceeding 80%.

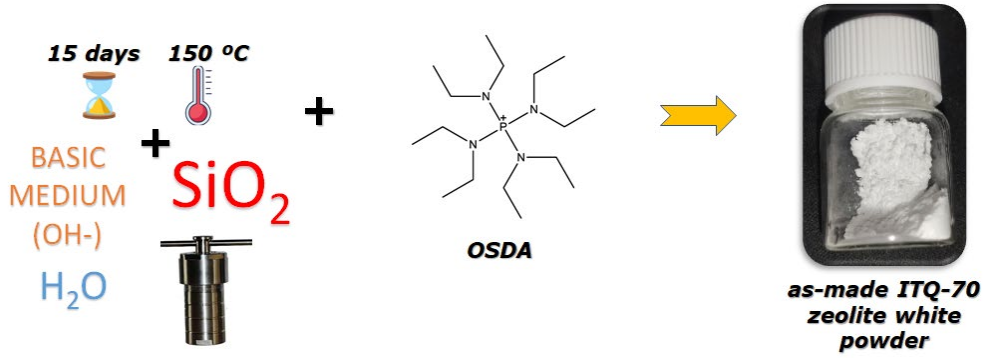

Figure 67. Simplified schematic of the hydrothermal synthesis process for zeolite ITQ-70.

The integrity and stability of the OSDA within the silicon framework were characterized by ^{1}H y ^{31}P solid-state NMR and elemental analysis (EA), as seen in the corresponding reference of this work.[106] EA revealed that the as-made zeolite exhibits a C/N molar ratio and an N/P molar ratio very close to 4, which agrees with the theoretical value for the pure OSDA cation (**Table 17**).

Table 17. Chemical compositions of as-made zeolite ITQ-70.

Sample	Expected ratio		Elemental analysis (wt. %)			Experimental ratio	
	C/N	N/P	C	N	P	C/N	N/P
ITQ-70	4	4	15.9	4.5	2.5	4.1	4.0

The ^{31}P-NMR spectrum shows two resonances at 43.0 ppm, as observed in the top spectrum of **Fig. 68A**. These signals align with the resonances of the pure organic cation, confirming its intact presence within the zeolite pores. The appearance of the double ^{31}P signal has also been noted in other studies of purely siliceous zeolites

synthesized with monocationic P-OSDAs, suggesting that the ADE cation may be situated in two chemically different environments within the structure or could exhibit two different structural conformations.[114] Meanwhile, the solid-state ^{13}C-NMR spectrum of the as-made ITQ-70 material displays signals at 40.0 and 12.0 ppm, as illustrated in **Fig. 68B**.

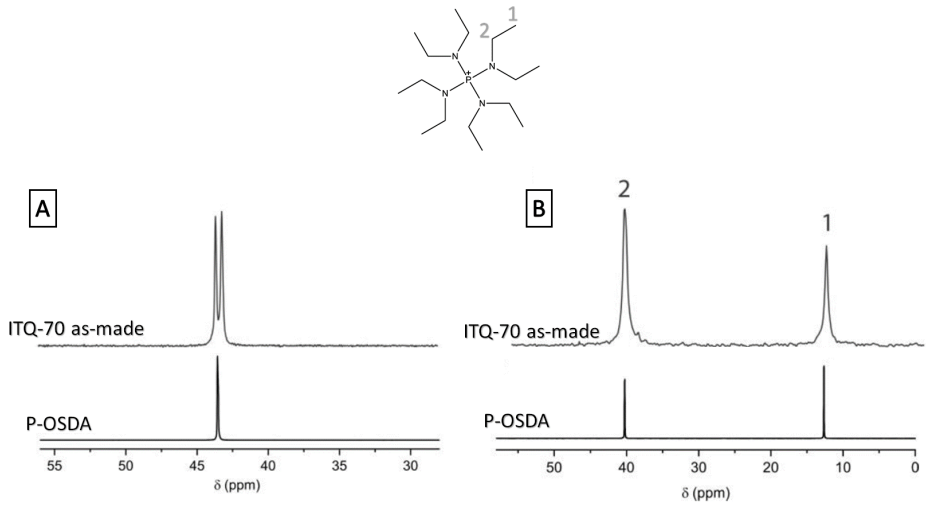

Figure 68. (A) Solid-state ^{31}P MAS-NMR spectra of zeolite ITQ-70 (top) compared with the liquid-state ^{31}P NMR spectra of the OSDA in deuterated water (bottom). (B) Solid-state ^{13}C MAS-NMR spectra of the as-made ITQ-70 (top) alongside the liquid-state ^{13}C NMR spectra of the pure OSDA in deuterated water (bottom).

Thermogravimetric analysis (TGA) of the as-made ITQ-70 reveals a 21% weight loss between 300 and 400 °C, attributed to the partial decomposition of the occluded OSDA within the zeolite (**Fig. 69**). This weight loss is typical for highly porous materials and occurs at relatively low temperatures, which are characteristic of zeolites with large pore sizes and high dimensionality. The early onset of this decomposition suggests that the zeolite framework features large pores, allowing the release of the OSDA. Additionally, the observed weight loss aligns closely with the combined carbon and nitrogen content obtained through elemental analysis [15.9% C + 4.5% N = 20.4%] (see **Table 17**).

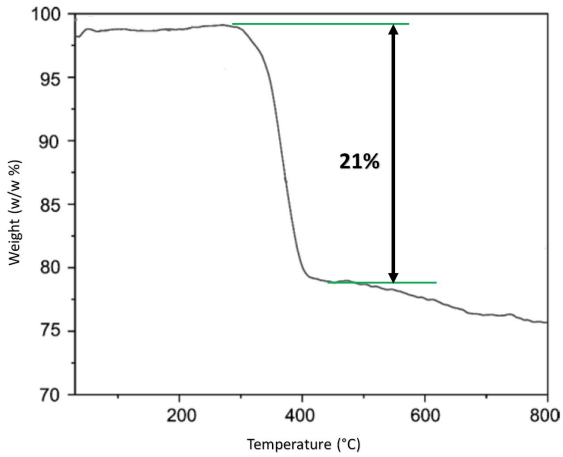

Figure 69. Thermogravimetric analysis of the as-made zeolite ITQ-70.

Once the optimal temperature for organic content removal in the zeolite ITQ-70 was identified via TGA, its structural stability was examined using in situ X-ray diffraction. The zeolite underwent thermal treatment up to 600ºC in a dry air flow, with diffraction patterns recorded at various temperatures and after cooling the calcined sample to 25ºC, as shown in **Fig. 70**.

The zeolite ITQ-70 remains mainly stable upon calcination, preserving peaks at low angles with high intensity. However, most of them (starting from 2θ = 10º) broaden and decrease in intensity until almost disappearing. This behavior is associated with local disorder occurring in the structure during the thermal treatment, which could be attributed to the total or partial condensation of structural defects (Q_3) present in zeolite ITQ-70. However, the two signals of higher intensity at angles 2θ = 5.3 and 6.9º remain unchanged even at 600ºC. Thus, although the crystallinity and some unit cell parameters vary significantly - as evidenced by the appearance of new signals (e.g., 2θ = 8.57º) - we can consider that the structural integrity of the zeolite is maintained during calcination.

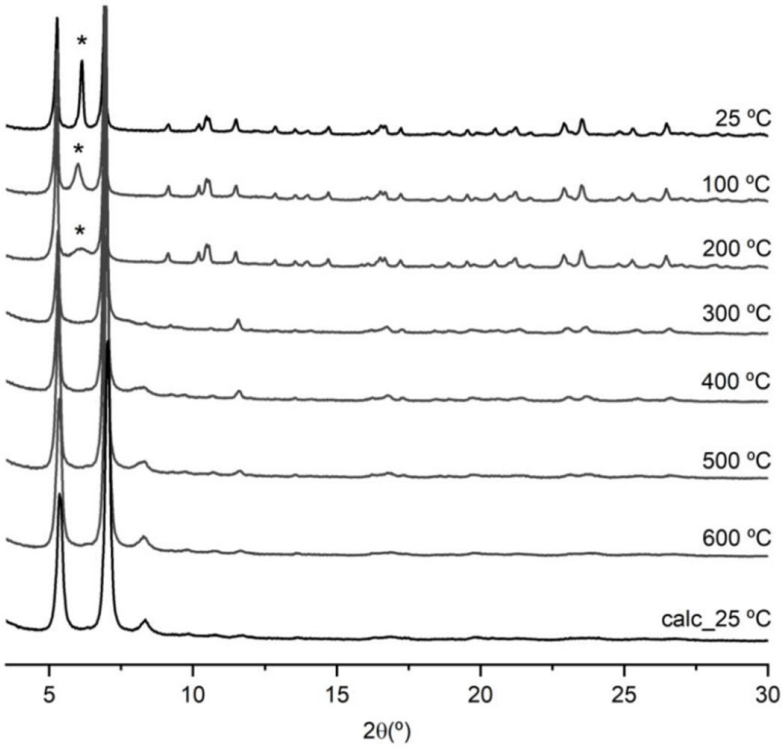

*Figure 70. From top to bottom, thermo-structural analysis of zeolite ITQ-70 under a dry air flow, monitored through in situ powder X-ray diffraction patterns. The sample used in this study contained minor impurities from an unidentified lamellar phase (marked as *).*

The morphology and crystal size of zeolite ITQ-70 were examined using field emission scanning electron microscopy (FESEM). The micrographs revealed the presence of small crystal sizes with a hexagonal bipyramid base shape (0.2 - 1 μm), too small for a structural determination by single crystal X-ray diffraction, and a non-homogeneous crystal size distribution, as seen in **Fig. 71**. Zeolite crystallization in basic media typically results in sub-micrometer-sized microporous materials, in contrast to those synthesized under fluorine media conditions.

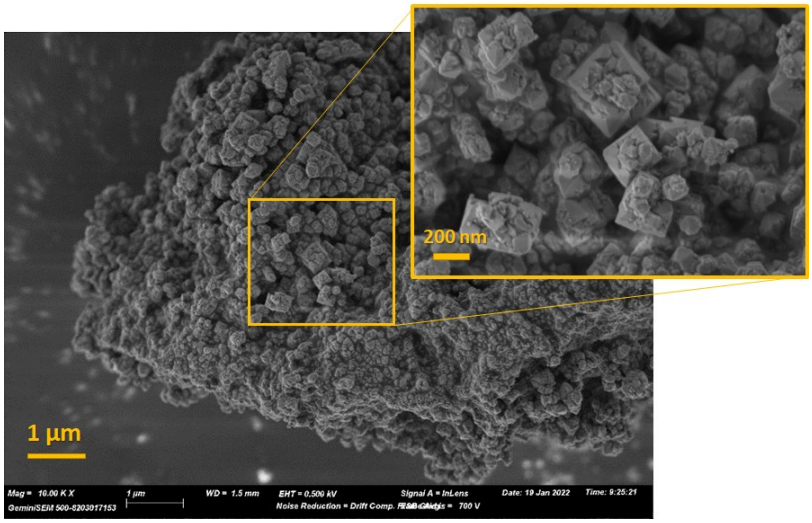

Figure 71. Field Emission Electron Microscopy (FESEM) micrographs of as-made ITQ-70 sample showing the crystal morphology.

Additionally, the comprehensive morphological analysis through HRTEM confirmed the existence of very small crystals, as shown in the TEM images of **Fig. 72**.

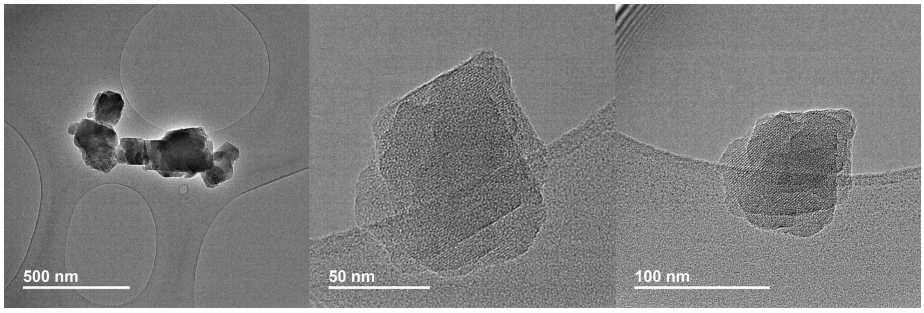

Figure 72. High-Resolution Transmission Electron Microscope (HRTEM) images of as-made zeolite ITQ-70 crystals showing the presence of multiple crystal domains in one single crystal.

The porosity/textural properties of calcined zeolite ITQ-70 were studied by measuring N_2 and Ar adsorption isotherms at 77 K and 87 K, respectively, as seen in **Fig. 73** and **74**. The Brunauer-Emmett-Teller (BET) surface area and t-plot micropore volume of zeolite ITQ-70 were calculated and found to be 967 m2 g^{-1} and 0.36 cm3 g^{-1}, respectively.[115] The Ar adsorption isotherm using the Horvath-Kawazoe method, evidences a very narrow micropore distribution centered at 9 Å, suggesting the presence of an extra-large pore opening.[116] These analyses confirm both the stability of the material during calcination and the microporous nature of this new zeolite. Moreover, the obtained values suggest that zeolite ITQ-70 is the pure silica-composed molecular sieve with the highest reported micropore volume to date. The zeolite ITQ-

70 exhibits superior adsorption capacity compared to any other commercial zeolite. The average pore diameter obtained is also higher than that of other large-pore three-dimensional zeolites. Therefore, the most reasonable hypothesis is that its structure contains a significantly higher number of micropores, which could make it an excellent candidate for molecular sieve applications.

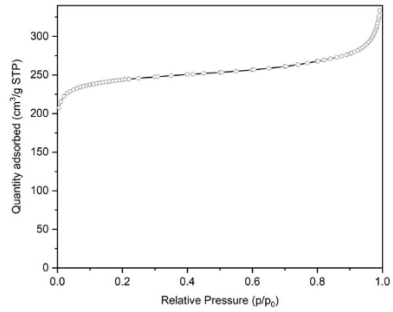

Figure 73. Nitrogen adsorption isotherm at 77 K of calcined zeolite ITQ-70.

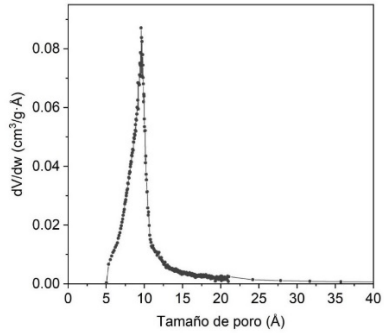

Figure 74. Horvath-Kawazoe differential pore-size distribution curve obtained from the Ar adsorption isotherm at 87 K of calcined zeolite ITQ-70.

The solid-state ^{29}Si NMR spectroscopy analysis of the as-made ITQ-70 showed interesting results displaying six symmetric resonances between -95 ppm and -125 ppm with relative intensities 1:1:1:1:1:0.2 (**Fig. 75a**). These signals can be categorized into two different groups: The first two signals within the δ range are associated with the Q_3 group [or $(SiO_3)SiOH$], contributing to 38% of the total Si; and the last four groups of signals are associated to the Q_4 region [or $(SiO_4)Si$], accounting for the remaining 62%. Thus, the presence of ordered Q_3 groups, consistent with the discussed results earlier, is confirmed. The peak labeled as F, at very high fields ($\delta^{29}Si$ = -120 ppm) may be associated to a T-O-T angle highly opened (>150°), which may indicate highly stressed Si sites within the structure.[117] The assignment and relative intensity of the observed signals are shown in the top right of table included in **Fig. 75c**.

On the other hand, the solid-state ^{29}Si NMR spectroscopy analysis of the calcined ITQ-70 showed an overlap of all peaks from the non-calcined form into two wide peaks that range from -96 ppm to -122 ppm (**Fig. 75b** and **Table 18**). In addition, the analysis using cross-polarization NMR (^{1}H-^{29}Si), which is shown as a dashed line, confirms the presence of Q_3 environments (Si-OH) in the calcined solid due to the increased relative intensity of the broad signal at $\delta^{29}Si$ = -103 ppm. The deconvolution of the original spectrum of the calcined zeolite ITQ-70 indicates that, at the time of the analysis, approximately 19% of Si remains in a Q_3 environment compared to the 38% of Si that the non-calcined zeolite exhibited.

Therefore, the results observed by ^{29}Si NMR and XRD during calcination could shed some light on the partial disorder observed in the calcined form of ITQ-70 and generated by a high number of structural connectivity defects. The partial condensation of these Si-O^-/SiOH could explain the observed loss of crystallinity.

Table 18. Summary of signal assignments, chemical shifts (δ, ppm), relative intensities, and types of structural defects (QN) identified in the non-calcined zeolite ITQ-70, as determined from ^{29}Si MAS NMR spectra. The table includes integration data corresponding to the observed signals.

Signal	δ (ppm)	Relative intesity	Q_N
A	-97.33	0.19	Q3
B	-100.13	0.19	Q3
C	-107.24	0.19	Q4
D	-108.51	0.19	Q4
E	-110.38	0.19	Q4
F	-120.88	0.04	Q4

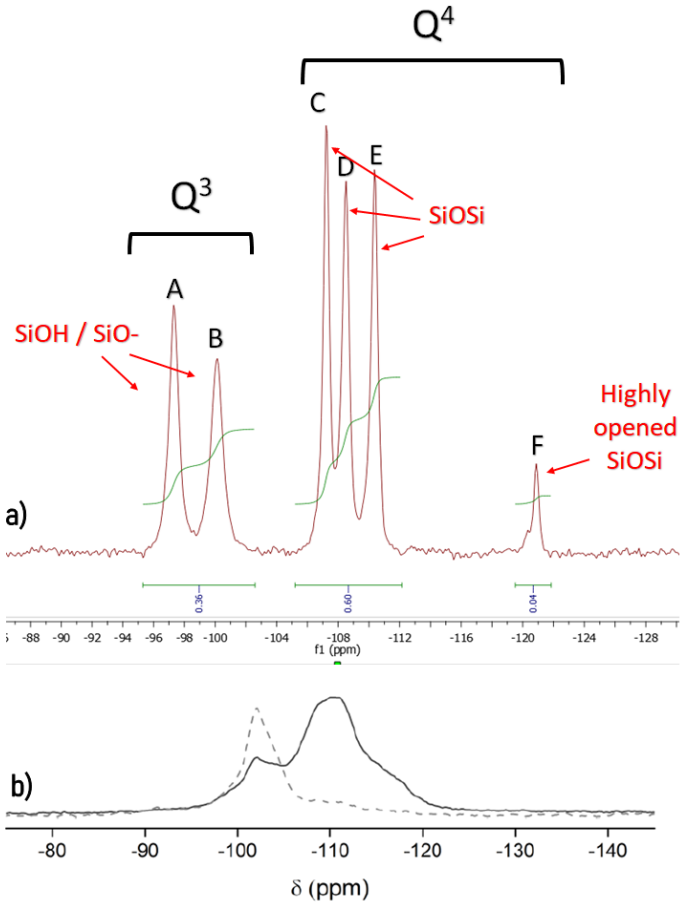

Figure 75. Solid state ^{29}Si-RMN spectra of zeolite ITQ-70 a) as-made b) calcined. In the dashed line, ^{1}H-^{29}Si Cross-Polarization (CP) NMR spectrum.

The analysis of as-made ITQ-70 using Double Quantum-Single Quantum (DQ-SQ) ^{29}Si-NMR, based on dipolar interactions among the ^{29}Si atoms, revealed connectivity correlations between neighboring Si atoms. Correlation signals manifested as peaks

in the NMR spectrum, where the chemical shift in the second dimension summed up the shifts in the first dimension of the involved Si signals. The resulting two-dimensional spectrum is illustrated in **Fig. 76** and **Table 19**. Signals A and B, associated with connectivity defects (Q^3), exhibited a clear connectivity pattern: A→B, C, E; B→A, C, D. Signal F, at high fields, exclusively connected with position C, completing the conventional tetrahedron (Q^4) by quadruplicate: F→4C. Additional connections included: C→A, B, D, F; D→B, C, E; E→A, D, E. These last two signals, assigned to Q_4 environments, repeated some connections to achieve complete tetrahedral coordination. Consequently, a comprehensive connectivity model for the structure of zeolite ITQ-70 can be predicted.

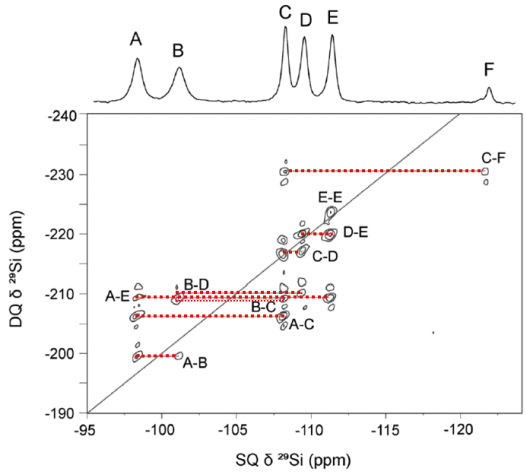

Figure 76. DQ-SQ of ^{29}Si-MAS-RMN of the as-made ITQ-70.

Table 19. Si-Si structural connectivities derived from 3DED and ^{29}Si MAS NMR spectrum of as-made ITQ-70 samples.

^{29}Si-NMR label		**A**	**B**	**C**	**D**	**E**	**F**	**Independent Si neighbours**	**Q^n**
	T-site	**Si4**	**Si2**	**Si5**	**Si6**	**Si3**	**Si1**		
A	**Si4**		x	x		x		3	Q^4
B	**Si2**	x		x	x			3	Q^3
C	**Si5**	x	x		x		x	4	Q^4
D	**Si6**		x	x		x		3	Q^3
E	**Si3**	x			x	x		3	Q^4
F	**Si1**			x				1	Q^4

5.2. PXRD CHARACTERIZATION

The PXRD analysis of ITQ-70 indicated that this material does not match any previously documented zeolite, suggesting that this is a new zeolitic structure. The red line in **Fig. 77** shows the powder diffraction pattern of the as-made ITQ-70 phase. Due to the peak broadening in the PXRD pattern of the calcined material, the studies were performed using the as-made sample.

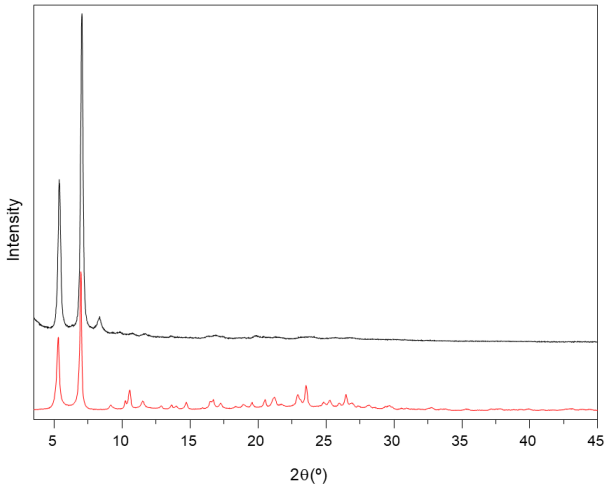

Figure 77. Powder X-ray diffraction patterns of as-made (bottom) and calcined (top) zeolite ITQ-70.

The as-made ITQ-70 sample was measured at room temperature using a Panalytical X'Pert PRO X-ray powder diffractometer equipped with a hybrid germanium (220) monochromator in the incident beam and a Panalytical X'Celerator detector. Prior to the measurement, the sample was placed and sealed in a glass capillary. The measurement was performed using CuKα_1 radiation (λ=1.5406 Å). The unit cell was determined using the program TREOR,[118] obtaining a hexagonal unit cell with parameters: a=b=19.283 Å and c=19.546 Å. The LeBail refinement of the cell parameters gave:

a=b=19.3429(11) Å, c=19.5965(14) Å

α=90°, β=90°, γ=120°

V=6349.69 Å^3

The analysis of the systematic extinctions indicated the most probable extinction symbol as P6$_2$ – –, corresponding to the possible space groups: P6$_2$ (#171), P6$_4$ (#172), P6$_2$22 (#180) and P6$_4$22 (#181). All these groups are chiral groups, being

#171 and #172, as well as #180 and #181, pairs of enantiomorphic space groups, that cannot be distinguished by PXRD.

Therefore, the determination of the as-made structure was attempted using PXRD data and using one of each pair of space groups, but these efforts did not produce satisfactory results. Therefore, it was decided to employ 3DED methods as potential alternative approaches.

5.3. 3DED CHARACTERIZATION

5.3.1. DATA ACQUISITION: JEOL 2100F TEM

The sample was first measured in a JEOL 2100F TEM at an accelerating voltage of 200 keV equipped with a field emission gun (FEG), at room temperature. Electron diffraction patterns were acquired with the GATAN Orius SC600A CCD camera, as shown in **Fig. 78**. Among the different variants for 3DED, a continuos rotation script (cRED) developed in the Instituto de Tecnología Química called Ultrafast-EDT together with a small selected area aperture SAED of diameter size 10 µm were used. Unfortunately, even though the first smaller condenser lens (C2) and a fast acquisition program were used to reduce electron radiation, any DP with reflection intensities appeared after collecting data from a large number of crystals, suggesting that the sample got damaged and lost its crystallinity at room temperatures. Therefore, an alternative electron microscope (next section) which provides both new TEM component such as the new radiation imaging technology including hybrid pixel detectors and cryoholder which allows to reduce the temperature at cryogenic conditions and hence reducing the damage of the crystals by the electron beam.

Figure 78. Electron diffraction patterns were obtained at room temperature from the as-made ITQ-70 sample using a 200 keV JEOL 2100F TEM. The patterns were collected in continuous rotation mode with a selected area aperture at tilt angles of -30º, -25º, and 20º. A TEM image of the analyzed crystal is shown in the top right corner.

5.3.2. DATA ACQUISITION: FEI TECNAI G2 TEM

A small amount of the white powder as-made ITQ-70 was gently crushed on an agate mortar and dispersed directly on a square 200-mesh copper Transmission Electron Microscope (TEM) grid covered by an extra thick 20-30 nm carbon layer (CFT200-CU-ET provided by Ted Pella). The grid was mounted on a Liquid nitrogen cooling tomography holder (Gatan model 636) used to reach a final temperature of 183 K before starting data collection. Although the selection of this temperature was initially considered to reach 93 K, distinctive ring patterns coming out from crystal water affect the quality of the data, as shown in **Fig. 79**. The sample was analyzed using a Transmission Electron Microscope FEI Tecnai G2 20 equipped with a thermionic cathode (LaB_6) at an acceleration voltage of 200 keV. Electron diffraction patterns were collected with a Timepix Quad's hybrid pixel detector (Amsterdam Scientific Instruments), model QTPX-262k (512×512, pixel size 55 μm) with a high dynamic range (16 bit). During data acquisition, a small C2 condenser aperture (20 μm diameter). In order to create mild illumination conditions, spot size 8 and the selected diameter for the semiparallel beam was set to 1.6 μm. 3D Electron Diffraction (3DED) patterns from 25 crystals were collected in continuous rotation mode through a maximum tilt range of ± 60° using self-written scripts[70] in Olympus Soft Imaging Solutions iTEM software for controlling the beam, goniometer, and detector. The exposure time for six data sets was set to 1s, and to 2 seconds for the other four data sets. The exposure time was set to 2s to recheck the quality of the intensities during the experiment. The goniometer rotation speed was adapted so that diffraction patterns cover an angular range of 0.5° during the continuous rotation of the crystal. The average total collection time for each data set was about 5 min. **Table 20** shows the details about the data collection. When comparing the values of the total accumulated electron dose, total exposure time, and electron dose rate, it is evident that the electron dose rate remains constant at 0.020 e/s·Å² across all crystals. Crystals with longer exposure times, such as 414 or 492 seconds, accumulate a higher total electron dose (e.g., 8.3 or 9.8 e/Å²), while those with shorter exposure times, around 197 seconds, receive a lower dose (e.g., 3.9 e/Å²). This shows that exposure time directly affects the total accumulated dose and, consequently, influences both the quality of the data collected and the potential for crystal damage.

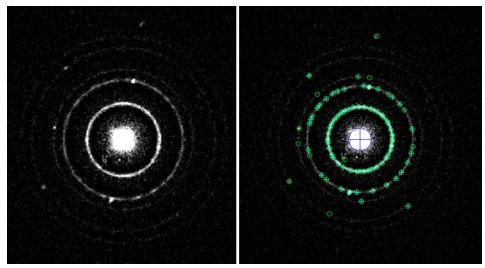

Figure 79. DP of as-made ITQ-70 at a temperature of 93K showing typical ring pattern from frozen water (left) and detected peaks processed by PETS2 software are indicated in green circles (right). These peaks interrupted the intensities extraction during data reduction.

Table 20. Individual crystallographic information and data collection condition of as-made ITQ-70 from ten crystals measured by 3DED at a temperature of 183K. Wavelength 0.02508 Å.

Data set	1	2	3	4	5	6	7	8	9	10
Crystal system	Hexagonal	Hexagonal	Hexagonal	Hexagonal	Hexagonal	Hexagonal	Hexagonal	Hexagonal	Hexagonal	Hexagonal
TEM	FEI Tecnai	FEI Tecnai	FEI Tecnai	FEI Tecnai	FEI Tecnai	FEI Tecnai	FEI Tecnai	FEI Tecnai	FEI Tecnai	FEI Tecnai
Protocol/Illumination mode	cRED in NBD	cRED in NBD	cRED in NBD	cRED in NBD	cRED in NBD	cRED in NBD	cRED in NBD	cRED in NBD	cRED in NBD	cRED in NBD
Sample preparation	Dry	Dry	Dry	Dry	Dry	Dry	Dry	Dry	Dry	Dry
Holder/Temperature	Cryo Transfer Tomography, Gatan/183 K	Cryo Transfer Tomography, Gatan/183 K	Cryo Transfer Tomography, Gatan/183 K	Cryo Transfer Tomography, Gatan/183 K	Cryo Transfer Tomography, Gatan/183 K	Cryo Transfer Tomography, Gatan/183 K	Cryo Transfer Tomography, Gatan/183 K	Cryo Transfer Tomography, Gatan/183 K	Cryo Transfer Tomography, Gatan/183 K	Cryo Transfer Tomography, Gatan/183 K
Detector	Timepix hybrid	Timepix hybrid	Timepix hybrid	Timepix hybrid	Timepix hybrid	Timepix hybrid	Timepix hybrid	Timepix hybrid	Timepix hybrid	Timepix hybrid
Data Acquisition Script	iTEM	iTEM	iTEM	iTEM	iTEM	iTEM	iTEM	iTEM	iTEM	iTEM
Space group (No.)	$P6_222$ (180)	$P6_222$ (180)	$P6_222$ (180)	$P6_222$ (180)	$P6_222$ (180)	$P6_222$ (180)	$P6_222$ (180)	$P6_222$ (180)	$P6_222$ (180)	$P6_222$ (180)
a (Å)	19.7329	19.7638	19.8186	19.7458	19.7802	19.9519	20.0299	19.899	19.9433	19.9797
b (Å)	19.7329	19.7638	19.8186	19.7458	19.7802	19.9519	20.0299	19.899	19.9433	19.9797
c (Å)	19.9544	19.9500	19.9457	19.9889	19.8926	20.1835	20.1118	20.1619	20.1844	20.0291
Volume (Å^3)	6729	6748.6	6784.6	6749.5	6740.4	6958.2	6987.8	6913.9	6952.5	6924.2
Crystal size (nm)	320 x 260	180 x 90	160 x 90	180 x 90	230 x 160	160 x 100	180 x 90	350 x 250	120 x 70	100 x 80
Initial angle (°)	-60	-45	-50	-50	-50	-50	-50	-50	-50	-60
Final angle (°)	45	45	50	50	50	50	50	50	50	60
Integration step (°)	0.5	0.5	0.5	0.5	0.5	0.5	0.5	0.5	0.25	0.25
Exposure time per frame (s)	0.987	2.047	2.047	2.047	2.047	0.987	0.987	0.987	1.023	1.023
No. Frames	210	180	200	200	200	200	200	200	400	480
Tilt speed (°/s)	0.506	0.244	0.244	0.244	0.244	0.506	0.506	0.506	0.244	0.244
Total exposure time (s)	207	372	414	414	414	197	197	197	414	492
Electron dose rate (e/s·Å^2)	0.020	0.020	0.020	0.020	0.020	0.020	0.020	0.020	0.020	0.020
Total, accumulated electron dose (e/Å^2)	4.1	7.4	8.3	8.3	8.3	3.9	3.9	3.9	8.3	9.8
Data Reduction/Software	PETS2.0	PETS2.0	PETS2.0	PETS2.0	PETS2.0	PETS2.0	PETS2.0	PETS2.0	PETS2.0	PETS2.0
Coverage (%)	94	99	99	100	100	100	100	100	100	100
Resolution (Å)	1	0.91	1	0.91	0.83	1.08	0.91	1.1	1.09	1.21
Num. Reflections (unique/all)	500/2280	609/3138	797/2379	1120/3150	1280/4064	890/1968	905/3274	637/1832	792/1898	338/1393
Redundancy	12.146	9.58	9.72	10.43	8.75	10.9	8.53	10.81	10.75	11.62
R_{int} (%)	39.07	34.06	20.59	22.64	21.14	17.99	28.59	29.3	22.37	33.05
Structure Solution Software	JANA2020	JANA2020	JANA2020	JANA2020	JANA2020	JANA2020	JANA2020	JANA2020	JANA2020	JANA2020

5.4. DATA REDUCTION AND FRAMEWORK STRUCTURE SOLUTION

PETS2.0 software was used to process all the 3DED datasets obtained in the previous step, which includes data merging, the peak search, unit cell determination, refinement of optical distortions, geometry optimization of the frame orientation, and intensity extraction. 3DED data from 25 different crystals were acquired. The images of the crystals are shown in **Fig. 80**. 10 datasets out of the 25 were selected based on the resolution and overall quality of the data (R_{int}<40%). For all the 10 different crystals, all the reflections can be indexed as hexagonal unit cell parameters shown in **Table 20** and Laue symmetry 6/mmm was determined based on R_{int} factor (<40 %). The resolution range found for the ten datasets was 0.83-1.21 Å (**Table 20** and **Fig. 81**) with data completeness (<94%).

After processing each of the ten data sets individually, the datasets were merged into a single large data set using PETS2.0 software by transforming the orientation angles of each frame so that it corresponded to a single orientation matrix (see **Table 21**). The reflection intensities showed a good fit with the single-peaked profile associated with a continuous rotation rocking curve as seen in **Fig. 82**. The orientation angles of each pattern concerning the orientation matrix were also refined. The data merging improved the redundancy and total number of reflections, and the merged data set contains 2470 frames. During the final integration of all merged reflection intensities, Laue class 6/mmm was estimated based on R_{int} of 19.13 and the completeness of the merged data is 100%. The global unit cell parameters used for indexing were a = 19.8878 Å, b = 19.8878 Å, c = 20.0371 Å, α = 90°, β = 90°, γ = 120° and the results are shown in **Table 21**. Then a single *hkl* file from all merged datasets was extracted and later used for *ab initio* structure determination.

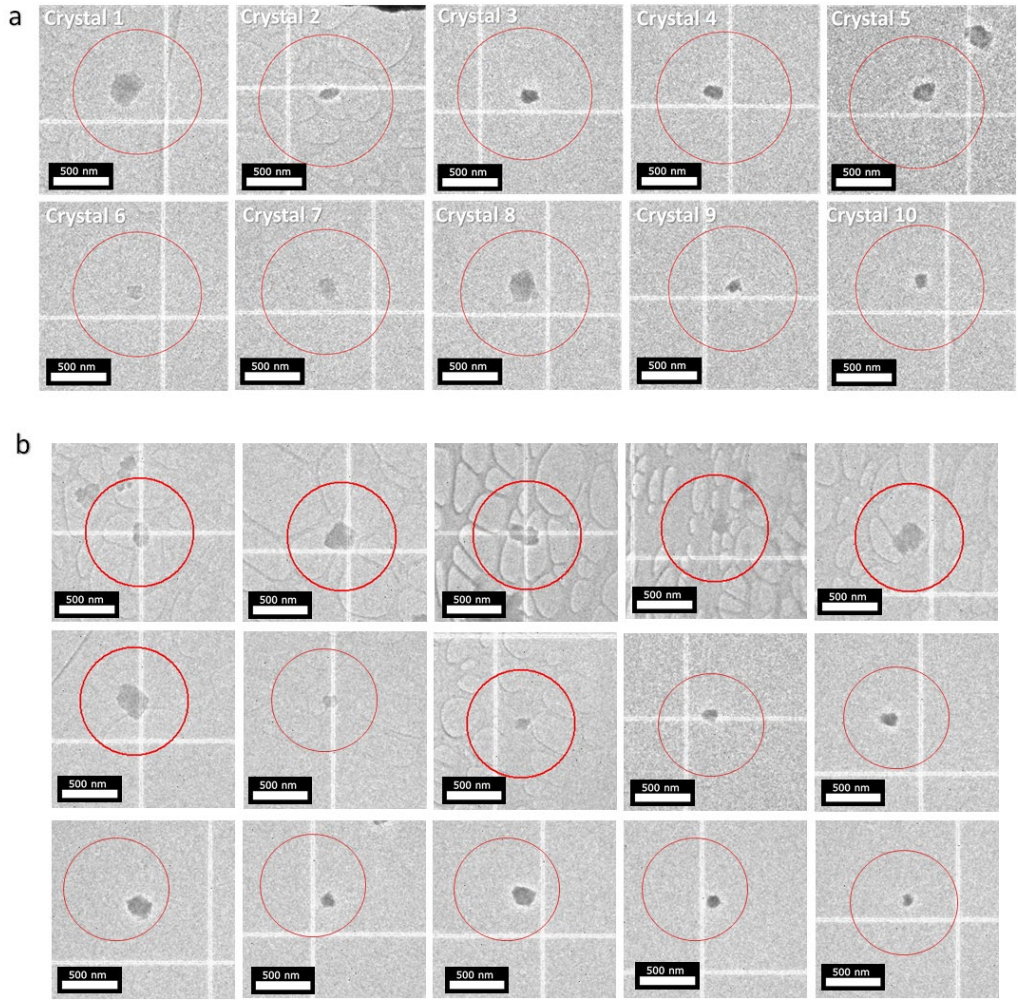

Figure 80. (a) TEM images of the 10 crystals from the as-made ITQ-70 sample that were selected for final data merging and intensity extraction. (b) TEM images of 15 out of 25 crystals that were excluded from ab initio structure determination due to limited resolution and overall data quality (Rint < 40%). The beam size used for imaging had a diameter of 1.6 μm, indicated by the red circle.

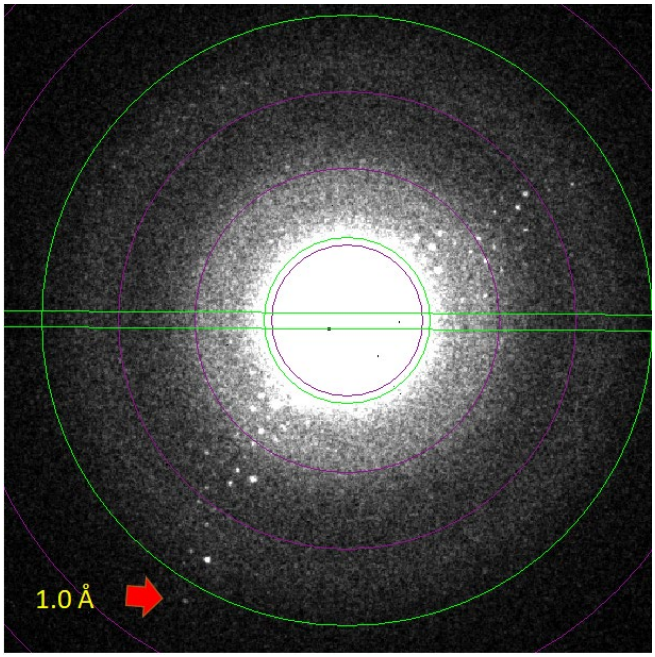

Figure 81. Raw frame displayed in PETS for the ITQ-70 sample at 0.91 Å (1.09 Å reciprocal space).One diffraction pattern from 3DED data of as-made ITQ-70 showing the resolution limit ring in reciprocal space (1.0 Å).

Table 21. Global crystallographic data after merging data from different crystals of as-made ITQ-70 sample.

Crystal system	Hexagonal
Space group (Num.)*	$P6_222$ (180)
***a* (Å)**	19.8878
***b* (Å)**	19.8878
***c* (Å)**	20.0371
Volume (Å³)	6863.4
Z	63
Wavelength (Å)	0.02508
Num. frames	2470
Coverage (%)	100
Resolution (Å)	0.91
R_{int} (%)	19.13
Num. reflections (unique)	1082
Num. reflections (total)	3192
Redundancy	19.95

*Possible space groups: $P6_2$, $P6_4$, $P6_222$, $P6_422$

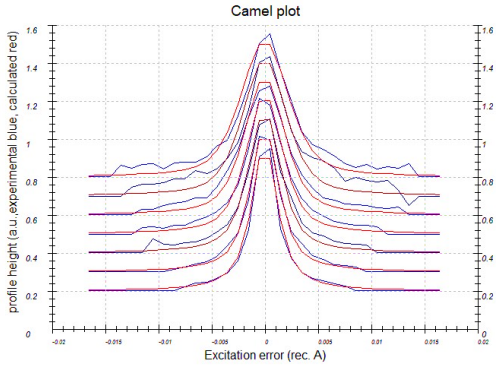

Figure 82. Averaged rocking curves of the strongest reflections across various diffraction data resolution intervals, plotted as a function of the deviation from the ideal Bragg condition (red curves), and fitted with the continuous-rotation single-peaked profile (blue dashed curves) from all 10 merged datasets.

The structure was solved assuming the reflections are kinematic ($I \sim |F_{hkl}|^2$) by the charge flipping algorithm as implemented in the program Superflip[43] interfaced in the crystallography data analysis program Jana2020[74]. The reflection intensities extracted from the global merged dataset were used for *ab initio* structure solution and refinement. Four possible space groups are compatible with the data (the enantiomorphic space groups $P6_222$ and $P6_422$, or $P6_2$ and $P6_4$). These groups, previously proposed from the preliminary indexation using PXRD data, were confirmed by the inspection of the systematic extinctions observed throughout the inspection of 2D sections of reciprocal space from the 3DED merged dataset (**Fig. 83**), as well as by the results in the automated space group search process in Jana2020 based on the *hkl* intensity values. Additionally, during the Jana2020 automated space group search process based on the *hkl* intensity values, the highly symmetric, non-centrosymmetric $P6_222$ and $P6_422$ space groups were selected over $P6_2$ due to their higher symmetry, which results in a lower number of parameters to be determined. Despite multiple attempts using the space group $P6_222$, no reasonable structure was found, as the resulting silicon framework appeared unconnected [resolution cutoff ($\sin\theta/\lambda$) = 0.55 Å, number of runs = 50]. To improve the structure solution, the resolution cutoff ($\sin\theta/\lambda$) was manually reduced to 0.5 Å, and the number of runs was increased to 70. As a result, charge-flipping iterations produced the first acceptable structure model, which consisted of 63 silicon atoms and 138 oxygen atoms within the unit cell, with 6 Si and 12 O atoms in the asymmetric unit. The refinement of the SiO_2 framework was initially processed against 3DED data without the OSDA model inside the voids. The preliminary framework structure, as well as the corresponding electrostatic potential map (difference Fourier map) are shown in **Fig. 84**. The atomic coordinates can be seen in **Table 22**. No further efforts were used in the $P6_422$ group, as both are indistinguishable due to the uncertainties related to dynamical effects during the data collection. A framework density of 9.2 T/1000 Å^3 could be derived beforehand. Accordingly, the five ^{29}Si NMR signals of equal intensity accounts for twelve silicon atoms per unit cell (12 Si/u.c.) each one and the weaker one at -121 ppm accounts for three silicon per the unit cell (3 Si/u.c) making a total of 63 Si/u.c, in good

agreement with the determined structure. This corresponds to 24 Q^3 and 39 Q^4 species per unit cell.

It is worth noting that there are 230 different space groups, categorized based on their symmetry properties into chiral and achiral, also named non-chiral groups. The latter are classified with 22 being Sohncke groups which are a specific subset of three-dimensional space groups in crystallography. They include only symmetry operations of the first kind, such as rotations, and translations. This means they do not include reflections or inversion operations, which would change the handedness (chirality) of the structure Chiral space groups are characterized by containing only proper rotations and translations, corresponding to non-centrosymmetric space groups. In contrast, achiral space groups include one or more improper symmetry operations, such as inversion, mirror, glide, or rotation-reflection operations, aligning them with centrosymmetric space groups. Therefore, the chirality of a specific crystal structure is determined by the symmetry elements present in its space group. However, it is important to recognize that the presence of a non-chiral space group does not necessarily mean the entire crystal structure is achiral, as local chirality may still exist at the molecular level.[119]

The intensity asymmetry of a Bijvoet pair of reflections in a single precession electron-diffraction pattern (reflections from HOLZs) was used to determine the handedness of zeolite nanocrystals.[61] This technique, however, requires collecting an oriented diffraction pattern, which is challenging due to the beam sensitivity of the material. Moreover, the technique uses the same physical effect, namely the dynamical diffraction, that can be used to determine the absolute structure directly from non-oriented 3D ED patterns.[120,60] In principle, we could thus determine the absolute structure from the 3D ED data. Unfortunately, the attempt to run dynamical refinement failed, because the data quality was insufficient and the structure is too

complex.

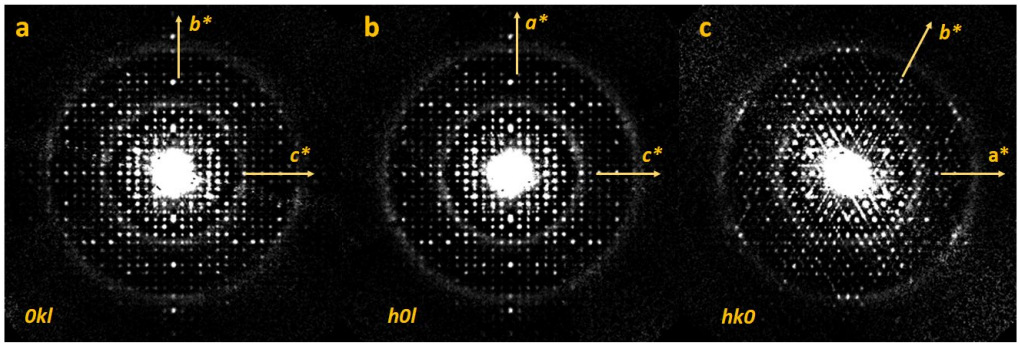

Figure 83. Reconstructed sections of the reciprocal space along 0kl, h0l and hk0 of the as-made zeolite ITQ-70 using global merged 3DED data.

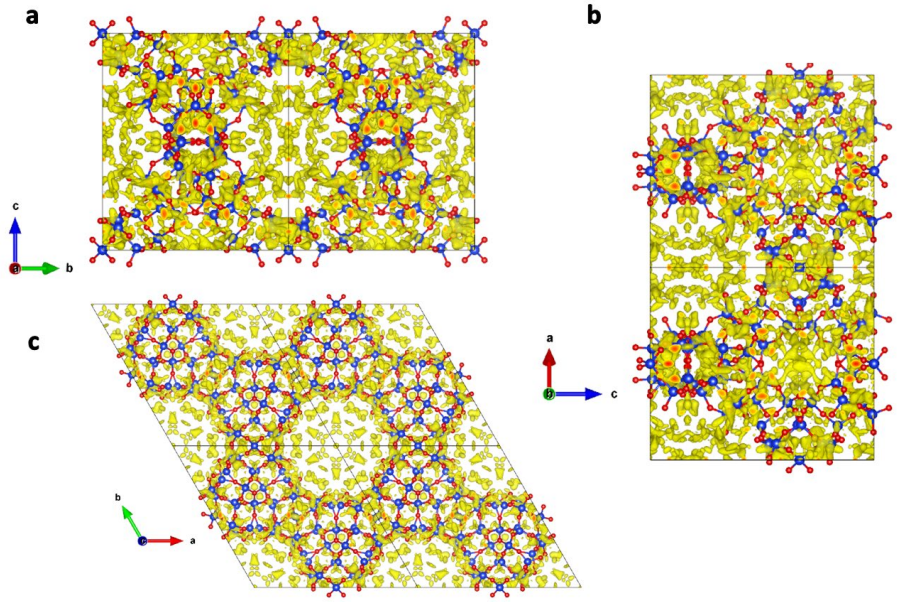

Figure 84. Preliminary framework structure (silicon: blue, oxygen: red) and difference Fourier map (0.15σ positive isosurface: yellow) of as-made ITQ-70 along a, b and c axis.

Table 22. Atomic coordinates of as-synthesized ITQ-70, determined from the ab initio structure solution of the silicon framework using 3D electron diffraction (ED) data.

Atom	Coordinates			Multiplicity & Wyckoff
	x	y	z	
Si1	0.500	0.500	0.333	3c
Si2	0.315	0.399	0.474	12k
Si3	0.704	0.406	0.386	12k
Si4	0.423	0.237	0.327	12k
Si5	0.440	0.353	0.436	12k
Si6	0.599	0.422	0.500	12k
O1	0.630	0.393	0.564	12k
O2	0.288	0.412	0.398	12k
O3	0.361	0.350	0.467	12k
O4	0.664	0.335	0.333	6i
O5	0.415	0.269	0.400	12k
O6	0.510	0.245	0.320	12k
O7	0.355	0.144	0.319	12k
O8	0.636	0.408	0.432	12k
O9	0.503	0.370	0.496	12k
O10	0.236	0.350	0.520	12k
O11	0.627	0.515	0.508	12k
O12	0.479	0.424	0.380	12k

5.5. LOCATION OF OSDA BY SIMULATED ANNEALING

Ab initio structural elucidation of the OSDAs inside the voids directly from 3DED data has been challenging due to possible OSDA disorder.[95,96] The large space generated within the main pore and based on the difference Fourier map, as seen in **Fig. 91**, suggested that the OSDA could be located in this region. For further elucidation of the OSDA molecule's structure, prior chemical information and solid-state ^{29}Si NMR studies were considered. To achieve full charge compensation, the six OSDA cations require six undercoordinated siloxy groups (SiO^-) as identified in the structure solved by 3DED. The two Q^3 signals, assigned to one Si (-100 ppm) and other Si (-97 ppm) sites, correspond to 12 silicon atoms per unit cell. Therefore, in addition to the six SiO^- groups per unit cell, the as-made zeolite ITQ-70 must also contain 18 SiOH groups per unit cell, contributing to a total of 24 Q^3 silicon atoms per unit cell. Additionally, elemental and thermogravimetric analyses indicated the presence of six OSDA molecules per unit cell (**Table 17**). Assuming that the positive charge of the OSDA is counterbalanced by 6 Q^3 SiO^- moieties per unit cell, the 18 remaining Q^3 must be silanol groups (Si-OH), resulting in the final chemical unit cell composition:

$$Si_{63}O_{114}\ (OH)_{18}(O^-)_6[PN_4C_{16}\ H_{40}]^+_6.$$

The organic template's heaviest atom types, P^+ cations, were tentatively assigned to the strongest peaks from the difference Fourier map. Nevertheless, the numerous tests assigning the P atom positions and the refinement of their anisotropic

displacement parameter (ADP) were unsustainable (R factors highly increased: Robs = 40.58 %, wR2all = 81.67 %, R1 = 56 %) collapsing towards the SiO_2 framework.

The ease of locating and refining OSDAs depends on several key factors. A rigid OSDA is generally easier to locate than a flexible one. Additionally, an OSDA that shares symmetry with the framework is simpler to refine than one without any symmetry correlation. Moreover, an OSDA positioned in a region of low symmetry is more easily identifiable than one situated near a symmetry element. To address the challenge of phosphorus cations lacking symmetry elements, we opted to use the classical simulated annealing (SA) structure solution method, implemented in the SIR2019 software.[59]

Starting from 3D models, this approach creates a random sequence of trial structures and then adjusts them until a satisfactory match is achieved between the calculated and experimental data. In the process of structure solution by SA, the system repeats the same loop while progressively lowering the temperature/energy until a satisfactory solution is obtained based on the lowest possible energy. However, a key limitation of SA is that the initial model must contain correct chemical information and connectivity of molecular fragments to arrive at the correct solution. This model can be constructed using available chemical data.

Prior to the SA, the structure of the pure OSDA was determined by single crystal X-ray diffraction (SCXRD). The refined structure is shown in **Fig. 85**. For this procedure, a small amount of tetrakis(diethylamino)phosphonium bromide was dissolved in ethanol and crystalized at room temperature in order to obtain large crystals. Then, a single crystal of 0.19 x 0.11 x 0.10 mm was selected and measured in a Bruker D98 VENTURE PHOTON-III C14 diffractometer using Mo Kalpha radiation, and its structure was solved and refined using SHELXT2018 and SHELXL2018. Details of the structure of the pure OSDA are deposited as a *.cif* file with reference 2379129 and is provided free of charge by the joint Cambridge Crystallographic Data Centre and Fachinformationszentrum Karlsruhe service.

It's crucial to note that during structure determination via SA, the interatomic connectivity, distances, and rigid parts of the molecules remain unchanged. In contrast, rotation, torsion angles, and global shift can be freely modified. For ITQ-70, two independent rigid body descriptions were used during the SA procedure. The first rigid body is the SiO_2 network and the second is the OSDA molecule. Structural connectivity of the silicon network was obtained by ab-initio structure solution from the 3DED data and structural connectivity of the OSDA molecule from the already known single crystal structure of the OSDA molecule. The OSDA molecule started with methylene groups assigned with only carbon atoms (without H atoms) for simplicity. For the SA process some instructions were applied: a resolution cutoff of 1.0 Å was applied using the R factor as a cost function, and a total number of runs was set to 10. Internal and External Degrees of Freedom (INTDIF and EXDOF, respectively) for Si network were fixed whereas, for OSDA, INTDIF and EXDIF were free to move

(degree of freedom includes translational positions (x, y, z), and rotation (θ) and torsional angles); and an anti-bump restraint with weight 1.0 and scale factor on distances 0.7 were activated to avoid close contacts between the Si framework and OSDA molecule. Dynamical occupancy corrections (DOC) were also activated for the OSDA molecule to consider special positions of the OSDA molecule. After the SA process, all the solutions were visibly similar with equal R factors (R-factor = 52.88, 53.92, 53.59, 53.79, 53.55, 53.89, 53.41, 53.16, 76.43, 53.02). In none of the solutions, the Si framework did not collapse with the OSDA molecule. In any case, the first solution with the lowest R factor (52.88) was used for further structural analysis (**Fig. 86b**). Interestingly, during the SA process, the OSDAs were placed in the central cavity whose positions resembled the difference Fourier map obtained by 3DED data before SA, which can be seen in **Fig. 86a** and **b**. At this stage, it was decided to refine against PXRD data instead of 3DED data.

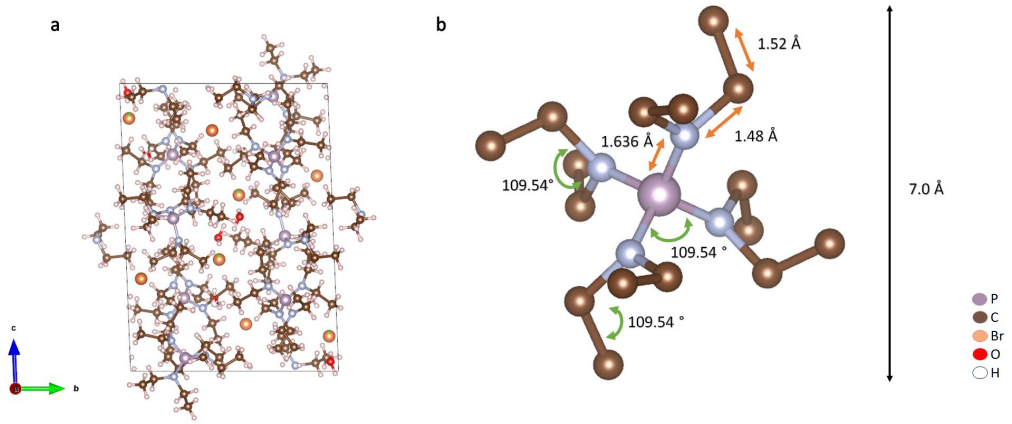

Figure 85. Single-crystal X-ray structure of the OSDA tetrakis(diethylamino)phosphonium cation. (a) View of the unit cell along the designated axis. (b) Isolated OSDA molecule after the removal of hydrogen atoms, water molecules, chloride, bromide, and other extraneous molecules. Distances (in orange) and angles (in green) obtained from the SCRXD analysis are illustrated. Atom labels are as follows: red for oxygen, white for hydrogen, brown for carbon, blue for nitrogen, pink for phosphorus, orange for bromide, and green for chloride.

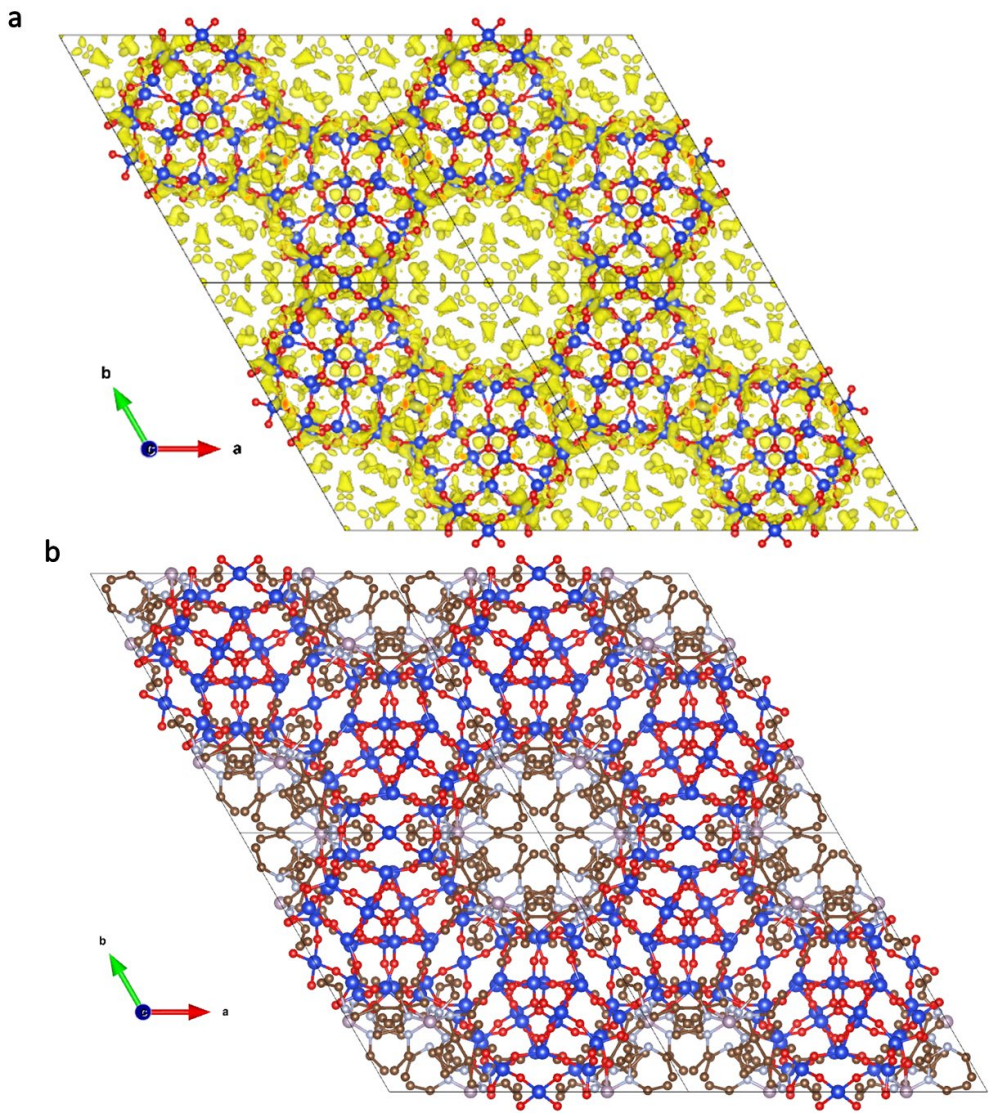

Figure 86. Structure of as-made ITQ-70: (a) Electrostatic potential map as obtained from the merged 3DED data (difference Fourier map) of as-made ITQ-70 along c axis. 0.15σ positive isosurfaces are shown in yellow. Silicon atoms are in blue and oxygen are in red. (b) Structure of ITQ-70 obtained by simulated annealing method viewed along c axis. The OSDA follows the helical geometry of the pore.

The as-made ITQ-70 model obtained was kinematically refined using the merged 3DED dataset with the software JANA2020. For the same atom type, the same isotropic thermal factors for Si, O, and atoms in the OSDA molecule were constrained to be equal. The occupancies corresponding to the OSDA atoms were constrained to be equal to one-half to match the sample's chemical composition. Electrons associated with the H atoms in the methyl and methylene groups were added to the electron density of their corresponding C, accordingly increasing their occupancies (occupancy

0.66 for CH2 and 0.75 for CH3, instead of 0.5). For the siliceous framework, the distance restraints applied were Si-O = 1.620(1) Å and Si-Si = 3.05(1) Å. For the OSDA, the distance restrains were P-N = 1.680(1) Å, N-C = 1.470(1) Å and C-C = 1.530(1) Å. Also, additional restraints for the angles were added: O(Si)O = 109.47(1)°, N(P)N = 109.47(1)°, P(N)C= 119.29(1)°, and N(C)C= 114.20(1)°. These restraints for the OSDA were calculated from the SCXRD data of the pure OSDA. The final refinement converged with the agreement factors R1 = 0.229 for unique 2116 reflections with Fo > 3σ(Fo), Robs = 0.202, wR2 = 0.221, and GooF = 6.95. Details of this refined structure of as-made ITQ-70 are deposited as a .cif file with reference 2386797 that is provided free of charge by the joint Cambridge Crystallographic Data Centre and Fachinformationszentrum Karlsruhe service. These attempts to refine the complete structure using a kinematic approach gave relatively high agreement factors, as well as some too short distances between the zeolitic framework and the atoms of the OSDA. Therefore, a further Rietveld refinement was performed using the PXRD data to confirm and optimize the complete structure of the as-made zeolite.

5.6. COMPUTATIONAL METHOD FOR OSDA LOCATION

The OSDA of ITQ-70 is located in two different but close and symmetry-related positions within the micropores, with each position having an occupancy of ½. The positions of the OSDA molecules identified by zeoTsda were subsequently refined using lattice energy minimization via GULP software,[121,122] resulting in a strong agreement between the experimental positions (obtained by 3DED) and the theoretical predictions as shown in **Fig. 87**. The fractional occupancies in the refined location indicate two possible orientations for each OSDA molecule. The presence of two varied OSDA positions is also supported by the observation of two equally intense ^{31}P NMR resonances in the spectrum of ITQ-70, as seen previously in **Fig. 68A**. The calculated van der Waals interaction energy for each OSDA molecule, performed without symmetry on a P1 cell, ranged from -70 to -82 kJ/mol, indicating that all OSDAs occupy stable locations within the structure. More details of the optimized atomic positions and refinement process is described in the Supporting Information section of the corresponding report.[106]

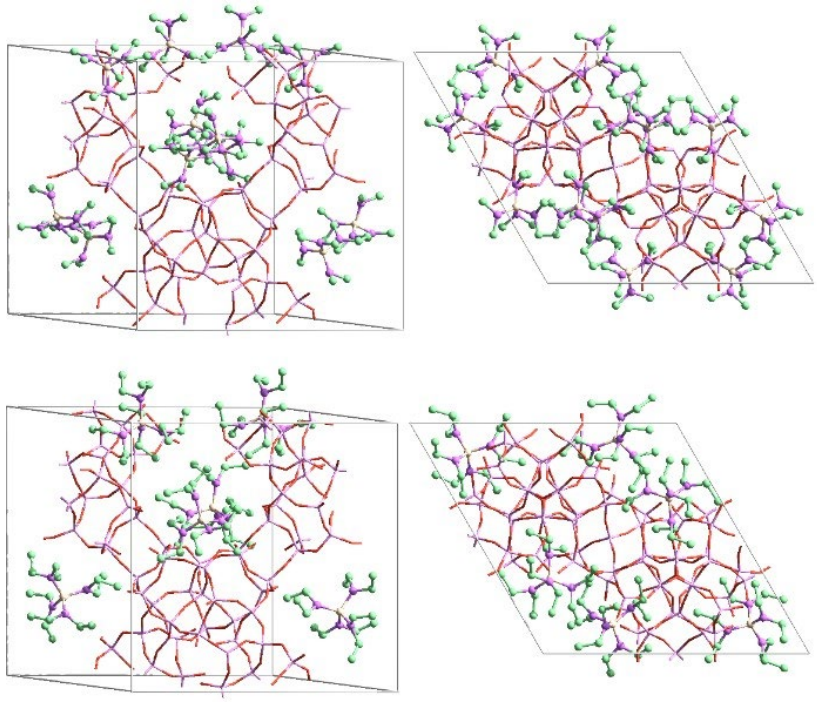

Figure 87. Experimental structure (top) and computational (bottom) views of the location of OSDA molecules (balls and sticks) in ITQ-70 (sticks).

***Dynamical Refinement Against 3DED**

The dynamical refinement of the ITQ-70 structure with the OSDA molecule, as obtained through computational methods, was not attempted. This decision was based on the frequent lack of convergence in kinematical refinement using 3DED data, with continuous change into negative thermal parameters, instable SDA positions, and occupancy. These might indicate inconsistent refinement of resulting models and could be attributed to the lack of information and low resolution of the 3DED data.

5.7. REFINEMENT AGAINST POWDER XRD DATA

The as-synthetized ITQ-70 starting model obtained by simulated annealing was refined against PXRD data by Rietveld refinement using the software FULLPROF. Some constraints and restraints were first applied to indirectly improve the data-to-parameter ratio. The same isotropic thermal factors for the same atom type, (a) Si, (b) O and (c) atoms in the OSDA molecule, were constrained. Due to instabilities in the refinement probably due to the large number of parameters and the mobility of the OSDA molecules, the isotropic thermal factors of O were not refined. The fractional occupancy factor corresponding to the OSDA atoms was constrained to be equal to one-half to match the chemical composition of the sample. Electrons corresponding to the H atoms in the methyl and methylene groups were then added to the electron density of their corresponding C, increasing their occupancies accordingly (occupancy 0.66 for CH_2 and 0.75 for CH_3, instead of 0.5).

For the siliceous framework the distance restrains were Si-O = 1.610(5) Å. As OSDA atoms were treated as rigid bodies in JANA, instead of using 3N atom coordinate parameters for each atom, only three translational parameters for the whole group were employed. For the OSDA, the distance restraints were P-N = 1.64(1) Å, N-C = 1.48(1) Å and C-C = 1.52(1) Å. Also, additional restraints for the angles were added in the form of distances between second neighbors: O(Si)O = 2.63(1) Å, N(P)N = 2.65(1) Å, P(N)C= 2.72(1) Å, N(C)C= 2.45(1) Å and C(N)C= 2.50(1) Å. These restraints for the OSDA were calculated from the SCXRD data of the pure OSDA. The number of profile parameters refined were eleven. After several attempts, the refinement led to OSDA molecules positioning along the main cavity in a helicoidal way around the silicon framework as shown in **Fig. 88.** The final refinement converged with the residual factors R_{wp} = 19.4, R_{exp} = 8.48, R_B = 9.80 and R_F = 5.50. The crystallographic data from the structure refinement are provided in **Table 23**, while. the atomic coordinates of the refined structure based on PXRD are detailed in **Table 24**. The Rietveld refinement plot is shown in **Fig. 89.**

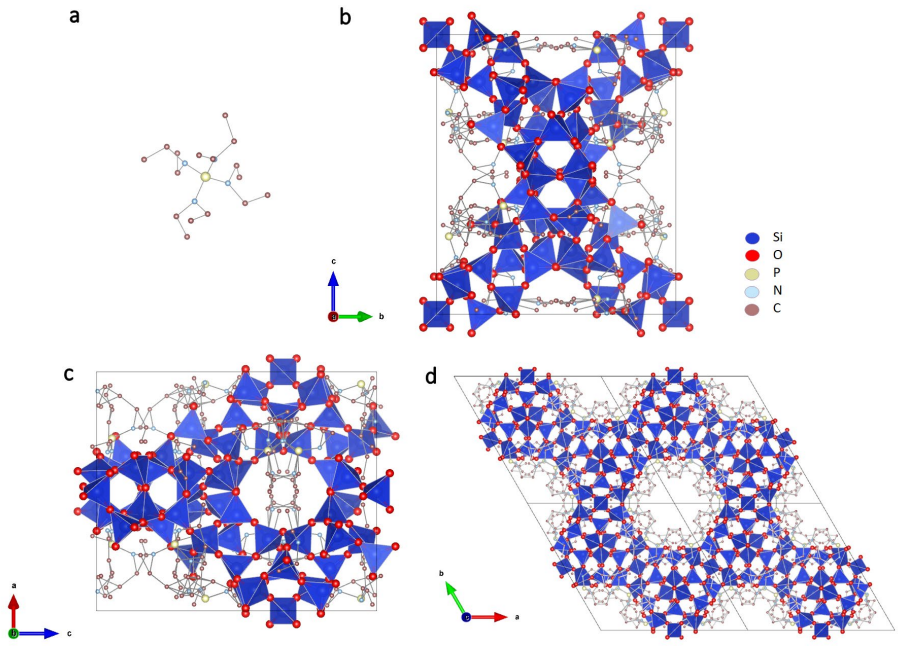

Figure 88. Structure of (a) organic structure directing agent and (b) as-made ITQ-70 structure refined against PXRD data. Views along a (b), b (c) and c (d). Blue tetrahedra: framework SiO_2, yellow: P, light blue: N, brown: C.

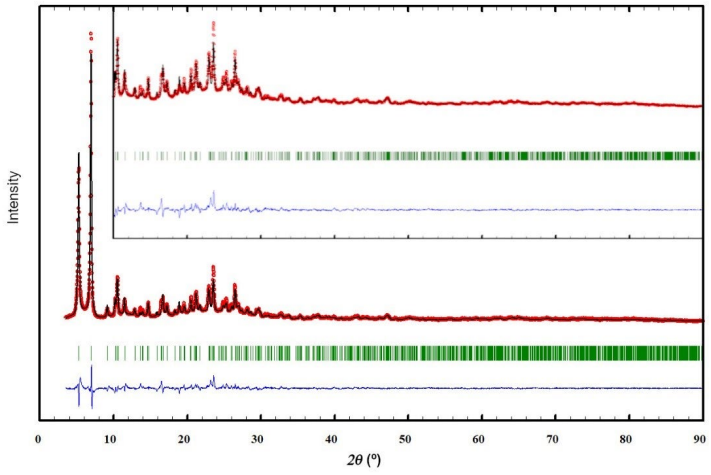

Figure 89. Rietveld refinement using PXRD of as-made ITQ-70. Red: Observed pattern; black: calculated pattern; blue: the difference between observed and calculated; green: positions of the Bragg reflections. Cu Kα radiation (λ = 1.5406 Å)

Table 23. Crystallographic data of structure refinement using PXRD data on as-made ITQ-70.

Crystal system	Hexagonal
Chemical composition (refined)	Si_{63} O_{138} P_6 N_{24} C_{136}
Chemical composition (expected)	Si_{63} O_{138} P_6 N_{24} C_{96} H_{258}
Space group	$P6_222$ #180
***a, b* (Å)**	19.295(2)
***c* (Å)**	19.508(3)
Volume (Å^3)	6289.7(14)
Z	1
2θ range (°) refined	3.5 to 90.0
Wavelength (Å)	1.54060
Nun. total reflections	2320
Num. geometric restrains	104
Distance Si-O (Å)	23
Distance P-N (Å)	4
Distance N-C (Å)	8
Distance C-C (Å)	8
Distance O(Si)**O (Å)**	35
Distance N(P)**N (Å)**	6
Distance P(N)**C (Å)**	8
Distance N(C)**C (Å)**	8
Distance C(N)**C (Å)**	4
Nun. structural parameters refined	112
Num. profile parameters refined	11
R_{wp}	19.4
R_{exp}	8.48
R_B	9.80
R_F	5.50

Numbers in parentheses are the esd's in the units of the least significant digit given.

Table 24. Atomic coordinates for as-made ITQ-70 after the refinement against PXRD data.

Atom	Atom coordinates			Uiso	Occupancy	Multiplicity & Wyckoff
	x	y	z			
Si1	1/2	1/2	1/3	0.01267	1	3c
Si2	0.3063(2)	0.3913(3)	0.4708(2)	0.01267	1	12k
Si3	0.7044(2)	0.4050(2)	0.38742(20)	0.01267	1	12k
Si4	0.4203(3)	0.2336(3)	0.3304(2)	0.01267	1	12k
Si5	0.4419(3)	0.3530(2)	0.4366(2)	0.01267	1	12k
Si6	0.6016(3)	0.4239(2)	0.5037(2)	0.01267	1	12k
O1	0.6235(3)	0.3995(5)	0.5755(3)	0.01900	1	12k
O2	0.2716(5)	0.3928(5)	0.3962(3)	0.01900	1	12k
O3	0.3621(4)	0.3508(5)	0.4663(4)	0.01900	1	12k
O4	0.66710(19)	0.33290(19)	1/3	0.01900	1	6i
O5	0.4156(5)	0.2674(3)	0.4042(3)	0.01900	1	12k
O6	0.5117(2)	0.2579(5)	0.3191(4)	0.01900	1	12k
OH7	0.3653(4)	0.1379(2)	0.3301(7)	0.01900	1	12k
O8	0.6380(4)	0.3971(5)	0.4411(4)	0.01900	1	12k
O9	0.5059(2)	0.3760(5)	0.4974(3)	0.01900	1	12k
OH10	0.2331(5)	0.3388(7)	0.5221(5)	0.01900	1	12k
O11	0.6396(5)	0.5195(2)	0.5011(4)	0.01900	1	12k
O12	0.4798(4)	0.4232(3)	0.3799(3)	0.01900	1	12k
P1	0.0724(3)	0.7561(3)	0.3784(3)	0.02533	0.5	12k
N1	0.1243(4)	0.8408(4)	0.3374(5)	0.02533	0.5	12k
N2	0.0655(4)	0.7753(5)	0.4584(3)	0.02533	0.5	12k
N3	-0.0169(3)	0.7053(5)	0.3449(4)	0.02533	0.5	12k
N4	0.1172(6)	0.7041(5)	0.3699(3)	0.02533	0.5	12k
C1	0.2002(5)	0.8596(5)	0.3026(9)	0.02533	0.666	12k
C2	0.2663(11)	0.9433(14)	0.321(3)	0.02533	0.75	12k
C3	0.0900(9)	0.8917(8)	0.3186(6)	0.02533	0.666	12k
C4	0.076(4)	0.928(4)	0.3827(10)	0.02533	0.75	12k
C5	-0.0136(14)	0.7301(13)	0.4945(14)	0.02533	0.666	12k
C6	-0.0147(19)	0.780(2)	0.555(2)	0.02533	0.75	12k
C7	0.1155(6)	0.8589(5)	0.4855(6)	0.02533	0.666	12k
C8	0.178(2)	0.8611(14)	0.535(2)	0.02533	0.75	12k
C9	-0.0900(5)	0.6740(9)	0.3877(5)	0.02533	0.666	12k
C10	-0.1429(8)	0.7059(9)	0.3621(11)	0.02533	0.75	12k
C11	-0.0291(8)	0.6560(7)	0.2817(4)	0.02533	0.666	12k
C12	-0.007(4)	0.593(3)	0.2973(14)	0.02533	0.75	12k
C13	0.1334(15)	0.6649(10)	0.4271(4)	0.02533	0.666	12k
C14	0.123(3)	0.5844(16)	0.4058(14)	0.02533	0.75	12k
C15	0.1479(7)	0.6968(6)	0.3018(4)	0.02533	0.666	12k
C16	0.089(2)	0.6172(19)	0.2689(17)	0.02533	0.75	12k

Numbers in parentheses are the esd's in the units of the least significant digit given. (a) Parameters without an esd were not refined. Coordinates equal to 1/2 or 1/3 are fixed by symmetry. Electrons corresponding to H have been included into the occupancy of their corresponding atoms of C.

5.8. STRUCTURE DESCRIPTION

With the zeolitic framework and the OSDA structures determined by 3DED and refined by PXRD, we can now describe how the zeolitic framework is constructed and how the OSDA is incorporated within it. The structure of ITQ-70 can be firstly constructed based on a $[4^2 5^2 6^2]$ unit (**Fig. 90a**). These units interconnect by sharing the Si1 site and linking their respective Si2 and Si5 sites through four O3 bridging atoms, as shown in **Fig. 90b**. This results in the formation of a $[4^4\ 5^4\ 6^4]$ cage with an additional silicon atom (Si1) located centrally (**Fig. 90c**). The central Si1 is bonded to four neighboring Si5 sites, leading to highly strained Si-O-Si angles of 163.5(4)º. This significant strain is reflected in the high-field resonance observed at -121 ppm in the ^{29}Si-NMR spectrum. Computational analysis, confirms that both Si1 and Si5 sites experience substantial strain in the Si1-O12-Si5 angles, as shown in **Table 25**. The strain analysis, using atomic coordinates from the experimentally determined unit cell and the methodology from a previous study,[122] employed the Vessal, Leslie, and Catlow force field, which is well-suited for accurately modeling the energetics of O-Si-O and Si-O-Si angles due to its double exponential functions.[123] **Table 26** indicates that several Si-O-Si angles are notably strained, including Si4-O2-Si2 (158.2° and 0.21 kcal/mol), Si1-O12-Si5 (163.4° and 0.29 kcal/mol), Si3-O6-Si4 (156.0° and 0.16 kcal/mol), Si3-O8-Si6 (156.6° and 0.16 kcal/mol), and Si6-O11-Si2 (156.2° and 0.15 kcal/mol). Given that n-rings can be broken down into 2×n Si-O bonds, n O-Si-O angles, and n Si-O-Si angles, the strain associated with each ring in the ITQ-70 structure can also be calculated. **Fig. 91** highlights the small cavity with one of the strained 5-rings (left) and one of the strained 6-rings (right). Both rings are indicated as yellow and blue colored balls. These rings are located within the small $[4^4\ 5^4\ 6^4]$ cavity, although the 6 rings are identified based on vertex symbols rather than their association with polyhedra. The high density of atoms in the $[4^4\ 5^4\ 6^4]$ cavity means that the most strained Si-O-Si angle (Si1-O12-Si5) is present twice in each of these highly strained rings. A comparison between the experimental and refined structures is provided in previous **Fig. 87**. The structural dimensions of the refined ITQ-70 have been further analyzed using ZeoTsites, a specialized program developed at ITQ that operates in Fortran77.[124] This program provides detailed output on TO and TT distances, TOT and OTO angles, and T atom connectivity. Additionally, it generates histograms of average T-O-T angles for different n-rings within the network. The resulting data can be found in **Tables 25, 26, 27 and 28**. Some topological properties of ITQ-70 (coordination sequences and vertex symbols) were calculated using the latest version (1.2.8.0) of zeoTsites,[125] and are provided in **Table 29**.

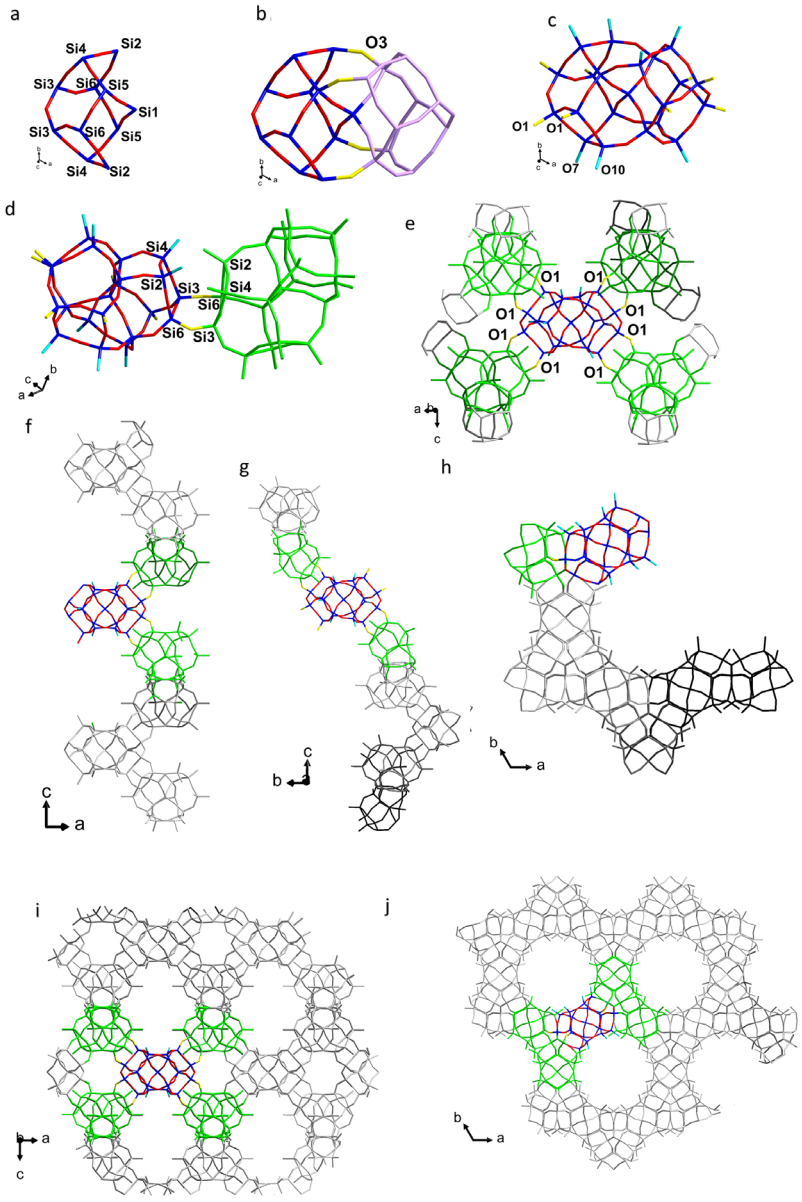

Figure 90. Graphic description of the structure of the as-made zeolite ITQ-70. (a) Basic $[4^2 5^2 6^2]$ unit. (b) $[4^4 5^4 6^4]$ cage containing the interstitial Si1 atom. (c) Terminal oxygens of the $[4^4 5^4 6^4]$ cage. (d) Connection of two $[4^4 5^4 6^4]$ cages forming a frustrated D4R unit. (e) Connectivity of the $[4^4 5^4 6^4]$ cage with four adjacent cages. (f) Helicoidal chain of $[4^4 5^4 6^4]$ cages connecting through the same $[4^2 5^2 6^2]$ unit. (g) Helicoidal chain of [445464] cages connecting through opposite $[4^2 5^2 6^2]$ units view along a. (h) Helicoidal chain of $[4^4 5^4 6^4]$ cages connecting through opposite $[4^2 5^2 6^2]$ units view along c. (i) ITQ-70 complete framework view along b. (j) ITQ-70 complete framework view along c. Blue: silicon; red: oxygen; yellow: linking O atoms; light blue: SiOH/SiO- oxygen atoms; pink: second $[4^2 5^2 6^2]$ unit in the cage; light green: adjacent cages; grey: additional cages forming the complete zeolitic structure.

Table 25. Refined Si-O-Si angles (°) in the zeolitic framework.

Si–O-Si	Angle (°)
Si6-O1-Si3	138.2(5)
Si4-O2-Si2	158.2(5)
Si2-O3-Si5	149.0(7)
Si3-O4-Si3	137.4(2)
Si5-O5-Si4	136.4(4)
Si3-O6-Si4	156.0(5)
Si3-O8-Si6	156.6(6)
Si6-O9-Si5	136.1(5)
Si6-O11-Si2	156.2(3)
Si1-O12-Si5	163.5(4)

Table 26. Strain (kJ/mol) due to each Si-O-Si angle of ITQ-70. Rings associated to each Si-O-Si and average structural data of each Si are also included. Data obtained using the experimental coordinates and force field by Vessal, Leslie and Catlow.[123]

T-O-T-label	T-O-T	TOT-Strain/O-atom	Number	Total TOT-Strain
Si3-O1-Si6	138.2	0.06	12	0.70
Si2-O2-Si4	158.2	0.21	12	2.51
Si2-O3-Si5	149.0	0.03	12	0.35
Si3-O4-Si3	137.4	0.07	12	0.43
Si4-O5-Si5	136.4	0.11	6	1.31
Si3-O6-Si4	156.0	0.16	12	1.86
Si3-O8-Si6	156.6	0.16	12	1.88
Si5-O9-Si6	136.1	0.11	12	1.38
Si2-O11-Si6	156.2	0.15	12	1.76
Si1-O12-Si5	163.4	0.29	12	3.46

Table 27. Ring sizes associated to the different Si-O-Si angles of ITQ-70.

Si-O-Si-labels	Ring size (multiplicity)
Si1-O12-Si5	5 (7) 6 (2)
Si2-O2-Si4	4 (1) 5 (2)
Si2-O3-Si5	5 (3) 18 (13)
Si2-O11-Si6	4 (1) 5 (1) 18 (13)
Si3-O4-Si3	5 (2) 18 (53)
Si3-O8-Si6	4 (2) 5 (1) 6 (1) 18 (13)
Si3-O1-Si6	4 (1) 18 (40)
Si3-O6-Si4	4 (1) 5 (1) 6 (1)
Si4-O5-Si5	5 (3) 6 (1)
Si5-O9-Si6	5 (3) 6 (1) 18 (13)

Table 28. Angles (°) and distances (Å) associated to the different Si-sites of ITQ-70.

T-label	O-T-O	T-O-T	T-O	T-T	Number
Si1	109.48	163.5	1.611	3.191	3
Si2	109.46	154.5	1.613	3.145	12
Si3	109.44	147.0	1.602	3.065	12
Si4	109.46	150.2	1.601	3.082	12
Si5	109.45	146.2	1.610	3.066	12
Si6	109.47	146.8	1.608	3.070	12

Table 29. Coordination sequences and vertex symbols of atoms in ITQ-70.

atom label	coordination sequence															number	vertex symbol
Si1	4	12	8	12	24	32	44	48	56	82	104	124	140	156	216	3	$5_2{\cdot}5_2{\cdot}5_2{\cdot}5_2{\cdot}6_2{\cdot}6_2$
Si2	3	7	12	15	21	32	40	44	59	85	103	121	130	166	223	12	4·*·5·*·5·*
Si3	4	9	14	19	20	25	41	57	74	84	91	120	157	195	214	12	$4{\cdot}5{\cdot}4{\cdot}18_{24}{\cdot}5{\cdot}*$
Si4	3	7	12	16	21	29	37	53	65	77	98	113	148	179	205	12	4·*·5·*·5·*
Si5	4	10	11	14	23	33	39	48	65	84	103	121	140	176	219	12	$5{\cdot}*{\cdot}5{\cdot}5_2{\cdot}5{\cdot}18_8$
Si6	4	9	14	16	22	30	37	54	71	84	100	115	150	185	221	12	$4{\cdot}5{\cdot}4{\cdot}18_8{\cdot}5{\cdot}18_8$

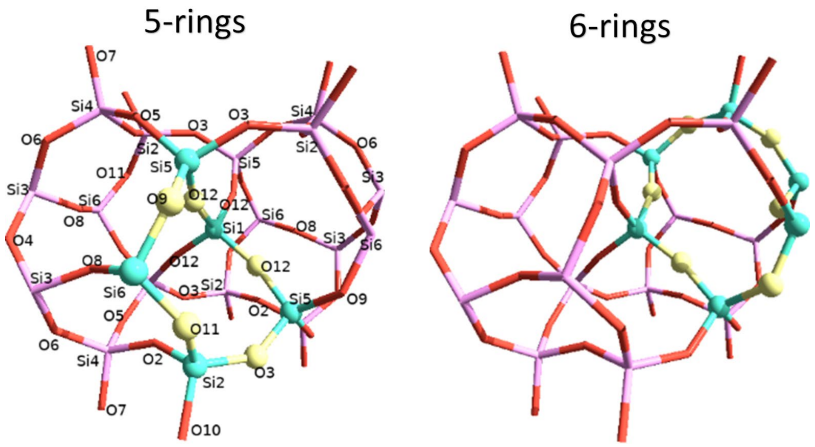

Figure 91. Small cavity [$4^4 5^4 6^4$] with a central atom of ITQ-70 highlighting (in balls and sticks format) two of the most strained 5-rings (left) and 6-rings (right).

The framework of ITQ-70 extends into a three-dimensional network due to the presence of four pairs of O1 atoms per cage, which link to four adjacent cages (**Fig. 90e**). This results in each cage, or [$4^4 5^4 6^4$] unit, forming a helicoidal chain along the c-axis (**Fig. 97f**). Considering the connectivity of opposite cage sites, a broader helicoidal chain along the c-axis is also formed (**Fig. 90g** and **Fig. 90h**), creating a gyroidal structure. This structure features 18-ring channels in the *ab* plane with a pore diameter of 10.8 Å (**Fig. 90i**) and additional 18-ring openings along the *c*-axis with a diameter of 11.0 Å (**Fig. 90j**). These intersecting channels result in large voids within

the structure, making ITQ-70, with a framework density of 10.0 T/1000 Å^3, the zeolite with the lowest reported density of oxygen-connecting T-atoms.

To confirm the silicon site connectivity, a 2D Double Quantum-Single Quantum (DQ-SQ) ^{29}Si MAS NMR spectrum was recorded, as previously seen in **Fig. 76**. Comparing the 2D DQ-SQ ^{29}Si NMR results with Si-Si connections derived from ED and powder XRD techniques allowed for accurate assignment of the ^{29}Si NMR signals to sites Si1-Si6 (**Table 19**). All ^{29}Si-NMR signals align perfectly with structural Si sites in ITQ-70, together with the results obtained from ED and X-ray diffraction.

Further insight into the distribution of silanol groups among the two separate underconnected Si species was obtained through ^{1}H-NMR experiments. The ^{1}H NMR spectrum of the as-synthesized zeolite ITQ-70 (**Fig. 92a**) shows two narrow peaks at 1.7 ppm and 3.5 ppm, corresponding to the hydrogen atoms of the OSDA cation. Additionally, two broader peaks at 8 ppm and 16 ppm, with a 2:1 intensity ratio, are attributed to SiOH groups. Given that ITQ-70 contains 18 SiOH groups per unit cell, these signals represent two different sites: one with 12 SiOH groups and the other with 6 SiOH groups per unit cell. As mentioned earlier, full charge compensation must be achieved. Based on the ^{29}Si MAS NMR spectrum, the two Q_3 signals, corresponding to the Si2 (-100 ppm) and Si4 (-97 ppm) sites, account for 12 Si atoms per unit cell. Thus, in addition to the 6 SiO^- per unit cell, the as-made zeolite ITQ-70 must contain 18 SiOH groups per unit cell, contributing to a total of 24 Q_3 Si atoms per unit cell. This corresponds to a Q_3 connectivity defect percentage of 38%, as indicated by the ^{29}Si-NMR data. This is consistent with the Q_3/Q_4 ratio calculated from the 3DED-derived structure, where 27 out of 63 Si atoms per unit cell (43%) are Si (OH/O^-) species (**Fig. 93**).

A 2D ^{1}H-^{29}Si heteronuclear correlation NMR spectrum (**Fig. 92b**) was used to assign the ^{1}H NMR signals to the Si-OH groups at Si2 and Si4 sites. The signal at δ ^{1}H = 16 ppm (6 SiOH/u.c.) exclusively correlates with Si2. In contrast, the signal at δ ^{1}H = 8 ppm (12 SiOH/u.c.) shows a cross peak with Si4 and a weaker correlation with Si2. This indicates that Si2 sites contain 6 Si-OH and 6 Si-O^-, while Si4 sites have 12 Si-OH.

A notable observation is that each pair of Si2 sites has one negatively charged group (SiO^-) and one protonated group (SiOH), producing a high chemical shift (δ^1H = 16 ppm) suggests strong hydrogen bonding. In the ITQ-70 structure, the O–O distance between two adjacent O10 atoms bonded to Si2 is very short, just 2.2 Å (**Fig. 102**). Although these Si2 sites are formally Si-O^- and Si-OH, the short O–O distance and strong hydrogen bonding suggest that the H and the negative charge are shared between the two O10 atoms rather than being localized on each atom. This model, represented as Si$O^{\delta-}$–H–$O^{\delta-}$Si, is supported by the high ^{1}H NMR chemical shift and the exclusive correlation of the 16 ppm resonance with the Si2 sites in the ^{29}Si NMR. Meanwhile, the ^{1}H NMR signals at 8 ppm from SiOH at Si4 also show a weaker cross peak with the ^{29}Si NMR signal of the Si2 sites, which can be explained

by the relatively short O-O distance of 2.75 Å between the O7 atom bonded to Si4 and the O10 atom (**Fig. 94**).

The local structure involving the Q_3 Si2 and Si4 sites in ITQ-70 is consistent with previous studies on defects in as-made zeolites. Similar interactions between silanol groups and SiO^- groups have been observed in high-silica ZSM-12, ZSM-5, SSZ-24, and SSZ-74 zeolites.[126,127] Their ^1H NMR spectra of all of them show a signal near 10 ppm attributed to SiOH···OSi hydrogen bonds with an O–O distance of 2.70 Å. In ZSM-5, SSZ-24, and SSZ-74, a second signal near 12 ppm is associated with distinct crystallographic sites with a slightly shorter O–O distance of 2.62 Å. Therefore, the unusually short O10–O10 distance in ITQ-70 aligns with the exceptional low field shift of the ^1H resonance in hydrogen-bonded $SiO^{\delta-}–H–O^{\delta-}Si$.

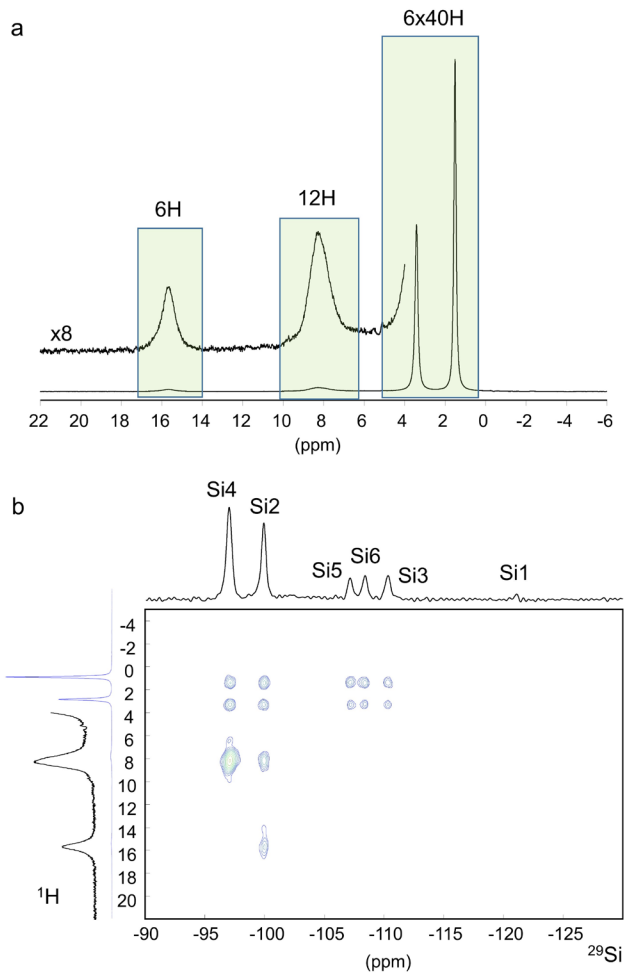

Figure 92. (a) ^{1}H-MAS- NMR of as-made zeolite ITQ-70; (b) 2D ^{1}H-^{29}Si heteronuclear chemical shift correlation (HETCOR) NMR of as-made zeolite ITQ-70.

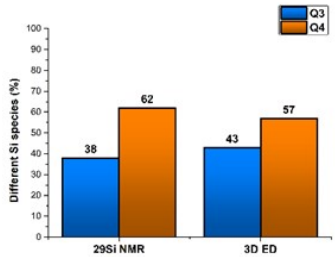

Figure 93. The compositions of different Si species, specifically Q^3 and Q^4, were identified using solid-state ^{29}Si NMR (left) and 3DED (right).

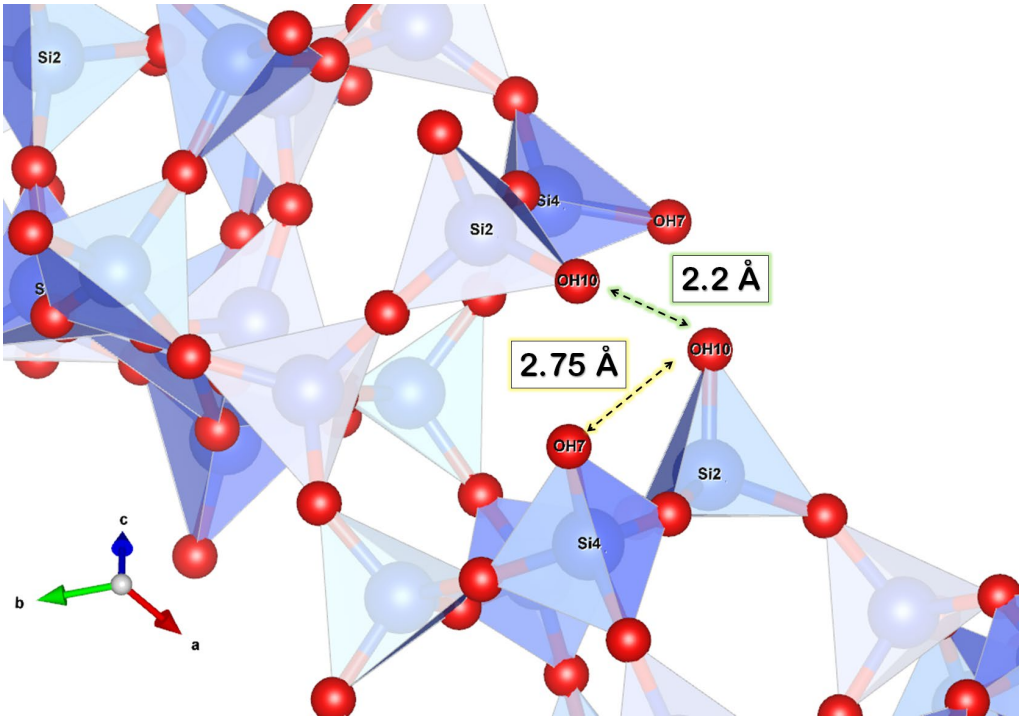

Figure 94. O-O distances in a section of the zeolite ITQ-70 viewed along the [111] axis. The inorganic silica framework is shown using blue tetrahedra, with oxygen atoms in red balls and silicon atoms in blue balls. The green arrow indicates the distance between two adjacent O10 atoms bonded to Si2 (2.2 Å), while the yellow arrow highlights the distance between the O7 atom, bonded to Si4, and the O10 atom (2.75 Å).

Appendix I presents a summary of the data acquisition, reduction, and refinement processes described in Chapter 5.

CHAPTER 6. STRUCTURE DETERMINATION OF AS-MADE ITQ-35 ZEOLITE

6.1. SYNTHESIS, CHEMICAL, THERMOGRAVIMETRIC, AND TEXTURAL ANALYSIS

This chapter presents the synthesis, characterization, and structure determination of a new as-made zeolite structure ITQ-35 combining 3DED, NMR, and PXRD techniques, among others. This compound was synthesized as a pure germanate form with the chemical composition of GeO_2 using a large cationic nitrogen-based OSDA that was previously synthesized by a photochemistry reaction of 2+2 cycloaddition. The di-tetraalkylammonium dication, employed as SDA, is a pyrrole compound named 2,2,3a,3b,5,5,6a,6b-octamethyldecahydrocyclobuta[1,2-c:3,4-c']dipyrrole-2,5-diium which was synthesized throughout a photochemically induced [2 + 2] cycloaddition reaction followed by a reduction reaction. The SDA used to synthesize pure Ge zeolite ITQ-35 is shown below in **Fig. 95**. The obtained SDA was further analyzed by ^{13}C-NMR supporting the stability of the desired pyrrole structure after its synthesis.

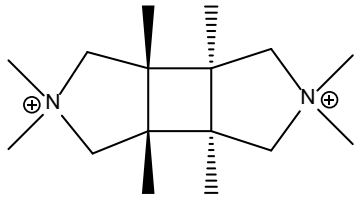

Figure 95. Structure of the 2,2,3a,3b,5,5,6a,6b-octamethyldecahydrocyclobuta[1,2-c:3,4-c']dipyrrole-2,5-diium used as SDA for zeolite Ge-ITQ-35.

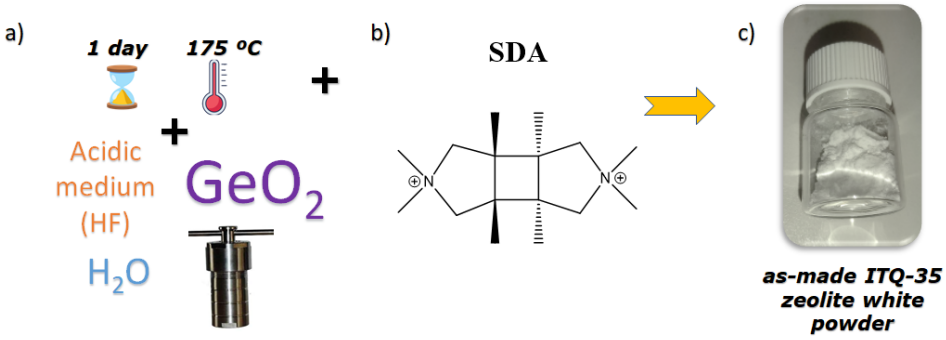

Figure 96. Schematic of the hydrothermal synthesis process: (a) Experimental conditions: Ge source, fluorine as a mobilizing agent, 1-day reaction time at 175°C. (b) Chemical structure of the di-tetraalkylammonium dication used as the OSDA in the synthesis. (c) Final product: zeolite ITQ-35 powder in its as-made form.

The new as-made zeolite ITQ-35 has been obtained with the di-tetraalkylammonium dication as OSDA in fluoride media from a gel of the following composition:

- GeO_2
- 0.25 $OSDA(OH)_2$
- 0.5 HF
- 7 H_2O

The synthesis was conducted hydrothermally in a Teflon-lined stainless-steel autoclave and heated at 175°C for one day, as shown in **Fig. 96**.

The synthesis resulted in a white, solid crystalline phase, confirmed by Powder X-ray Diffraction (PXRD) analysis. **Fig. 97** shows the diffraction pattern of the pure as-synthesized ITQ-35 phase.

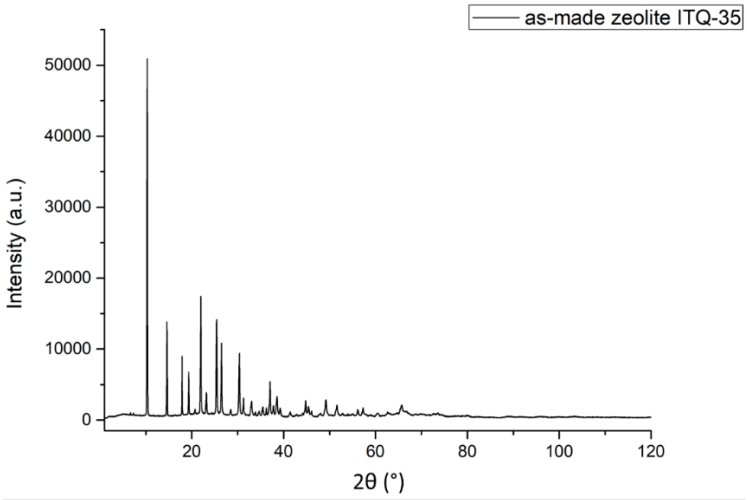

Figure 97. Powder XRD pattern of as-made zeolite ITQ-35.

Elemental analysis of nitrogen, carbon, and hydrogen (N, C, H) content reveals a C/N ratio in the final as-made ITQ-35 close to 7, aligning with the theoretical C/N ratio. This suggests that the organic molecules remain largely intact within the zeolite pores (see **Table 30**). This conclusion is further supported by ^{13}C MAS NMR spectroscopy (see **Fig. 98**), which shows four peaks, confirming that the SDA molecules are indeed preserved inside the zeolite structure.

Table 30. Elemental analysis of selected as-made ITQ-35 sample.

Theoretical C/N ratio	Experimental weight contents (wt%)		Experimental Molar Ratios
	C	N	C/N ratio
8	14.33	2.08	6.9

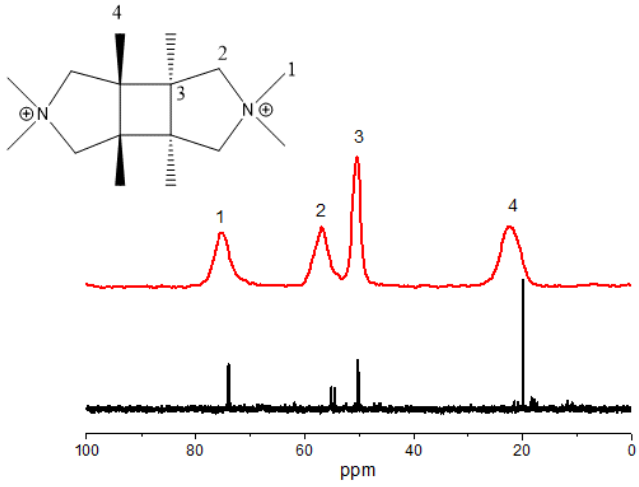

Figure 98. ^{13}C MAS NMR spectra of SDA (bottom) and as-made zeolite ITQ-35 prepared with SDA (top). The SDA spectrum (bottom) in its iodide was obtained in D_2O solution.

Thermogravimetric (TG) analysis revealed a weight loss of 16.73% between 200 and 700 °C, indicating the decomposition of the occluded OSDA and suggesting an open framework (**Fig. 99**). The observed weight loss aligns closely with the sum of the C and N percentages obtained from elemental analysis [14.33% + 2.08% =

16.41%] (see **Table 30**). However, the weight increased between 700°C and 800°C is more challenging to interpret, possibly linked to the oxidation of Ge species.

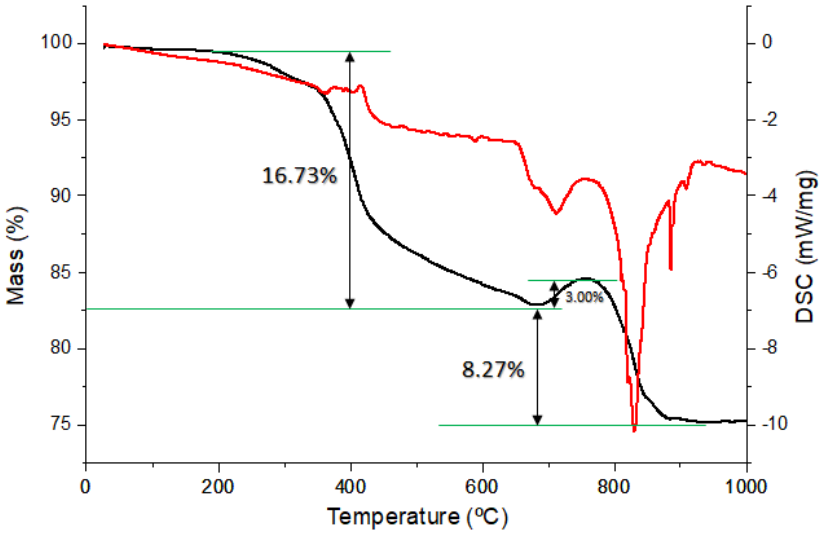

Figure 99. TGA (black line) and DTA curve (red line) of as-made ITQ-35 sample.

The ^{19}F-MAS-NMR spectroscopy analysis of the ITQ-35 sample reveals a resonance at -10 ppm, typically associated to the presence of fluorine anions within D4R cages of germanium-rich zeolites (**Fig. 100**). The fluorine weight content, calculated from the peak at -10 ppm corresponding to DR4-entrapped fluoride anions, is determined to be 1.8%.

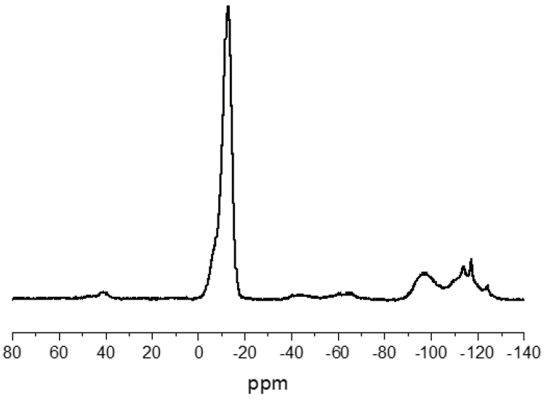

Figure 100. ^{19}F-NMR spectra of as-made zeolite ITQ-35. The weight content of F calculated from the peak at -10 ppm, corresponding to the F entrapped within the D4R, is 1.8%.

The morphology and crystal size of zeolite ITQ-35 were examined using field emission scanning electron microscopy (FESEM). The micrographs revealed the presence of crystals with a cubic shape, with sizes ranging from 2 to 10 μm (**Fig. 101**).

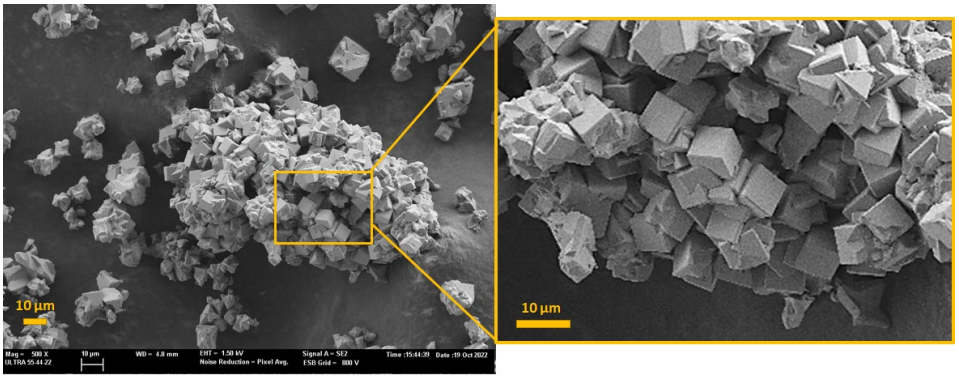

Figure 101. FESEM micrographs of Ge-ITQ-35 sample showing the cubic morphology. No more other phases were analyzed by SEM technique.

The Energy Dispersive X-ray Spectroscopy (EDS) analysis coupled with FESEM over the as-made ITQ-35 crystals revealed the elemental distribution and quantification across 29 distinct regions of the zeolite structure. This analysis revealed an average Ge/F ratio of 6.8±1.5, as shown in **Fig. 102** and summarized in **Table 31**.

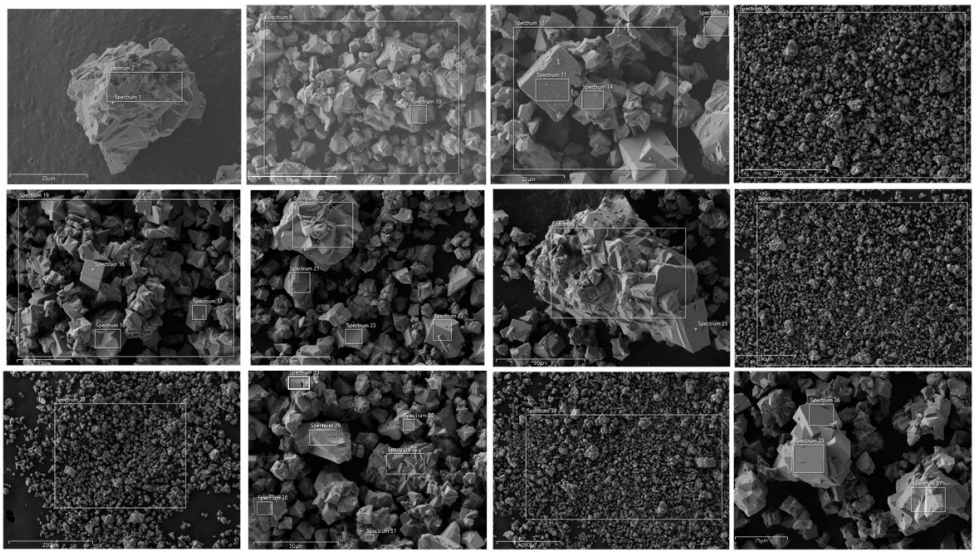

Figure 102. HRFESEM images and EDS analysis across 29 different regions of as-made ITQ-35 crystals. Area EDS analysis is shown in white squares.

Table 31. Ge/F ratio from EDS analysis across 29 different areas of as-made ITQ-35 sample.

Spectrum	Atomic Ge %	Atomic F %	Ge / F
2	18.72	3.1	6.0
9	32.85	4.62	7.1
10	41.95	4.16	10.1
11	31.03	5.25	5.9
12	34.03	4.76	7.1
13	83.2	16.8	5.0
14	26.99	5.31	5.1
15	31.05	4.6	6.8
16	26.41	5.19	5.1
17	29.89	4.82	6.2
18	35.78	4.3	8.3
19	34.98	5.08	6.9
20	31.38	4.6	6.8
21	31.67	4.89	6.5
22	32.19	4.38	7.3
23	29.05	5.02	5.8
24	32.05	4.8	6.7
25	36.7	4.17	8.8
26	30.21	5	6.0
27	30.01	5.17	5.8
28	29.3	4.7	6.2
29	45.02	3.77	11.9
30	35.85	4.63	7.7
31	34.53	4.59	7.5
32	35.01	4.6	7.6
33	33.6	5.13	6.5
34	82.12	17.88	4.6
35	27.72	4.71	5.9
36	28.29	4.55	6.2
37	30.29	4.94	6.1
Ge/F RATIO AVERAGE			**6.8±1.5**

6.2. PXRD CHARACTERIZATION

The phase of as-made zeoliteITQ-35 was measured in a High-Resolution Panalytical X'Pert PRO X-ray powder diffractometer (HR-XRPD) instrument, equipped with an hybrid germanium (220) monochromator, in a capillary at room temperature with Bragg-Brentano geometry, using $CuK_{\alpha 1}$ radiation (λ=1.5406; divergence slit: fixed = 1/4°; goniometer arm length: 240mm; detector: Panalytical X'Celerator; tube voltage and intensity: 45 kV, 40 mA; scan range: 1.0° to 120.0° (2θ), scan step size: 0.017° (2θ); counting time: 5000.6 s/step). The Bragg intensities were analyzed throughout the indexation of the XRD pattern with the program JANA2020.[128] During the unit cell determination, the background was manually estimated, and the peaks were searched automatically. The pattern was indexed in cubic symmetry, being the most probable extinction symbol I - - -, corresponding to the space groups *I*23 (197), $I2_13$ (199), *Im*-3 (204), *I*432 (211), *I*-43*m* (217) and *Im*-3*m* (229). The following unit cell parameters were extracted from the LeBail profile fitting of the as-made ITQ-35 pattern:

$$a=b=c=17.1671 \text{ Å}, \alpha=\beta=\gamma=90°, \text{ and } V=5059.3 \text{ Å}^3$$

The R parameters extracted from the LeBail fit profile are the following: N° points=6032, N° profile parameters=8, GooF=2.59. R_p=6.12 and wR_p=8.53. The as-made zeolite is obtained with sharp peaks and without significant impurities or amorphous material, as evidenced by the powder pattern shown in **Fig. 103**.

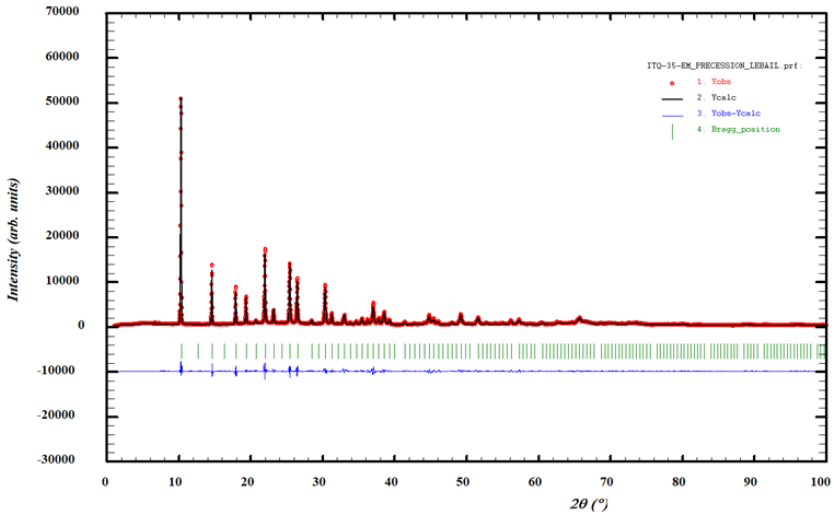

Figure 103. LeBail profile refinement of the X-ray diffraction pattern of the cubic as-made zeolite ITQ-35. The red points are experimentally observed data. The solid black line is the calculated profile. The green sticks show the Bragg position. The solid blue line shows the difference between the observed and the calculated profiles.

Attempts to remove the OSDA by calcination lead, in all our tests, to the complete amorphization of the sample as soon as the ODSA is removed, even when the treatment is performed under a completely dry atmosphere in an Anton-Paar reaction chamber XRK900 attached to the diffractometer. So, the attempts to solve the structure of this material were performed using the as-made, OSDA containing sample.

6.3. 3DED CHARACTERIZATION

6.3.1. DATA ACQUISITION: FEI TECNAI G2 TEM

The powder as-made ITQ-35 sample was dispersed straight into a square 200-mesh copper Transmission Electron Microscope (TEM) grid covered by an extra thick 20-30 nm carbon layer (CFT200-CU-ET provided by Ted Pella). The transmission electron microscope (TEM) FEI Tecnai G2 20 equipped with a thermionic cathode (LaB_6) at an acceleration voltage of 200 keV was used to analyze the sample. The grid was placed on a Liquid nitrogen cooling tomography holder (Gatan model 636). The holder was temperature-controlled to 183 K to improve the stability of the crystal

under the electron beam. Three varied strategies were applied for the electron diffraction (ED) pattern acquisition: precession-assisted electron diffraction tomography stepwise (PEDT), continuous rotation electron diffraction (cRED), and a combination of PEDT and cRED. These three methods are based on a tilting approach using self-written scripts in Olympus Soft Imaging Solutions iTEM software for combining beam, goniometer, and detector control. ED frames were acquired with a Timepix Quad's hybrid pixel detector (Amsterdam Scientific Instruments), model QTPX-262k (512×512, pixel size 55 μm), and a high dynamic range of 16 bits. A total of three crystals were analyzed using these three strategies.

The first dataset from a crystal of 2.8 x 2.3 μm was collected by stepwise PEDT, which was optimized using a CA2 diameter of 10 μm, a spot size of 6, and a semi-parallel beam size of 0.52 μm in diameter (see **Table 32**). The image of the crystal and the 2D projections of the reconstructed reciprocal space can be seen in **Fig. 104**. 72 ED frames were collected through a tilt range of 61° (from -30.0° to +30.0°). The integration step was set to 1.00° and the exposure time per frame to 1.0s. The average total collection time was about 1.0 min. The precession semi-angle was calibrated to 1.00° using the NanoMEGAS-Digistar P1000 device.

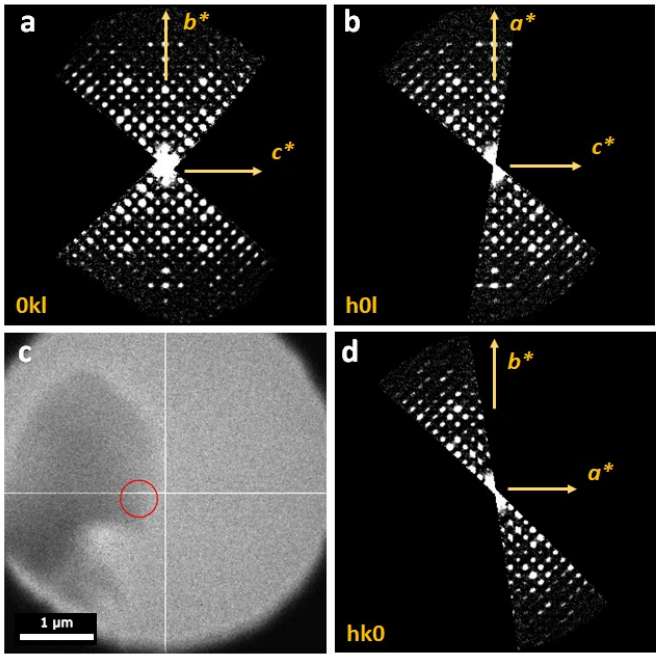

Figure 104. (a) 0kl, (b) h0l, and (d) hk0 plane sections of the 3D reconstructed reciprocal space of the first crystal collected by 3DED of the as-made ITQ-35. (c) TEM image of the crystal measured using PEDT. The red circle indicates the illuminated area during data collection (beam diameters: 0.52 μm).

The second dataset from a crystal of 2.4 x 1.4 μm was obtained by the acquisition in continuous rotation mode, which was optimized using a condenser aperture (CA2)

of 10 μm of diameter, a spot size of 7, and a semi-parallel beam size of 0.85 μm in diameter. The image of the crystal and the 3D projections of the reconstructed reciprocal space can be seen in **Fig. 105**. 110 ED frames were collected through a tilt range of 61° (from -30.0° to +30.0°). The integration step was set to 0.5° and the exposure time per frame to 1s (see **Table 32**). The average total collection time was about 1.97 min.

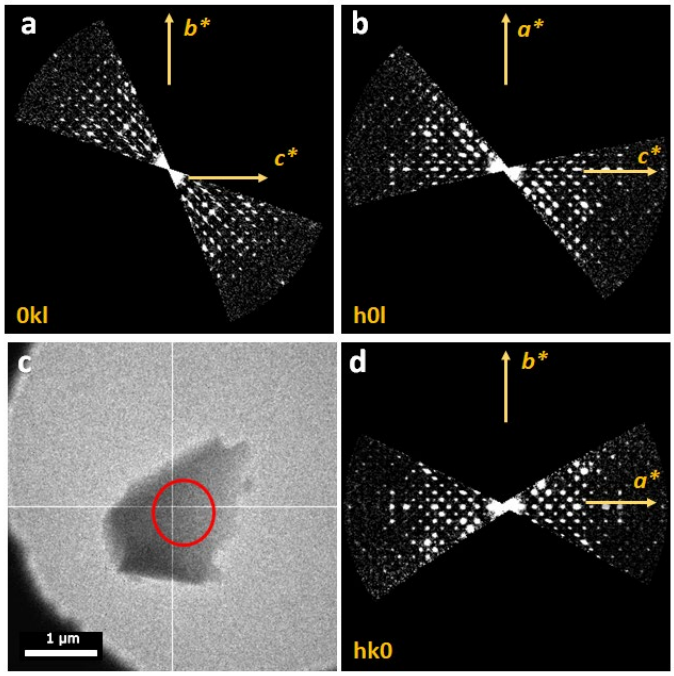

Figure 105. (a) 0kl, (b) h0l, and (d) hk0 plane sections of the 3D reconstructed reciprocal space of the second crystal collected by 3DED of the as-made ITQ-35. (c) TEM image of the crystal measured using cRED. The red circle indicates the illuminated area during data collection (beam diameters: 0.85 μm).

The third crystal of 2.3x1.3 μm was analyzed by the combination of PEDT and cRED, which was optimized using a CA2 diameter of 10 μm, a spot size of 7, and a semi-parallel beam size of 0.65 μm in diameter. The image of the crystal and the 2D projections of the reconstructed reciprocal space can be seen in **Fig. 106**. 320 ED frames were collected through a tilt range of 81° (from -40.0° to +40.0°). In order to combine both acquisition strategies, the precession semi-angle, the goniometer rotation speed, and the exposure time were optimized to 1.00°, 0.506°/s, and 0.5s, respectively, giving rise to an integration step of 0.25° (see **Table 32**). The precession of the beam was calibrated using the NanoMEGAS-Digistar P1000 device. The average total collection time was about 2.6 min.

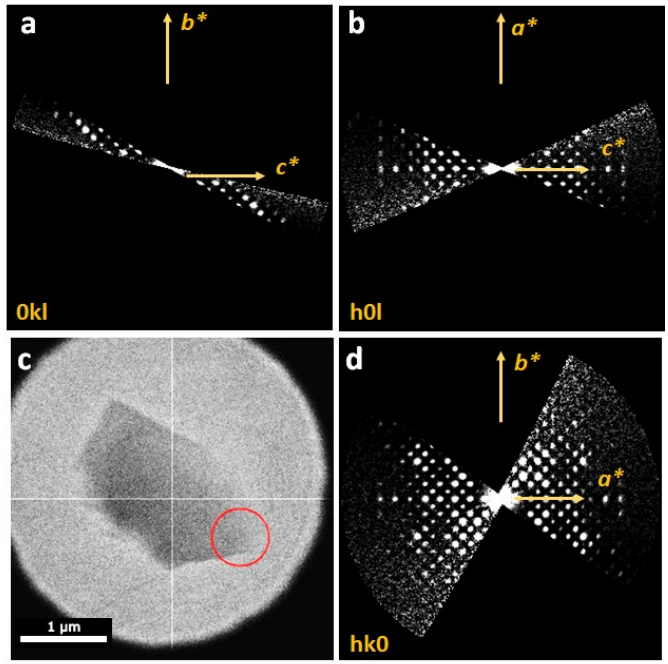

Figure 106. (a) 0kl, (b) h0l, and (d) hk0 plane sections of the 3D reconstructed reciprocal space of the third crystal collected by 3DED of the as-made ITQ-35. (c) TEM image of the crystal measured using PEDT+cRED. The red circle indicates the illuminated area during data collection (beam diameters: 0.65 µm).

Table 32. 3DED Experimental parameters of PEDT, cRED, and combination of PEDT+cRED, at cryo condictions (T=183 K) and crystallographic data of the structure of as-made ITQ-35

Protocol/Illumination mode	PEDT	cRED	cRED+PEDT
Crystal system	Cubic	Cubic	Cubic
TEM	FEI Tecnai G2 20 200 keV	FEI Tecnai G2 20 200 keV	FEI Tecnai G2 20 200 keV
Sample preparation	Dry	Dry	Dry
Holder/Temperature	Cryo Transfer Tomography, Gatan/183 K	Cryo Transfer Tomography, Gatan/183 K	Cryo Transfer Tomography, Gatan/183 K
Detector	Timepix Quad's hybrid pixel	Timepix Quad's hybrid pixel	Timepix Quad's hybrid pixel
Data Acquisition Script	iTEM software	iTEM software	iTEM software
Space group (Num.)	*I m* -3 *m* (229)	*I m* -3 *m* (229)	*I m* -3 *m* (229)
a (Å)	17.7548	17.7307	17.893
b (Å)	17.7548	17.7307	17.893
c (Å)	17.7548	17.7307	17.893
Volume (Å^3)	5596.91	5574.10	5728.59
Z	64	64	64
λ (Å)	0.02508	0.02508	0.02508
Crystal size (µm)	2.8 x 2.3	2.4 x 1.4	2.3 x 1.3
Initial angle (°)	-30.0	-30.0	-40.0
Final angle (°)	30.0	-30.0	40.0
Integration step (°)	1.00	0.50	0.25
Precession angle (°)	1.00	-	1.00
Exposure time per frame (s)	1.000	0.987	0.493
Num. Frames	61	120	320
Tilt speed (°/s)	-	0.506	0.506
Total exposure time (s)	61	120	158
Beam diameter (µm)	0.52	0.85	0.65
Electron dose rate (e/Å^2·s)	0.077	0.076	0.072
Total, accumulated electron dose (e/Å^2)	4.7	9.1	11.3
Data Reduction/Software	PETS2.0	PETS2.0	PETS2.0
Coverage (%)	99	97	96
Resolution (Å)	0.91	0.91	0.91
Num. Reflections (unique/all)	417/398	411/368	414/230
Redundancy	12.34	12.44	6.13
R_{int} (%)	12.88	21.92	24.68
Structure Solution Software	JANA2020	JANA2020	JANA2020

Some differences become evident when comparing the electron dose rate and total accumulated electron dose across the PEDT, cRED, and PEDT+cRED datasets. The electron dose rates are similar, with PEDT dataset slightly higher at 0.077 e/Å²·s, followed by cRED at 0.076 e/Å²·s, and PEDT+cRED at 0.072 e/Å²·s. The lower dose rate observed in the PEDT+cRED dataset suggests less beam exposure, which may reduce the risk of beam damage. However, the total accumulated electron dose reveals more pronounced differences: PEDT exhibits the lowest total accumulated dose at 4.7 e/Å². This indicates a more controlled approach in the PEDT dataset, designed or aimed to minimize sample damage. In contrast, cRED shows a higher accumulated dose of 9.1 e/Å², and the PEDT+cRED dataset reaches 11.3 e/Å². The increased dose in the PEDT+cRED dataset suggests a more intensive data collection, which could enhance data quality but also increases the risk of beam damage. These results underscore the balance between lower exposure in PEDT and the enhanced data collection at the cost of higher exposure in cRED and PEDT+cRED.

6.4. DATA REDUCTION AND FRAMEWORK STRUCTURE SOLUTION

The three 3DED datasets were independently analyzed using the PETS2 program. During the processing of all 3DED datasets, a cubic lattice was found, indexed in the following average unit cell parameters: a = 17.79(8) Å and volume V = 5633(83) Å^3 and the unit cell dimensions for each dataset can be seen in **Table 32**. Observing the reconstructed reciprocal space from all datasets and systematic extinctions (see **Fig. 104, 105 and 106**), the reflection condition *hkl*: *h*+*k*+*l* revealed a body-centered cubic lattice (extinction symbol: *I*---). The possible space groups are *I*23 (197), I2$_1$3 (199), *Im*-3 (204), *I*432 (211), *I*-43*m* (217), and *Im*-3*m* (229), in good agreement with the PXRD results. This confirms that the selected crystals are representative of the whole sample, and do not correspond to some minor impurities. Although the resolution was limited to 0.91 Å, the high symmetry of the crystal structure of the as-made ITQ-35 resulted in datasets with high completeness, which may lead to an approachable structure solution by direct methods. After the peak search, refinement of optical distortions, optimization of the frame geometry, the optimization of the reflection profile, and the final integration step, the Laue symmetry m-3m was estimated based on the Rint factors and resolution: 12.88% [0.91 Å], 21.92% [0.91 Å], 24.68 % [0.91 Å] corresponding respectively to PEDT, cRED and combination of PEDT+cRED datasets. An independent *hkl* file with the extracted intensities for each dataset was generated. A notable observation is that the reflection intensities from different data collection strategies showed a good fit with their respective profiles: the precession data exhibits a double-peak, the continuous rotation rocking curve shows a single peak, and the PEDT+cRED data exhibits a mixed double-single peak pattern, as shown in **Fig. 107**.

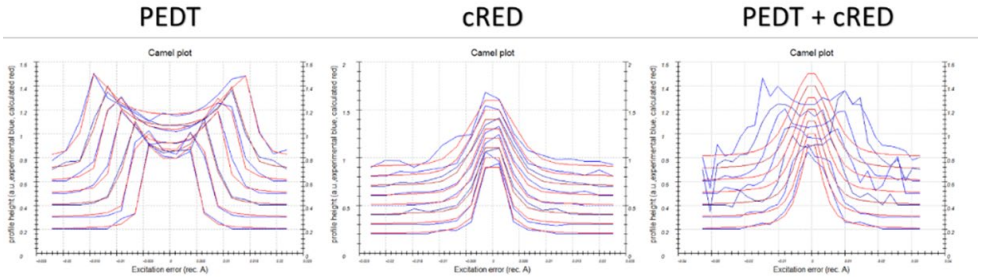

Figure 107. Averaged rocking curves of the strongest reflections at different diffraction data resolution intervals as a function of the deviation from perfect Bragg condition (red curves) and fitted by (left) the precession double-peak, (middle) continuous-rotation single-peaked profile and (right) PEDT+cRED curve (blue dashed curves).

The three *hkl* files were imported into the JANA2020 program, and the structure was kinematically ($I \sim |Fhkl|^2$) solved *ab initio* using the charge-flipping algorithm

implemented in the Superflip program. After only ten cycles of structure solution, the high crystal symmetry and completeness (100%) of each dataset led to the first structure solution model crystallizing in the *Im*-3*m* space group. The resulting structures followed the same GeO_2 germanate-based framework in all datasets without the presence of OSDA molecules. The germanium-based framework was refined against 3DED data resulting in the model shown in **Fig. 108**, demonstrating its reproducibility despite the use of alternative 3DED strategies. This figure shows the Fourier maps of each dataset at isosurface level δ=0.2 (yellow clouds), with similar aspects between each other. **Fig. 109** shows the germanate framework from the precession dataset as sticks and balls. The formation of D4R cages was evident from the *ab initio* structure solution that is shown as purple tetrahedra. These cages can be related to the incorporation of fluorine anions during the synthesis, and are in good agreement with the ^{19}Si NMR data shown above.

It was decided to select and continue with the kinematical refinement of the GeO_2 framework with the data based on the data obtained from PEDT, primarily due to the low R_{int} value of 12.88% observed at a resolution of 0.91 Å. Distance d(Ge-O) = 1.721(1)Å and angle O-Ge-O = 109.47(1) restrictions were applied and the temperature factors for atoms corresponding to the same element were constrained to be equal. The atomic coordinates of the germanate framework and fluorine atoms, as shown in **Table 33**, are obtained after the convergence of several kinematical refinement cycles (ADPs were isotropically refined: B_{iso}). Furthermore, the structure model presents 64 Ge atoms, 128 O atoms, and 8 F- anions per unit cell as well as 2 Ge atoms, 4 O atoms, and 1 F- anion in the asymmetric unit.

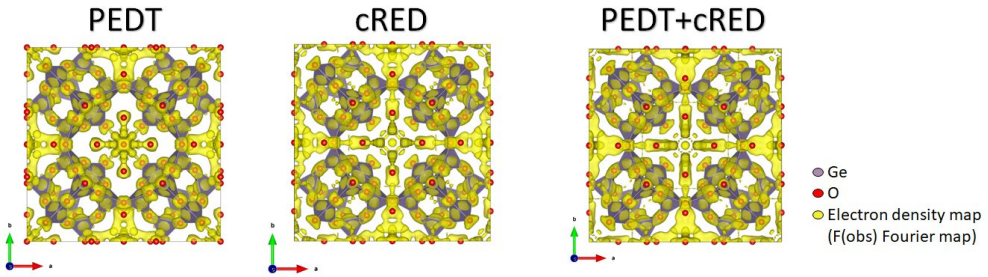

Figure 108. Initial model structure solution of the as-made zeolite ITQ-35, viewed along the a-axis, using 3DED datasets from PEDT (left), cRED (middle), and PEDT+cRED (right). The F(obs)-Fourier map shows 0.2σ positive isosurfaces, highlighted in yellow. Ge tetrahedra are depicted in purple, and oxygen atoms are shown in red.

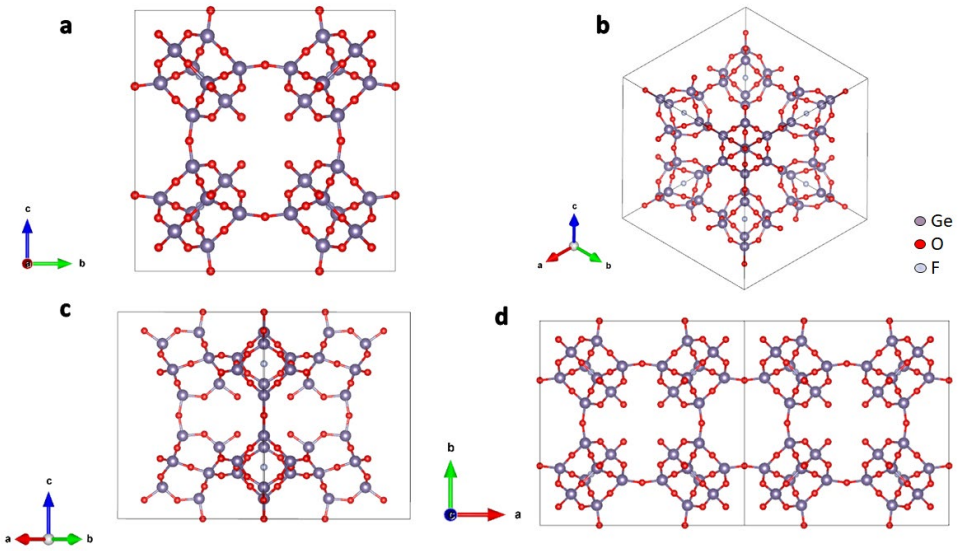

Figure 109. Germanate framework of the as-made ITQ-35 solved using PEDT. The structure is shown in ball-and-stick representation, viewed along (a) the a-axis, (b) the b-axis, and (c) the ab plane. Panel (d) shows a double unit cell. Germanium atoms are colored purple, oxygen atoms are in red, and fluoride anions are in sky blue. Note that the OSDA was not included in the refinement.

Table 33. Atomic coordinates of as-made Ge-ITQ-35 sample obtained by ab-initio structure solution from the PEDT data. Im-3m; a=b=c=17.7548; α=β=γ=90º.

Atom	x	y	z	Biso	Multiplicity & Wyckoff
Ge1	0.2828(5)	0.2828(5)	0.0977(6)	0.039(8)	48d
Ge2	0.1609(9)	0.1609(9)	0.1609(9)	0.039(8)	16d
O1	0.2999(16)	0.2999(16)	0	0.016(9)	24d
O2	0.2148(5)	0.2148(5)	0.107(2)	0.016(9)	48d
O3	0.099(3)	0.099(3)	0.099(3)	0.016(9)	16d
O4	0.3662(6)	0.25	0.1338(6)	0.016(9)	48d
F1	0.25	0.25	0.25	1.15(18)	8d

This framework contains structural defects associated with germanol (GeOH) or germanoxy (GeO^-) species, containing terminal oxygens (-OH or $-O^-$), known as Q^3 species. Pointing to the center of the unit cell, eight terminal oxygen atoms are highlighted in red in **Fig. 110**. As each unit cell includes two cavities, this brings to a total number of 16 Q^3 per unit cell. A clearer illustration of the large cavities is shown in **Fig. 111**. The *ab initio* structure model reveals six 8R cavities, that are halved, resulting in three full cavities per unit cell. Additionally, one-eighth of eight 12R cavities, along with one full 12R cavity, give a total of two 12R cavities per unit cell. The content of Q^3 species per unit cell (Q^3/u.c.) is 16, leading to a Q^3/Q^4 ratio of 1/4.

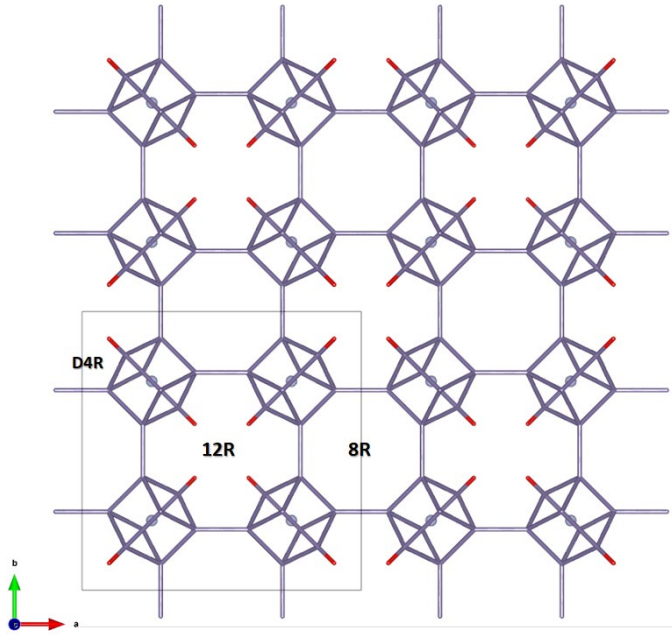

Figure 110. The 3D framework structure of ITQ-35 is viewed along [001] direction. The 8- and 12-ring channels extend along the [100], [010], and [001] directions. T–T bonds (T = Ge) are shown as purple sticks, fluoride anions are depicted in blue, and terminal OH/O⁻ groups are highlighted in red for clarity.

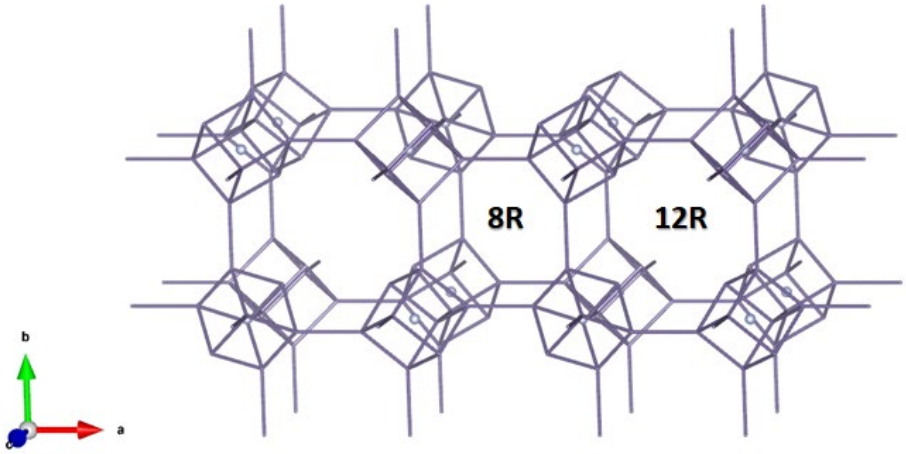

Figure 111. Structure of as-made zeolite Ge-ITQ-35 obtained by 3DED data. The structure model is viewed along the ab axis as heteroatoms T-T bonds (in purple). The OSDA was not included in the refinement. Three-dimensional 8x8x8-ring and 12x12x12 channel systems can be seen along the b-axis. D4R cages can be recognized. One additional unit cell along a axis was used and oxygen atoms were omitted for clarity.

6.5. STRATEGIES FOR OSDA LOCATION

6.5.1. KINEMATICAL REFINEMENT

After carrying out the kinematical refinement and subsequent convergence through charge-flipping, a difference electrostatic potential map was generated, represented by [F(obs)-F(calc) – difference Fourier]. **Fig. 112** shows the z=0.00 section of this map, with a positive 1.26σ contour level. This difference Fourier map can assist in the localization of the OSDA and can be also seen as a three-dimensional difference Fourier map, with an isosurface level of 0.5σ, in **Fig. 113**. It reveals a filled region situated at the center of the unit cell which may be attributed to the organic guest molecule.

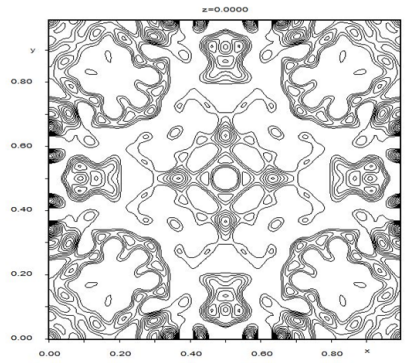

Figure 112. Observed positive difference Fourier map (z = 0.00) showing the electron-density distribution from 3DED data analysis of the as-made ITQ-35 crystal. Contour lines represent increasing electron density levels, with the two-dimensional map highlighting regions above the 1.26σ threshold.

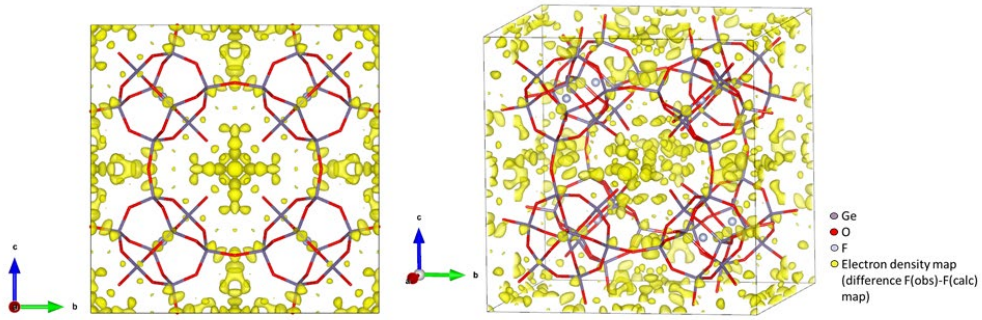

Figure 113. Observed three-dimensional positive difference F(obs)-F(calc) Fourier map of the electron-density distribution from 3DED data analysis of the as-made ITQ-35 crystal. The isosurface is displayed at a 0.5σ level.

In a preliminary analysis to determine whether the guest molecule occupies the cavities of the *ab initio* solved GeO_2 framework, we measured the 8R and 12R cavities, assuming a van der Waals radius of 2.7 Å for oxygen atoms. As shown in **Fig. 114**, the 8R cavity has a pore aperture of 3.41 x 3.41 Å, while the 12R cavity exhibits a larger aperture of 4.43 x 4.43 Å. Additionally, the diagonal O-O distances within the cavities, as illustrated in **Fig. 115**, reveal that the 8R cavity has a volume of 3.41 x 3.41 x 3.41 Å, whereas the 12R cavity provides a significantly larger void space of 7.38 x 8.46 x 10.14 Å. This suggests that the OSDA is more likely to occupy the 12R

channel system, given its greater available volume compared to the 8R channel system.

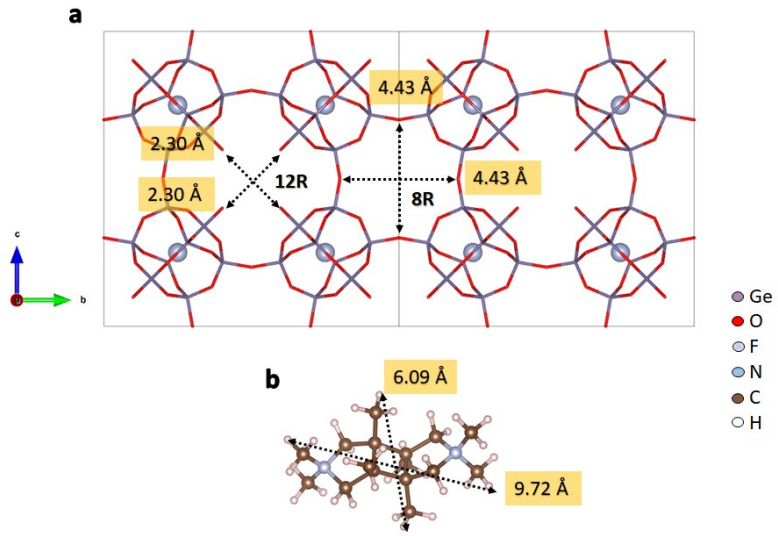

Figure 114. (a) Pore aperture sizes of as-made zeolite ITQ-35. (b) dicationic pyrrole guest molecule.

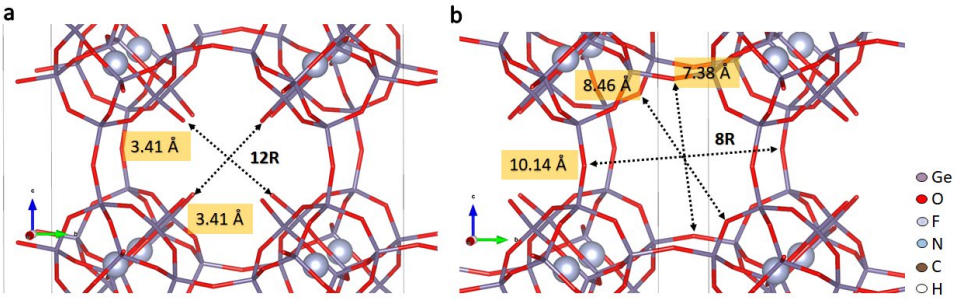

Figure 115. (a and b) Void volume sizes of the two-channel system types (8R and 12R) in the as-made zeolite ITQ-35.

The graphical interface of JANA2020 was used to assign the centered peaks of the difference Fourier map to carbon atoms, as shown in **Fig. 116**. However, refinement attempts were unsuccessful even after several cycles, resulting in the fragmentation of C-C bonds and elevated temperature factors for the organic atoms. Consequently, the process was stopped yielding a model lacking chemical coherence, with the following structure factors: R(obs) ~ 52.4, wR(obs) ~ 207.6, R(all) ~ 83.18, wR(all) ~ 269.6, and GOF ~ 7.27. Additional efforts to directly assign OSDA atoms did not result in any improvement. Thus, we considered determining the organic template by other methods explained in the next sections.

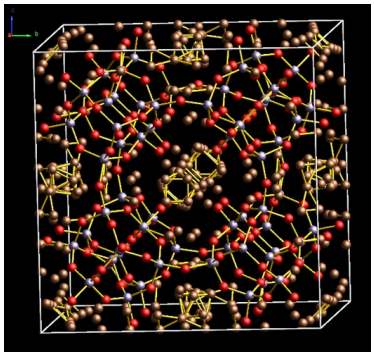

Figure 116. Structural model of the as-made ITQ-35 during refinement using the JANA2020 graphical interface. Germanium atoms are shown in purple, oxygen atoms in red, and carbon atoms in brown.

6.5.2. SIMULATED ANNEALING

To successfully assign the remaining OSDA atoms located within the channels using direct methods, high-quality data with a high signal-to-noise ratio and high resolution is necessary. Additionally, a well-ordered distribution of the OSDA is required, where it adopts a configuration that must fill the channels. It is important to note that in most cases, the symmetry of the OSDA is lower than that of the framework, highlighting the disorder of the guest molecule and hence, the complexity of characterizing it. Therefore, the simulated annealing (SA) structure solution method, implemented in SIR2019 software, was used for this purpose.

Firstly, as the structure of the OSDA used in this synthesis was not available on the CCDC database,[1] we decided to model from scratch the dication in three dimensions manually using ChemDraw 19.0.[105] The trans-configuration of the methyl groups was considered significant as it was the only configuration obtained as a product in the [2 + 2] cycloaddition reaction. The drawn dicationic pyrrole was then imported into the interactive auto-optimization tool provided by Avogadro software to determine its optimized geometry.[129] Then, this model was optimized using molecular modeling programs like Avogadro which generated an approximate model. This adjustment of the molecule, as shown in **Fig. 117**, was exported as a *mol* file and used as one of the molecular fragment inputs for the SA instructions.

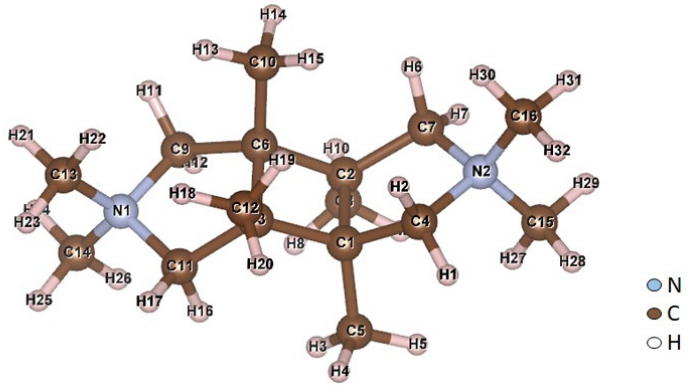

Figure 117. Dicationic pyrrole salt modeled by ChemBiodraw 19.0 and used for the SA method as the mol input file.

Our second objective was to determine the number of OSDA molecules per unit cell to establish the chemical composition as part of the SA instructions. The method used for this calculation was thermogravimetric analysis (TGA), as discussed in the previous section. The inorganic framework of the unit cell consists of 64 Ge atoms, 128 O atoms, and 8 F^- anions. TGA indicated a weight loss of 16.73%, corresponding to 6 OSDA guest molecules per unit cell. To simplify post-refinement via charge flipping in JANA, hydrogen atoms were excluded from the total composition. The structure of the OSDA molecule is shown below in **Fig. 118**. Consequently, the final SA instructions included 64 Ge, 128 O, 8 F, 12 N, and 96 C atoms in the unit cell composition.

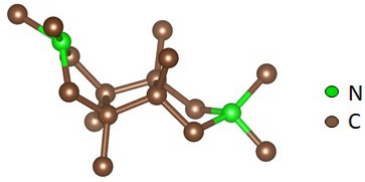

Figure 118. OSDA molecule is used as one of the fragments for the SA process.

Thirdly, the first fragment (GeO_2 framework) together with the second fragment (OSDA) were imported as rigid-body models into the simulated annealing program. The program was then instructed to use the R factor as the cost function, set the resolution cutoff to 0.97 Å, and the total number of runs to 10. The parameters for

the first fragment, including both the Internal and External Degrees of Freedom (INTDOFs and EXTDOFs), were kept fixed, while those for the OSDA fragment were refined with unrestricted mobility. These parameters include translational positions (x, y, z), rotation (θ), and torsion angles. Additionally, to prevent any close contact between the OSDA molecule and the Si framework, an anti-bump restraint with a weight of 1.0 and a scale factor of 0.7 on distances was selected. SA was attempted multiple times, resulting in ten structural model solutions. The first solution, shown in **Fig. 119**, was found to be converging in a minimum and had the lowest R factor of 87.40. All ten solutions had similar R factors ranging from 87.40 to 89.68, with the latter two solutions having slightly higher values (87.40, 87.40, 87.40, 87.40, 87.41, 87.41, 87.42, 87.43, 89.63, 89.68). The guest molecule was observed to occupy the voids in the inorganic framework during the SA cycles, but the carbon atoms visually appeared disordered and poorly defined, i.e. atoms in not defined positions. This is reflected in the form of a bunch of atoms. The atom coordinates and their respective symmetry sites and occupancies can be seen in **Table 34.**

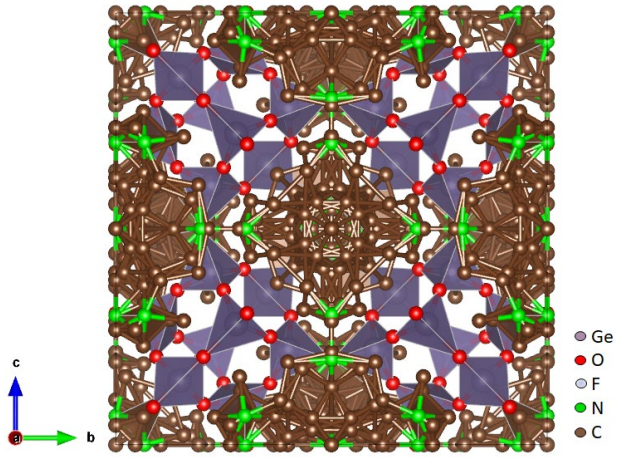

Figure 119. Structure model of as-made ITQ-35 obtained by SA.

Table 34. Atom coordinates of as-made ITQ-35 obtained by SA. Im-3m; a=b=c=17.7548; α=β=γ=90º.

Atom	Coordinates			Uiso	Multiplicity & Wyckoff	Occupancy
	x	y	z			
Ge1	0.6004	0.7794	0.7794	0.038	48k	1
Ge2	0.6482	0.6482	0.6482	0.038	16f	1
O1	0.5000	0.8040	0.8040	0.038	24h	1
O2	0.6423	0.7500	0.8577	0.038	48i	1
O3	0.5940	0.7033	0.7033	0.038	48k	1
O4	0.5871	0.5871	0.5871	0.038	16f	1
F1	0.7500	0.7500	0.7500	0.038	8c	1
N1	0.5000	0.5668	0.7991	0.038	48j	1
N2	0.5000	0.3020	1.0000	0.038	24g	1
C1	0.5343	0.4378	0.9555	0.038	96l	1
C2	0.5000	0.3963	0.8813	0.038	48j	1
C3	0.5919	0.4810	0.8994	0.038	96l	1
C4	0.5573	0.3660	1.0000	0.038	48j	1
C5	0.5000	0.5000	1.0000	0.038	6b	1
C6	0.5677	0.4323	0.8282	0.038	48k	1
C7	0.5000	0.3087	0.8988	0.038	48j	1
C8	0.4130	0.4130	0.8649	0.038	48k	1
C9	0.5451	0.5000	0.7656	0.038	48j	1
C10	0.6254	0.3746	0.7904	0.038	48k	1
C11	0.5657	0.5657	0.8696	0.038	48k	1
C12	0.6756	0.4800	0.9314	0.038	96l	1
C13	0.5225	0.6572	0.7869	0.038	96l	1
C14	0.4361	0.5639	0.7288	0.038	48k	1
C15	0.4356	0.3130	1.0616	0.038	96l	1
C16	0.5000	0.2141	1.0000	0.038	24g	1

Despite the last SA results, we decided to tackle the problem by focusing on the initial configuration of the OSDA fragment. One approach was to use ChemBioDraw 19.0 to draw an atomic arrangement of the guest molecule as symmetrically as possible, in hopes of achieving a more accurate atom positioning of the guest molecule within the voids and hence, a lowering in R factors. This was reached by positioning the two nitrogen atoms parallel to the vertical axis that passes perpendicular through the cyclobutene plane as seen in **Fig. 120**. At this time, we decided to not optimize this geometry configuration using Avogadro software. The aim of using this arrangement was to mimic the electron density observed in the inner part of the 12R.

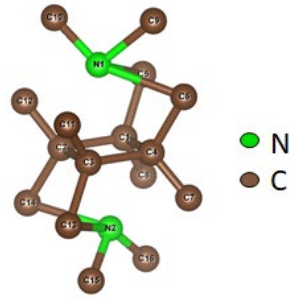

Figure 120. OSDA molecule symmetrically drawn used for SA.

Therefore, this new configuration molecule was used as a second fragment for a new SA processing and the same instructions used for the previous simulated annealing work were replicated: R factor as cost function, resolution cutoff to 0.97 Å, total number of runs to 10, fixing all degrees of freedoms corresponding to GeO_2 network whereas those describing OSDA molecule (second rigid body) were refined (translational positions (x, y, z), and rotation (θ) and torsional angles) and anti-bump restrains with weight 1.0 and scale factor on distances 0.7. In case some carbon or

nitrogen atoms from OSDA molecule could rely on special positions within the unit cell, Dynamical Occupancy Corrections (DOC) were also activated. Overall, 17 parameters were refined, of which 15 were EXTDOF and 2 were INTDOFs. After seven hours and ten runs, SA successfully led to a structure model that converged in local minima as evidenced by the R factor of 50.63 (**Fig. 121**). Moreover, all ten runs resulted in the same structure, with R factors of 50.63, 50.64, 50.64, 50.65, 50.66, 50.66, 50.66, 50.66, 50.67, and 50.67. Despite these positive outcomes, it remains important to determine the SDA proportion per unit cell. In the context of the SA experiment, this may not be a significant finding; however, it should still be considered in subsequent steps.

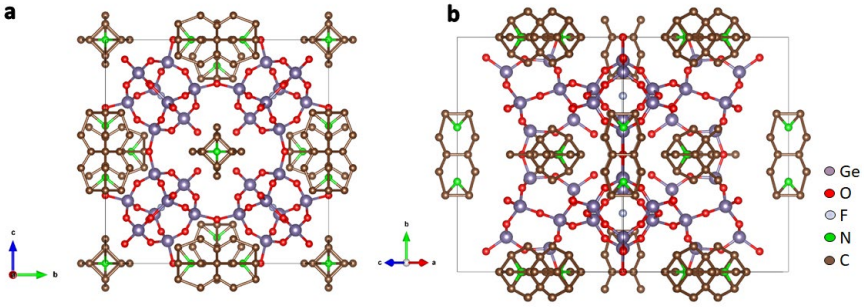

Figure 121. Structure model of as-made ITQ-35 obtained by the second SA experiment.

The atom coordinates and their respective symmetry occupancies can be seen in **Table 35**. As it may be denoted from the table when activating DOCs, the occupancies of some overlapping OSDA atoms was changed to zero value and were removed manually and organized (atom label) from the output SA file as seen in **Table 36**.

Table 35. Atom coordinates of as-made ITQ-35 obtained by the second SA experiment. Im-3m; a=b=c=17.7548; α=β=γ=90º.

Atom	Coordinates			Multiplicity & Wyckoff	Symmetry
	x	y	z		
Ge1	0.6004	0.7794	0.7794	48k	..m
Ge2	0.6482	0.6482	0.6482	16f	.3m
O1	0.5000	0.8040	0.8040	24h	m.m2
O3	0.6423	0.7500	0.8577	48i	..2
O4	0.5940	0.7033	0.7033	48k	..m
F1	0.7500	0.7500	0.7500	8c	.-3m
O6	0.5871	0.5871	0.5871	16f	.3m
C1	0.5343	0.4378	0.9555	24g	mm2 . .
C2	0.5000	0.3963	0.8813	24g	0
C3	0.5919	0.4810	0.8994	24g	0
C4	0.5573	0.3660	1.0000	24g	0
C5	0.5000	0.5000	1.0000	48j	m..
C6	0.5677	0.4323	0.8282	48j	0
C7	0.5000	0.3087	0.8988	12e	4m. m
C8	0.4130	0.4130	0.8649	48j	0
C9	0.5451	0.5000	0.7656	48j	0
C10	0.6254	0.3746	0.7904	48j	m..
C11	0.5657	0.5657	0.8696	48j	0
C12	0.6756	0.4800	0.9314	48j	0
N1	0.5000	0.5668	0.7991	48j	0
N2	0.5000	0.3020	1.0000	48j	0
C13	0.5225	0.6572	0.7869	48j	0
C14	0.4361	0.5639	0.7288	12e	0
C15	0.4356	0.3130	1.0616	48j	0
C16	0.5000	0.2141	1.0000	48j	0

Table 36. Atom coordinates of as-made ITQ-35 obtained by the second SA experiment after removing atoms with zero occupancy and reordering atom label. Im-3m; a=b=c=17.7548; α=β=γ=90º.

Atom	Coordinates			Uiso	Multiplicity & Wyckoff
	x	y	z		
Ge1	0.6004	0.7794	0.7794	1.0000	48k
Ge2	0.6482	0.6482	0.6482	1.0000	16f
O1	0.5000	0.8040	0.8040	1.0000	24h
O2	0.6423	0.7500	0.8577	1.0000	48i
O3	0.5940	0.7033	0.7033	1.0000	48k
O4	0.5871	0.5871	0.5871	1.0000	16f
F1	0.7500	0.7500	0.7500	1.0000	8c
N1	0.5000	0.3087	0.8988	1.0000	12e
C1	0.5343	0.4378	0.9555	1.0000	24g
C2	0.5000	0.5000	1.0000	1.0000	48j
C3	0.6254	0.3746	0.7904	1.0000	48j

If the data is fitted well, the observed and calculated Fourier maps are expected to exhibit a certain degree of similarity. If we look at the superimposed map in **Fig. 122** we can see there is a slight similarity between the structure obtained by SA and the difference Fourier map obtained by the electron density map obtained by 3DED data.

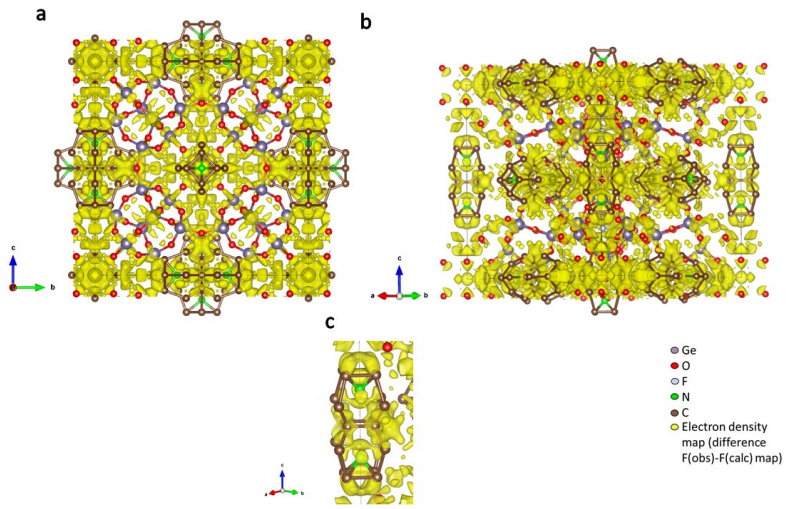

Figure 122. Superimposed structural model of the as-made ITQ-35 from the second SA experiment, overlaid with the electron density map (difference F(obs)-F(calc)) obtained from 3DED data at a 0.4σ level: (a) viewed along the a-axis, (b) along the [110] axis, and (c) showing the representation of the OSDA.

The second independent alternative used to find the OSDA position within the cavities is described in the next section.

6.5.3. COMPUTATIONAL METHODS

Although the use of techniques like the simulated annealing method has been studied, the subsequent refinement kinematical refinement of some parameters did not yield the desired convergence since the SDA positions, occupancy, and U_{iso} were not stable, therefore the model calculated from simulated annealing processes was discarded for further uses.[130]

Therefore, it was decided to employ an alternative software to calculate the possible spatial configuration of OSDAs within the unit cell with the software called zeoTsda (already mentioned in Chapter 3). By previously assigning certain parameters such as, atom types, sp^3, $sp^{2,}$ or *sp* hybridization, and atomic charges, the template molecule is introduced as a rigid body with translational and rotational parameters free to move whereas the zeolite atoms are kept fixed. The number of OSDA occluded per unit cell is considered a parameter to be optimized as well. After the experiment was run for 12 hours and the ΔE energies (eV) were auto-compared from all combinations, *zeoTsda* yielded a favorable result with a structured output following the minimum energy of -8.2 eV, as shown in **Fig. 123**, which the calculated total number of OSDAs per unit cell was 6. The model of van der Waals radii in **Fig. 123a and b** further confirms the remarkable spatial fit between the zeolite micropore and the SDA molecule. In **Fig. 123c**, it can be observed that the SDA is located in the 12R cavity system with the box dimensions of 11.91 x 5.25 x 5.25 Å measured from Ge to Ge atoms.

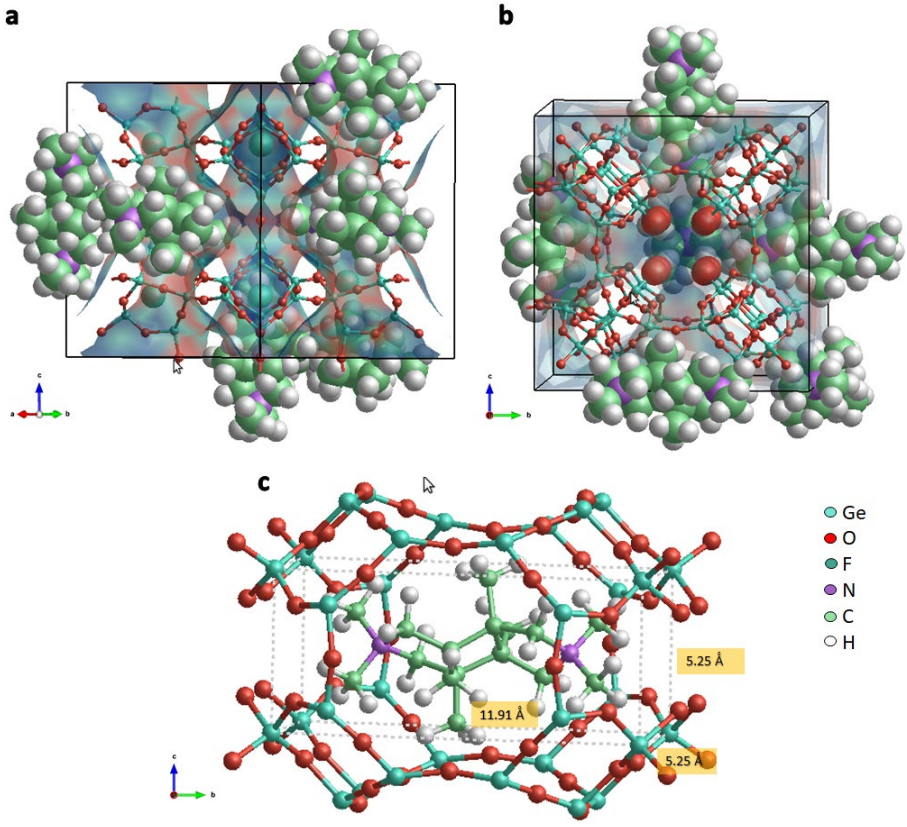

Figure 123. Optimized geometries of OSDA molecule within the micropores of as-made ITQ-35 calculated by zeoTsda (a) viewed along [110] axis (b) along a-axis. Oxygen atoms from the 8R cavity and are possible GeOH/GeO$^-$ are highlighted (c) 12R cavity system with 11.91 x 5.25 x 5.25 Å box dimensions where the OSDA is located. Ge atoms are marked in sky blue color, oxygen atoms in red, fluorine anions in blue, nitrogen atoms in purple, carbon atoms in green, and hydrogen atoms in white.

Considering the number of fluoride anions and organic dications per unit cell previously determined, the number of F^- per unit cell in the as-synthetized optimized model will be 8, while each unit cell contains six dications, resulting in a sum of twelve positive charges. Eight of these positive charges are counterbalanced by the eight fluoride anions. This configuration aligns with the integration peak at a shift of -10 ppm in the ^{19}F-MAS NMR spectrum (**Fig. 100**), which can be attributed to F atoms trapped within the D4R cages. The remaining positive charges could be counterbalanced by 4 Q^3 defects in the form of GeO^-, while the other under-connected Ge-sites correspond to 12 GeOH, with a total of 16 Q^3 sites within the unit cell. Therefore, the chemical composition of the compound can be described by the formula unit:

$$\mathbf{Ge_{64}\,O_{120}\,(OH)_{12}\,(O^-)_4\,(F^-)_8\,.\,6\,(N_2C_{16}H_{32})^{2+}}$$

6.6. REFINEMENT AGAINST PXRD DATA

The as-made ITQ-35 model obtained by the molecular dynamics was used as the initial structure model input for the Rietveld refinement method using PXRD data with the software JANA. Isotropic displacement factors for the same atom type were constrained to be equal, and fractional occupancy factors for all OSDA atoms were set equal at an occupancy of 0.125. To simplify the modeling of OSDA atoms as a rigid body in JANA, only three translational parameters for the whole group were used instead of 3N atom coordinate parameters for each atom. For the germanate framework, distance and angle restraints of Ge-O=1.72(1) Å and O-Ge-O=109.4(1)°, respectively, were applied. The final refinement converged with the agreement factors R_1 = 0.084 for 354 reflections with $F_o > 3\sigma(F_o)$ and 0.085 for all 359 data. R_{wp} = 0.100, R_p = 0.073, R_B = 0. 129, GooF = 3.06 as shown in **Table 37**. The Rietveld plot can be seen in **Fig. 124**. Considering these calculations, the complete hybrid inorganic and organic structure of the as-made ITQ-35 retrieved from Rietveld refinement against PXRD data crystallizes in the space group *Im*-3*m* with the following unit cell parameters*: a* = *b* = *c* = 17.1677(5) Å; *α* = *β* = *γ* = 90°, *V*= 5059.9(2) Å^3. The final structure of ITQ-35 and the OSDA molecule representation can be seen **Fig. 125**. The atom coordinates are shown in **Table 38**.

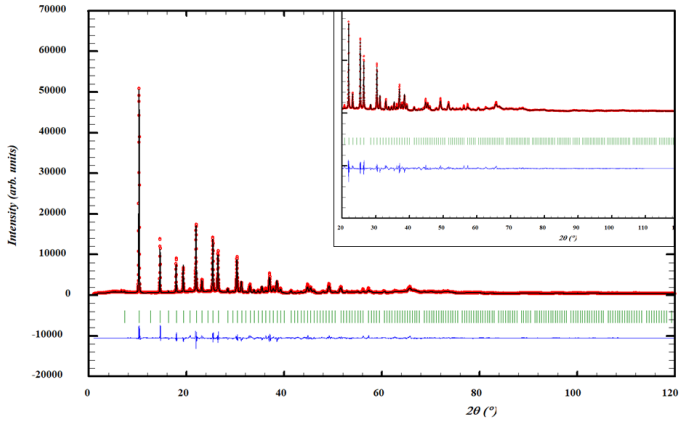

Figure 124. Rietveld refinement analysis performed on the X-ray diffraction pattern of as-made ITQ-35. Red data points show the observed XPRD pattern. Black lines are the calculated XRPD pattern. Blue lines are difference profiles and green vertical tick marks give the positions of the Bragg reflections. The inset shows the detail corresponding to the 2θ range from 20° to 120°. Residual values: R_{wp} = 0.100, R_p = 0.073, R_B = 0. 129, R_F = 0.085 and GooF = 3.06. Wavelength corresponds to Cu Kα1,2 (λ = 1.5406 Å).

Table 37. Crystallographic data from Rietveld refinement of the PXRD data on as-made ITQ-35 sample.

Chemical Composition	Ge64 O136 F8 N12 C192 H378
Refined composition	Ge0.94 O2 F0.11 N0.18 C2.82
Space group (Num.)	*Im*-3*m* (229)
a (Å)	17.1677(5)
Volume (Å^3)	5059.9(2)
Z	96
2θ range (°)	7.978 to 109.859
Wavelength (Å)	1.540598
Num. Unique reflections (I > 3 sigma(I))	354
Num. total reflections	359
Num. Geometric Restraints	20
Distance Ge-O	8
Angle O-Ge-O	12
Num. Structural refined parameters	19
Num. Profile refined parameters	22
R_{wp}	0.1
Rp	0.073
GooF	3.06
wR_2	0.094
R_B	0.129
R_1	0.085

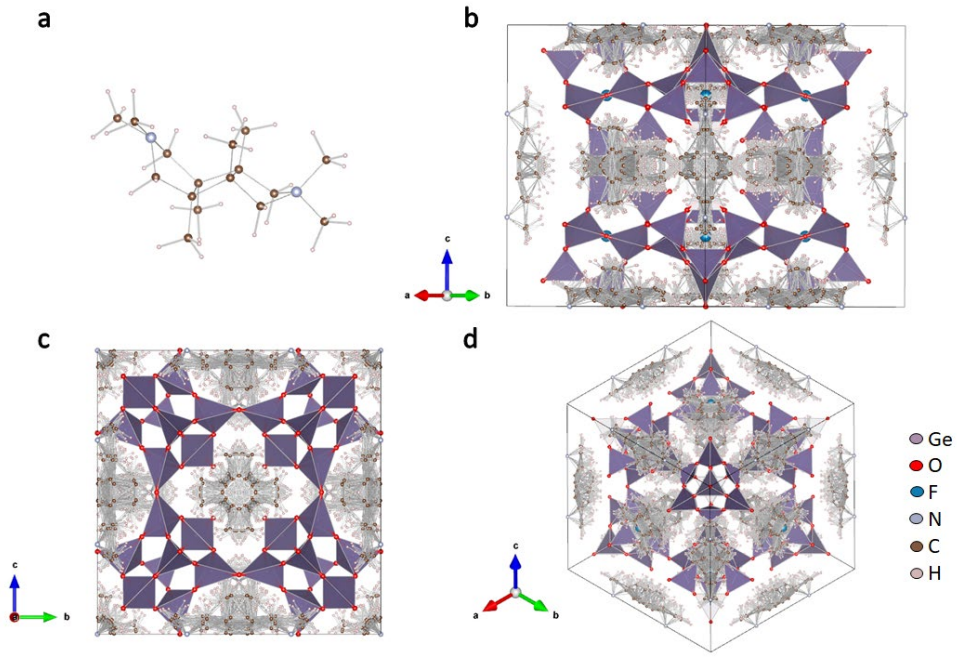

Figure 125. Structure of (a) organic structure directing agent and (b) as-made ITQ-35 structure refined against PXRD data viewed along [110], (c) [100] and (d) [111] directions. Purple: Germanium, Oxygen, white: hydrogen, brown: carbon, sky blue: nitrogen, blue: fluoride anion.

Table 38. Atomic coordinates for as-made Ge-ITQ-35 after the refinement against PXRD data. Space group= Im-3m; a=b=c=17.1677(5); α=β=γ=90º.

Atom	coordinates			Biso	Occupancy	Multiplicity & Wyckoff
	x	y	z			
Ge1	0.28008(13)	0.28008(13)	0.09920817)	0.0381(10)	1	48k
Ge2	0.1572(2)	0.1572(2)	0.1572(2)	0.0381(10)	1	16f
O1	0.2980(8)	0.2980(8)	0	0.035(4)	1	24h
O2	0.2084(5)	0.2084(5)	0.0954(7)	0.035(4)	1	48k
O3	0.1025(10)	0.1025(10)	0.1025(10)	0.035(4)	1	16f
O4	0.3631(5)	0.25	0.1369(5)	0.035(4)	1	48i
F1	0.25	0.25	0.25	0.022(10)	1	8c
N1	0.6712(11)	0.5150(17)	0.5727(16)	0.016(8)	0.125	96l
C1	-0.1120(11)	0.463(2)	0.5632(19)	0.016(8)	0.125	96l
C2	-0.1046(11)	0.380(2)	0.528(2)	0.016(8)	0.125	96l
C3	0.8039(11)	0.574(2)	0.580(2)	0.016(8)	0.125	96l
C4	-0.0327(11)	0.5025(19)	0.5391(19)	0.016(8)	0.125	96l
C5	-0.1215(12)	0.472(3)	0.6524(19)	0.016(8)	0.125	96l
C6	0.8167(11)	0.496(2)	0.5373(19)	0.016(8)	0.125	96l
C7	-0.0175(11)	0.3757(19)	0.4981(19)	0.016(8)	0.125	48j
C8	-0.1184(12)	0.312(2)	0.585(3)	0.016(8)	0.125	96l
C9	0.7356(11)	0.4527(19)	0.5443(19)	0.016(8)	0.125	96l
C10	0.8385(12)	0.501(3)	0.4502(19)	0.016(8)	0.125	48j
C11	0.7205(11)	0.564(2)	0.6169(18)	0.016(8)	0.125	96l
C12	0.8033(12)	0.651(2)	0.532(3)	0.016(8)	0.125	96l
C13	0.6293(11)	0.5425(18)	0.5077(16)	0.016(8)	0.125	96l
C14	0.6166(11)	0.4654(17)	0.6245(16)	0.016(8)	0.125	96l
C15	0.0731(11)	0.4252(19)	0.5982(16)	0.016(8)	0.125	96l
C16	0.0863(11)	0.4706(19)	0.4654(16)	0.016(8)	0.125	96l

6.7. STRUCTURE DESCRIPTION

In this manner, the initial ITQ-35 framework can be built using the following four composite building units (CBUs): two new kinds of natural tiles [12^6] and [$8^4 12^2$] containing 12T and 24T atoms (T = Ge), respectively; a D4R [4^6] cage and a [$4^4 12^2$] cage (named *t-gie-1*) shown in **Fig. 126**. The CBU [4^6] has been already reported in a large number of zeolite frameworks due to the presence of Ge atoms within the synthesis that lead to the formation of highly tensioned CBUs such as D4R. The ^{19}F-MAS-NMR spectroscopy measurements of the Ge-ITQ-35 sample indicate the presence of unique resonance at -10 ppm (see **Fig. 100**), which is a characteristic of the presence of fluorine anions located in D4R cages of germanium-rich zeolites.[131,132] The natural tiling *t-gie-2* [$4^4 12^2$] has been already reported in the zeolitic imidazole framework (ZIFs) STU-1.[133] The as-made ITQ-35 presents 8R and 12R rings. The [12^6] and [$8^4 12^2$] cages form a tri-directional 12 x 12 x 12 and 8 x 8 x 8-ring channel system, respectively, and are connected to each other via [$4^4 12^2$] cages. The channels consisting of 12 and 8 rings are straight and oriented along the same [001], [110], and [110] directions. The larger pore size (12 rings) measures a pore size of 2.30 Å x 2.30 Å in diameter, while the other 8 rings have a larger diameter of 4.43 Å x 4.43 Å (see **Fig. 116**, after subtracting two times the Van der Waals radii of oxygen atoms, 2.7 Å). ITQ-35 exhibits a relatively low framework density of 12.6 T atoms per 1000 Å^3 representing the lowest value for a pure germanate zeolite with chemical composition GeO_2 after ASU-7 (ASV) and ASU-9 (AST)[134], and IM-10 (UOZ)[135], see **Table 39**.

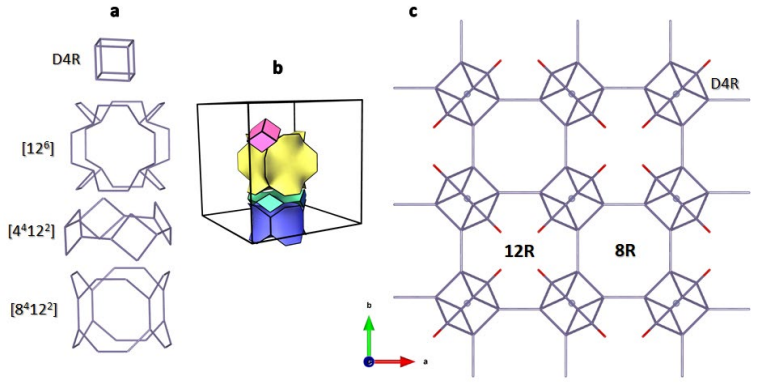

Figure 126. Construction of framework structure of ITQ-35. (a) the D4R [4^6] (8T) and the new [12^6] (32T), [$8^4 12^2$] (24T) and t-gie-2 [$4^4 12^2$] (16T) CBUs (b) zeolite natural tiling representation. [12^6] in yellow, t-cub [46] in pink, [$8^4 12^2$] in blue and t-gie-2 [$4^4 12^2$] in green. The pictures of tiling are performed with the 3dt program (http://www.gavrog.org) (c) The 3D framework structure of ITQ-35 viewed along [001] direction. The 8 and 12-ring channels are formed along [100], [010] and [001] directions. T-T bonds (T=Ge) are represented in purple sticks, fluoride anions in blue, and terminal OH/O- groups are highlighted in red for clarity.

Table 39. Framework T density values of zeolite ITQ-35 compared with other pure germanate zeolites.

Zeolite	Composition	Framework density (T/1000 Å^3)	Channel	Ref.
IM-10 (UOZ)	$Ge_{40}O_{80}$	19.5	Dense	135
ASU-7 (ASV)	$Ge_{20}O_{40}$	19.1	12	134
ASU-9 (AST)	$Ge_{40}O_{80}$	15.8	Dense	134
FOS-5 (BEC)	$Ge_{32}O_{64}$	15.1	12 x 12 x 12	136
ITQ-35	$Ge_{64}O_{128}$	12.6	12 x 12 x 12	This work

Appendix I presents a summary of the data acquisition, reduction, and refinement processes described in Chapter 6.

CHAPTER 7. CONCLUSIONS

This chapter includes the general conclusions of this thesis, showing diverse strategies employed for the structural characterization of four zeolite materials and different crystalline standard samples. The results of this thesis lead to the detailed conclusions outlined in each chapter and are summarized as follows:

ITQ-52

- 3D Electron Diffraction (3DED) experiments were conducted on the as-made N-ITQ-52 and C-ITQ-52 samples. These experiments included continuous rotation and precession electron diffraction techniques performed at room temperature using various Transmission Electron Microscopes (TEM).
- The application of these two 3DED techniques resulted in the determination of the complete zeolitic framework of the materials, and the generation of electron density maps suggesting the approximate location of the Organic Structure Directing Agent (OSDA).
- The positions of guest molecules within the zeolite structures were determined through simulated annealing.
- The complete structures were refined and obtained via the methods using PXRD data, which allowed the location also the boron atoms in the framework. The final results are consistent with the chemical analysis, indicating the accuracy of the structural models.
- Both OSDAs are located in very similar locations, as could be expected from their structural and geometrical similarities. The different density distribution in the OSDA, with a more dispersed charge distribution in the aminophosphonium compared with the alkylphosphonium cation, may favor the location of the boron species on different T-sites of the framework. This could open the possibility of controlling the preferential incorporation of trivalent elements like boron in specific T-sites of ITQ-52 by using the appropriated OSDA, with potential implications on the catalytic properties of the final zeolitic materials.

ITQ-70

- The structure of a new zeolite, named ITQ-70, has been determined by rapid continuous rotation electron diffraction, a new generation of electron detectors, and cryo-temperature tools. The silica framework structure has been solved *ab initio* using 3DED data.
- The determination of the inorganic framework has been carried out via the charge-flipping algorithm using the data obtained by 3DED, and the organic guest molecule has been located by simulated annealing. The complete model was further refined refinement using PXRD data.
- The structural model for zeolite ITQ-70 is entirely consistent with the framework connectivities proposed based on the ^{29}Si NMR (DQ-SQ) analysis and computational results of structural strain. This zeolite features 18-ring channels, structured around a building unit containing highly strained silicon atoms. Notably, the as-made ITQ-70 exhibits 38% of its silicon atoms as under-connected Q^3 silanol or siloxy groups, achieving the lowest framework density

(10.0 T/1000 $Å^3$) observed among known zeolites containing oxygen connecting the T-atoms.

- Comprehensive structural characterization using 3D-electron diffraction, molecular modelling and magic-angle spinning nuclear magnetic resonance techniques have provided a clear description of the zeolite, detailing (i) the inorganic silica framework, (ii) the position of OSDAs within the zeolite's porosity, and (iii) the identification of both siloxy and silanol functionalities.

ITQ-35

- The structure of a new zeolite, ITQ-35, has been determined. ITQ-35 features three-directional 8R and 12R cavities and contains connected D4R units. This zeolite, synthesized as a pure germanate (GeO_2), is obtained using a new class of organic structure-directing agents created through a photochemically induced [2+2] cycloaddition route for amine synthesis.
- The hybrid organic-inorganic structure of ITQ-35 was determined using precession electron diffraction tomography (PEDT). The *ab initio* structure solution revealed that the inorganic framework of ITQ-35 consists on 64 germanium atoms, 128 oxygen atoms, 8 fluoride anions, and 6 OSDA molecules per unit cell. This composition was confirmed by thermogravimetric and elemental analyses.
- Simulated annealing methods were employed to determine the guest molecule's structure, which allowed the spatial fit between the zeolite micropore and the organic guest molecule within the voids. This structure revealed the presence of structural defects, specifically GeOH and GeO^- species.

The results provide insight into the optimization of the 3DED method, demonstrating its reliability and effectiveness in solving structural materials, including the organic guest molecules within the zeolites.

APPENDIX I

This APPENDIX I provides a **Summary of Data Acquisition, Reduction, and Refinement for chapter 4, 5 and 6.**

In this thesis, different 3D Electron Diffraction (3DED) protocols were employed. Each chapter highlights a strategic approach to data acquisition, reduction, and refinement. Below is a summary of **chapter 4** and a Summary Experimental Table:

1. **Data Acquisition**
   - Two 3DED protocols were used: **Stepwise PEDT**, and **Continuos Rotation (cRED).**
   - Three TEMs were used: **JEOL 2100F**, **JEOL 2100-LaB_6**, and **FEI Tecnai G2 20** all at room temperature
2. **Data Reduction**
   - Datasets were processed with **PETS2.0.** Compared to other TEM instruments, the **FEI Tecnai G2 20** achieved improved results, with **resolutions <0.63 Å** and **completeness <76%**. **Total, accumulated electron dose >3.025 e/Å^2**.
3. **Data Refinement**
   - All dataset was **kinematically refined against 3DED** by **JANA2020** obtaining the silicoboride framework and the electrostatic potential within the cavities.
   - The data from **FEI Tecnai G2 20** show improved electrostatic potential, thus was processed by **simulated annealing**. The OSDA model was manually drawn by Chemdraw 19.0 software.
   - The data from **FEI Tecnai G2 20** was dynamically refinement against 3DED giving unsatisfactory structures and unsuccessful convergence.
   - The structure models obtained by **SA** were **refined against PXRD** for the **final refinement**.

The data sets used for the simulated annealing and for final refinement of the structure models are highlighted in yellow.

Summary Experimental Table for chapter 4

Sample	TEM	Data Set	Protocol	Critical Parameter	Purpose
C-ITQ-52	JEOL 2100F	Data Set 1	Stepwise PEDT (SAED mode)	Rint = 20.26%, completeness = 66% and resolution = 1.0 Å	Initial *ab-initio* structure solution
	JEOL 2100-LaB_6	Data Set 2	Stepwise PEDT (NBD mode)	Rint = 17.31%, completeness = 67% and resolution = 1.0 Å	Improved *ab-initio* structure solution
	FEI Tecnai G2 20	**Data Set 3**	**cRED (NBD)**	**Rint = 17.3%, completeness = 54% and resolution = 0.55 Å. Total, accumulated electron dose=1.836 e/Å²**	**Simulated Annealing and final refinement**
N-ITQ-52	JEOL 2100F	Data Set 1	Stepwise PEDT (NBD mode)	Rint = 22.52%, completeness = 62% and resolution = 1.0 Å	Initial *ab-initio* structure solution
		Data Set 2		Rint = 25.26%, completeness = 49% and resolution = 1.0 Å	Initial *ab-initio* structure solution
	JEOL 2100-LaB_6	Data Set 3	Stepwise PEDT (NBD mode)	Rint = 14.48%, completeness = 63% and resolution = 1.0 Å	Initial *ab-initio* structure solution
	FEI Tecnai G2 20	Data Set 4	**Stepwise PEDT (NBD)**	Rint = 16.53%, completeness = 76% and resolution = 0.58 Å. Total, accumulated electron dose=2.775 e/Å²	Data merging
		Data Set 5		Rint = 21.44%, completeness = 85% and resolution = 0.63 Å. Total, accumulated electron dose=3.025 e/Å²	Data merging
		Merged Data Set (from 4 and 5)		**Rint = 24.58%, completeness = 90% and resolution = 0.58 Å**	Failed dynamical refinement (incorrect structure convergence). **Simulated annealing. Final refinement**

Below is a summary of **chapter 5** and a Summary Experimental Table.

1. **Data Acquisition**
   - One 3DED protocol was used at different temperatures: **cRED in SAED mode at room temperature,** and **cRED in NBD mode at cryo conditions (T=183K).**
   - Two TEMs were used: **JEOL 2100F** and **FEI Tecnai G2 20**.
2. **Data Reduction**
   - Datasets from **FEI Tecnai G2 20** were processed with **PETS2.0** with **resolutions between 0.83-1.21 Å** and **completeness < 94%**. **Total, accumulated electron dose >9.8 e/Å^2.** All ten datasets were merged into one with PETS2.0.
3. **Data Refinement**
   - All dataset was **kinematically refined against 3DED** by **JANA2020** obtaining the SiO_2 framework and the electrostatic potential within the cavities.
   - The SiO_2 framework structure obtained from the merged dataset was processed by **simulated annealing**. The OSDA model was obtained from Single-Crystal X-Ray Diffraction technique.
   - The SiO_2+OSDA structure obtained by simulated annealing was checked by **computational methods**.
   - **Dynamical refinement** against 3DED was not attempted due to low resolution data and local disorder.
   - The structure models obtained by **SA** were **refined against PXRD** for the **final refinement**.

Summary Experimental Table for chapter 5

Sample	TEM	Data Set	Protocol	Critical Parameter	Purpose
ITQ-70	JEOL 2100F	Data Set 1	cRED (SAED mode) at room temperature	No reflections	No reflections and no structure solution
	FEI Tecnai G2 20	Data Set 1	**cRED + cryo conditions**	Rint = 39.07%, completeness = 94%, resolution = 1.0 Å. Total, accumulated electron dose = 4.1 e/Å^2	Data merging
		Data Set 2		Rint = 34.06%, completeness = 99% and resolution =0.91 Å. Total, accumulated electron dose=7.4e/Å^2	
		Data Set 3		Rint = 20.59%, completeness = 99% and resolution = 1.0Å. Total, accumulated electron dose=8.3e/Å^2	
		Data Set 4		Rint = 22.64%, completeness = 100% and resolution = 0.91Å. Total, accumulated electron dose=8.3e/Å^2	
		Data Set 5		Rint = 21.14%, completeness = 100% and resolution = 0.83Å. Total, accumulated electron dose=8.3e/Å^2	
		Data Set 6		Rint = 17.99%, completeness = 100% and resolution = 1.08Å. Total, accumulated electron dose=3.9e/Å^2	
		Data Set 7		Rint = 28.59%, completeness = 100% and resolution = 0.91Å. Total, accumulated electron dose=3.9e/Å^2	
		Data Set 8		Rint = 29.3%, completeness = 100% and resolution = 1.1Å. Total, accumulated electron dose=3.9e/Å^2	
		Data Set 9		Rint = 22.37%, completeness = 100% and resolution = 1.09Å. Total, accumulated electron dose=8.3e/Å^2	
		Data Set 10		Rint = 33.05%, completeness = 100% and resolution = 1.21Å. Total, accumulated electron dose=9.8e/Å^2	
		Merged Data Set		**Rint = 19.13%, completeness = 100%, redundancy 19.95, resolution = 0.91 Å**	Dynamical refinement no attempted (low resolution data). **Simulated annealing. Final Refinement**

Below is a summary of **chapter 6** and a Summary Experimental Table:

1. **Data Acquisition**
   - Three 3DED protocols were used: **Stepwise PEDT**, **Continuos Rotation (cRED)** and **PEDT+cRED.**
   - The TEM **FEI Tecnai G2 20** was used at cryo conditions (T=183K).
2. **Data Reduction**
   - Datasets were processed with **PETS2.0** with **resolutions <0.91 Å** and **completeness < 96%**. **Total, accumulated electron dose >11.3 e/Å².**
3. **Data Refinement**
   - All dataset was **kinematically refined against 3DED** by **JANA2020** obtaining the GeO_2 framework and the electrostatic potential within the cavities.
   - The **PEDT** dataset showed the lowest total, accumulated electron dose of 4.7 e/Å² compared to others. Therefore, this was processed by **simulated annealing**. The OSDA model was manually drawn by Chemdraw 19.0 software. The obtained structure was subsequent kinematically refinement against 3DED. The refinement of some parameters did not yield the desired convergence since the SDA positions, occupancy, and Uiso were not stable, therefore the model calculated from simulated annealing processes was discarded.
   - The OSDA was then located by **molecular dynamics**.
   - The structure model obtained by the **molecular dynamics** was **refined against PXRD** for the **final refinement**.

The data sets used for the simulated annealing and for final refinement of the structure models are highlighted in yellow:

Summary Experimental Table for chapter 6

Sample	TEM	Data Set	Protocol	Critical Parameter	Purpose
ITQ-35	**FEI Tecnai G2 20**	**Data Set 1**	**PEDT+cryo**	**Rint = 12.88%, completeness = 99%, resolution = 1.0 Å. Total, accumulated electron dose = 4.7 e/Å²**	Simulated annealing attempted. **OSDA located by molecular dynamics. Final refinement**
		Data Set 2	cRED+cryo	Rint = 21.92%, completeness = 97%, resolution = 1.0 Å. Total, accumulated electron dose = 9.1 e/Å²	Initial *ab-initio* structure solution
		Data Set 3	PEDT+cRED+cryo	Rint = 24.68%, completeness = 96% and resolution =0.91 Å. Total, accumulated electron dose=11.3e/Å²	Initial *ab-initio* structure solution

APPENDIX II

3DED PROTOCOL

This APPENDIX II provides a manual/protocol to perform a 3DED experiment in the JEOL 2100F TEM. This manual includes the acquisition data procedure in detail by two different illumination condition modes: Selected area aperture electron diffraction (SAED) and nanobeam electron diffraction mode (NBD).

An extensive review of these techniques, including their different settings, can be found in the following references:

- Ute Kolb et al., Towards automated diffraction tomography: part I--data acquisition, *Ultramicroscopy* 107 (2007) 507-513.
- Mauro Gemmi et al., 3D Electron Diffraction: The Nanocrystallography Revolution, *ACS Nano*, 15 (2), (2021) 2730-2737.
- Sergi Plana Ruiz et al. Fast-ADT: a fast and automated electron diffraction tomography setup for structure determination and refinement", *Ultramicroscopy* 211 (2020) 112951.
- J. Simancas-Coloma, et al. Ultrafast Electron Diffraction Tomography for Structure Determination of the New Zeolite ITQ-58. *J. Am. Chem. Soc.*, 138(32), 2022, 10116–10119.

Before initiating a 3DED experiment, refer to **Fig. 127**. This figure presents a preliminary experiment report template that can be completed to record various acquisition parameters. This practice ensures a systematic approach to data collection and aids in maintaining consistency throughout the experiment.

TEM measurements-Manual Diffraction Tomography

Date:___/___/____

Responsible person:_____

Sample: _____

Data Folder: _____

Grid Position: _____

TEM characteristics:

C2 aperture: _____ (____ micron)

Selected area aperture: ____ (____ micron)

Spot size: _____

Diffraction Focus :

CL3:

IL1:

Detector characteristic:

Camera length: _____ cm

Pixel size: _____1/nm

Pixel dimension: _____

Exposure time: _____

Detector binning: ___

Experimental data details:

Tilt range: ____ to ____

Tilt step: ____

Precession: _____ (˚)

Patterns collected: _____

Specimen Position:

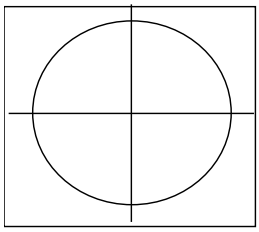

Additional Notes:

Script used: Comments:

Figure 127. Experiment report template for 3DED measurements.

SAED MODE

One method for collecting 3DED data involves switching to TEM mode and using the SAED knob situated on the external TEM column. The following outlines the steps to conduct a 3DED experiment in TEM mode. Words highlighted in black refer to **panel control knobs**; words within squares refer to any bottom of the software's window or software; bold words refer to **parameters and values.**

1. FIND THE CRYSTAL

- Once the microscope technicians have inserted the grid with the "high tilt specimen (60)" holder into the TEM, press **TEM** mode, select **SPOTSIZE 5** and **ALPHA 3**
- **Center on the middle of the grid**

2. OPEN GONIOTOOL FOCUS (Z HEIGHT)

- Find a suitable crystal within the middle area of the specimen position window using the **TRACKBALL** and pressing **SA MAG** bottom with the magnification knob **MAG/CAM L** ranging **8.000x-30.000x**.
- Save crystal position in the window Dialogue > Specimen position (left computer monitors) and memorize the position in the software
- Expand the beam with the **BRIGHTNESS** knob.
- At GonioTool software, set **f1/RATE: mode CMD (command); x y z TX TY / 60 60 12 2 12 / 100 100 0 0 0; SET**
- Press **STD** Focus in the right control panel
- At window MOVE, set **-TX 5 +TX**, and in **f1 TX 5 TY 12**, **ON (to activate the tilt speed)** → tilt the goniometer +/- 15°
- Use buttons **↑Z** and **↓Z** in the right control panel to minimize the shift when tilting the sample.

3. CONDENSER APERTURE

- Go to the isolated empty area of the sample using the trackball, while working with the fluorescent screen.
- For the condenser aperture (CA) centering: Select the desired condenser aperture (**10, 40, 100, 250 µm** in diameter (CA)). If the crystal sample

is unstable under the beam, use the **10** or **40 µm** apertures. When using the **10** or **40 µm** condenser aperture, it is not necessary to use the beam stop as long as you work with camera exposure times below **1 second** in camera view.

- Focus the beam using **BRIGHTNESS** and center the beam using **SHIFT X, Y**.
- Expand the beam using **BRIGHTNESS**.
- Adjust the beam with the **CA** dials on the column → ***The beam expands concentrically from the center***
- ***Repeat until properly centered***

4. HIGH TENSION CENTERING, TILTS AND BEAM SHIFTS (TEM TECHNICIAN WORK)

High Tension (HT) centering

- Expand the beam using **BRIGHTNESS**.
- **MAGNIFICATION 50k**, focus the beam using **BRIGHTNESS**, and center the beam using **SHIFT X, Y**.
- Press **HT WOBBLER** on the right panel and **BRIGHT TILT** on the left panel. Use **DEF/STIG X** and **DEF/STIG Y** to minimize movement.
- If the beam appears round when focused, skip the **COND STIG** step. If the beam looks oval, correct astigmatism. Press **COND STIG** and use **DEF/STIG X, Y** to make the beam round.

Tilts

- Focus the beam using **BRIGHTNESS**.
- Maintenance > Alignment > Compensator Tilt > Wobbler Tilt X, and with the **DEF/STIG X** deflector knob, make the split beam a single point. Deactivate Wobbler Tilt X.
- Activate Wobbler Tilt Y and do the same with **DEF/STIG Y**. Deactivate it.
- If the beam movement is not linear but appears as an ellipsoid, press Angle under the Compensator line and convert the ellipsoid back to a line using **DEF X** or **DEF Y**.

Shifts

- Press **SA DIFF** on the right panel to enter diffraction mode.
- Turn the **BRIGHTNESS** dial completely clockwise.
- Manipulate the **DIFF FOCUS** knob to obtain the caustic point (should resemble the Mercedes Benz logo). Go to a camera length close to **200 cm** for better alignment.
- Maintenance > Alignment > Compensator Shifts > Wobbler Shifts X, and with the **DEF/STIG X** deflector knob, make the split beam a single point. Deactivate it.
- Activate Wobbler Tilt Y and do the same with **DEF/STIG Y**. Deactivate it.

5. ASTIGMATISM CORRECTION

- This step is necessary when diffraction spots are not perfectly circular.
- Maintenance > Alignment > IL STIG, and with the **DEF/STIG X** deflector knob, make the caustic point round. Deactivate it. Do the same with **DEF/STIG Y**.
- Slightly focus and defocus the caustic point with **DIFF FOCUS** to ensure it remains round.
- If the point does not stay round, repeat astigmatism correction in the IL STIG step.
- Minimize the diameter of the caustic point by adjusting the **DIFF FOCUS** dial.

6. PRECESSION ALIGNMENT

Using the fluorescent screen

PRECESSION ANGLE (by the technician)

- Turn on the DigiStar Nanomegas P1000 precession unit and its PC. Open DigiStar Control. Select Operate mode and never work in Align mode.
- Choose a precession angle of **1°**.

SA MAG

- Work in **SA-MAG** value at **30,000x** magnification. Reduce the beam using the Brightness to a point.
- Turn **ON** **precession**, turn **OFF** **Descan** (Digistar panel).
- Go to **BEAM PIVOT POINT** The spot should appear as a circle
- Make the beam as small as possible using the **4 DIALS** on the Digistar panel (first **AMPLITUDES**, then **PHASES**).
- Increase **MAGNIFICATION** to **150k** for better alignment.
- Switch **PRECESSION** **ON** and **OFF** to check alignment → ***The beam with precession ON should stay as small as with precession OFF.***
- In **SA-MAG** mode at **50,000x**, minimally expand the beam with **BRIGHTNESS** so that it is not a point.
- (Optional) For better alignment in **SA-MAG**, go with the **TRACKBALL** to a nearby crystal, reduce, center the beam minimally to the size of the crystal and proceed with this **DESCAN ALIGN** alignment.
- Switch to **SA-DIFF** mode.
- Go to camera length **80 cm** with **MAG/CAM L** dial.
- **PRECESSION ON, DESCAN ON** (Digistar panel)
- Go to **DESCAN ALIGN**
- Center the point with the **PLA** button and **DEF/STIG X, Y**. Reduce the size of the spot by adjusting the Brightness
- Make the beam as small as possible with the **4 DIALS** on the Digistar panel (first the **AMPLITUDES** and then the **PHASES**).
- Swap **PRECESSION** **ON** and **OFF** to check the alignment → ***the beam with precession ON stays as small as in precession OFF*** → ***Precession is aligned***
- To search for crystal, have **Precession** in **OFF** and switch to **SA-MAG** mode from magnification **10,000x**.

7. CAMERA SETTING AND DATA COLLECITON SCRIPT

Remove the fluorescent screen

For ultrafast aquisition

- In Gatan Micrograph, click on Camera View.
- Setup Focus: **154, 160, 1178, 1184** **Binning 2**. Corrections: Gain normalized; Mode: User; Time(s) 0.5 s
- Advanced settings > Quality: **Fast**
- Autoexposure: 50, 20, 90, 1, 0.1. Streak corrections.
- Have the Streak correction **activated**. Standard Values: **50/20/90/1/0.1**.
  - Open Pablo's script located in Local Disk (C:) > Pruebas SEMIE > Scripts_Pablo > Select file: **Dynamic_TEM4.s**
  - Double click

(OPTIONAL) For stepwise acquisition

- In Gatan Micrograph, click on Camera Acquire.
- Select **Binning 2** and note down this value.
- Time: select **0.5 seconds** and note down this value.
- Advanced settings > Quality: **Fast**
- Have the Streak correction activated. Standard Values: **50/20/90/1/0.1**.
- Load Pablo's script located in Local Disk (C:) > SEMIE Tests > Script_Pablo > Select file: **static.s**

8. SAED

- Put the fluorescent screen (F1).
- Once the script is open. If possible, expand the beam to the maximum of the large fluorescent screen with **BRIGHTNESS**.
- In the microscope column, introduce the **1st** or **2nd** **SMALLEST SELECTED AREA APERTURE** knobs (thick handle). It is advisable to work with the **2nd** smallest one as the crystal will remain in the diffracted area and will not be lost along the tilt path.

- Center the SA using the **two small DIALS** (the front and the side). Remove again selected area aperture **SA** → ***Selected area aperture is aligned. Remove it at this moment.***

9. CAMERA LENGTH AND LAST PRECESSION ALIGNMENT

- Go to the desired crystal and center it with the **TRACKBALL**.
- Enter the desired **SA**.
- Press **SA-DIFF**
- In Digital Micrograph > Camera inserted > Start View and lift the fluorescent screen with **F1** (left control panel).
- Select a camera length with the **MAG/CAM L** knob in such a way that the diffraction points are sufficiently separated while a high number of reflections can be observed.
- Press the **PLA** button and use **DEF/STIG X and Y** to center the central spot of the diffraction pattern.
- Adjust the "Defocus" with the **DIFF FOCUS** dial (right control panel) to have well-defined spots (first a coarse adjust, and later a fine one).
- Activate the precession **PRECESSION ON**, **DESCAN ON** (Digistar panel)
- In the Descan Align window of the Digistar, define the spots with the **4 DIALS** first with the **AMPLITUDES** and then the **PHASES** → ***Precession and diffraction points corrected***
- **PRECESSION OFF**

Use the beamstop when using a large condenser lens to avoid damaging the detector and obtaining a better quality of the diffraction spots. This is not necessary with the two smaller condensers, to avoid losing the image of the direct beam.

10. DATA COLLECTION

- Press **SA-MAG**

- Go to the **starting angle** using GonioTool. If the acquisition starts from **-30°**, it would be first required going to **-32°** and then change the direction of inclination going to **-30°**.
- If the crystal is not within the selected area, slightly reposition it with the **TRACKBALL**.
- (OPTIONAL; ask technician first) Press **F2** for **beam blanking**. This way the damaging the crystal while loading the scripts will be avoided.
- Note the **initial angle** before starting.

For ultrafast acquisition

- Scripts > Execute
- Select range > D: View **4118K** in View window)
- File name: Write the name of the sample
- Choose directory > Save
- A window will appear where value of the **Tilt Range** will be entered. An example would be to enter the value **60** to go from **-30°** to **+30°**.
- **PRECESSION ON DESCAN**
- **F2** to deactivate beam blanking (OPTIONAL; see note above)
- Press **SA-DIFF**
- Acquire
- Note down the **final angle** and the **camera length**
- Stop view > **F1** → ***Diffraction patterns acquired***

(OPTIONAL) For stepwise acquisition

- Scripts > Execute
- Choose directory and name. Save.
- A window will appear where the value of the **final angle** and the value of the **tilt step** (in the case of zeolites select **1°**) will be entered.
- **PRECESSION ON**, **DESCAN OFF**
- **F2** to deactivate beam blanking
- Press **SA-DIFF**
- Acquire

- Note the **final angle** and the **camera length** → ***Diffraction patterns acquired***

11. HIGH RESOLUTION CRYSTAL IMAGEN

- **PRECESSION OFF**.
- Press **SA-MAG**
- Remove the **SELECTED AREA APERTURE**
- In GonioTool > TX Neutral to return to **zero angle**.
- Insert the **2nd LARGEST CONDENSER APERTURE** and center as before.
- Start View
- We lift the fluorescent screen **F1**
- Camera inserted > Camera acquire. Check that it is in High Quality > Exposure time between **1-2 seconds**.
- Improve contrast with **BRIGHTNESS**
- Focus crystal with **FOCUS > OBJ. FOCUS**
- Start Acquire. Save

NBD MODE

An alternative approach to acquiring 3DED data includes switching to the NBD mode. This section contains the procedure for performing a 3DED experiment within the NBD mode. It's crucial to follow the **first six steps** as outlined in the SAED mode protocol.

7. CAMERA SETTING AND DATA COLLECITON SCRIPTS

- Press **SA-MAG**
- Go to the **starting angle** using GonioTool. If the acquisition starts from **-30°**, it would be first required going to **-32°** and then change the direction of inclination going to **-30°**.
- If the crystal is not within the selected area, slightly reposition it with the **TRACKBALL**.
- Press **F2** for **beam blanking**. This way the damaging the crystal while loading the scripts will be avoided.
- Note the **initial angle** before starting
-

GATAN MICROGRAPH-BASED ULTRAFAST AND STEPWISE SCRIPTS

For ultrafast acquisition

- Scripts > Execute
- Select range > D: View **4118K** in View window)
- File name: Write the name of the sample
- Choose directory > Save
- A window will appear where value of the **Tilt Range** will be entered. An example would be to enter the value **60** to go from **-30°** to **+30°**.
- **PRECESSION ON** **DESCAN OFF**
- **F2** to deactivate beam blanking
- Press **SA-DIFF**
- Acquire
- Note down the **final angle** and the **camera length**

For stepwise acquisition

- Scripts > Execute
- Choose directory and name. Save.
- A window will appear where the value of the **final angle** and the value of the **tilt step** (in the case of zeolites select **1°**) will be entered.
- **PRECESSION ON**, **DESCAN OFF**
- **F2** to deactivate beam blanking
- Press **SA-DIFF**
- Acquire
- Note the **final angle** and the **camera length** → ***Diffraction patterns acquired***

FAST-ADT SCRIPT

- Stop view > **F1** → ***Diffraction patterns acquired***

  - In Gatan Micrograph, a new menu Fast-ADT should appear with two submenus Acquisition and Stack Split. Select Acquisition.
  - In Parameters Setup, TEM Imaging must be activated. Select Initial Angle, Final Angle, and Tilt Step. (The program has limited up to angles +/- 70°)
  - With the Go to (°) option, we can go to specific angles much faster. The Undo option is set to go back to the last angle where the stage was before having clicked "Go to".
  - Camera exposure time at **0.5 s**
  - Select **Binning 2**.
  - Lift the fluorescent screen **F1**. Start view
  - Click on Acquire CCD Image
  - Expand the beam to the maximum with **BRIGTHNESS** and center the beam with **SHIFT X and Y**
  - In the Beam Settings window, click on Get Beam Settings. The program informs that the beam should be adjusted with the beam expanded to the maximum and centered and with the magnification that we are going to use to acquire the frames. Click OK.
  - In the second window, reduce the beam to the desired beam size. To do this, draw a line in Gatan Micrograph. Double click on it and in the Integration Width box select **20**. OK.
  - In the histogram window, select the range from the beginning of the mountain in the graph to the end.
  - Reduce or expand the beam with **BRITGHNESS** until the diameter matches the desired beam size and center the beam on the screen with **SHIFT X and Y**. The beam size can vary depending on the size of the crystal. Generally, they are used between **200 -600 nm**. Note down the chosen value. Click OK.
  - In the third window in the box that appears, we write the size of the beam that we noted. OK.
  - The fluorescent screen **F1** will shuffle automatically. Lift the small fluorescent screen if it is not in place.
  - In the fourth window, switch to **SA-DIFF** mode
  - With the STINGRAM camera in VT Contrast, select **2 ms** of **exposure time** to better adjust the point.

- Vary the IL1 until we reduce to a point the central beam with **DIFF FOCUS**. OK
- Switch to **SA-MAG** mode and Start view.
- In the Beam Settings window, see that the green button appears indicating that the configuration has been established.
- Lift the fluorescent screen **F1**.
- Click on Test Beam Shift Value and center the beam with the **SHIFTS X and Y**. OK
- Again, click on Test Beam Shift Value.
- Press OK bottom four times: OK, OK, OK, OK. The program will move the beam making a cross. *Check that the beam reaches the edges of the screen and continue seeing the complete beam. On the contrary, if the size of the beam is too large or small, vary the standard value of 600 in Beam Shift Value.
- Click on Calibrate. The *BeamShiftCalibration.txt* file is created in the *FastADT_Storage* folder.
- Check the Cross correlation. Press OK and close the window.
- In the Crystal Tracking File click on Acquire (…).
- Check that the values of initial, final angle, and tilt step are correct.
- Move with the **TRACKBALL** towards the desired crystal.
- Press OK. Start View
- Lower the fluorescent screen **F1**.
- With the Set Image Setting in green and with the beam expanded on our crystal, we go to the initial angle of acquisition with GonioTool -TX. *Remember that you have to go a few angles further from the initial angle to change the direction of rotation and thus avoid the hysteresis of the goniometer. That is, if we want to acquire from -30°, we first go to -32° and go back to -30°.
- Lift the screen **F1**.
- Click on Acquire (…) again and many images corresponding to frames every 5° will come out. Click OK. The fluorescent screen automatically goes down.
- Press F2 on the left control panel. This will do beam blanking to stop irradiating the sample.
- Place the red box on the crystal of the first window.
- Click on Process. And OK.
- Check in each window that the box is located on the crystal of interest. And minimize all windows. *They are never closed, only minimized.
- Click on Process again. And Ok.
- Click on Generate. And Ok and we save the 2nd tracking file that is generated in the TEM Users folder. And Ok. *If at this point an error window appears <<Attempt to dispatch…>> You have to click on Reset

Cryst. Track. Steps and go back to the initial section of the first Acquire (…).

- Click on Load Tracking File and select the Tracking File that have been saved earlier.
- The program will automatically direct the goniometer to the initial angle.
- Deactivate the beam blanking by pressing **F2**.
- Lower the fluorescent screen with **F1**.
- At this point, the beam can be directed with the mouse and see if the crystal is at some point on the screen. *Be careful. From this step do not touch the trackball.
- Stop Start View and close the CCD window.
- Click on Initial Beam Position. And Ok.
- Drag a window of CCD to the right and we will see a hidden window behind.
- Place the red circle where we want the crystal acquisition to start. *The red box is the current position of the beam. It doesn't matter where it is left
- Press Beam position again. And Ok.
- The program will close everything
- Activate Camera Inserted
- Switch to **SA-DIFF** mode.
- **PRECESSION ON** and **DESCAN ON**. If possible, make a final adjustment of the precession with the **4 DIALS**.
- We click on START. It will start acquiring the 3DED patterns.
- Check that the initial, final angle, and exposure time were the same as those that generated the crystal tracking file.
- The frames are saved manually Save as > .dm3
- When the session is over, it is necessary to delete the .dm4 format files that are saved in C/ FAST ADT-STORAGE.
- The frames will be saved as .dm3 and as .tiff (unsigned 16-bit).

8. HIGH RESOLUTION CRYSTAL IMAGE

- **PRECESSION OFF**.
- Press **SA-MAG**
- Remove the **SELECTED AREA APERTURE**
- In GonioTool > TX Neutral to return to **zero angle**.
- Insert the **2nd LARGEST CONDENSER APERTURE** and center as before.
- Start View
- We lift the fluorescent screen **F1**

- Camera inserted > Camera acquire. Check that it is in High Quality > Exposure time between **1-2 seconds**.
- Improve contrast with **BRIGHTNESS**
- Focus crystal with **FOCUS > OBJ. FOCUS**
- Start Acquire. Save

PROTOCOL IMAGES

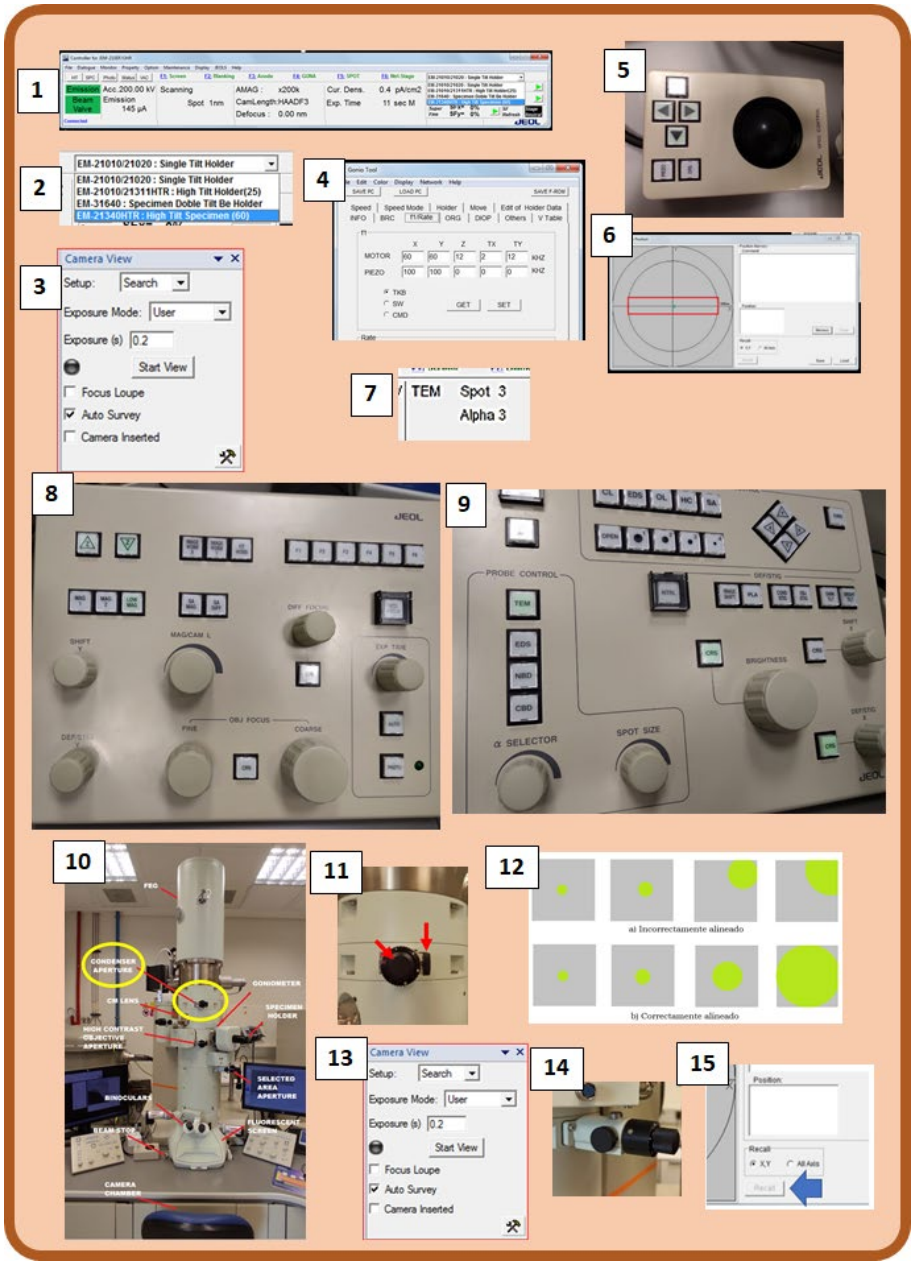

Figure 128. Images from the 3D ED protocol.

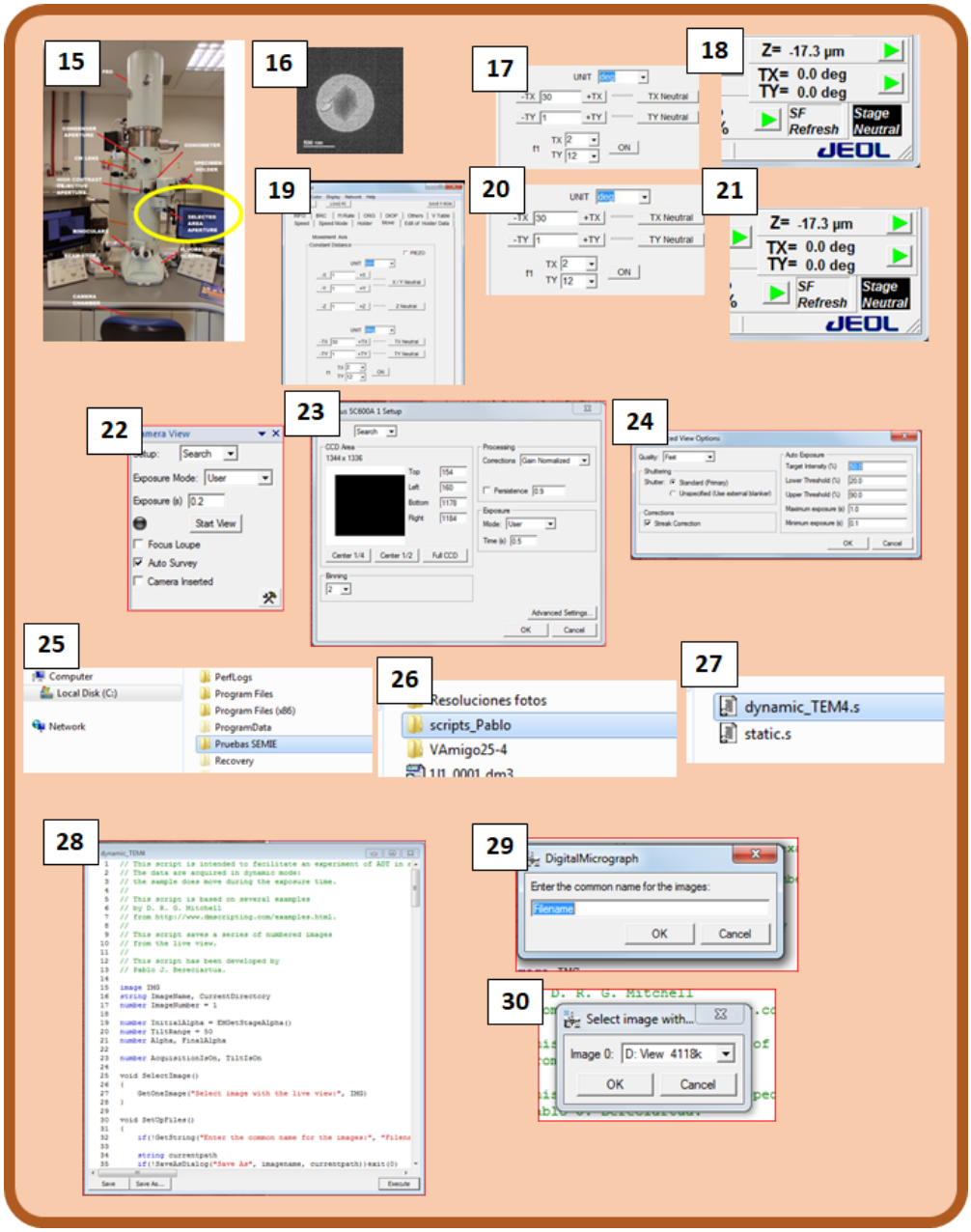

Figure 129. Images from the 3D ED protocol.

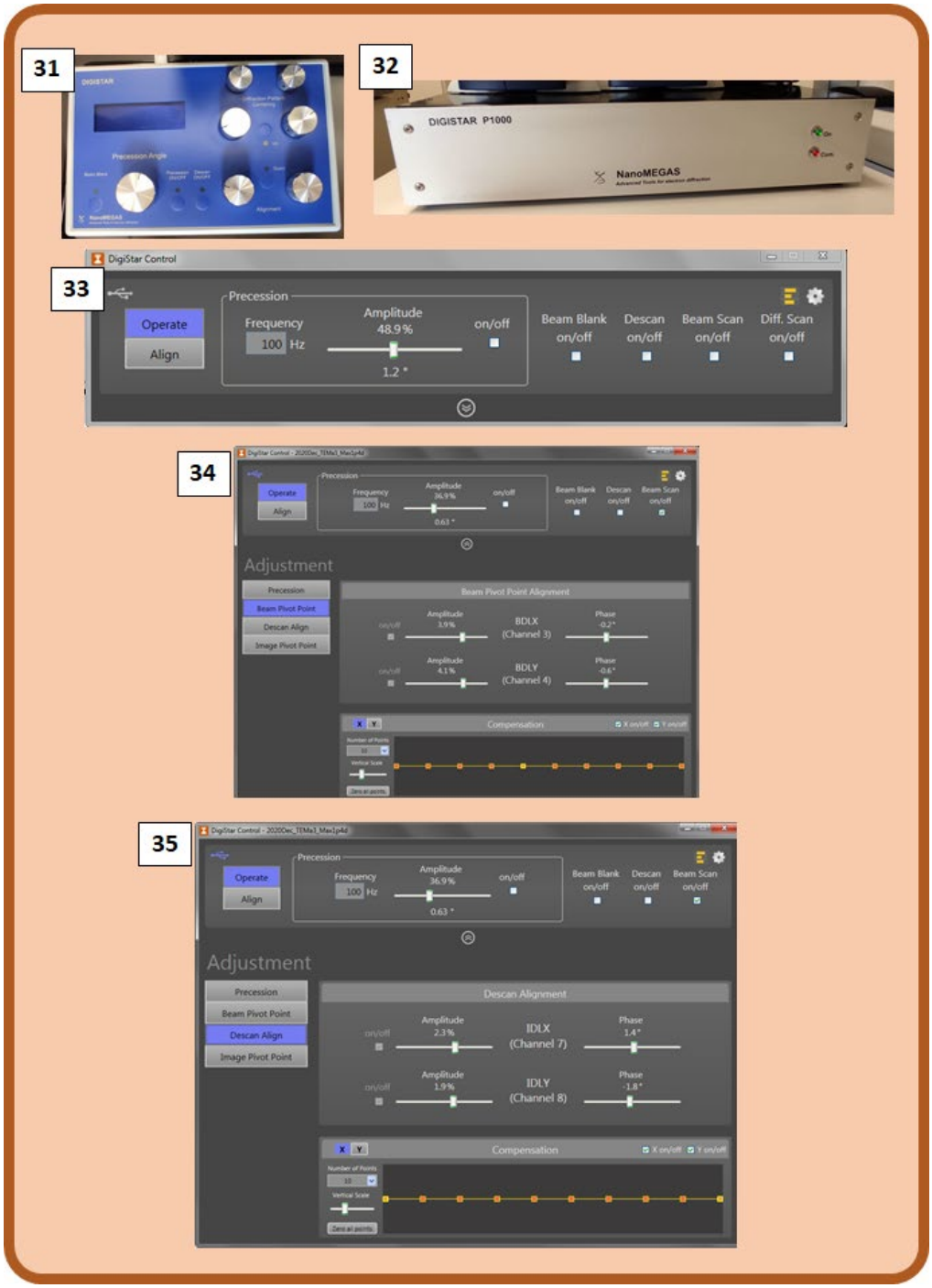

Figure 130. Images from the 3D ED protocol.

APPENDIX III

ELECTRON DOSE ANALYSIS

At UPV-TEM service no Faraday cage was available, so we have followed these steps below to measure the electron dose during the 3DED experiment. Additionally, electron dose measurements at TEM in Prague was conducted similarly:

1. **Counts/e^- camera conversion:** Search the conversion efficiency of the detector. In the case of the CCD model Gatan Orius installed in the Jeol 2100F in València UPV has a conversion efficiency of ~4 (according to the datasheet available 2-8 counts/primary electron at 100 KeV). That means that 1 electron generates ~4 counts. For the Timepix camera model QTPX-262k, the efficiency is 4.2 at 200KeV
2. **Mean counts:** Import any acquired image obtained by either SAED or NBD mode into the free available software ImageJ. Draw a square within the diffracted area, open the tool "histogram" Analyze>Histogram and take the mean value of counts. In this example is 215.

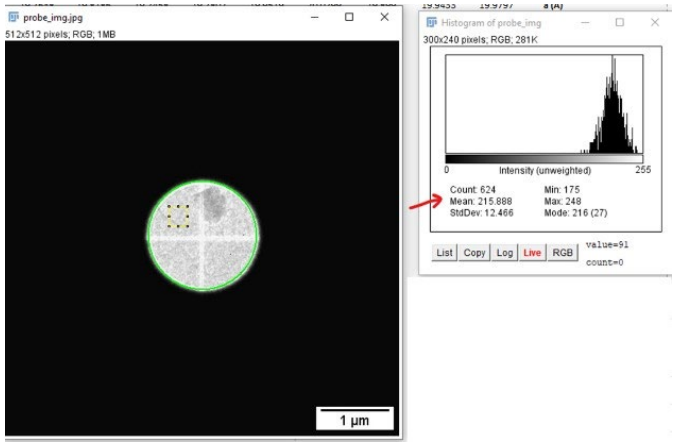

Figure 131. ImageJ graphical interface software.

3. **Electron/pixel:** Take the mean count value and the conversion efficiency of the detector to obtain the electron/pixel ratio: 215/4 = 53.75 $e^-\cdot pixel^{-1}$.
4. **Pixel squared area:** Take the pixel size value of the image, which, in this case, is 11.1 nm/pixel and square that number: 11.1^2 = 123.21 $nm2\cdot pixel^{-1}$ which gives the pixel squared area.
5. **Electron dose ratio ($e^-/Å^2s$):** Take the exposure time applied to record the image, in this case, 1s and then, 53.75 / 123.21·1 = 0.43 $el\cdot nm^{-2}\cdot s^{-1}$.
6. **Electron dose ratio per frame ($e^-/Å^2$frame):** If the exposure time for the frame acquisition was 0.5 s, then 0.43 · 2 = 0.86 $e^-\cdot nm^2\cdot frame^{-1}$ that given the unit conversion, the electron dose ratio received by the sample was 0.0086 $e^-\cdot Å^{-2}\cdot frame^{-1}$.

7. **Total electron dose ($e^-/Å^2$frame):** electron dose ratio multiplied by the total collecting time is the total electron dose that the sample has received during the complete acquisition time. In continuous rotation mode, it is coincident to the electron dose ratio per frame multiplied by the number of frames, e.g. 0.0086 $e^-/Å^2$frame times 61 frames is 0.086 total $e^-/Å^2$.
8. **Total accumulated electron dose** ($e^-/Å^2$)**:** electron dose ratio multiplied by the total collecting time is the total electron dose that the sample has received during the complete acquisition time. Since there is a beam blacking process involved during the acquisition of DPs in stepwise precession, it is coincident to the electron dose ratio multiplied by the total time without beam blacking which the sample is exposed, e.g. exposure time for the frame acquisition was 0.5 s times 61 frames is 30.5 s. Then, 0.0043 $e^-/Å^2 \cdot s^1$ times 0.5s is 0.131 $e^-/Å^2$.

LIST OF PUBLICATIONS

Published:

1. Palamara, E., Palles, D., Kamitsos, E. I., Pratim Das, P., **Tirado, Juan. I**., Nicolopoulos, S., & Zacharias, N. (2023). *Fragments of luxury: Opaque glass from the Palace of Mystras, Greece*. J. Archaeolog. Sci.: Rep., 51, 104145.
2. **Juan I. Tirado**, Andrés Sala, Antonio Bordes, Partha Pratim Das,* Lukáš Palatinus, Stavros Nicolopoulos, Jose L. Jordá,* Alejandro Vidal-Moya, Teresa Blasco, German Sastre, Susana Valencia, Fernando Rey "Synthesis and Structure Determination by 3D Electron Diffraction of the Extra-large Pore Zeolite ITQ-70" Angewandte Chemie International Edition (2024).
3. **Juan I. Tirado**, Partha Pratim Das*, Jose L. Jorda*, Lukas Palatinus, Sergi Plana-Ruiz, Jorge Simancas, Raquel Simancas, Stavros Nicolopoulos, Susana Valencia, Fernando Rey* "Structure determination of as-made zeolite ITQ-52 by three-dimensional electron diffraction" Microporous and Mesoporous Materials (2024).

In writing progress:

4. **Juan I. Tirado**, Jose Valero, Partha Pratim Das, Lukáš Palatinus, Jose L. Jordá, Angel Cantín, Susana Valencia and Fernando Rey. A New Pure Germanate Zeolite-Type ITQ-35 Solved By Precession Electron Diffraction Tomography.

CURRICULUM VITAE

BIRTHDATE: 10/03/1994

CONTACT:

+34 671 629 904

juanticasta@gmail.com

juanignaciotirado.wordpress.com

Juan Ignacio Tirado

C/ Pobla de Farnals, Valencia, 46022, Spain

INFORMATION:

- Availability to travel
- Car drive licence

SKILLS:

- Advanced electron microscopy techniques (TEM, STEM, SEM)
- Chemical analysis techniques (NMR, IR, HPLC, GC, XRF, UV, Raman, TGA, DSC)
- 3D electron diffraction (3D ED)
- Sample preparation for electron crystallography
- Data acquisition and processing (e.g., DigitalMicrograph, Gatan, Fast-ADT, Instamatic)
- Crystallography software. Structural determination and refinement (e.g., PETS2.0, eADT, JANA2020, SIR2019, FullProf Suite, X'pert HighScore, Mercury, VESTA, Diamond)
- Materials characterization and analysis (1H, 13C, 29Si, 27Al and 19F NMR, thermogravimetry)
- Scientific programming and data visualization (Python, Vesta, Mercury, Diamond)
- Strong analytical and problem-solving skills

HOBBIES:

- Piano
- Sports: Basketball, tennis, padel, football, running (marathon) and rugby.
- Cinema and books
- Homebrew beer

Juan I. Tirado

CHEMIST. ELECTRON CRYSTALLOGRAPHER AND MICROSCOPIST

Dedicated Electron Crystallographer with a proven track record in characterizing crystalline materials at the nanoscale using advanced electron microscopy techniques. Seeking an opportunity to contribute expertise in electron crystallography to cutting-edge research projects and facilitate scientific advancements

PROFFESIONAL EXPERIENCE

PHD RESEARCHER IN SUSTAINABLE CHEMISTRY (2019-PRESENT)

Instituto de Tecnología Química (UPV-CSIC). Valencia, Spain.

SEVERO OCHOA CSIC-UPV DOCTORAL SCHOLARSHIP "Catalyst Characterization: Advanced Electron Diffraction Techniques for Structural Elucidation of Microporous Materials" Supervisors: Jose Luis Jordá Moret and Partha Pratim Das

PHD RESEARCH STAY (2022)

Czech Academy of Sciences, Institute of Physics. Prague, Czech Republic

Software training programs such as PETS2, JANA, and Superflip. Similarly, direct training with the electron microscope analyzing new samples synthesized at ITQ and other centres. This includes optimizing parameters for TEM experiments, implementing dynamic refinement, and ultimately achieving the characterization of crystal structures.

LOGISTICS AND PRODUCTION ASSISTANT (2019)

DHL, SOPRONEM and WEDI GmbH. Emsdetten, North Rhine-Westphalia, Germany.

PERSONAL LABORATORY RESEARCHER (2017-2018)

University of Valencia. Valencia, Spain

"Approach to haptenic synthesis of alternariol mycotoxin". Academic mentor: Profesor Antonio Abad Somovilla

RESEARCH ASSISTANT. INTERSHIP (2017)

Parc Científic de la Universitat de València. Internship. Valencia, Spain.

Research project: "Metal complex synthesis and x-ray analysis"

POLYMER CHEMIST (2016-2017)

Cologne University of Applied Sciences. Internship. Leverkusen, Germany.

Synthesis of Copolymers for drug delivery. Polymer Characterization. Polymer Compounding. Drug Delivery. Drug Development

EDUCATION

DOCTORAL DEGREE IN SUSTAINABLE CHEMISTRY (2019-PRESENT)

Instituto de Tecnología Química (ITQ) - Valencia Polytechnic University (UPV)

MASTER IN ORGANIC CHEMISTRY (2017-2018)

University of Valencia (UV)

ERASMUS PROGRAMME INTERNSHIP. DEGREE IN CHEMISTRY (2016 - 2017)

Cologne University of Applied Sciences

DEGREE IN CHEMISTRY (2012 - 2017)

University of Valencia (UV)

ELEMENTAL MUSICION GRADE SPECIALIZING IN VIOLIN (2006 - 2010)

Academy of Music. El Ejido, Almeria, Spain

LANGUAGES

SPANISH (NATIVE) AND CATALAN

ENGLISH (C1 - OFFICIAL CERTIFICATION)

GERMAN (B1 - OFFICIAL CERTIFICATION)

Dedicated Electron Crystallographer with a proven track record in characterizing crystalline materials at the nanoscale using advanced electron microscopy techniques. Seeking an opportunity to contribute expertise in electron crystallography to cutting-edge research projects and facilitate scientific advancements

PUBLICATIONS

- **SYNTHESIS AND STRUCTURE DETERMINATION BY 3D ELECTRON DIFFRACTION OF THE EXTRA-LARGE PORE ZEOLITE ITQ-70. PUBLISHED**

  Angewandte Chemie (International ed. in English), e202416515. Advance online publication. 2024

  Tirado, J. I., Sala, A., Bordes, A., Das, P. P., Palatinus, L., Nicolopoulos, S., Jordá Moret, J. L., Vidal-Moya, A., Blasco, T., Sastre, G., Valencia, S., & Rey, F.

- **STRUCTURE DETERMINATION OF AS-MADE ZEOLITE ITQ-52 BY ELECTRON DIFFRACTION TOMOGRAPHY. PUBLISHED**

  Microporous and Mesoporous Materials, Volume 382, 113392, ISSN 1387-1811. 2024.

  Juan I. Tirado, Partha Pratim Das, Jose L. Jorda, Lukas Palatinus, Sergi Plana-Ruiz, Jorge Simancas, Raquel Simancas, Stavros Nicolopoulos, Susana Valencia, Fernando Rey

- **FRAGMENTS OF LUXURY: OPAQUE GLASS FROM THE PALACE OF MYSTRAS, GREECE. PUBLISHED**

  J. Archaeolog. Sci.: Rep., 51, 104145. . Oct 2, 2023

  Palamara, E., Palles, D., Kamitsos, E. I., Pratim Das, P., Tirado, J. I., Nicolopoulos, S., & Zacharias, N.

- **In writing progress: A New Pure Germanate Zeolite-Type ITQ-35 Solved By Precession Electron Diffraction Tomography**

RESEARCH STAY IN OTHER CENTERS

- **Synchrotron Diffraction Experiment at MSPD line, CELLS ALBA Synchrotron. Cerdañola del Vallés, Barcelona, Spain (2020).**
- **Electron Diffraction Tomography Experiment at Centres Científics i Tecnològics Universitat de Barcelona microscope servicies. Barcelona, Spain (2021).**
- **X-ray Absorption Experiment at BL22 CLAESS line, CELLS ALBA Synchrotron. Cerdañola del Vallés, Barcelona, Spain (2021).**
- **Electron Diffraction Tomography Experiments at FZU - Institute of Physics of the Czech Academy of Sciences. Prague. Czech Republic (2022).**

PROFESSIONAL CONGRESSES AND CONFERENCES

- **ONLINE ASSISTANCE: 7TH ENMIX YOUNG RESEARCHERS MEETING (EUROPEAN NANOMATERIALS INSTITUTE OF EXCELLENCE). 2020**
- **ONLINE ASSISTANCE: XXIX SIMPOSIO DEL GRUPO ESPECIALIZADO DE CRISTALOGRAFÍA Y CRECIMIENTO CRISTALINO 2021.**
- **ONLINE ASSISTANCE: 41ST AD HOC WORKSHOP ON JANA2020: ELECTRON DIFFRACTION. PRAGUE. FZU-INSTITUTE OF PHYSICS OF THE CZECH ACADEMY OF SCIENCES. 2021.**
- **ONLINE ASSISTANCE AND ORAL COMMUNICATION: YOUNG RESEARCHERS CIS 2021. 2021.**
- **ONLINE ASSISTANCE AND POSTER PRESENTATION: 25TH CONGRESS AND GENERAL ASSEMBLY OF THE INTERNATIONAL UNION OF CRYSTALLOGRAPHY (IUCR 2021). PRAGUE. 2021.**
- **ORAL COMMUNICATION: 20TH INTERNATIONAL ZEOLITE CONFERENCE (IZC 2022). VALENCIA. 2021.**
- **POSTER PRESENTATION: 6TH EUROPEAN CRYSTALLOGRAPHIC SCHOOL. INTERNATIONAL CONGRESS. 2021.**
- **ORAL COMMUNICATION: WORKSHOP ON ELECTRON CRYSTALLOGRAPHY AT ELECTRON MICROSCOPY FOR MATERIALS SCIENCE (EMAT) ANTWERP UNIVERSITY. 2023**

CV REFERENCES

ITQ-UPV: JJORDA@ITQ.UPV.ES

NANOMEGAS SPLR: PARTHA@NANOMEGAS.COM

REFERENCES

1 Johnson, N. Electron diffraction data in the CSD. CCDC https://www.ccdc.cam.ac.uk/Community/blog/2020-05-04-electron-diffraction-data-in-the-csd/ (2020)

2 Zou, X., Hovmöller, S., Oleynikov, P., Zou, X., Hovmöller, S., & Oleynikov, P. (2011). Electron Crystallography. Oxford University Press.

3 Palatinus, L., Brázda, P., Boullay, P., Perez, O., Klementová, M., Petit, S., ...Mintova, S. (2017). Hydrogen positions in single nanocrystals revealed by electron diffraction. Science, 28082587.

4 Ångström, J., Chen, H., & Wan, W. (2018). Accurate lattice-parameter determination from electron diffraction tomography data using two-dimensional diffraction vectors. J. Appl. Crystallogr., 51(4), 982–989.

5 Serebrennikova, P. C., Komarov, V. Yu., Sukhikh, A. S., & Gromilov, S. A. (2021). ON THE ACCURACY OF DETERMINING UNIT CELL PARAMETERS OF SINGLE CRYSTALS ON MODERN LABORATORY DIFFRACTOMETERS. J. Struct. Chem., 62(5), 682–691.

6 Zhang Q, Mayoral A and Li J et al. Electron microscopy studies of local structural modulations in zeolite crystals. Angew Chem Int Ed 2020; 59: 19403–13.

7 Li C, Zhang Q and Mayoral A. Ten years of aberration corrected electron microscopy for ordered nanoporous materials. ChemCatChem 2020; 12: 1248–69.

8 Thomas JM, Terasaki O and Gai PL et al. Structural elucidation of microporous and mesoporous catalysts and molecular sieves by high-resolution electron microscopy. Acc Chem Res 2001; 34: 583–94.

9 Wan W, Su J and Zou XD et al. Transmission electron microscopy as an important tool for characterization of zeolite structures. Inorg Chem Front 2018; 5: 2836–55.

10 De Broglie, L. (1925). Recherches sur la theorie des quanta. Ann. de Phys, (10), 34.

11 Girelli Consolaro, V., Rouchon, V., & Ersen, O. (2024). Electron beam damages in zeolites: A review. Microporous Mesoporous Mater., 364, 112835.

12 Dorset, D. L., & Hauptman, H. A. (1976). Direct phase determination for quasi-kinematical electron diffraction intensity data from organic microcrystals. Ultramicroscopy, 1(3), 195–201.

13 Weirich, T. E., Zou, X. D., Ramlau, R., Simon, A., Cascarano, G. L., Giacovazzo, C., & Hovmöller, S. (2000). Structures of nanometre-size crystals determined from selected-area electron diffraction data. Acta Crystallogr., Sect. A: Found. Crystallogr., 56(1), 29–35.

14 Roshko, A., Burton, G., & Geiss, R. (2022). Simple Method to Determine the Rotation Between a TEM Image and Diffraction Pattern. Microsc. Microanal., 28(S1), 782–783.

15 Dorset, D. L., Roth, W. J., & Gilmore, C. J. (2005). Electron crystallography of zeolites – the MWW family as a test of direct 3D structure determination. Acta Crystallogr., Sect. A: Found. Crystallogr., 61(5), 516–527.

16 Dorset, D. L., Gilmore, C. J., Jorda, J. L., & Nicolopoulos, S. (2007). Direct electron crystallographic determination of zeolite zonal structures. Ultramicroscopy, 107(6), 462–473.

17 Gemmi, M., Mugnaioli, E., Gorelik, T. E., Kolb, U., Palatinus, L., Boullay, P., ...Abrahams, J. P. (2019). 3D Electron Diffraction: The Nanocrystallography Revolution. ACS Cent. Sci., 5(8), 1315–1329.

18 Davisson, C., & Germer, L. H. (1927). Diffraction of Electrons by a Crystal of Nickel. Phys. Rev., 30(6), 705–740.
19 Varano, C. (2022). Pioneers in Optics: Ernst Ruska (1906–1988). Microscopy Today, 30(2), 46–46.
20 Buerger, M. J. (1964). The Precession Method in X-ray Crystallography. Wiley.
21 Weirich, T. E., Ramlau, R., Simon, A., Hovmöller, S., & Zou, X. (1996). A crystal structure determined with 0.02 Å accuracy by electron microscopy. Nature, 382, 144–146.
22 Vincent, R., & Midgley, P. A. (1994). Double conical beam-rocking system for measurement of integrated electron diffraction intensities. Ultramicroscopy, 53(3), 271–282.
23 Own, C. S. Y. (2005). System design and verification of the precession electron diffraction technique (Doctoral dissertation, Northwestern University). AND. Nanomegas. (2023, October 09). Retrieved from https://nanomegas.com/precession-electron-diffractionand-applications.
24 Kolb, U., Gorelik, T., Kübel, C., Otten, M. T., & Hubert, D. (2007). Towards automated diffraction tomography: Part I—Data acquisition. Ultramicroscopy, 107(6), 507–513.
25 Mugnaioli, E., Gorelik, T., & Kolb, U. (2009). "Ab initio" structure solution from electron diffraction data obtained by a combination of Automated Diffraction Tomography and Precession Technique. Ultramicroscopy, 109, 758–65.
26 Zhang, D.; Oleynikov, P.; Hovmöller, S.; Zou, X. Collecting 3Delectron diffraction data by the rotation method. Z. Kristallogr.2010,225,94−102(82).
27 Rozhdestvenskaya, I., Mugnaioli, E., Czank, M., Depmeier, W., Kolb, U., Reinholdt, A., & Weirich, T. (2010). The structure of charoite, (K,Sr,Ba,Mn)15–16(Ca,Na)32[(Si70(O,OH)180)](OH,F)4.0·nH2O, solved by conventional and automated electron diffraction. Mineral. Mag., 74(1), 159–177.
28 Kolb, U., Gorelik, T. E., Mugnaioli, E., & Stewart, A. (2010). Structural Characterization of Organics Using Manual and Automated Electron Diffraction. Polym. Rev., 385–409.
29 D. Denysenko, M. Grzywa, M. Tonigold, B. Streppel, I. Krkljus, M. Hirscher, E. Mugnaioli, U. Kolb, J. Hanss, D. Volkmer, Elucidating gating effects for hydrogen sorption in MFU-4-Type triazolate-based metal-organic frameworks featuring different pore sizes, Chem. – Eur. J. 17 (2011) 1837–1848, https://doi.org/10.1002/chem.201001872.
30 Jiang J, Jorda JL, Yu J, Baumes LA, Mugnaioli E, Diaz-Cabanas MJ, Kolb U, Corma A. Synthesis and structure determination of the hierarchical meso-microporous zeolite ITQ-43. Science. 2011 Aug 26;333(6046):1131-4. doi: 10.1126/science.1208652. PMID: 21868673.
31 Nederlof, I., van Genderen, E., Li, Y.-W., & Abrahams, J. P. (2013). A Medipix quantum area detector allows rotation electron diffraction data collection from submicrometre three-dimensional protein crystals. Acta Crystallogr., Sect. D: Biol. Crystallogr., 69(7), 1223–1230.
32 Brent L. Nannenga, Dan Shi, Leslie, A. G. W., & Gonen, T. (2014). High-resolution structure determination by continuous-rotation data collection in MicroED. Nat. Methods, 25086503.
33 Van Genderen, E., Clabbers, M. T. B., Das, P. P., Stewart, A., Nederlof, I., Barentsen, K. C., ...Abrahams, J. P. (2016). Ab initio structure determination of nanocrystals of organic pharmaceutical compounds by electron diffraction at room temperature using a Timepix quantum area direct electron detector. Acta Crystallogr., Sect. A: Found. Adv., 72(2), 236–242.
34 Palatinus, L., Brázda, P., Boullay, P., Perez, O., Klementová, M., Petit, S., ...Mintova, S. (2017). Hydrogen positions in single nanocrystals revealed by electron diffraction. Science, 355(6321), 166–169.

35 Gao, C., Li, J., Yin, S., Lin, G., Ma, T., Meng, Y., ...Wang, C. (2019). Isostructural Three-Dimensional Covalent Organic Frameworks. Angew. Chem. Int. Ed., 58(29), 9770–9775.

36 Kolb, U., Mugnaioli, E., & Gorelik, T. E. (2011). Automated electron diffraction tomography – a new tool for nano crystal structure analysis. Cryst. Res. Technol., 46(6), 542–554.

37 Palatinus, L., Brázda, P., Jelínek, M., Hrdá, J., Steciuk, G., & Klementová, M. (2019). Specifics of the data processing of precession electron diffraction tomography data and their implementation in the program PETS2.0. Acta Crystallogr., Sect. B: Struct. Sci., Cryst. Eng. Mater., 75(4), 512–522

38 Mugnaioli, E., & Kolb, U. (2013). Applications of automated diffraction tomography (ADT) on nanocrystalline porous materials. Microporous Mesoporous Mater., 166, 93–101.

39 Hua, W., Chen, H., Yu, Z.-B., Zou, X., Lin, J., & Sun, J. (2014). A Germanosilicate Structure with 11×11×12-Ring Channels Solved by Electron Crystallography. Angew. Chem. Int. Ed., 53(23), 5868–5871.

40 Guo, P., Shin, J., Greenaway, A. G., Min, J. G., Su, J., Choi, H. J., ...Zou, X. (2015). A zeolite family with expanding structural complexity and embedded isoreticular structures. Nature, 524, 74–78.

41 Martínez-Franco, R., Moliner, M., Yun, Y., Sun, J., Wan, W., Zou, X., & Corma, A. (2013). Synthesis of an extra-large molecular sieve using proton sponges as organic structure-directing agents. Proc. Natl. Acad. Sci. U.S.A., 110(10), 3749–3754.

42 Smeets, S., McCusker, L. B., Baerlocher, C., Mugnaioli, E., & Kolb, U. (2013). Using FOCUS to solve zeolite structures from three-dimensional electron diffraction data. J. Appl. Crystallogr., 46(4), 1017–1023.

43 Palatinus, L., Petříček, V., & Corrêa, C. A. (2015). Structure refinement using precession electron diffraction tomography and dynamical diffraction: theory and implementation. Acta Crystallogr., Sect. A: Found. Adv., 71(2), 235–244.

44 Petříček, V., Palatinus, L., Plášil, J., & Dušek, M. Zeitschrift für Kristallographie - Crystalline Materials, 2023, 238(7-8), 271–282.

45 Plana-Ruiz, S., Krysiak, Y., Portillo, J., Alig, E., Estradé, S., Peiró, F., & Kolb, U. (2020). Fast-ADT: A fast and automated electron diffraction tomography setup for structure determination and refinement. Ultramicroscopy, 211, 112951.

46 Wan, W., Sun, J., Su, J., Hovmöller, S., & Zou, X. (2013). Three-dimensional rotation electron diffraction: software RED for automated data collection and data processing. J. Appl. Crystallogr., 46(6), 1863–1873.

47 Nannenga, B. L., Shi, D., Leslie, A. G. W., & Gonen, T. (2014). High-resolution structure determination by continuous-rotation data collection in MicroED. Nat. Methods, 11, 927–930.

48 Jones, C., Martynowycz, M. W., Hattne, J., Fulton, T. J., Stoltz, B. M., Rodriguez, J. A., ...Gonen, T. (2018). The CryoEM Method MicroED as a Powerful Tool for Small Molecule Structure Determination. ACS Cent. Sci., 4(11), 1587–1592.

49 Smeets, S., & Wan, W. (2017). Serial electron crystallography: merging diffraction data through rank aggregation. J. Appl. Crystallogr., 50(3), 885–892.

50 Database of Zeolite Structures. (accessed on 5 September 2024). Retrieved from http://www.iza-structure.org/databases

51 Gruene, T., & Mugnaioli, E. (2021). 3D Electron Diffraction for Chemical Analysis: Instrumentation Developments and Innovative Applications. Chem. Rev., 121(19), 11823–11834.

52 Tinti, G., Fröjdh, E., van Genderen, E., Gruene, T., Schmitt, B., de Winter, D. A. M., ...Abrahams, J. P. (2018). Electron crystallography with the EIGER detector. IUCrJ, 5(2), 190–199.
53 What is Pixel Binning in CCD Cameras? - Oxford Instruments. (2024, January 17). Retrieved from https://andor.oxinst.com/learning/view/article/ccd-binning
54 Qu, H., Ma, Y., Li, B., & Wang, L. (2020). Hierarchical zeolites: synthesis, structural control, and catalytic applications. emergent mater., 3(3), 225–245.
55 Kordala, N., & Wyszkowski, M. (2024). Zeolite Properties, Methods of Synthesis, and Selected Applications. Molecules, 29(5), 1069.
56 Wan, W., Su, J., Zou, X. D., & Willhammar, T. (2018). Transmission electron microscopy as an important tool for characterization of zeolite structures. Inorg. Chem. Front., 5(11), 2836–2855.
57 Huang, Z., Willhammar, T., & Zou, X. (2021). Three-dimensional electron diffraction for porous crystalline materials: structural determination and beyond. Chem. Sci., 12(4), 1206–1219.
58 Camalli, M., Carrozzini, B., Cascarano, G. L., & Giacovazzo, C. (2011). From Sir2008 to Sir2011: the role of electron diffraction. Cryst. Res. Technol., 46(6), 555–560.
59 Burla, M. C., Caliandro, R., Carrozzini, B., Cascarano, G. L., Cuocci, C., Giacovazzo, C., Polidori, G. (2015). Crystal structure determination and refinement via SIR2014. J. Appl. Crystallogr., 48(1), 306–309.
60 Klar, P. B., Krysiak, Y., Xu, H., Steciuk, G., Cho, J., Zou, X., & Palatinus, L. (2023). Accurate structure models and absolute configuration determination using dynamical effects in continuous-rotation 3D electron diffraction data. Nat. Chem., 15, 848–855.
61 Ma, Y., Oleynikov, P., & Terasaki, O. (2017). Electron crystallography for determining the handedness of a chiral zeolite nanocrystal. Nat. Mater., 16, 755–759.
62 Ge, M., Yang, T., Xu, H., Zou, X., & Huang, Z. (2022). Direct Location of Organic Molecules in Framework Materials by Three-Dimensional Electron Diffraction. J. Am. Chem. Soc., 144(33), 15165–15174.
63 Wagner, A., Merkelbach, J., Samperisi, L., Pinsk, N., Kariuki, B. M., Hughes, C. E., ...Palmer, B. A. (2024). Structure Determination of Biogenic Crystals Directly from 3D Electron Diffraction Data. Cryst. Growth Des., 2024.
64 Mugnaioli, E., Lanza, A. E., Bortolozzi, G., Righi, L., Merlini, M., Cappello, V., ...Gemmi, M. (2020). Electron Diffraction on Flash-Frozen Cowlesite Reveals the Structure of the First Two-Dimensional Natural Zeolite. ACS Cent. Sci., 6(9), 1578–1586.
65 Cho, J., Willhammar, T., & Zou, X. (2023). The synergistic development of electron crystallography and zeolite discovery. Microporous Mesoporous Mater., 358, 112400.
66 Mathieu, Y., Paillaud, J.-L., Caullet, P., & Bats, N. (2004). Synthesis and characterization of IM-10: a new microporous silicogermanate with a novel topology. Microporous Mesoporous Mater., 75(1), 13–22.
67 Wang, J., Ma, C., Liu, J., Liu, Y., Xu, X., Xie, M., ...Liu, Z. (2023). Pure Silica with Ordered Silanols for Propylene/Propane Adsorptive Separation Unraveled by Three-Dimensional Electron Diffraction. J. Am. Chem. Soc., 145(12), 6853–6860.
68 Luo, Y., Fu, W., Wang, B., Yuan, Z., Sun, J., Zou, X., & Yang, W. (2022). SCM-25: A Zeolite with Ordered Meso-cavities Interconnected by 12 × 12 × 10-Ring Channels Determined by 3D Electron Diffraction. Inorg. Chem., 61(10), 4371–4377.
69 Jo, D., Zhao, J., Cho, J., Lee, J. H., Liu, Y., Liu, C.-j., ...Hong, S. B. (2020). PST-24: A Zeolite with Varying Intracrystalline Channel Dimensionality. Angew. Chem. Int. Ed., 59(40), 17691–17696.

70 Krysiak, Y., Maslyk, M., Silva, B. N., Plana-Ruiz, S., & Pastore, H. O. (2021). The Elusive Structure of Magadiite, Solved by 3D Electron Diffraction and Model Building. Chem. Mater., 33(9), 3207–3219.

71 Nanomegas. (2024, July 18). Retrieved from https://nanomegas.com

72 Simancas, J., Simancas, R., Bereciartua, P. J., Jorda, J. L., Rey, F., Corma, A., ...Mugnaioli, E. (2016). Ultrafast Electron Diffraction Tomography for Structure Determination of the New Zeolite ITQ-58. J. Am. Chem. Soc., 138(32), 10116–10119.

73 Palatinus, L., Brázda, P., Jelínek, M., Hrdá, J., Steciuk, G., & Klementová, M. (2019). Specifics of the data processing of precession electron diffraction tomography data and their implementation in the program PETS2.0. Acta Crystallogr., Sect. B: Struct. Sci., Cryst. Eng. Mater., 75(4), 512–522.

74 Petříček, V., Dušek, M., & Palatinus, L. (2014). Crystallographic Computing System JANA2006: General features. Zeitschrift für Kristallographie - Crystalline Materials, 229(5), 345–352.

75 M. C. Burla, R. Caliandro, B. Carrozzini, G. L. Cascarano, C. Cuocci, C. Giacovazzo, M. Mallamo, A. Mazzone, and G. Polidori. J. Appl. Cryst., vol. 48, pp. 306–309, Feb. 2015.

76 Palatinus, L., & Chapuis, G. (2007). SUPERFLIP – a computer program for the solution of crystal structures by charge flipping in arbitrary dimensions. J. Appl. Crystallogr., 40(4), 786–790.

77 J. Rodriguez-Carvajal, "FULLPROF: A Program for Rietveld Refinement and Pattern Matching Analysis", Abstracts of the Satellite Meeting on Powder Diffraction of the XV Congress of the IUCr, p. 127, Toulouse, France (1990).

78 Gálvez-Llompart, M., Cantín, A., Rey, F., & Sastre, G. (2019). Computational screening of structure directing agents for the synthesis of zeolites. A simplified model. Zeitschrift für Kristallographie - Crystalline Materials, 234(7-8), 451–460.

79 T. Blasco, A. Corma, M. J. Díaz-Cabañas, F. Rey, J. A. Vidal-Moya, C. M. Zicovich-Wilson, J. Phys. Chem. B 2002, 106, 2634–2642.] [Y. Wang, J. Song, H. Gies, Solid State Sci. 2003, 5, 1421–1433

80 Thomas, J. M., Klinowski, J., Ramdas, S., Hunter, B. K., & Tennakoon, D. T. B. (1983). The evaluation of non-equivalent tetrahedral sites from 29Si NMR chemical shifts in zeolites and related aluminosilicates. Chem. Phys. Lett., 102(2), 158–162.

81 T. Willhammar, A. W. Burton, Y. Yun, J. Sun, M. Afeworki, K. G. Strohmaier, H. Vroman, X. Zou, J. Am. Chem. Soc 2014, 136, 13570–13573.

82 Juan I. Tirado, Partha Pratim Das*, Jose L. Jorda*, Lukas Palatinus, Sergi Plana-Ruiz, Jorge Simancas, Raquel Simancas, Stavros Nicolopoulos, Susana Valencia, Fernando Rey* "Structure determination of as-made zeolite ITQ-52 by three-dimensional electron diffraction" Microporous and Mesoporous Materials (2024). SUBMITTED

83 Simancas, R., Jordá, J. L., Rey, F., Corma, A., Cantín, A., Peral, I., & Popescu, C. (2014). A New Microporous Zeolitic Silicoborate (ITQ-52) with Interconnected Small and Medium Pores. J. Am. Chem. Soc., 136(9), 3342–3345.

84 Dorset, D. L., Strohmaier, K. G., Kliewer, C. E., Corma, A., Díaz-Cabañas, M. J., Rey, F., & Gilmore, C. J. (2008). Crystal Structure of ITQ-26, a 3D Framework with Extra-Large Pores. Chem. Mater., 20(16), 5325–5331.

85 Dorset, D. L., Kennedy, G. J., Strohmaier, K. G., Diaz-Cabañas, M. J., Rey, F., & Corma, A. (2006). P-Derived Organic Cations as Structure-Directing Agents: Synthesis of a High-Silica Zeolite (ITQ-27) with a Two-Dimensional 12-Ring Channel System. J. Am. Chem. Soc., 128(27), 8862–8867.

86 Corma, A., Diaz-Cabanas, M. J., Jorda, J. L., Rey, F., Sastre, G., & Strohmaier, K. G. (2008). A Zeolitic Structure (ITQ-34) with Connected 9- and 10-Ring Channels Obtained with Phosphonium Cations as Structure Directing Agents. J. Am. Chem. Soc., 130(49), 16482–16483.

87 Hernández-Rodríguez, M., Jordá, J. L., Rey, F., & Corma, A. (2012). Synthesis and Structure Determination of a New Microporous Zeolite with Large Cavities Connected by Small Pores. J. Am. Chem. Soc., 134(32), 13232–13235.

88 Yun, Y., Hernández, M., Wan, W., Zou, X., Jordá, J. L., Cantín, A., ...Corma, A. (2015). The first zeolite with a tri-directional extra-large 14-ring pore system derived using a phosphonium-based organic molecule. Chem. Commun., 51(36), 7602–7605.

89 Tsuchiya, K., Tsunoji, N., Sasaki, Y., Uemura, M., Onishi, M., Sadakane, M., & Sano, T. (2020). Triple-template system for phosphorus-modified AFX/CHA intergrowth zeolite. Microporous Mesoporous Mater., 309, 110540.

90 Lin, Q.-F., Gao, Z. R., Lin, C., Zhang, S., Chen, J., Li, Z., ...Chen, F.-J. (2021). A stable aluminosilicate zeolite with intersecting three-dimensional extra-large pores. Science, 374(6575), 1605–1608.

91 Li, J., Gao, Z. R., Lin, Q.-F., Liu, C., Gao, F., Lin, C., ...Yu, J. (2023). A 3D extra-large-pore zeolite enabled by 1D-to-3D topotactic condensation of a chain silicate. Science, 379(6629), 283–287.

92 Martinez-Ortigosa, J., Millán, R., Simancas, J., Hernández-Rodríguez, M., Vidal-Moya, J. A., Jordá, J. L., ...Rey, F. (2024). Crystalline phase transition in as-synthesized pure silica zeolite RTH containing tetra-alkyl phosphonium as organic structure directing agent. J. Mater. Chem. A, 12(2), 876–891.

93 Pinar, A. B., McCusker, L. B., Baerlocher, C., Schmidt, J., Hwang, S.-J., Davis, M. E., & Zones, S. I. (2015). Location of Ge and extra-framework species in the zeolite ITQ-24. Dalton Trans., 44(13), 6288–6295.

94 Pinar, A. B., McCusker, L. B., Baerlocher, C., Hwang, S.-J., Xie, D., Benin, A. I., & Zones, S. I. (2016). Synthesis and structural characterization of Zn-containing DAF-1. New J. Chem., 40(5), 4160–4166.

95 Smeets, S., McCusker, L. B., Baerlocher, C., Elomari, S., Xie, D., & Zones, S. I. (2016). Locating Organic Guests in Inorganic Host Materials from X-ray Powder Diffraction Data. J. Am. Chem. Soc., 138(22), 7099–7106.

96 Smeets, S., & McCusker, L. B. (2017). Location of Organic Structure-Directing Agents in Zeolites Using Diffraction Techniques. Insights into the Chemistry of Organic Structure-Directing Agents in the Synthesis of Zeolitic Materials. Springer.

97 Sáez-Ferre, S., Lopes, C. W., Simancas, J., Vidal-Moya, A., Blasco, T., Agostini, G., ...Oña-Burgos, P. (2019). Use of Alkylarsonium Directing Agents for the Synthesis and Study of Zeolites. Chem. Eur. J., 25(71), 16390–16396.

98 Schwesinger, R., & Schlemper, H. (1987). Peralkylated Polyaminophosphazenes— Extremely Strong, Neutral Nitrogen Bases. Angew. Chem., Int. Ed. Engl., 26(11), 1167–1169.

99 Electron Microscopy Service: UPV. (2024, August 09). Retrieved from http://www.upv.es/entidades/SME/indexi.html

100 Ccitub, S. (2024, May 15). Technologies | CCiTUB. Retrieved from https://www.ccit.ub.edu/EN/m2.html

101 Transmisní elektronový mikroskop FEI Tecnai G2 20. (2024, August 09). Retrieved from https://www.fzu.cz/en/services/equipment-and-technologies/experimental-equipments/transmisni-elektronovy-mikroskop-fei

102 Zhang, C., Kapaca, E., Li, J., Liu, Y., Yi, X., Zheng, A., ...Yu, J. (2018). An Extra-Large-Pore Zeolite with 24×8×8-Ring Channels Using a Structure-Directing Agent Derived from Traditional Chinese Medicine. Angew. Chem. Int. Ed., 57(22), 6486–6490.

103 Inge, A. K., Huang, S., Chen, H., Moraga, F., Sun, J., & Zou, X. (2012). The Structure of a Complex Open-Framework Germanate Obtained by Combining Powder Charge-Flipping and Simulated Annealing. Cryst. Growth Des., 12(10), 4853–4860.

104 Xu, Y., Liu, L., Chevrier, D. M., Sun, J., Zhang, P., & Yu, J. (2013). Germanate with Three-Dimensional 12 × 12 × 11-Ring Channels Solved by X-ray Powder Diffraction with Charge-Flipping Algorithm. Inorg. Chem., 52(18), 10238–10244.

105 Cousins, K. R. (2011). Computer Review of ChemDraw Ultra 12.0. J. Am. Chem. Soc., 133(21), 8388–8388

106 Juan I. Tirado, Andrés Sala, Antonio Bordes, Partha Pratim Das,* Lukáš Palatinus, Stavros Nicolopoulos, Jose L. Jordá,* Alejandro Vidal-Moya, Teresa Blasco, German Sastre, Susana Valencia, Fernando Rey "Synthesis and Structure Determination by 3D Electron Diffraction of the Extra-large Pore Zeolite ITQ-70" Angewandte Chemie International Edition (2024). SUBMITTED

107 Sala Gascón, A. (2024). Síntesis y caracterización avanzada de materiales zeolíticos mediante el empleo de nuevos agentes orgánicos directores de estructura. Universitat Politècnica de València.

108 Yamasaki, Y., Tsunoji, N., Takamitsu, Y., Sadakane, M., & Sano, T. (2016). Synthesis of phosphorus-modified small-pore zeolites utilizing tetraalkyl phosphonium cations as both structure-directing and phosphorous modification agents. Microporous Mesoporous Mater., 223, 129–139.

109 Rey, F., & Simancas, J. (2017). Beyond Nitrogen OSDAs. Insights into the Chemistry of Organic Structure-Directing Agents in the Synthesis of Zeolitic Materials. Springer.

110 Dorset, D. L., Kennedy, G. J., Strohmaier, K. G., Diaz-Cabañas, M. J., Rey, F., & Corma, A. (2006). P-Derived Organic Cations as Structure-Directing Agents: Synthesis of a High-Silica Zeolite (ITQ-27) with a Two-Dimensional 12-Ring Channel System. J. Am. Chem. Soc., 128(27), 8862–8867.

111 Corma, A., Diaz-Cabanas, M. J., Jorda, J. L., Rey, F., Sastre, G., & Strohmaier, K. G. (2008). A Zeolitic Structure (ITQ-34) with Connected 9- and 10-Ring Channels Obtained with Phosphonium Cations as Structure Directing Agents. J. Am. Chem. Soc., 130(49), 16482–16483.

112 Yun, Y., Hernández, M., Wan, W., Zou, X., Jordá, J. L., Cantín, A., ...Corma, A. (2015). The first zeolite with a tri-directional extra-large 14-ring pore system derived using a phosphonium-based organic molecule. Chem. Commun., 51(36), 7602–7605.

113 Lin, Q.-F., Gao, Z. R., Lin, C., Zhang, S., Chen, J., Li, Z., ...Chen, F.-J. (2021). A stable aluminosilicate zeolite with intersecting three-dimensional extra-large pores. Science, 374(6575), 1605–1608.

114 Simancas Coloma, J. (2022). Synthesis and Characterization of Zeolitic Materials Using Phosphorous Organic Structure Directing Agents. Universitat Politècnica de València.

115 Thommes, M., Kaneko, K., Neimark, A. V., Olivier, J. P., Rodriguez-Reinoso, F., Rouquerol, J., & Sing, K. S. W. (2015). Physisorption of gases, with special reference to the evaluation of surface area and pore size distribution (IUPAC Technical Report). Pure Appl. Chem., 87(9-10), 1051–1069.

116 G. Horváth, K. Kawazoe, J. Chem. Eng. Japan 1983, 16, 470.

117 Thomas, J. M., Klinowski, J., Ramdas, S., Hunter, B. K., & Tennakoon, D. T. B. (1983). The evaluation of non-equivalent tetrahedral sites from 29Si NMR chemical shifts in zeolites and related aluminosilicates. Chem. Phys. Lett., 102(2), 158–162.

118 Werner, P.-E., Eriksson, L., & Westdahl, M. (1985). TREOR, a semi-exhaustive trial-and-error powder indexing program for all symmetries. J. Appl. Crystallogr., 18(5), 367–370.
119 Fecher, G. H., Kübler, J., & Felser, C. (2022). Chirality in the Solid State: Chiral Crystal Structures in Chiral and Achiral Space Groups. Materials, 15(17), 5812.
120 Brázda, P., Palatinus, L., & Babor, M. (2019). Electron diffraction determines molecular absolute configuration in a pharmaceutical nanocrystal. Science, 364(6441), 667–669.
121 Kiselev, A. V., Lopatkin, A. A., & Shulga, A. A. (1985). Molecular statistical calculation of gas adsorption by silicalite. Zeolites, 5(4), 261–267.
122 Catlow, C. R. A., Freeman, C. M., Vessal, B., Tomlinson, S. M., & Leslie, M. (1991). Molecular dynamics studies of hydrocarbon diffusion in zeolites. J. Chem. Soc., Faraday Trans., 87(13), 1947–1950.
123 B. Vessal, M. Leslie, and C. R. A. Catlow; Molecular Dynamics Simulation of Silica Glass; Mol. Simul. 1989, 3, 123-136.
124 Sastre, G., & Gale, J. D. (2001). ZeoTsites: a code for topological and crystallographic tetrahedral sites analysis in zeolites and zeotypes. Microporous Mesoporous Mater., 43(1), 27–40.
125 Bermúdez, D., & Sastre, G. (2017). Calculation of pore diameters in zeolites. Theor. Chem. Acc., 136(10), 1–11.
126 Brunklaus, G., Koller, H., & Zones, S. I. (2016). Defect Models of As-Made High-Silica Zeolites: Clusters of Hydrogen-Bonds and Their Interaction with the Organic Structure-Directing Agents Determined from 1H Double and Triple Quantum NMR Spectroscopy. Angew. Chem. Int. Ed., 55(46), 14459–14463.
127 Koller, H., Lobo, R. F., Burkett, S. L., & Davis, M. E. (1995). SiO-.HOSi hydrogen bonds in as-synthesized high-silica zeolites. The Journal of Physical Chemistry, 99(33), 12588-12596.
128 V. Petříček, M. Dušek, L. Palatinus, Z. Kristallogr. 2014, 229, 345-352.
129 Hanwell, M. D., Curtis, D. E., Lonie, D. C., Vandermeersch, T., Zurek, E., & Hutchison, G. R. (2012). Avogadro: an advanced semantic chemical editor, visualization, and analysis platform. J. Cheminf., 4(1), 1–17.
130 M. C. Burla, R. Caliandro, B. Carrozzini, G. L. Cascarano, C. Cuocci, C. Giacovazzo, M. Mallamo, A. Mazzone, G. Polidori, J. Appl. Crystallogr. 2015, 48, 306–309.
131 J. A. Vidal-Moya Ph.D Thesis, Universitat Politècnica de València (2004).
132 Wang, Y., Song, J., & Gies, H. (2003). The substitution of germanium for silicon in AST-type zeolite. Solid State Sci., 5(11), 1421–1433.
133 Zhou, X.-P., Li, M., Liu, J., & Li, D. (2012). Gyroidal Metal–Organic Frameworks. J. Am. Chem. Soc., 134(1), 67–70.
134 Wang, Y., Song, J., & Gies, H. Solid State Sci., 2003, 5(11), 1421–1433.
135 Conradsson, T., Dadachov, M. S., & Zou, X. D. Microporous Mesoporous Mater., 2000, 41(1), 183–191.
136 Conradsson, T., Zou, X., & Dadachov, M. S. (2001). 09-O-03 FOS-5, a novel zeotype with 3D interconnected 12-ring channels. Studies in Surface Science and Catalysis. Elsevier.